PADOVA UNIVERSITY

SCIENCE FACULTY

PHYSICS DEPARTMENT "G. GALILEI"

PhD THESIS

Measurement of beauty production at HERA with a $D^* + \mu$ tag.

Advisor: *Dott. Riccardo Brugnera*

Coordinator: *Prof. Attilio Stella*

Student: *Andrea Longhin*

31 October 2003

UNIVERSITÀ DEGLI STUDI DI PADOVA

FACOLTÀ DI SCIENZE MM. FF. NN.

DIPARTIMENTO DI FISICA "G. GALILEI"

DOTTORATO DI RICERCA IN FISICA

XVI ciclo

Measurement of beauty production at HERA with a $D^* + \mu$ tag.

Coordinatore: *Ch.mo Prof. Attilio Stella*

Supervisore: *Dott. Riccardo Brugnera*

Dottorando: *Andrea Longhin*

31 Ottobre 2003

Alla mia famiglia e a Sara

Ships in harbor are safe but
that's not what ships are built for.

A trattenermi
fu l'atroce sensazione che,
se avessi interferito in
un modo qualsiasi
con l'opera del Fato,
cercando di razionalizzare
il suo fantastico dono,
quel dono mi sarebbe stato strappato
come il palazzo in cima alla montagna
di quella fiaba orientale,
che scompariva
non appena un aspirante proprietario
domandava al custode
come mai
tra la roccia nera e le fondamenta
si vedesse chiaramente,
da lontano,
una striscia di cielo
al tramonto.

Abstract

In this dissertation the production of *beauty* quarks (or b-quarks) in *electron (positron)–proton* collisions has been studied in events with a muon and a charged D^* meson in the final state:

$$e^{\pm}p \;\rightarrow\; e^{\pm}\, b\bar{b}\, X \;\rightarrow\; e^{\pm}\, \mu D^*\, X'$$

The measurement is based on events produced at the HERA lepton–proton collider (Hamburg, Germany) which achieves a center of mass energy of $\sim$ 300-318 GeV. The events were measured in the ZEUS experiment during the years 1996–2000 and correspond to an integrated luminosity of 114 pb^{-1}.

The signal was extracted using the charge correlations and angular distributions of the muon with respect to the D^* meson. The low transverse-momentum thresholds for the muon and D^*-meson allow a measurement of beauty production close to the kinematic limit. Cross sections of beauty production with a muon and a D^* meson in the final state were calculated considering both the decay of the $D^{*+} \rightarrow D^0(K^-\pi^+)\pi_s^+$ and $D^{*+} \rightarrow D^0(K^-\pi^+\pi^-\pi^+)\pi_s^+$ and the corresponding charge conjugate modes. The study covers the *photoproduction* regime, in which the boson exchanged between the proton and the electron (positron) has very low virtuality ($Q^2 \simeq 0$) as well as the *deep inelastic scattering* regime which is instead characterised by large momentum transfer between the electron and the proton.

The results were compared to the predictions provided by Monte Carlo simulations and QCD predictions at NLO. Differential cross sections in the transverse momentum of the produced b–quark and its rapidity were also measured. Even though for moderate b–quark transverse momenta the NLO QCD is expected to provide accurate predictions, the obtained results exhibit an excess of about a factor 3 with respect to the expectations.

Riassunto

In questa tesi la produzione di quark *beauty* in collisioni *elettrone (positrone)–protone* è stata studiata in eventi con un muone ed un mesone D^* nello stato finale:

$$e^{\pm}p \;\; \rightarrow \;\; e^{\pm}\, b\bar{b}\, X \;\; \rightarrow \;\; e^{\pm}\, \mu D^*\, X'$$

La misura si basa su un campione di eventi prodotti al collisore leptone–protone HERA (Amburgo, Germania) grazie al quale si raggiungono energie nel centro di massa di $\sim$ 300-318 GeV. Gli eventi sono stati misurati dal rivelatore ZEUS durante gli anni 1996-2000 e corrispondono ad una luminosità integrata di 114 pb^{-1}.

Il segnale è stato estratto sfruttando le correlazioni in carica ed angolo tra il muone ed il mesone D^*. Le basse soglie in momento trasverso per il muone ed il mesone D^* consentono di misurare la produzione di beauty vicino al limite cinematico. Le sezioni d'urto per la produzione di beauty con un muone ed una D^* nello stato finale sono state calcolate considerando sia il decadimento $D^{*+} \rightarrow D^0(K^-\pi^+)\pi_s^+$ che $D^{*+} \rightarrow D^0(K^-\pi^+\pi^-\pi^+)\pi_s^+$ e i rispettivi coniugati di carica. Lo studio riguarda sia il regime di *fotoproduzione*, in cui il bosone scambiato tra l'elettrone (positrone) ed il protone ha virtualità molto bassa ($Q^2 \simeq 0$), che il regime di *diffusione profondamente inelastica* che è invece caratterizzato da un grande momento trasferito tra l'elettrone ed il protone.

I risultati sono stati confrontati con la predizione delle simulazioni Monte Carlo e della QCD al next–to–leading–order. Sono anche state misurate le sezioni d'urto differenziali nel momento trasverso e nella rapidità del quark beauty. Sebbene la QCD al NLO sia in grado, in linea di principio, di fornire predizioni accurate, i risultati ottenuti si mostrano in eccesso rispetto alle attese di un fattore circa 3.

Contents

Introduction **11**

1 Heavy flavour production: a theoretical and experimental overview **15**

1.1 Kinematics of ep collisions . . . 15

1.2 Fundamentals of QCD . . . 17

1.2.1 The perturbative QCD framework . . . 18

1.3 Heavy Flavour production at HERA . . . 21

1.3.1 Direct and resolved processes . . . 21

1.3.2 Heavy flavour production in DIS and photoproduction . . . 23

1.3.3 Heavy flavour production cross section calculation . . . 23

1.3.4 Calculation of the partonic level cross section at NLO . . . 24

1.4 Experimental results on heavy quark production . . . 30

1.4.1 Heavy quark production results at HERA . . . 32

1.4.2 Heavy quark production results at fixed–target experiments . . . 48

1.4.3 Beauty production results at e^+e^- colliders . . . 50

1.4.4 Beauty production results at hadron colliders . . . 51

2 Experimental setup **57**

2.1 The HERA collider . . . 57

2.2 The ZEUS detector . . . 60

2.2.1 Overview of the main components . . . 60

2.2.2 The Central Tracking Detector (CTD) . . . 62

2.2.3 The Small-angle Rear Tracking Detector (SRTD) . . . 64

2.3 The ZEUS Uranium-scintillator calorimeter (UCAL) . . . 65

2.3.1 Energy resolution and compensation . . . 65

2.3.2 Mechanical structure and readout . . . 66

2.4 Muon detectors . . . 67

2.4.1 The Barrel and rear muon chambers (BRMUON) . . . 68

2.4.2 The Forward muon chambers (FMUON) . . . 70

2.4.3 The backing calorimeter (BAC) . . . 72

2.5 Luminosity measurement . . . 72

2.5.1 Trigger and data acquisition . . . 74

3 Physics simulation **77**

3.1 General structure of an event generator . . . 77

3.2 The HERWIG Monte Carlo . . . 78

3.3 The PYTHIA Monte Carlo . . . 79

3.4 The RAPGAP Monte Carlo . . . 80

3.5 The detector simulation . . . 80

3.6 Monte Carlo samples used for the analysis . . . 81

3.6.1 Beauty events simulation . . . 82

3.6.2 Charm events simulation . . . 82

4 Event selection and reconstruction **83**

4.1 Data selection at trigger level . . . 83

4.1.1 Description of the trigger selection . . . 83

4.1.2 Time stability of the selection . . . 87

4.2 Separation of deep inelastic scattering and photoproduction events . . . 89

4.2.1 y and Q^2 reconstruction . . . 89

4.2.2 Definition of deep inelastic scattering and photoproduction events . . . 90

4.3 D^* reconstruction . . . 90

4.3.1 $D^* \rightarrow (K\pi)\pi$ channel . . . 91

4.3.2 $D^* \rightarrow (K\pi\pi\pi)\pi$ channel . . . 91

4.3.3 Kinematical correlations and background studies . . . 91

4.3.4 D^* final cuts . . . 92

4.4 Muon reconstruction: the BREMAT matching package . . . 94

4.4.1 Matching algorithm tests . . . 96

4.4.2 Muon final cuts . . . 97

4.5 Muon + D^* final sample . . . 99

4.6 Resolution studies . . . 99

5 Cross section measurement **103**
5.1 Basic concepts and motivation . . . 103
5.2 Branching ratios . . . 104
5.3 Sources of $D^*\mu$ events and $D^*\mu$ charge–angle correlations . . . 105
5.4 μD^* variables and signal extraction . . . 109
5.5 Background sources . . . 110
5.5.1 Fake muons . . . 111
5.5.2 Fake D^* . . . 112
5.6 Final selection . . . 115
5.7 Final data samples . . . 118
5.8 Extraction of events from b decays . . . 119
5.8.1 Beauty signals in the $K\pi$ channel . . . 121
5.8.2 Beauty signals in the $K3\pi$ mode . . . 122
5.9 Data–Monte Carlo comparison: control plots . . . 123
5.10 Visible cross section measurement . . . 127
5.10.1 Visible cross sections in the $K\pi$ mode . . . 128
5.10.2 Visible cross sections in the $K3\pi$ mode . . . 130
5.11 Systematic uncertainties . . . 131
5.11.1 Gluon splitting from light quark events . . . 134
5.11.2 Monte Carlo implementations of the muon spectrum. . . . 134
5.12 Visible cross sections summary . . . 135
5.13 Comparison with the theoretical predictions . . . 135
5.13.1 Monte Carlo predictions . . . 135
5.13.2 b–quark level cross section and comparison with the NLO prediction . . . 136

6 Differential cross sections **143**
6.1 Kinematic correlations between the b–quarks and the μD^* system . . . 143
6.2 Differential cross sections . . . 145

Summary and Outlook **151**

A Fake–muon studies **153**
A.1 Introduction . . . 153
A.2 Hadron samples . . . 153
A.3 Some definitions . . . 154
A.4 Study of fake–muons from pions via the decay $K^0_S \to \pi^+\pi^-$ . . . 156
A.4.1 5 $d.o.f.$ matching fakes . . . 159
A.4.2 Dependence on the value of the minimal matching–probability . . . 162
A.5 Study of fake–muons from protons via the decay $\Lambda \to p\pi$ . . . 164
A.6 Study of fake–muons from kaons via the decay $\phi \to K^+K^-$ . . . 166
A.7 Study of fake–muons from pions and kaons via the decay $D^* \to D^0(\to K\pi)\pi_s$ . . . 168
A.8 Fake–muon probabilities: comparison of the different samples . . . 173
A.9 Conclusions . . . 177

B Data Monte Carlo comparison - additional plots **179**

Acknowledgments **193**

Introduction

Experimental results in the field of High Energy Physics are currently interpreted in the framework of the *Standard Model* of particle physics (SM). This theory predicts matter to be made up of elementary constituents: *quarks* and *leptons*. Six kinds of quarks are present being different in virtue of the quantum number called *flavour*. From the lightest to the heaviest they are called: *up*, *down*, *strange*, *charm*, *beauty* (or *bottom*) and *top*. Six leptons exist as well, three being electrically charged, the *electron* (e), *muon* (μ) and *tau* (τ) and three being neutral (*neutrinos*: ν_e ν_μ ν_τ). Each of these particles have a partner made of anti–matter.

The formalism of the SM provides a unified description of the *electromagnetic* and *weak* forces. The strong forces are described by the part of the theory called *Quantum CromoDynamics* (*QCD*). Each interaction is mediated by specific particles called *vector bosons*, the massless *photon* and the massive W and Z^0 for the electro–weak force and the *gluon* for the strong force. QCD describes how quarks are bound together to form *hadrons*. The quarks are not detected as free particles but they are always bound with an antiquark to form *mesons* (as the *pion* or *kaon*) or with two other quarks to form *baryons* (as the *proton* and the *neutron*). The quark masses range from few MeV (i.e. a million electron–Volts[1]) for the up quark to hundreds of GeV (or billion electron–Volts) for the top quark. These values are not predicted by the SM.

All the particles needed by the SM have been detected by the experiments except the so called *Higgs boson* which is responsible for the generation of the mass. The search for this particle as well as other particles appearing in extensions of the SM is the main motivation for the ongoing construction of the collider with the highest centre-of-mass energy ever realized, the *Large Hadron Collider* at CERN in Geneva.

Ordinary matter is essentially composed by protons, neutrons and electrons. Protons and neutrons are built by *up* and *down* quarks. The *charm*, *beauty* and *top* quarks are generally called *heavy quarks*, since their mass is larger than the energy scale at which the quarks are confined into hadrons, $\Lambda \sim 250$ MeV. In nature at present, heavy quarks are only produced in high energy collisions, e.g. in the interactions induced by cosmic rays, and their existence is ephemeral. Hadrons containing heavy quarks are not stable. They decay very rapidly to lighter hadrons and leptons in about 10^{-12} s. Therefore, to study their properties they are produced in a controlled environment in which their decay products can be detected, e.g. particle accelerators and detectors.

The first evidence for the beauty quark (or b–quark) came during the summer of 1977 by a team of physicists led by Leon M. Lederman at Fermilab with the discovery of the Υ meson in collisions of protons on a fixed target. This meson was interpreted as being the most stable bound state of a a b and anti–b quark ($\bar{b}$).

Nowadays, b–quarks are produced in several experiments of high energy physics. Both the *production* and *decay* properties of b-quarks are extremely interesting. Decays of b-hadrons are used to measure the violation of CP symmetry, a combination of two symmetry transformations: the charge conjugation (C) which transforms a particle in its antiparticle and the parity (P) which is equivalent to reflection in space. Indeed two new "factories" of B-mesons, PEPII at SLAC (USA) and KEKB at KeK (Japan), with the indeed recently confirmed CP violation in the B system.

On the other hand, b-quark production provides an excellent ground to test the predictions of QCD. This is the aspect of B physics which is interesting for this thesis. It is generally believed, in fact, that the mass of the beauty quark, being around three times larger than that of the charm quark, allows perturbative QCD predictions to be more reliable. Due to a phenomenon called "asymptotic freeedom" the strong force becomes, in a certain sense, "less strong" in the presence of a large energy scale (the beauty quark mas in our case) and thus the mathematical approach used in the calculations is on a firmer ground.

[1] The electron-Volt corresponds to $1.78 \cdot 10^{-36}$ Kg.

In the last years the study of b-quark production has been an intriguing topic since several experiments at proton-antiproton ($p\bar{p}$) colliders (like UA1, CDF and D0) have measured production rates higher than those predicted by the most precise QCD calculations available. Similar measurements are also performed in $\gamma\gamma$ processes at electron-positron (e^+e^-) colliders (as LEP) and at the HERA electron-proton (ep) collider. Also in these very different environments QCD seems to be underestimating beauty production. As we will discuss in this dissertation, the correct description in terms of QCD of the b-quark production rate is still on its way towards a complete clarification.

The purpose of this dissertation is to present an original measurement of b-quark production in ep collisions at HERA.

HERA (*Hadron Electron Ring Anlage*) is the first and so far only ep collider ever built. At the centre–of–mass energy available at HERA, $\sqrt{s}$ = 318 GeV, the cross section of beauty production is much higher than at the previous fixed–target experiments, having centre–of–mass energies two orders of magnitude lower: there, beauty production could not be observed. Beauty production in ep interactions proceeds through two main processes: *deep inelastic scattering*, where the virtuality of the exchanged photon goes from some GeV^2 to the kinematic limit of 10^5 GeV^2 , and *photoproduction* processes, in which the exchanged particle is an almost real photon, whose virtuality has a mean value of $\sim 10^{-3}$ GeV^2.

The analysis presented in this thesis will cover both these kinematic regimes using a rather different philosophy with respect to previous beauty studies at HERA. These are based on the study of the transverse momentum of leptons with respect to the axis of associated jets. The experimental signature used in this analysis to isolate the beauty signal is the presence in the final state of a muon and a charged D^* meson.

$$ep \rightarrow b\bar{b}X \rightarrow \mu D^* X'$$

These two particles are particularly suited to signal the presence of heavy flavour production. They can both arise from b as well as c quarks but the beauty component can be separated from the charm one by studying the correlations in charge and angle between the muon and the D^* meson.

The $D^{*\pm}$ is a vector meson made up by a c and a light $\bar{d}$ quark with a mass of 2.01 GeV. Since it decays through the mediation of strong interaction its lifetime is very short ($\sim 10^{-23}$ s). In this analysis we will use the decays of the charged D^* to a pion and a D^0 meson (a $c\bar{u}$ meson) which happens in about 68 % of the cases. The D^0 meson decays on its turn to a pion and a kaon with a probability of about 4 %. The decay of the D^0 into a charged kaon and three charged pions whose branching ratio is higher (7.5 %), will also be used in this analysis.

Semileptonic decays of heavy quarks are mediated by the weak interaction. They can decay to lighter quarks via the emission of a W–boson giving a lepton and the corresponding neutrino. The semileptonic mode into muons is used being frequent and experimentally easy to study.

The μD^* final state offers the advantage of selecting a data sample enriched in b quarks and with strongly suppressed backgrounds from other processes, which allows low-p_T-threshold cuts to be applied on the muon and D^*. This possibility extends the sensibility towards b quarks produced with transverse momenta lower than the beauty mass where the bulk of the cross section is concentrated.

This analysis therefore complements measurements based on leptons with high transverse momentum which instead, due to the need to tag jets, are sensitive to b–production at higher transverse momenta. The possibility to access a partially new kinematic region is also important since it is interesting to study whether the excess over predictions which was observed in several previous measurements is enhanced in this particular regime or not.

The data sample used for the analysis corresponds to an integrated luminosity of 114 pb^{-1} collected by the ZEUS experiment in the years between 1996 and 2000.

***

This dissertation has the following structure. In **Chapter 1** we give an introduction to the theory of heavy quark production in ep collisions with particular emphasis on the QCD predictions at the *next–to–leading order* level (*NLO*). The last part of the Chapter contains an overview on the current experimental knowledge on heavy quark production in $p\bar{p}$ e^+e^- and ep collisions.

In **Chapter 2** the HERA collider and the ZEUS detector are presented. Particular stress is put on the detector components which data were directly used in our analysis: the inner tracking devices, the main calorimeter and the muon chambers. The general structure of the trigger system is also described.

In **Chapter 3** a brief description of the Monte Carlo generators used in this work is reported, showing in particular the common and different aspects of the physics simulation.

The specific selection which we introduced at trigger level in order to efficiently select events with D^* mesons and muons will be explained in **Chapter 4**. Here we will also study the performance of the reconstruction algorithms used to identify and measure the muons and D^* mesons and to separate the photoproduction and deep inelastic scattering regimes. A first discussion on the choice and optimisation of the final selection cuts will be also be found in this Chapter.

Chapter 5 describes the measurement of the fraction of beauty events in the final data sample selected as described in Chapter 4. The selection efficiency on the signal will be estimated with the Monte Carlo programs and this will allow the extraction of the cross section of beauty production in the kinematic regions defined by the applied cuts. This was done in both photoproduction and deep inelastic scattering by employing two different decay modes of the D^* meson. The extracted beauty fraction will be cross checked by comparing the distributions of several relevant kinematic variables in the data and in the Monte Carlo prediction obtained by mixing the signal and background according to the measured relative fraction. The measured cross sections will be first compared to the leading–order plus parton–shower Monte Carlo predictions an then converted at quark level in order to be compared to the expectations of QCD at next–to–leading order.

Our analysis will be completed in **Chapter 6**. The kinematic features of the produced b–quarks have been investigated by measuring differential cross sections in the quark variables after restricting to a region in which a quite pure sample of beauty candidates can be selected. These results will also be compared to the theory predictions at NLO.

The discussion of the measurements and the conclusions which can be drawn from our results are then collected in the final Chapter. Some further studies are included in the Appendices. The background arising from particles erroneously being identified as muons (*fake muons*) has been widely studied by counting the occurrence of muon candidates arising from hadronic tracks (pions, kaons and protons) coming from particular decays of the K^0_S, Λ, ϕ and D^0 particles. The description of this background by the Monte Carlo is tested and the results summarised in **Appendix A**. This study is particularly meaningful in the context of this analysis since it is the first in which muons reaching the inner muon chambers only have been used in the study of beauty.

Appendix B collects additional data Monte Carlo comparison plots which are described in Chapter 5.

The results on the beauty cross section in photoproduction in the $K\pi$ decay mode of the D^* meson which are presented in this work have been published by the ZEUS Collaboration as a contributed paper to the International Conference on High Energy Physics, ICHEP02 held in Amsterdam, The Nederlands (July, 2002) [1]. The extension of these results in the deep inelastic scattering regime was sent to the International EuroPhysics Conference on High Energy Physics, EPS03, Aachen, Germany, (July 2003) [2].

Chapter 1

Heavy flavour production: a theoretical and experimental overview

In the first part of this Chapter a theoretical overview on the physics of ep interaction will be given. This will serve as an introduction to understand the basic points which are relevant for the theoretical calculations on heavy quark production at HERA. The calculations, to which our experimental result will be compared, will be described there.

The second part of the Chapter will deal with a brief summary of the experimental knowledge accumulated so far on heavy quark production. This review will span over the results obtained in fixed target and collider ($p\bar{p}$, e^+e^-, ep) experiments. For obvious reasons particular stress will be put on the results already produced at HERA, for which we will also briefly account on charm measurements.

1.1 Kinematics of ep collisions

The most suitable way to probe the structure of matter is to perform *scattering* experiments. This approach was pioneered by Rutherford in the year 1909. In that famous experiment small projectiles, in that case α particles, were shot against an extended fixed target, a thin gold foil. The study of the final state allows to probe the structure of the target. At HERA 27.5 GeV electrons (positrons) collide with 920 GeV (820 GeV up to 1998) protons.

The interaction between a lepton and proton is described in the electro–weak part of the Standard Model in terms of the exchange of an intermediate vector boson, γ or Z^0 in *Neutral Current* interactions (NC) and W in *Charged Current* (CC), as shown in Figure 1.1. NC processes preserve the identity of the initial state lepton while CC interactions lead to a final state neutrino.

The kinematic description of the interactions between electrons (positrons) and protons is done through particular variables defined by the four–momenta of final and initial state particles. Let's write down the process:

$$e(p_e) + p(P) \rightarrow l(p_l) + X(P')$$

where we indicate the outgoing lepton with l and indicate the four–momenta of the particles with the symbols in brackets. We can then define the following relevant variables:

- the centre–of–mass energy squared s:

$$s = (p_e + P)^2 = m_e^2 + m_p^2 + 2(E_e E_p - \vec{p_e} \cdot \vec{p_p}) \simeq 4E_e E_p \tag{1.1}$$

  HERA achieves a center–of–mass energy of 318 GeV (300 GeV up to year 1998). An electron beam energy of $\sim$ 54 TeV would be needed to reach the same $\sqrt{s}$ on a fixed target (in that case $s \sim 2E_e m_p$).

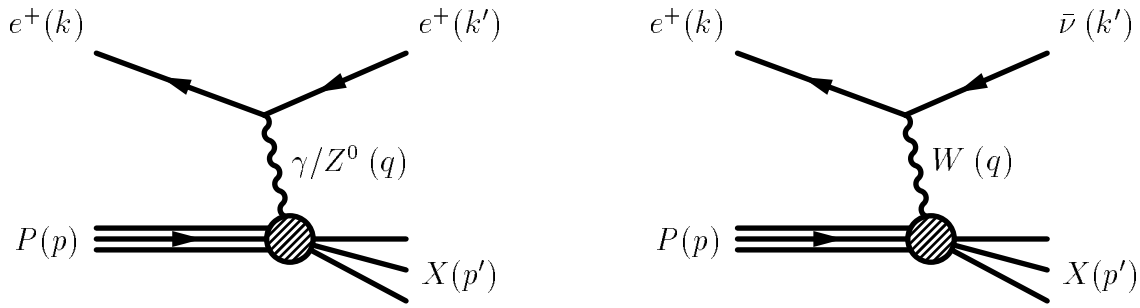

Figure 1.1: *Electron–proton scattering in Neutral Current (NC) (***Left***) and Charged Current (CC) (***Right***) processes.*

- Q^2, the negative square of the momentum transfer (the virtuality of the exchanged boson):

$$Q^2 = -q^2 = -(p_e - p_l)^2 > 0 \tag{1.2}$$

  By applying the Heisenberg uncertainty principle, this variable can be intuitively related to the spatial "resolution" with which the exchanged boson probes the proton: the quantum wavelenght of the boson (λ) is in fact inversely proportional to $\sqrt{Q^2}$: $\lambda \sim h/Q$ (with $Q^2 = 40.000\, GeV^2 \rightarrow \lambda \sim 10^{-18}$ m i.e. about one thousandth of the proton size). [1]

- the Bjorken–x scaling variable:

$$0 < x = \frac{Q^2}{2P \cdot Q} < 1 \tag{1.3}$$

  which, in the infinite momentum frame[2], is the fraction of the proton momentum carried by the parton interacting with the lepton. The available x range at HERA spans for about six orders of magnitude, from $\sim\ 10^{-6}$ to $\sim\ 1$.

- the *inelasticity*,

$$0 < y = \frac{P \cdot Q}{P \cdot p_e} < 1 \tag{1.4}$$

  which, in the proton rest frame, is the fraction of the lepton momentum transferred to the exchanged boson.

- the centre–of–mass energy W of the $\gamma(Z^0, W^{\pm})$-p system:

$$W^2 = (q + P)^2 \simeq sy - Q^2 \tag{1.5}$$

The kinematic variables given above are not independent. Once the centre–of–mass energy $\sqrt{s}$ is given, the kinematic of the event is completely determined by the knowledge of two of the other variables defined above. Usually the (x,y) or (x,Q^2) couple is chosen. Physically this is equivalent to the knowledge of the angle θ_e and energy (E'_e) of the scattered lepton ($Q^2 = 2E_eE'_e(1 + \cos\theta_e)$, $y = 1 - (E'_e/2E_e) \cdot (1 - \cos\theta_e)$). The (x, Q^2) coverage of at HERA is depicted in Figure 1.2 (Left).

The Q^2 variable is used to distinguish between two kinematic regimes, the *deep–inelastic scattering* (*DIS*) and the *photoproduction* (*PHP*) regime.

[1] Keeping in mind that to a good approximation $Q^2 \simeq sxy$, and x and y (see next) are bound to unity, it becomes clear that the maximum Q^2 kinematically achievable at HERA is up to ~ 40.000 GeV^2.

[2] The infinite momentum frame is defined as the reference system in which the proton is moving with very high momentum, at limit infinite, so that the masses are negligible. In this frame the proton can be considered as a parallel stream of particles, all moving in the same direction, since the transverse momenta are negligible. The relativistic time dilation slows down the time at which the proton constituents interact to each other, so that in the scattering with the lepton they can essentially be considered as free particles.

The DIS regime is operatively defined by the requirement on the squared momentum transferred, Q^2 in the event, to be much larger than the proton mass. In this case, within the frame of HERA detectors, the incoming lepton is deflected by an angle large enough to allow its measurement in the main detector.

The photoproduction regime on the other hand is defined as the complementary situation in which the squared momentum, Q^2 , is of the order of 1 GeV^2 or less. In this case the incoming lepton is scattered at a very small angle and it usually escapes into the beam pipe. The median value of the Q^2 distribution is $\sim 10^{-4}$ GeV^2. In photoproduction processes, since the photon virtuality is almost equal to zero ($Q^2 \sim 0$), the photon exchanged between the lepton and the proton is "almost" on–shell and it is commonly referred as being a "quasi–real" particle.

The contribution from weak interactions is almost negligible in the photoproduction regime, since at low Q^2 ($\sim$ "long distance processes") the Z^0 and W boson propagators terms in the cross section are highly suppressed by the heavy mass of such bosons (they are expressed as $Q^2/(M^2_{W/Z}+Q^2)$). Therefore the lepton–proton interaction in this regime can be in practice thought of as the scattering of a real photon on a proton (hence the name). The contribution coming from the exchange of massive boson becomes relevant at high Q^2 when the electromagnetic and weak interactions are of comparable strength. HERA has provided a clear and stunning evidence of this electroweak unification at $Q^2 \sim M^2_{W,Z^0}$ by measuring the Q^2–dependence of the NC and CC cross sections (see Figure 1.2 (Right)).

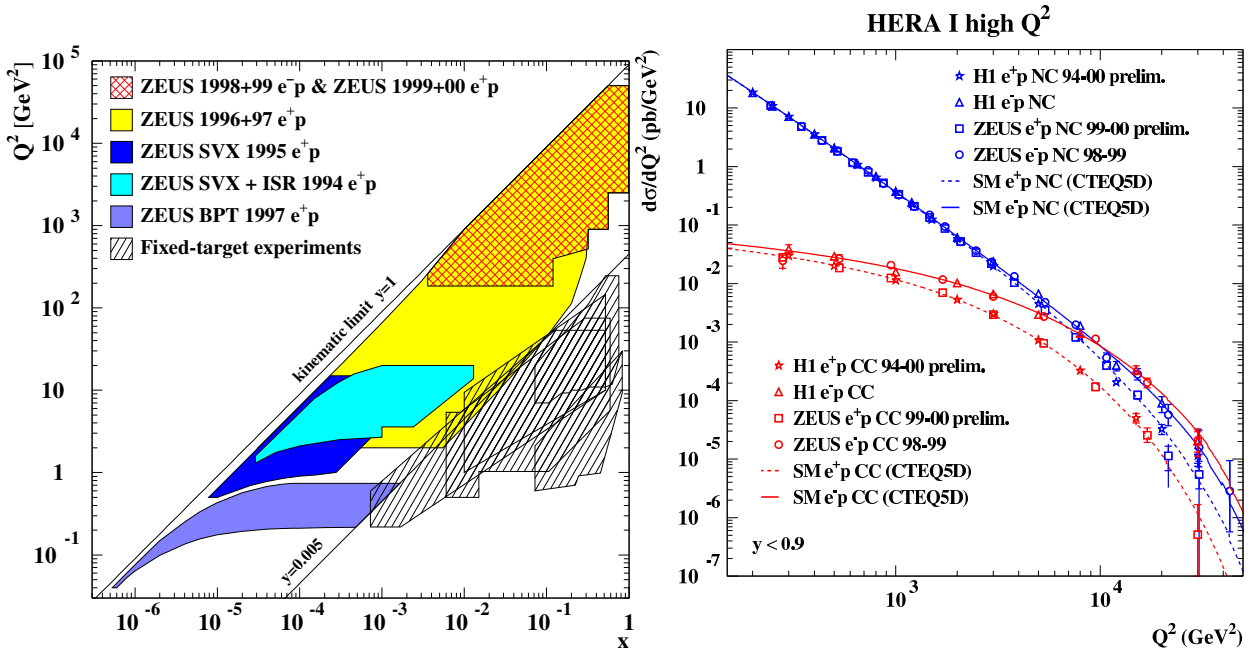

Figure 1.2: **Left**: *(x,Q^2) plane covered by HERA in comparison to fixed target experiments. The coverage of x and Q^2 is extended by about two orders of magnitude.* **Right**: *Neutral Current and Charged Current cross sections as a function of Q^2*

The yield of physics measurements which have been carried out at HERA is very rich, the most important one being the determination of the proton structure functions and of the gluon density in a previously unexplored wide kinematical range. We will not deal with this in detail since it is not directly connected to the measurement which is the subject of this work. We will go directly to a description of the partonic processes which can be studied at HERA in a quite clean environment. As an introduction some concepts are presented which will be useful when describing the theory of heavy flavour production at HERA.

1.2 Fundamentals of QCD

In the 1970's QCD (*Quantum Cromo Dynamics*) was developed as the field theory governing the strong interaction between quarks and gluons and therefore as the basis for the interaction between hadrons including the nuclear forces.

QCD is a nonabelian gauge theory based on the $SU(3)$ symmetry group. Each quark has three possible "charges" related to the *colour* quantum number and the strong interaction is mediated via the exchange of eight different coloured gauge particles, called *gluons*. The gluon always carry a combination of colour and anticolour and the emission of one gluon change the colour number of the quark (anticolour for the antiquarks). Since the symmetry group of the colour quantum number ($SU(3)_C$) is non-abelian, the gluons also carry a net colour charge themselves and therefore couple to each other. This is the main difference with QED, in which the photon is a neutral particle (and the group is the abelian $U(1)_{em}$). The self-coupling of the gluon is the reason for the strong (QCD) coupling constant α_S to become large at small energies (large distances) and to decrease at high energies (small distances). This property of QCD is used to explain the observed behaviour of the strong interaction:

- *Asymptotic freedom*: at high energies (or small distances) the strong interaction proceeds via colour fields of reduced strength and the quarks and gluons behave as essentially free, non–interacting particles. This property is needed to explain why in deep-inelastic scattering the hard interaction between the boson and the parton can be calculated with non-interacting partons during the time scale in which the interaction takes place. That is, this property explains the success of the naïve (not so much after all ...) *quark parton model* approach [3]. As we will see in section 1.2.1, this property allows the application of perturbation theory to calculate scattering amplitudes.
- *Confinement*: at low energy (or large distances) the strength of the colour field is increasing (the potential behaves as $V(r) \sim \lambda r$) and in this way the quarks and gluons can never be observed as free particles. If two interacting partons are separated, the energy of the field increases so much that it creates new interacting particles and at the end (that is, at long time scales) we are left with colourless hadrons containing the partons. This is the way QCD explains the confinement of the partons, which are not observed as free particles at long time scales. It should be noted that the outgoing partons can be separated and observed as different objects, although each of these partons will be confined in a different hadron. What are not observed as free particles are coloured partons, although the partons, as well as their quantum numbers, can be studied experimentally.

1.2.1 The perturbative QCD framework

QCD gives a successful description of the strong interaction, containing in a natural way the properties of asymptotic freedom and confinement. However, these properties make especially difficult to obtain predictions for the soft limit, where hadrons live and are observed in the experimental setup. Nevertheless, by choosing appropriate observables the perturbative approach can be applied profitably, giving rise to a good predictive power. This section gives a description of the way perturbative QCD (pQCD) is actually implemented in order to provide quantitative predictions.

From the Lagrangian density for QCD different couplings appear in the theory. They can be related to the following processes:

- A (anti)quark radiating a gluon, which is dictated by the quark-gluon coupling which, in turn, is formally equal to the coupling between an electric charge and the electromagnetic field. The same coupling is related to the process in which a gluon splits into a quark-antiquark pair.
- A gluon splitting into two or three gluons, which is dictated by the self–interaction coupling of the gluon.

These processes are proportional to the strong coupling constant, so if the energy scale associated to the process is large enough, then the coupling is small and the interaction can be described by a perturbative expansion. This expansion allows the equations describing the processes to be solved in the limit where the strong coupling constant is small (*hard processes*).

On the other hand, if the energy scales are small, i.e. the interacting partons become further apart, then the strong coupling constant becomes very large and the perturbative approach is no longer valid. In order to be able to make predictions for the measurements performed in a collider, QCD should be studied in reactions in which the hard processes are dominant versus the non–perturbative ones. Usually the hard process occurs as a first step in the collision

[3] This is the model introduced by Feynman et al. in the sixties to interpret the first fixed target experimental results on ep scattering obtained at SLAC. In this context Feynmann introduced the idea of *partons*, to be later identified with the *quarks* which had been introduced by Gell–Mann to explain the spectrum of hadrons.

and afterwards, the soft, non-perturbative, process gives rise to the final-state hadrons (*hadronisation*) from the partons taking part in the hard process.

Perturbative QCD is applied to obtain predictions for the partons dynamics, and the results can be considered reliable if the hadronisation process does not hide the properties of the partonic state; that is, if the experimental measurement can be related to the parton dynamics in some direct way.

Even in the region where perturbative QCD can be applied, additional difficulties are present in the calculations. In the same way as in QED, different types of divergences appear when the vacuum fluctuations (*UV divergences*) or radiation of partons with very small relative transverse momentum with respect to the original parton (*IR divergences*) are included. Both are dealt with by following the standard regularisation procedures. This mechanism is very often called *renormalisation* when it is applied to get rid of the UV divergences. To remove the IR divergences the regularisation is made selecting observables which are insensitive to these particular divergences. This type of observable is called *infrared-safe* The use of infrared-safe observables allows a complete separation of the hard process from the soft process in a formal way.

When the interaction contains hadrons in the initial state, as in the case of deep-inelastic scattering, it is impossible to be fully insensitive to the soft phenomena (including IR divergences) occurring within the hadrons, or in the steps leading from the free, initial hadron to the hard interaction. In that case, a complete regularisation mechanism is needed to separate (factorise) the theoretical description into a calculable hard and a soft part. This mechanism is called *factorisation* and is very similar to the renormalisation procedure. We will describe both in the next sections.

1.2.1.1 Renormalisation

In the calculation of Feynman diagrams containing loops, divergent integrals occur. The resulting divergence is known as *ultraviolet (or UV) singularity*. In a so–called regularisation procedure the integrals are made "temporarily finite" by introducing, for example, a gluon mass, an ultraviolet momentum cut–off or a fractional space–time dimension. The mathematical expressions are then well–defined, though they have a divergent limit.

The regularised divergences are then adsorbed into a redefinition of the bare parameters in the lagrangian which are not observable, into the physical (observable) quantities through a *renormalisation* procedure. This leads to the introduction of a new dimensional parameter μ_R, the so–called *renormalisation scale*. Renormalised quantities in the theory, such as the strong coupling α_S, depend explicitly on μ_R.

The procedure is not unique, i.e. there is a renormalisation scheme choice which is chosen depending on the properties of the parameters which are needed in the calculation. Of course, the physical results cannot depend on this choice; however, a theoretical dependence is usually obtained in pQCD since the perturbative expansion is performed only to a given order. The renormalisation scheme determines the values of the physical parameters when calculated to a given order in the pertubative approach. The $\overline{MS}$ renormalisation scheme is the most widely used [4].

It is legitimate to impose any physical observable (when calculated without approximations) to be invariant under variations of the renormalisation scale. This requirement is formally expressed by the *renormalisation group equation* (RGE):

$$\mu_R^2 \frac{d}{d\mu_R^2}\Gamma = 0 \tag{1.6}$$

where Γ is the observable we are interested in. In the perturbative approach, this equation has to be applied to the perturbative expansion of the observable, and in pQCD we have

$$\Gamma = \Gamma_0 + \alpha_S\Gamma_1 + \alpha_S^2\Gamma_2 + \ldots \tag{1.7}$$

and the renormalisation group equation transforms into

$$\mu_R^2 \frac{d}{d\mu_R^2} \sum_{j=0}^{N} \alpha_S^j \Gamma_j = \mathcal{O}(\alpha_S^{N+1}) \tag{1.8}$$

[4] Another common choice is the DIS scheme which has the property that at any order in the perturbative expansion the structure functions are computed as linear combinations of the quark distribution functions. This property is not preserved in other renormalisation schemes, including the $\overline{MS}$ scheme.

that is the variation of the observable with the scale is given by terms which were not included in the perturbative expansion.

It is very common to use this relation to estimate the size of the theoretical uncertainty of the observable coming from the truncation of the perturbative expansion at order N in α_S . This estimation is obtained by analysing the variation of the pQCD theoretical prediction with the renormalisation scale; that is by computing the prediction for different choices of this scale one can estimate the size of the truncated orders in the series.

1.2.1.2 Factorisation

Consider as an example the case where the quark which interacts with the electron emits a gluon with a transverse momentum k_T with respect to the initial quark. Calculating the cross section it turns out that there is a singularity for the limit $k_T \to 0$ (*infrared divergency*). This case has to be taken into account since the virtual photon can distinguish between a quark and a collinear quark–gluon pair carrying the same overall momentum. The key to understanding what is happening is to realise that the limit $k_T \to 0$ corresponds to a long–range ("soft") part of the strong interaction which is not calculable in perturbation theory. The procedure by which this problem is solved is very similar to that of renormalisation.

First the singularity is made temporarily finite e.g. by introducing a cut–off or a fractional space–time dimension. This regularised divergence of perturbation theory is then removed by absorbing it into the definitions of physical quantities through a factorisation procedure. This procedure introduces a new dimensional scale, the so–called *factorisation scale* μ_F.

This scale sets the separation between soft and hard processes occurring in the parton system which configures the initial-state hadron.

Let's now consider lepton–hadron scattering. Assume that all partonic cross sections $\hat{\sigma}_i$ for all initial partons i are known at a factorisation scale μ_F. Then the *factorisation theorem* states that the final cross section can be calculated by

$$\sigma = \sum_i \int_0^1 f_{i,h}(\xi, \mu_F) \hat{\sigma}_i\,(\xi, \mu_F)\, d\xi \tag{1.9}$$

The $f_{i,h}(\xi, \mu_F)$ function is called parton density function (PDF). Intuitively it represents the probability density to find a parton i with a momentum fraction ξ in the hadron h. It only depends on the parton i and the hadron h to which this parton belongs. The cross section $\hat{\sigma}_i$ only depends on the partonic interactions and is considered to be independent of the target hadron.

The parton density functions $f_{i,h}(\xi, \mu_F)$ which are derived from the bare PDFs after that IR–singularities have been readsorbed cannot be calculated from first principles in perturbation theory, since they receives contributions from the long–distance (non–perturbative) part of the strong interaction. Nevertheless once they have been measured experimentally, they can be used in several different environments (*PDF universality*). This is possible thanks to the presence of equations which specify the dependence of the PDFs on the process scale. They are derived by stating that, when calculated to all orders in α_S, σ in 1.9 can not depend any more on μ_F (which has a degree of arbitrariness):

$$\frac{\partial \sigma}{\partial \ln \mu_F} = \mu_F \frac{\partial \sigma}{\partial \mu_F} = 0 \tag{1.10}$$

Such an equation leads to the DGLAP[5] equation [19], an evolution equation for the PDFs:

$$\mu_F \frac{\partial}{\partial \mu_F} \begin{pmatrix} q_i(x,\mu_F) \\ g(x,\mu_F) \end{pmatrix} = \frac{\alpha_S}{2\pi} \sum_{q_j, \bar{q}_j} \int_x^1 \frac{d\xi}{\xi} \begin{pmatrix} P_{q_i\, q_j}(\frac{x}{\xi}, \alpha_S) & P_{q_i\, g}(\frac{x}{\xi}, \alpha_S) \\ P_{g\, q_j}(\frac{x}{\xi}, \alpha_S) & P_{g\, g}(\frac{x}{\xi}, \alpha_S) \end{pmatrix} \begin{pmatrix} q_i(x,\mu_F) \\ g(x,\mu_F) \end{pmatrix} \tag{1.11}$$

where g is the gluon density, q_i is the quark density for flavour i and $\alpha_S \equiv \alpha_S(\mu_F)$. The functions P_{ab}, which are called *splitting functions* or *evolution kernels*, are calculable as power series in α_S.

Note that because of charge conjugation invariance and $SU(n_f)$ flavour symmetry no distinction is needed between quarks and antiquarks and that the splitting functions P_{qg} and P_{gq} are independent of the quark flavour. The evolution kernel $P_{q_i q_j}$ in leading order is zero unless $q_i = q_j$.

[5] Dokshitzer-Gribov-Altarelli-Parisi

The leading–order splitting functions $P_{ab}^{(0)}(z)$ can be interpreted as the probabilities to find a parton a after a branching of parton b. The variable z denotes the fraction of the longitudinal momentum of the parent parton. The transverse momentum of the daughter parton is assumed to be much smaller than μ_F. Both the leading–order and next–to–leading–order contributions to the DGLAP splitting functions have been calculated.

For some observables, like the ones used in hadron production, the theoretical predictions are not completely infrared-safe since the process transforming the final-state partons into the observable hadrons (also known as *fragmentation*) is not free of new divergences. The kind of divergences that appear are the same as those removed using the factorisation mechanism, but now related to the final state processes. When this kind of observables is under study, a new regularisation procedure is needed, so as to absorb all these divergences into fragmentation functions, which again factorise in the expression to compute the observable. These functions are the equivalent of the parton densities, but now giving the information on the probability for a parton to transform into a given hadron with the corresponding momentum fraction and energy scale.

The isolation of all divergences for any process in deep-inelastic scattering has left as inheritance the residual and non-physical dependence of the prediction on, at least, two scales. These dependencies characterise the precision of a calculation and if the changes produced by the scale variations are large, the next order(s) has to be calculated to gain accuracy in the theoretical predictions.

In some cases (for example charm production at HERA), some terms (for example depending on the ratio between the transverse momentum of the quark and its mass) appear at all orders of the perturbative expansion. It may happen in certain regions of the phase space these coefficients to become large enough to spoil the accuracy of the calculation since higher–order terms can not be safely neglected. In this cases the important terms are identified and their contribution taken into account through a *resummation* procedure.

1.3 Heavy Flavour production at HERA

After the description of a few introductory concepts and of the general problems which arise in the calculations we will now go more specifically on the description of the theoretical predictions on heavy flavour production at HERA.

Heavy quark photoproduction is a phenomenon of considerable interest since it is closely related to hadroproduction, but it is considerably simpler since the incoming photon is much better understood than an incoming hadron. It is a clean testing ground for perturbative QCD, and helps in understanding the proton and the photon structure.

Heavy flavour photoproduction has been extensively studied in fixed–target experiments [3], at a centre–of–mass energy of ~ 30 GeV, but at the lepton–proton collider HERA, which operates at a centre–of–mass energy of ~ 300 GeV, another kinematic region can be explored, where both beauty and charm production can be observed.

Since the b mass is much heavier than the c mass, perturbative QCD calculations are expected to be more reliable.

1.3.1 Direct and resolved processes

In γp interactions the photon can be thought to act in two different ways. In the *direct photon* processes (also referred to as *pointlike* component), the photon couples directly to a parton in the proton, whereas in *resolved photon* processes the photon acts as a source of partons, one of which takes part in the hard interaction. Resolved photon processes originate from the γ fluctuation into a $q\bar{q}$ or a more complex state, and depending on the relative transverse momentum between the partons this can be a bound state (as in the so called *Vector Dominance model* [4]) (*hadronic component*) or a perturbatively calculable state (*anomalous component*). Examples of direct (resolved) photon processes are shown in Figure 1.3 (1.4).

In the theoretical cross section calculations, the emission of a collinear light parton from the photon before the γp interaction, as depicted in 1.4, leads to infrared–singularities in the photon–hadron cross section. These singularities are re–absorbed by introducing the concept of photon structure functions [5]. A "factorisation" scale μ_γ is set at which singularities coming from collinear parton emission are subtracted, and the photon structure functions depend on this scale. Neither the pointlike nor the hadronic component are separately independent of μ_γ, since the subtracted

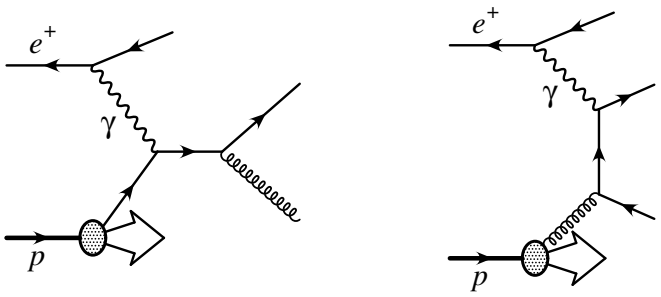

Figure 1.3: *Leading order direct photon processes:* **Left***: QCD Compton.* **Right***: Boson–gluon fusion.*

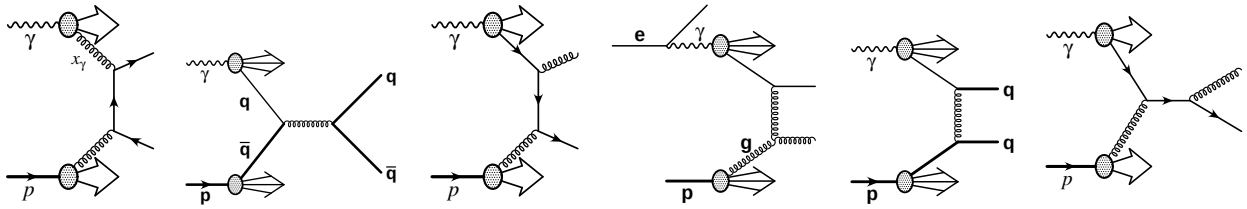

Figure 1.4: *Examples of leading order resolved photon processes.*

term in the pointlike component is responsible for the redefinition of the photon structure functions in the hadronic component.

The strict interplay between the direct and resolved components can be fully understood considering the details of the calculation of the pointlike and hadronic component. Firstly the partonic cross sections for the direct processes $\gamma + j \rightarrow Q + \bar{Q} + X$ and resolved $i + j \rightarrow Q + \bar{Q} + X$ are evaluated. After the ultraviolet renormalisation, the quantities $d\sigma_{\gamma i}$ and $d\sigma_{ij}$ have still some divergences due to the collinear emission of a massless final–state parton by one of the incoming partons. These divergences are subtracted using the factorisation theorem.
The collinear divergences arising from the emission of collinear quarks from the incoming photon, in the pointlike component, are re–absorbed into the partonic densities of the photon. These appear in the hadronic component. From the discussion above it can be concluded that, since the pointlike and hadronic component are so strongly related, only their sum has a physical meaning, and that beyond the LO the discrimination between direct and resolved processes is ambiguous.

As an example, the process in Figure 1.5 is part of the $\mathcal{O}(\alpha_{em}\alpha_S^2)$ cross section, and therefore can be thought of as a direct process at NLO, but if the virtuality of the propagator, k_T^2, is less than μ^2, then its contribution is already included in the LO resolved process. Nevertheless, bearing in mind the previous discussion, the terms direct and resolved component will be used again, since a first–order approximation can be used in order to get a physical picture of the separation between the two components.

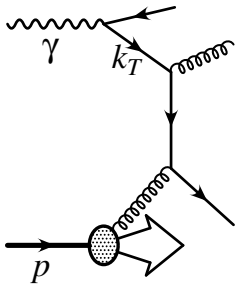

Figure 1.5: *A photon–proton interaction. If the virtuality k_T of the propagator shown in the figure is lower than the factorisation scale μ_γ the process is included in the resolved calculation at leading order, otherwise it is thought of as a direct process at next–to–leading order.*

1.3.2 Heavy flavour production in DIS and photoproduction

As we have seen ep collisions can be divided according to the value of Q^2 into photoproduction and deep–inelastic scattering. Depending on this different theoretical issues appear which lead to a separate treatment in the two cases. For example the choice of the most relevant hard scale for the process is not trivial. In the DIS case the production of heavy quarks is an interesting multi-scale problem since both the Q^2 and mass or p_T of the relevant quarks can be good candidates.

Furthermore in the DIS regime, the relative importance of the processes contributing to heavy flavour production are expected to be different than in the photoproduction regime. The parton densities in the photon, in fact, fall rapidly to zero when the photon virtuality approaches the value of the quark mass, as it is pointed out in Reference[6, 7, 8].

In the Feynmann picture this can be intuitively supported by thinking that the time scale on which the photon can fluctuate into an hadronic state is much reduced when the photon virtuality is getting high.

In Reference [9] it is shown that as long as the virtuality Q^2 of the exchanged photon is much lower than the factorisation scale, $Q^2/\mu_F^2 <\sim 10^{-1}$, the partonic content of the photon remains relevant.

If we pose as a rule of thumb the resolved parton content of the photon to be discernible provided it contributes significantly more than 10% to the involved production rate, we see that this condition is almost never satisfied for heavy quark (c, b) electroproduction. In Figure 1.6 the case of beauty quarks is shown. In these calculations, the parton density used are GRV94 [10] for the proton, while those used for the photon are described in [11]. The b–quark mass is set to 4.75 GeV, and the factorisation scale to $\mu_F = 4m_b^2$.

The smallness of the resolved contribution of virtual photons ($Q^2 > 0$) to the heavy quark electroproduction cross section implies that ep scattering at HERA, in the high Q^2 regime, is dominated by the direct boson–gluon fusion process, whereas the resolved contributions are expected to be small.

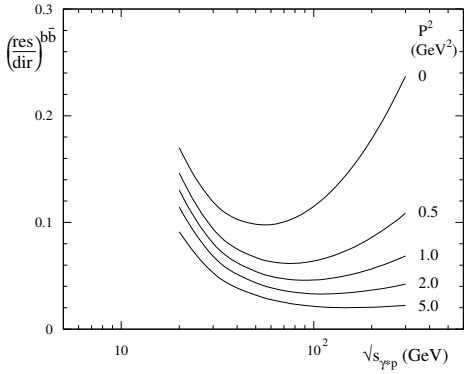

Fig. 2

Figure 1.6: *The ratio of the resolved to the direct contribution to beauty production cross section in LO QCD as a function of the $\gamma^* p$ center of mass energy for various fixed values of the photon virtuality Q^2 (referred as P^2 in the plot) (in GeV^2 units).*

Therefore, in the study of heavy flavour production at HERA, a comparison between DIS and PHP results is useful to the understanding of the two different photon behaviours. Keeping this in mind, we will now describe in more detail the derivation of the predicted cross section in the case of photoproduction where the hadronic component is expected to be more relevant.

1.3.3 Heavy flavour production cross section calculation

Given the two different photon behaviours, a differential photon–hadron cross section can be written as the sum of a pointlike and a hadronic photon contribution:

$$d\sigma^{(\gamma p)}(P_\gamma, P_p) = d\sigma^{(\gamma p)}_{point}(P_\gamma, P_p) + d\sigma^{(\gamma p)}_{hadr}(P_\gamma, P_p) \tag{1.12}$$

where P_γ and P_p are the four–momenta of the photon and the proton, respectively. Using the factorisation theorems in QCD [12], the two contributions can be written as:

$$d\sigma^{(\gamma p)}_{point}(P_\gamma, P_p) = \sum_j \int dx f_j^{(p)}(x, \mu_F) d\hat{\sigma}_{\gamma j}(P_\gamma, xP_p, \alpha_s(\mu_R), \mu_R, \mu_F, \mu_\gamma) \tag{1.13}$$

$$d\sigma^{(\gamma p)}_{hadr}(P_\gamma, P_p) = \sum_{ij} \int dx dy f_i^{(\gamma)}(x, \mu_\gamma) f_j^{(p)}(y, \mu'_F) d\hat{\sigma}_{ij}(xP_\gamma, yP_p, \alpha_s(\mu'_R), \mu'_R, \mu'_F, \mu_\gamma) \tag{1.14}$$

Here the $f_i^{(\gamma)}$ are the partonic densities in the photon, and in a similar way the $f_j^{(p)}$ are the partonic densities in the proton; μ_R and μ'_R are renormalisation scales, μ_F and μ'_F are factorisation scales for singularities arising from strong interactions, and μ_γ (defined in 1.3.1) is a factorisation scale for singularities arising from the electromagnetic vertex. The hadronic parton densities obey the usual DGLAP evolution equations [13] in μ_F,

$$\frac{df_i(x,\mu_F)}{d\log\mu_F^2} = \frac{\alpha_S}{2\pi}\int\frac{dy}{y}P_{ki}f^k(y/x,\mu_F) \tag{1.15}$$

whereas the photonic parton density, not calculable in perturbation theory, obey a renormalisation group equation [14] that can be obtained by slightly modifying the DGLAP equation:

$$\frac{\partial f_i^{(\gamma)}}{\partial\log\mu^2} = \frac{\alpha_S}{2\pi}P_{i\gamma} + \frac{\alpha_S}{2\pi}\sum_j P_{ij}\oplus f_j^{(\gamma)} \tag{1.16}$$

At lowest order

$$P_{i\gamma} = N_c e_i^2(x^2+(1-x)^2) \tag{1.17}$$

where N_c is the number of colours and e_i is the electric charge in units of the positron charge. Equation 1.16 differs from the evolution equation of the hadron densities for the presence of the first term, which is due to the direct coupling of the photon and the quarks.

Since the photon parton densities are quite soft, the contribution from the hadronic component becomes important only for large centre–of–mass energy and small masses of the produced particles. In heavy quark production, this can affect charm production much more than beauty production.

The ep level cross section can finally be expressed in terms of the γp cross section $d\sigma^{\gamma p}(P_\gamma,P_p)$ in 1.12, and of the *equivalent photon flux* in the Weizsäcker-Williams (WWA) approximation [15]:

$$\frac{d\sigma_{ep}}{dy} = \frac{\alpha}{2\pi}\frac{1+(1-y)^2}{y}ln\frac{Q^2_{max}}{Q^2_{min}(y)}\sigma_{\gamma p}(W^2) \tag{1.18}$$

The y and W variables have been defined already in Section 1.1 while $Q^2_{min} = m_e^2y^2/(1-y)$ and Q^2_{max} is instead determined by the experimental geometrical acceptance.

1.3.4 Calculation of the partonic level cross section at NLO

The calculation of the NLO cross section for heavy flavour production has been performed recently. Firstly R.K. Ellis and P. Nason evaluated the QCD corrections to the direct $\gamma p \to QX$ process [16], and their calculations were then confirmed by Smith and van Neerven [17]. We will report a brief description of these results outlining the most important features of the calculation.

In particular we will describe in some detail the diagrams whose amplitudes enter in the calculations at NLO of the partonic level cross sections $\hat{\sigma}_{ij}$ and $\hat{\sigma}_{\gamma j}$ appearing in the factorised cross section expression of Equations 1.13, 1.14.

At Leading Order (i.e. $\alpha_S\ \alpha_{em}$), heavy flavour production proceeds via the so–called *boson–gluon fusion* process (Left plot in Figure 1.3), in which a photon from the incoming lepton interacts with a gluon from the proton giving a $Q\bar{Q}$ pair in the final state:

$$\gamma + g \to Q + \bar{Q} \tag{1.19}$$

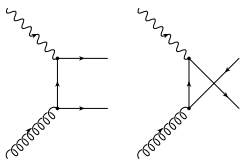

The evaluation of these diagrams is known since a while [18, 19]. The partonic cross section for the process 1.19 is given by

$$\hat{\sigma}_{\gamma g\to Q\bar{Q}} = \frac{2\pi\alpha e_Q^2\alpha_s(\mu^2)}{(\hat{s}+Q^2)^3}\left\{\left[\hat{s}^2+Q^4+4m_Q^2(\hat{s}^2-2m_Q^2)\right]ln\left(\frac{1+\beta}{1-\beta}\right) - \left[(\hat{s}-Q^2)^2+4\hat{s}m_Q^2\right]\beta\right\} \tag{1.20}$$

where $\alpha_s(\mu^2)$ is the strong interaction constant at the energy scale of the process, e_Q and m_Q the charge and mass of the produced heavy quark, $\sqrt{\hat{s}}$ is the center of mass energy in the γ g system and $\beta \equiv (1 - 4m_Q^2/\hat{s})^{0.5}$. A theoretical analysis of the differential distributions for this reaction reveals that the average transverse momentum (p_T) of the heavy quark or anti–quark is of the order of its mass and the p_T distribution falls rapidly to zero as $p_T \gg m$. Further the heavy quarks are mainly produced near the center of the rapidity range.

At the next order in α_S (i.e. $\alpha_S^2\ \alpha_{em}$) one has to consider the corrections due to emission of a gluon from one of the quark lines in the final state:

$$\gamma + g \rightarrow Q + \bar{Q} + g \qquad (1.21)$$

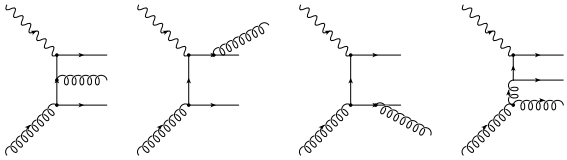

At this level of perturbative expansion new mechanisms also arise with the presence of a light quark in the initial and final state:

$$\gamma + q \rightarrow Q + \bar{Q} + q \qquad (1.22)$$

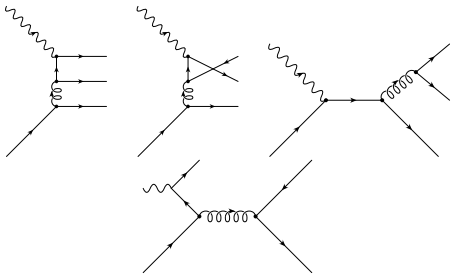

The order $\alpha_{em}\alpha_S^3$ Feynmann diagrams for the virtual corrections to the reaction $\gamma g \rightarrow Q\bar{Q}$ were also calculated. They are illustrated in the following Figure:

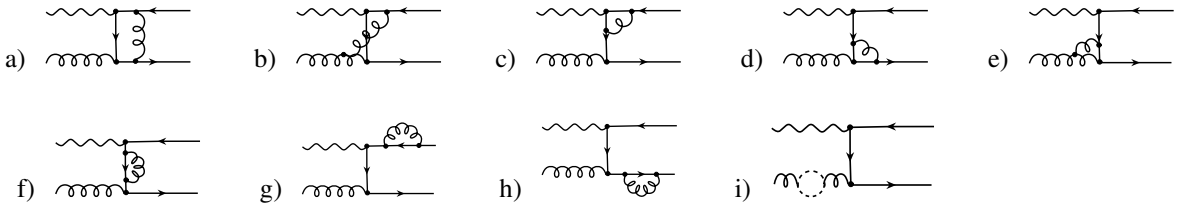

Additional graphs are obtained by reversing the arrows on the heavy quark lines, except for graph b). Gluon self energy corrections in i) with dotted lines represent gluon, ghost and quark loops.

The hadronic component, in which the photon fluctuates into quarks and gluons before the hard interaction, has to be added to these direct photon processes:

$$gg \rightarrow Q\bar{Q} \qquad (1.23)$$

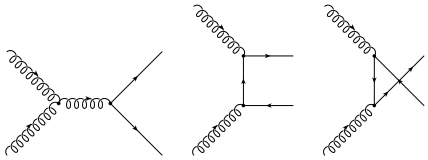

$$q\bar{q} \rightarrow Q\bar{Q} \qquad (1.24)$$

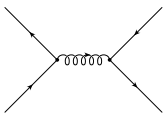

In Table 1.1 the total cross section for beauty quark production (with $m_b = 4.75$ GeV) at HERA is presented (for

		DIS			$\overline{MS}$	
	$Q = m_b/2$	$Q = m_b$	$Q = 2m_b$	$Q = m_b/2$	$Q = m_b$	$Q = 2m_b$
α_s	0.237	0.190	0.162	0.237	0.190	0.162
$\sigma_{\gamma g} O(\alpha_s)$	4.94	4.60	4.36	4.30	4.16	4.02
$\sigma_{\gamma g} O(\alpha_s^2)$	1.92	1.62	1.72	1.71	1.54	1.68
$\sigma_{\gamma q} O(\alpha_s^2)$	0.92	0.15	-0.21	0.98	0.20	-0.17
$\sigma_{qq} O(\alpha_s^2)$	0.14	0.12	0.11	0.15	0.12	0.11
$\sigma_{gg} O(\alpha_s^2)$	0.85	0.64	0.53	0.73	0.57	0.48
σ_{tot}	8.77	7.13	6.51	7.87	6.59	6.12

Table 1.1: *Partial and total cross sections (nb) for the process $\sigma(ep \to b\bar{b}X)$ at HERA ($\sqrt{s}$ =314 GeV) in the DIS and $\overline{MS}$ renormalisation schemes. $m_b = 4.75$ GeV is assumed. (Reference [20])*

$\sqrt{s} = 314$ GeV). To get an impression of the theoretical errors the numbers for both the DIS and the $\overline{MS}$ are presented. The mass factorisation scale dependence is also investigated for the values of the scale Q of $m/2$, m and $2m$ where $\alpha_S = 0.237, 0.190, 0.162$ respectively.

The various contributions to the heavy quark production cross section are given separately: the photon–gluon fusion process at leading order ($\sigma_{\gamma g}$), its correction at order α_s^2 and the LO contributions due to resolved photon processes, ($\sigma_{qq} O(\alpha_s^2)$, $\sigma_{gg} O(\alpha_s^2)$).

The largest contribution is given by the γg channel ($\sim 80\%$), although the other terms are not negligible.

From Table 1.1 we infer that the sensitivity of the cross section to the scale choice does not decrease after adding the $O(\alpha_S^2)$ corrections to the Born result. In particular the magnitude of $\sigma_{q\gamma}$ heavily depends on the chosen scale.

In the same Reference the differential distributions in the transverse momentum of the b quark, p_T, the rapidity y and the Feynmann x_F are also given. The shape of these distributions is not greatly modified with respect to the analogous ones at leading order.

The NLO corrections for parton–parton scattering, needed for the hadronic part (whose LO diagrams are presented in Figures 1.23, 1.24), were produced by P. Nason, S. Dawson and R.K. Ellis in [21] and by W. Beenakker et al. in [22].

The diagrams producing corrections to the $q\bar{q} \to Q\bar{Q}$ process at LO are here shown:

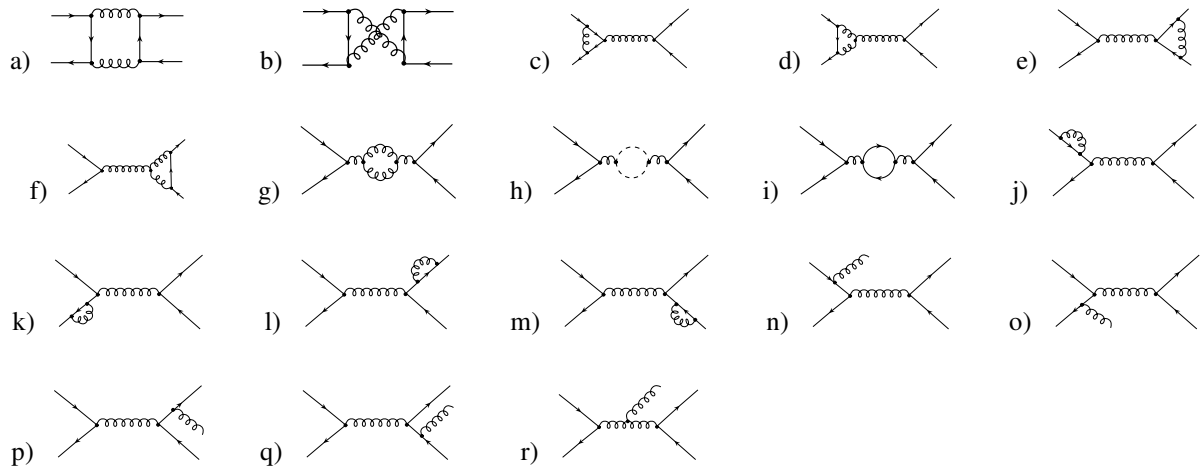

At this order additional production mechanisms arise in which a light (anti-)quark is present in the initial and final state. The graphs for these processes $g\bar{q} \to \bar{q}Q\bar{Q}$ $gq \to qQ\bar{Q}$ can be obtained by the graphs n) o) p) q) r) by crossing. Topologically they are equal to those for the process $\gamma q \to q\bar{Q}Q$ ($\gamma q \to q\bar{Q}Q$) shown in the Figure beside equation 1.22 after replacing the photon with a gluon.

The corrections at NLO to the $gg \to Q\bar{Q}$ have also been calculated. They are shown here :

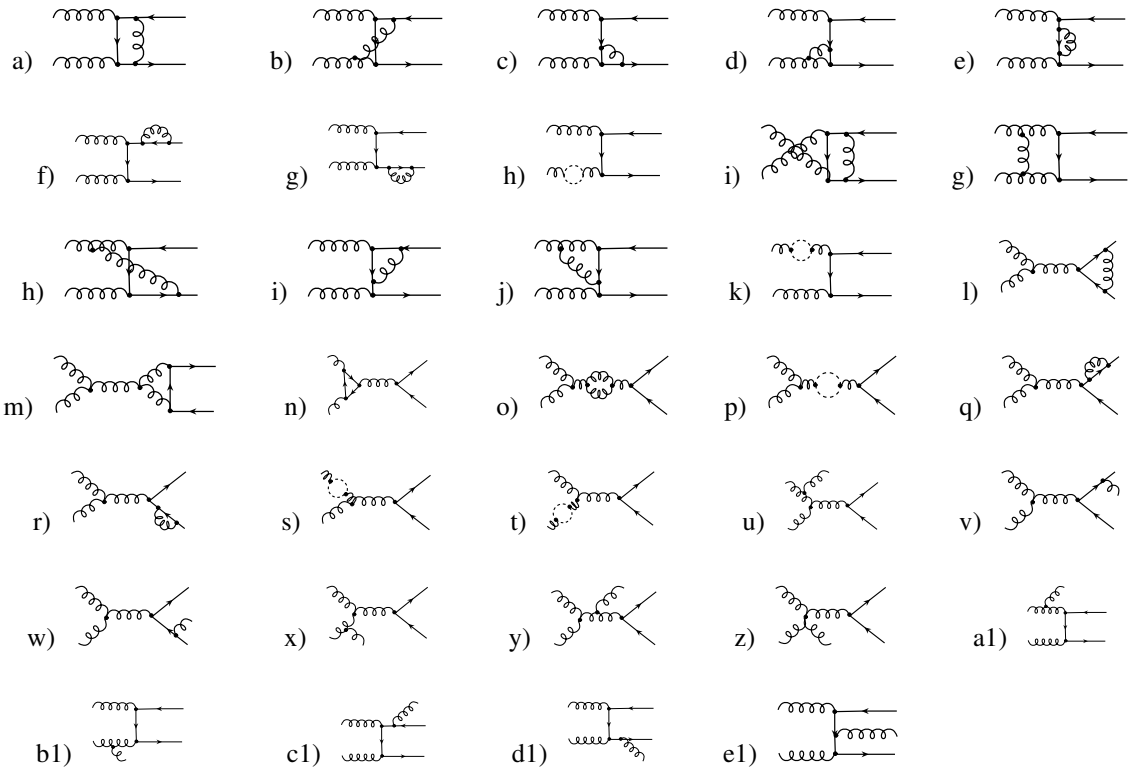

The various parton cross sections which have been computed in the previous sections still contain initial state collinear divergences. These singularities have to be removed via mass factorisations.

The previous calculations have been collected by S. Frixione et al. who have then developed a FORTRAN computer code [23, 24] that integrate the NLO formulas producing cross sections useful for comparison with data. This tool, which is called FMNR after the name of the authors, was used in this analysis to calculate the theoretical prediction.

In the DIS regime similar calculations have been carried out [25] and implemented into a FORTRAN code called HVQDIS which was also used for our analysis.

These perturbative QCD calculations rely on the fact that the mass of the heavy quark acts as a cut–off for infrared singularities so that the splitting processes in which a heavy quark is involved are finite order by order in perturbation theory. For this reason the calculations in [16, 17, 21] have been done with a modified version [26] of the $\overline{MS}$ subtraction scheme, in which the heavy quark effects decouple in processes involving momenta much smaller than the heavy quark mass. This implies that the heavy quark does not contribute to the evolution of the running coupling constant or of the structure function. Therefore subprocesses initiated by an intrinsic heavy flavour generated by the structure function (the so–called *flavour excitation processes*) are not present. This method is referred to as the *massive scheme*.

Nevertheless, the NLO one particle inclusive differential distributions contain terms like $\alpha_S \log(p_T^2/m^2)$ which become large in the high–p_T limit. This is reflected in a large sensitivity to the choice of the renormalisation and factorisation scales, and therefore in a large uncertainty in the theoretical predictions. Also terms like $\alpha_S \log(W/m)$ can become large at HERA energies.

To partially overcome these difficulties the so–called *massless schemes* have been worked out. In this approach the heavy quarks are treated as additional active flavours above some threshold, of the order of the quark mass. Below this threshold the heavy quarks revert to inactive flavours, the light quarks and gluons being the only active partons, as in the massive scheme. In this approach, the resummation of the $\alpha_S \log(p_T^2/m^2)$ terms to all orders is performed with the so–called Perturbative Fragmentation Function (PPF) technique [27].

The PPF approach is based on the assumption that the heavy quarks act as if they were massless when their momenta are much larger than their masses. Therefore the usual $\overline{MS}$ scheme is used, assuming all the quarks to be massless, subtracting the singularities also from their lines and introducing a fragmentation function to absorb the final state

divergences. This fragmentation function contains the logarithmic terms, so that their resummation is possible. However, the method is not reliable in the region $p_T \sim m_Q$, and in particular the total cross section is not calculable in the massless scheme due to the occurrence of divergences.

The calculations described in the following paragraphs are based on a fixed order massive approach so the logarithmic terms in $\alpha_S \log(p_T^2/m^2)$ are neglected. The indetermination on the theoretical cross section calculations due to the choice of the input parameters will be investigated. The pointlike and hadronic components will be analysed separately in order to estimate the different sources of uncertainties in the two cases [28].

The concern of using the massless approach is particulary motivated in the case of charm for which the resummed terms ($\alpha_S \log(p_T^2/m^2)$) are much more relevant than in the case of beauty due to the difference in mass.

The flavour excitation component is however included in our simulation through the presence in the Monte Carlo of several diagrams taking into account the possibility of the heavy quark to come from the photon or proton. A a more detailed description of the Monte Carlo simulation used in the analysis is given in Chapter 3. The LO diagrams to be added when we allow one (or both) of the partons from the γ (p) to be a heavy quark are here shown [6]:

$$Qq \rightarrow Qq \qquad (1.25)$$

$$Qg \rightarrow Qg \qquad (1.26)$$

$$Q\gamma \rightarrow Q\gamma \qquad (1.27)$$

$$Qg \rightarrow Qg \qquad (1.28)$$

$$Qq \rightarrow Qq \qquad (1.29)$$

$$Q\bar{Q} \rightarrow Q\bar{Q} \qquad (1.30)$$

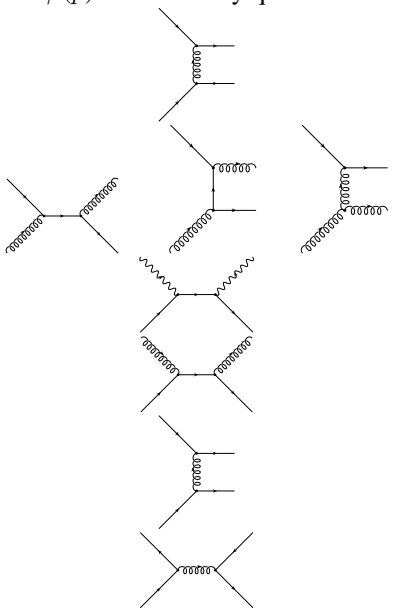

Having outlined the basic features of the calculation we will report on the uncertainties both in the case of charm and beauty production. These consideration are specific to the photoproduction case.

1.3.4.1 Uncertainties on the charm cross section

In charm photoproduction at HERA, large QCD radiative effects, which were not a problem in fixed–target experiments, are present due to the higher centre–of–mass energy. These radiative effects, proportional to $\alpha_{em}\alpha_S^2 \log(W/4m_c^2)$, where W is the centre–of–mass energy of the photon–proton system and m_c the charm mass, are the first manifestation of a tower of corrections behaving as $\alpha_{em}\alpha_S(\alpha_S \log(W/4m_c^2))^n$, coming from the small–x region. In order to evaluate the importance of these effects, the various contributions to the charm pointlike cross sections are shown as a function of x, evaluated as the ratio of the partonic over the hadronic centre–of–mass energy $\hat{w}/W$ (Figure 1.7). In the Figure the proton renormalisation and factorisation scales are set to the charm mass m_c , while the MRSA [29] parton densities are used for the proton. A hump, away from the threshold region, is clearly visible for NLO g and q contributions. The effect becomes even more important if, instead of choosing the MRSA parton densities for the proton, which have a relatively singular gluon distribution at small x, other parton densities, with a more regular behaviour at small x, as, for example, HMRS B [30], are used (Figure 1.7, Right). The importance of the small–x region can be estimated by the size of the hump relative to the total cross section. The conclusion is that small–x effects can have a considerable size in $c\bar{c}$ quark production at the HERA energies.

The hadronic component of the $c\bar{c}$ cross section is also sensitive to the gluon distribution in the photon in the small–x region. Small–x effects are present and they can give a contribution of 45% to the total cross section at the HERA

[6] Following a consolidated convention the upper parton is here intended to come from the photon and the bottom one from the proton.

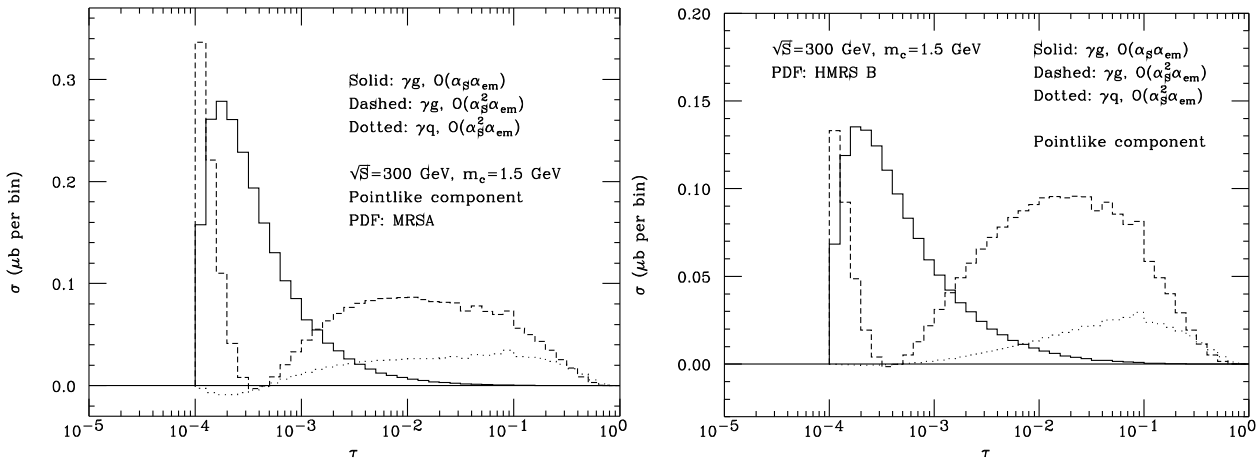

Figure 1.7: **Left***: The $O(\alpha_{em}\alpha_S)$ γg, $O(\alpha_{em}\alpha_S^2)$ γg and $O(\alpha_{em}\alpha_S^2)$ γq contributions to the total charm photoproduction cross section as a function of the variable $\tau = \frac{w}{W}$. The proton renormalisation and factorisation scales have been taken equal to the charm mass, while the proton parton densities used are MRSA.* **Right** *As for the Left plot, but with HMRS B proton parton densities (from Reference [28]).*

energy (20% at 50 GeV) if MRSA and GRV-HO parton densities are used for the proton and the photon, respectively. The dominant contribution to the hadronic cross section comes from events with x_γ between 10^{-2} and 10^{-1} where the x_γ variable is defined as the fraction of the photon momentum which takes part in the hard interaction. [28]. Some indications on the gluon density in the photon can come from results on dijet photoproduction at HERA [33], but the statistics are limited and do not allow to distinguish between different NLO parametrisations or different gluon densities in the photon. A reasonable way to estimate the uncertainty due to the choice of the gluon density in the photon is to take the sets GRV-HO [34] and LAC1 [35] as the two extremes. At the highest photon–proton centre–of–mass energy available at HERA, the prediction for the hadronic component with LAC1 is an order of magnitude higher than the prediction with GRV-HO.

Nevertheless, the uncertainty on the final result is much smaller than other uncertainties. Other important inputs in the computation of the total cross section are the value of the QCD scale, Λ, and the gluon density in the proton. For the calculations reported here, Λ has been chosen to vary in the interval 151 MeV $< \Lambda <$ 220 MeV in order to keep into account the values obtained from deep–inelastic scattering and e^+e^- data. The gluon density in the proton at relatively small x is constrained by deep–inelastic scattering data, but at very small x the gluon density is not known with precision. For the calculations reported here, the two sets MRSD-0 and CTEQ2MF, differing strongly at small x, yet consistent with the experimental parametrisations [32], has been used as the two extreme possibilities. The cross section is found to be very sensitive to the charm mass, whose variation changes the cross section up to a factor 4. It is also sensitive to the scale, giving a difference of a factor two for the lower choice.

The comparison between the theoretical predictions and the experimental results [36, 37] is shown in Figure 1.8, where only the uncertainty due to the choice of the renormalisation scale is shown. Even if this is just a part of the theoretical indetermination, it should be noticed that the data are in reasonable agreement with the curves obtained by choosing m_c = 1.5 GeV, MRSG for the proton and GRV-HO for the photon parton densities. Also the fact that all the data can be described with a single choice of the input parameters is not trivial since the HERA centre–of–mass energy is an order of magnitude higher than that of the fixed–target experiments whose results are plotted in the Figure. Some points have to be noticed, regarding the experimental measurement of the $c\bar{c}$ cross section. In charm analyses, the detectors are sensitive to the production in the central rapidity region and a p_T cut is usually applied to the data in order to reject background events. Therefore the total cross section has to be extrapolated to the full rapidity and momentum range, and this means extrapolating to the small–x region, which is poorly known. The extrapolation is therefore subject to large uncertainties.

1.3.4.2 Uncertainties on the beauty cross section

In beauty photoproduction, the uncertainties found in the case of charm are strongly reduced. The small–x problem, analysed in the same way as for charm, has been found to increase the value of the total cross section by $\sim 20\%$.

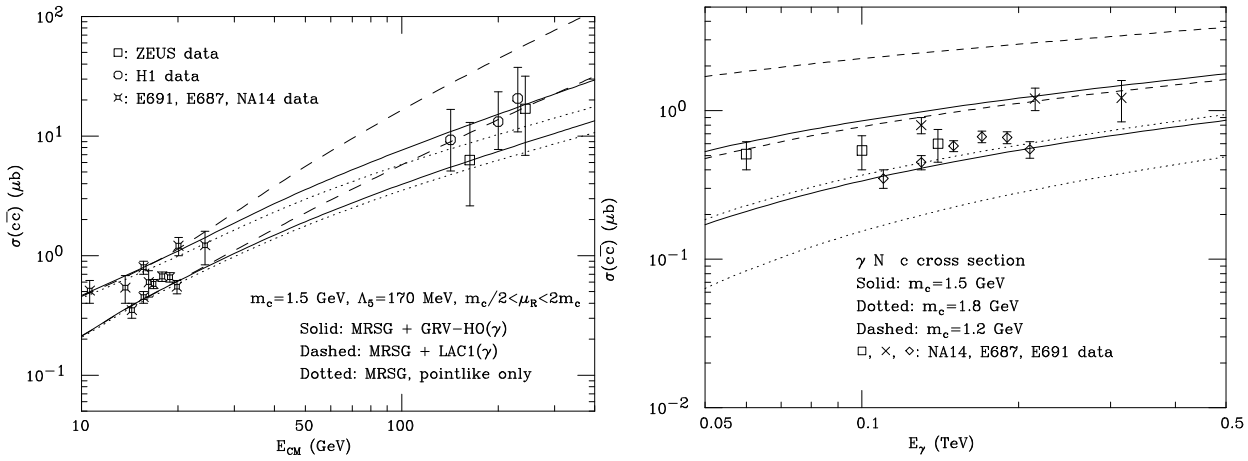

Figure 1.8: **Left***: total cross section for $c\bar{c}$ photoproduction as a function of the p centre–of–mass energy. Theoretical predictions and experimental data from Reference [36] and [37] are shown.* **Right***: total cross section for $c\bar{c}$ production in γN collisions, compared to NLO QCD predictions.*

The values of the total cross section for the pointlike and hadronic components are shown in Tables 1.2 and 1.3, where the central value for the renormalisation and factorisation scales has been set to $m_b = 4.75$ GeV (in the column labelled as "DEF").

The pointlike cross section can be varied up to a factor 2 by simultaneously modifying all the input parameters in the direction that makes the cross section larger or smaller. For example at $\sqrt{s_{\gamma p}} = 280$ GeV the lower limit is 41 nb while the upper limit is 101 nb. [28].

Coming to the hadronic component, the largest uncertainty comes from the choice of the parton density of the photon, as in the case of charm. However, in beauty photoproduction the small–x region is probed to a less extent than in the case of charm so the dependence on the photon density is milder. The difference on the estimated cross section is a factor 3 (to be compared to a factor 10 of the charm case (Section 1.3.4.1)) if GRV-HO and LAC1 sets are used as the two extreme possibilities.

In electroproduction, in the limits of the Weizsäcker Williams approximations, the sensitivity to the input parameter is considerably reduced and the hadronic component can constitute at most a 75 % of the pointlike contribution even if a "soft" gluon parametrisation for the gluon density in the photon (as the LAC1) is chosen.

The most interesting results are found when analyzing the single particle inclusive distributions [20]. The quark–transverse momentum of the produced b–quark, in particular, can be predicted with higher accuracy: it depends mildly on the chosen photon PDF (Figure 1.9) [38] if a cut on pseudorapidity is applied by imposing $\mid \eta \mid < 1.5$. [7].

We will perform our measurement in this regime, i.e. not considering the high pseudorapidity region of the cross section which is the one where the prediction has the largest uncertainties. The evalution of the theoretical error will be more specifically discussed in the last part of this Chapter in the context of comparison with the experimental data and in Chapters 5 and 6 where the predicted cross section will be compared with our results.

1.4 Experimental results on heavy quark production

Heavy quark production has been studied intensively, first at fixed–target experiments, and then at the colliders like HERA and the Tevatron. In the following sections the results obtained by the various experiments will be summarised, with particular emphasis on beauty production at HERA.

[7] The pseudorapidity η is defined as: $\eta = -\log(\tan(\theta/2))$, θ being the polar angle in the laboratory frame taken as zero in the proton direction.

		μ_R		μ_F		m_b (GeV)	
E_{CM}	DEF	$m_b/2$	$2m_b$	$m_b/2$	$2m_b$	4.5	5
Proton PDF set MRSA							
100 GeV	22.90	26.00	20.36	21.87	23.63	27.41	19.28
280 GeV	64.30	75.44	56.09	57.81	66.95	75.31	55.32
Proton PDF set CTEQ2MF							
100 GeV	24.91	27.93	22.33	23.80	25.73	29.70	21.02
280 GeV	62.91	73.08	55.24	56.27	65.80	72.76	54.71
Proton PDF set MRSD 0							
100 GeV	23.03	26.19	20.45	22.18	23.63	27.75	19.26
280 GeV	74.76	87.24	65.43	69.22	76.93	88.76	63.52
Proton PDF set CTEQ2M							
100 GeV	22.96	25.92	20.50	22.04	23.54	27.50	19.31
280 GeV	65.33	75.96	57.32	59.43	67.51	76.40	56.23
Proton PDF set CTEQ2ML							
100 GeV	25.07	29.53	21.76	23.38	25.92	30.03	21.07
280 GeV	71.04	86.84	60.42	61.74	74.39	82.99	61.20

Table 1.2: *Pointlike component of the total beauty cross section (nb), in p collisions, for different choices of the input parameters.*

		μ_R		μ_F		μ_γ		m_b (GeV)	
E_{CM}	DEF	$m_b/2$	$2m_b$	$m_b/2$	$2m_b$	$m_b/2$	$2m_b$	4.5	5
Photon PDF set GRV-HO									
100 GeV	4.244	5.589	3.290	4.246	4.258	3.883	4.525	5.444	3.347
280 GeV	27.63	38.67	20.74	25.68	29.13	25.39	28.68	34.29	22.48
Photon PDF set LAC1									
100 GeV	6.693	9.264	5.053	7.157	6.394	7.161	6.348	9.309	4.890
280 GeV	98.45	137.2	74.05	96.07	100.6	106.4	92.18	128.7	76.15

Table 1.3: *Hadronic component of the total beauty cross section (nb), in p collisions, for different choices of the input parameters.*

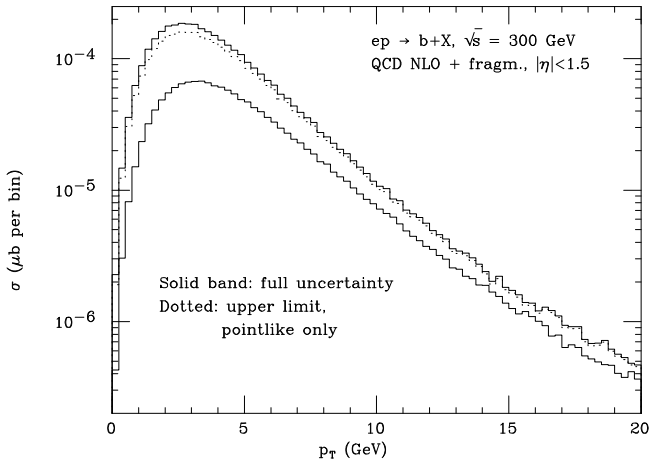

Figure 1.9: *Uncertainty on the B–hadron transverse momentum for beauty electroproduction in the Weizsäcker-Williams approximation with Peterson fragmentation and a cut on pseudorapidity of the hadron.*

1.4.1 Heavy quark production results at HERA

At the lepton–proton collider HERA, working at a centre–of–mass energy of $\sim$ 300 GeV, the study of heavy quarks is a subject of great interest. At that energy, as was shown in Sections 1.3.4.1 and 1.3.4.2, the $c\bar{c}$ production cross section is of the order of 1 μb, while the beauty cross section is of the order of 10 nb. With the integrated luminosity collected until 2000, very large statistics are available for the study of charm production, and also beauty analyses can be carried on and give significant results.

In the following we will first illustrate a selection of published and preliminary results of the ZEUS and H1 Collaborations on beauty production. Due to the its intrinsic relevance in our context and to the fact that we will largely deal with D^* in this analysis, we will also report on the most recent results released by the ZEUS collaboration on charm production studied both in photoproduction and DIS.

1.4.1.1 Beauty

The study of beauty production at HERA has been carried on by both the experiments ZEUS and H1, which have released several results (as journal papers or conference preliminaries) in both photoproduction and deep–inelastic scattering regime.

The most widely used experimental technique to measure beauty production is based on samples of events with two jets and a muon (electron) in the final state. Both the lifetime signature and the large mass of b flavoured hadrons can be used to determine the fraction of beauty quark events in the sample.

These are reflected respectively in a broad distribution of the transverse lepton momentum with respect to the associated jet axis (p_T^{rel}) [8] and a large impact parameter of the lepton track relative to the primary vertex (δ). The leptons coming from the decay of the massive beauty hadrons have a characteristic p_T^{rel} distribution peaked at 2 GeV, while muons from light flavour and charm backgrounds are in general collinear with the jet, with a p_T^{rel} distribution peaked close to zero. Similar discrimination power is provided by the study of the impact parameter distribution.

The fraction of b quark events in the final sample is determined on a statistical basis, by fitting to the distributions of the p_T^{rel} and δ observables in the data with adjustable fractions of beauty, charm and light-quark components, the shapes of which are taken from Monte Carlo (MC) simulations.

ZEUS uses the p_T^{rel}–based signal extraction only while H1 also uses the impact parameter information taking profit of their central silicon tracker [40].

In this kind of analyses the fraction of the total $E - P_z$ carried by the two highest-p_T jets:

$$x_{obs}^{\gamma} \equiv \frac{\sum_{j=1,2}(E_j - P_{j,z})}{(E - P_z)_{event}} \tag{1.32}$$

is studied since it corresponds at leading order to the fraction of the exchanged-photon momentum entering in the hard scattering process. It provides a tool to measure the relative importance of the photon–gluon fusion diagram $\gamma g \rightarrow b\bar{b}$, that gives a peak at $x_{obs}^{\gamma} \sim 1$, and of other contributions, such as gluon–gluon fusion (with a gluon coming from the photon) or higher–order diagrams, that are distributed over the whole x_{obs}^{γ} range.

H1 beauty photoproduction results with semi–leptonic muons

The H1 Collaboration has first studied the production of b quarks in the photoproduction regime [39] using a sample of 6.6 pb^{-1} collected during 1996 data taking. Lately this result was updated by including more data and a refined analysis technique which takes benefit of lifetime information ([41]). Most recently a larger data sample collected in the years 1999–2000 (center–of–mass–energy $\sqrt{s} = 318$ GeV) corresponding to an integrated luminosity of about 48 pb^{-1} was used (about three times larger than in the previous analysis). We will focus on this latest more significant result ([42]) in which differential measurements were also presented.

[8] Defining $p^{j-\mu} = p^j - p^\mu$, p^μ and p^j being the momenta of the muon and of the jet, respectively:

$$p_T^{rel} = \frac{|p^\mu \times p^{j-\mu}|}{|p^{j-\mu}|} \tag{1.31}$$

In this analysis the accepted range of negative four-momentum transfer squared was restricted to $Q^2 < 1$ GeV^2 while the inelasticity cut was set at $0.2 < y < 0.8$, where y was calculated using the Jacquet-Blondel method [47]. Jets were reconstructed using the inclusive k_T algorithm [46] with radius $R = 1$ in the η-ϕ plane. The E_T-recombination scheme was applied giving massless jets. The selection requires at least two jets with transverse energy $p_T^{jet1(2)} > 7(6)$ GeV, of which at least one contains a muon candidate. Muons were identified in the barrel part of the instrumented iron, corresponding to polar angles $35^\circ < \theta^\mu < 130^\circ$, and were required to have transverse momenta $p_T^\mu > 2.5$ GeV. The final event sample consists of 1452 events.

For each muon candidate, the impact parameter was calculated in the plane transverse to the beam axis. Its magnitude is given by the distance of closest approach of the track to the primary event vertex. Its sign is positive if the intercept of the track with the jet axis is downstream of the primary vertex, and negative otherwise. Decays of long-lived particles are signalled by positive impact parameters, whereas the finite track resolution yields a symmetric distribution centered on zero. The transverse profile of the beam interaction region at HERA has a Gaussian width of about 145μm in the horizontal and of about 25μm in the vertical direction. The muon track candidate under consideration was excluded from this fit. An average muon impact parameter resolution of 80μm is achieved with comparable contributions from the muon track resolution and the primary event vertex position uncertainty.

The fraction of beauty events in the data was determined from a combined fit to the two-dimensional distribution of and p_T^{rel} by adopting the shapes predicted by the PYTHIA Monte Carlo. The fit yields a sample composition of $f_b = (30.7 \pm 2.5)$ % (beauty), $f_c = (60.6 \pm 4.5)$ % (charm) and $f_{uds} = (8.7 \pm 4.0)$ % (light flavours). Here the errors refer to the statistical uncertainties. The reliability of the two-dimensional fit was demonstrated by using the one-dimensional δ and p_T^{rel} projections. The obtained signal and background fractions are in good agreement using these different methods.

The Left hand plot in Figure 1.10 shows the measured impact parameter distribution in the data together with histograms indicating the contributions from b production and from the c and uds backgrounds using the relative fractions obtained in the two-dimensional fit. The data are well described by the sum of the estimated contributions. In the Right hand plot in Figure 1.10 the observed p_T^{rel} distribution is shown.

The shapes of distributions in the data for several variables (p_T^μ, η^μ, $p_T^{jet1(2)}$, x_γ^{obs}) have been compared to those obtained using the PYTHIA Monte Carlo components in the relative fractions provided by the fit. They have been found to be adequately described by the simulations.

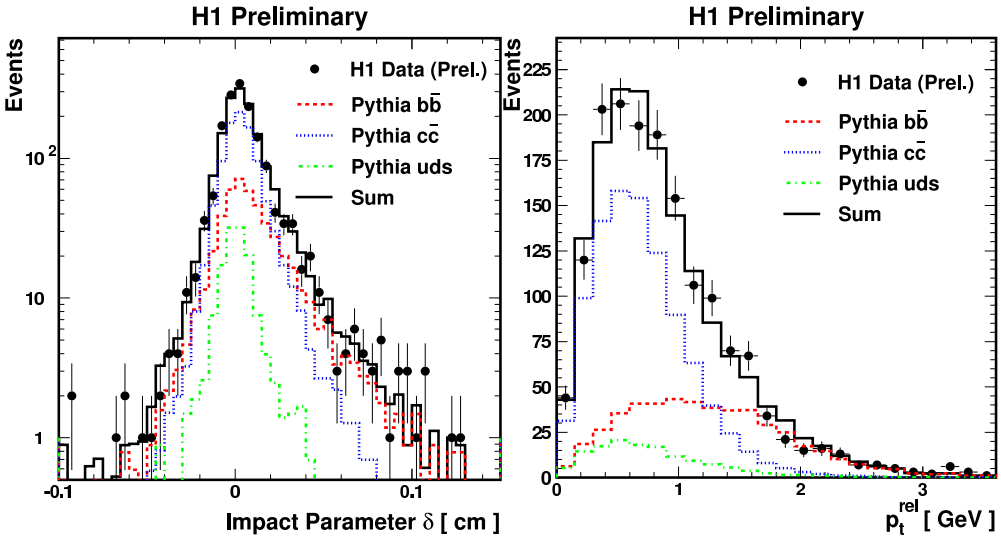

Figure 1.10: *Distribution of impact parameter δ (Left) and p_T^{rel} (Right) of the muon track. The data (points) are compared with the Monte Carlo simulation (solid line). The decomposition of the Monte Carlo distribution into the b (dashed line), the c (dotted line) and the light quark (dashdotted line) components is determined from a fit to the two-dimensional distribution of δ and p_T^{rel}.*

Monte Carlo event samples for the processes $ep \to eb\bar{b}X$, $ep \to ec\bar{c}X$ and light quark production were generated using the PYTHIA program which is based on leading order QCD and parton showers. PYTHIA simulates direct and

resolved photon processes and also includes excitation processes, in which one heavy quark (c or b) originates from the resolved photon or the proton. The CTEQ5L parton densities were used for the proton and those of GRVG-LO for the photon. The light quark sample was used to simulate the background from fake muons, i.e. hadrons misidentified as muons, and decays of light mesons into muons.

The program CASCADE, a Monte Carlo generator which implements the CCFM parton evolution equation In this Monte Carlo heavy quark production is obtained from the $\mathcal{O}(\alpha_S)$ matrix elements for the process $\gamma g^* \rightarrow b\bar{b}$ in which the initial gluon can be off–shell. The gluon density, unintegrated in the transverse momentum (k_T), is obtained from an analysis of the proton structure functions based on the CCFM equations. In the event generation the mass of the b quark was set to 4.75 GeV, and the scale of α_S to the transverse mass m_T CASCADE was used for cross checks and for comparisons with the measured cross sections.

Dijet event samples which fulfill the same selection criteria as the signal sample, but without the muon trigger and muon-identification requirements, were used to study the tracking and jet reconstruction resolutions. The resolutions of the Monte Carlo simulations were tuned so that the PYTHIA light quark event sample accurately describes these data samples.

The program for fixed order massive NLO calculations by Frixione et al. [23, 24] was modified to facilitate the comparison of the calculation with the visible cross sections in the experimentally accessible kinematic range. The outgoing partons (b quark, $\bar{b}$ quark and the gluon) were combined into jets using the inclusive k_T jet–algorithm (in the E_T-scheme)[46]. The b quark was then fragmented to a B–hadron using the Peterson fragmentation function with a fragmentation parameter $\epsilon = 0.0033$ which subsequently decays into a muon. The muon decay spectrum takes both direct and cascade decays via charm into account. The calculation was performed for a b quark mass of 4.75 GeV with factorisation and renormalisation scales defined as $\mu_R = \mu_F = \sqrt{m_b^2 + p_T^{b,2}}$. Systematic errors were estimated by varying the b quark mass up and down by 0.25 GeV and μ_R and μ_F up and down by factors of two. These variations were performed simultaneously and lead to cross section changes of 25%. For the structure functions the DIS-scheme parametrisations CTEQ5D for the proton and GRV-G HO for the photon were taken. The cross section variation when using other proton structure functions such as MRSG or MRST1 is less than 8% in all regions of the measurement. The uncertainty due to variations of the fragmentation parameter by 25% is below 3%.

The obtained parton level cross sections were corrected to the hadron level using the PYTHIA Monte Carlo generator. The corrections are smaller than 20% in all bins of the measurement except for the region $0.5 < x_\gamma^{obs} < 0.75$ where the correction is 40%. If the Monte Carlo generator CASCADE is used the calculated cross sections at hadron level is generally 15% – 20% smaller than those obtained from PYTHIA.

The dijet-muon beauty production cross section, $\sigma_{vis}(ep \rightarrow eb\bar{b}X \rightarrow ejj\mu X)$, was measured in the visible range $Q^2 < 1$ GeV^2 , $0.2 < y < 0.8$, $p_T^\mu > 2.5$ GeV, $-0.55 < \mu < 1.1$, $p_T^{jet1(2)} > 7(6)$ GeV and $|\eta^{jet}| < 2.5$. The cross section was defined for jets which include all final state particles. The muon must be associated with one of the two jets. The visible cross section is measured as $\sigma_{vis}(ep \rightarrow eb\bar{b}X \rightarrow e\ jj\ \mu X') = (42.5 \pm 3.4(stat.) \pm 8.9(sys.))$ pb. The dominant sources of the systematic uncertainty are the muon identification efficiency and the modeling of the tracking and vertexing resolutions. Dependence on the physics model was studied by using for the modeling of beauty and charm events alternatively the CASCADE Monte Carlo simulation and by using either Peterson [18] or Lund [20] fragmentation. In comparison the prediction from the NLO QCD calculation including fragmentation and hadronisation corrections is $(24.1^{+7.2}_{-5.1})$ pb. Taking the errors of both measurement and theory into account the calculation is below the measurement by a factor 1.5.

The differential cross sections were measured as functions of the pseudorapidity η^μ, the transverse momentum of the muon p_T^μ and of x_γ^{obs} (see Figure 1.11). The cross section values were determined separately for each bin, using the beauty fraction from the fit to the two-dimensional distribution of p_T^{rel} and in that bin.

The data have been compared with expectations obtained from the PYTHIA and CASCADE generators and the prediction from the QCD NLO calculation. For PYTHIA the contribution from resolved events is displayed separately in the Figures. While both generators, PYTHIA and CASCADE, give a good description of the shapes of the μ and x_γ^{obs} distributions observed in the data, their predictions lie significantly too low. The disagreement in normalisation appears to decrease towards larger values of p_T^μ (third plot in Figure 1.11). The comparison of the data with the QCD NLO prediction shows that the μ and x_γ^{obs} distributions are well described in shape. In contrast the p_T^μ dependence of the prediction appears to be somewhat harder than the measured leading to good agreement at large p_T^μ (fourth plot of Figure 1.11).

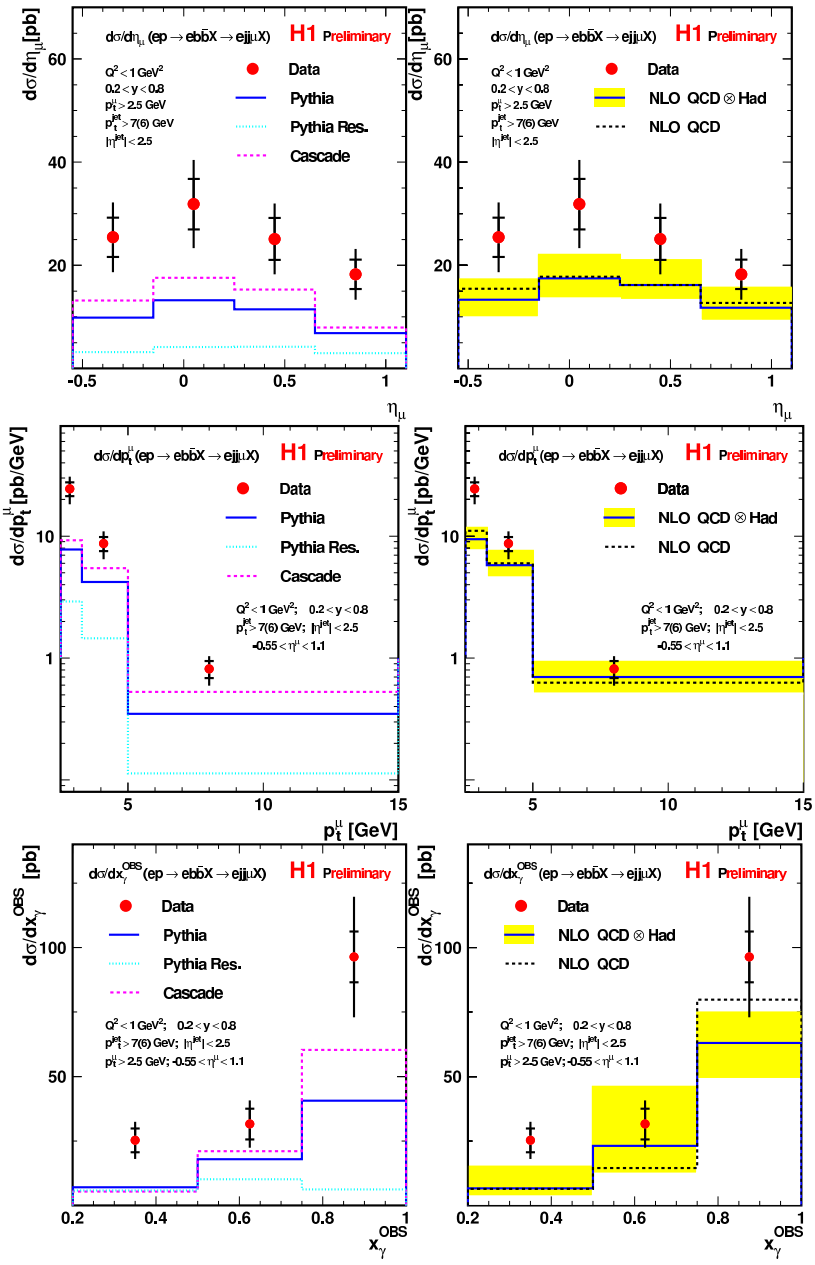

Figure 1.11: *From top to bottom: differential dijet muon beauty production cross sections $d\sigma/d\eta^\mu$, $d\sigma/dp_T^\mu$, $d\sigma/dx_{obs}^\gamma$ in the range $Q^2 < 1$ GeV^2, $0.2 < y < 0.8$, $p_T^\mu > 2.5$ GeV, $-0.55 < \eta^\mu < 1.1$, $p_T^{j1(2)} > 7(6)$ GeV and $|\eta_j| < 2.5$. The inner error bars show the statistical error, the outer error bars represent the statistical and systematic uncertainty added in quadrature. In the Left column plots the measurements are compared to the predictions from the Monte Carlo generator program* PYTHIA *(solid line), the resolved contribution to the* PYTHIA *cross section (dashed-dotted line) and* CASCADE *(dashed line). In the right column plots the measurements are compared to the prediction from a pQCD NLO calculation at parton level (dashed line) and hadron level (solid line). The band shows the uncertainty obtained from a simultaneous variation of the b–quark mass, μ_R and μ_F (see text).*

Using the same data sample as described above, including the jet requirements, an inclusive muon cross section ($ep \to b\bar{b}X\mu X$) is determined. The chosen kinematic region contains events with $Q^2 < 1$ GeV^2, $0.1 < y < 0.8$, $p_T^\mu > 2$ and $35^\circ < \theta < 130^\circ$, and the AROMA program is used for the extrapolation into the unmeasured phase space. The result is $\sigma = (177 \pm 14(stat.) \pm 37(sys.))$ pb. The systematic error does not include a contribution from the uncertainty of the extrapolation. The result is good in agreement with previous measurements of the inclusive $b\mu X$ cross section. In the earlier measurements the measured cross sections were given after extrapolation using LO QCD

Monte Carlo simulations. The results showed large deviations from the NLO QCD expectation. Good agreement of this analysis with the previous measurements is found when using the same extrapolation procedure, as discussed in the previous paragraph. More recently, the HERA beauty data have been compared with NLO QCD predictions calculated in the experimentally accessible kinematic region using the latter procedure the predictions from NLO QCD are in significantly better agreement with the data, but still fall somewhat low. The excess above expectations from NLO QCD and also from the leading order parton shower Monte Carlo generators PYTHIA and CASCADE appears to decrease somewhat towards larger values of p_T^μ.

ZEUS beauty photoproduction results with semi–leptonic muons

The first measurement on beauty in the muon channel released by ZEUS dates back to 1999 when the data collected in the years 1996-97 were used [43]. We will now describe some more recent results which are on their way towards publication and appeared partially as preliminary results [44, 45] . They contain a larger statistic (110 pb^{-1}) and the measurement of differential cross sections. After this we will report on an early result which was obtained using the semi–leptonic decay of beauty in the electron channel.

Muons were reconstructed online by matching in position and momentum tracks reconstructed in the central drift chamber (CTD Section 2.2.2) with a muon track reaching the outer BRMUON chambers or crossing at least four planes in the Forward muon chambers (FMUON Section 2.4.2). Three regions of good acceptance were defined depending on the angular acceptance of the F/BRMUON and of the CTD and the requirement that the muons reach the external chambers:

$$\begin{array}{rlll} \text{Rear}: & -1.6 < \eta^\mu < -0.9 & p^\mu > 2.5\ \text{GeV} & \\ \text{Barrel}: & -0.9 < \eta^\mu < 1.3 & p_T^\mu > 2.5\ \text{GeV} & \\ \text{Forward}: & 1.48 < \eta^\mu < 2.3 & p^\mu > 4\ \text{GeV},\ \ \mathrm{p_T^\mu} > 1\ \text{GeV} & \end{array} \tag{1.33}$$

where η^μ, p^μ and p_T^μ are the muon pseudorapidity, momentum and transverse momentum, respectively.

Jets were reconstructed running the k_T algorithm [46] in the longitudinal-boost invariant mode on the so called energy flow objects (*EFOs*) which combine the information from calorimetry and tracking, corrected for the presence of muons and for energy loss in dead material. The E recombination scheme, in which the jet four-momentum is the sum of the input four-momenta, was used. A sample of dijet events with one muon was selected requiring one muon in one of the three regions defined in Equations 1.33 and two jets with pseudorapidity $|\eta^j| < 2.5$, and transverse momentum $p_T^j > 7$ GeV for the highest-p_T^j jet and $p_T^j > 6$ GeV for the other; a reconstructed vertex compatible with the nominal interaction point, no scattered electron candidate found in the CAL, and $0.2 < y < 0.8$ (using the Jacquet Blondel method). The jet–muon association was obtained from the k_T algorithm. To assure a reliable p_T^{rel} measurement, the jet transverse momentum calculated not including the muon was asked to be $p_T^{j-\mu} > 2$ GeV. After this selection the final sample consists of 3660 events.

The distributions in the data for the most relevant variables were compared in shape to the PYTHIA MC sample in which the relative fractions of beauty, charm and LF have been mixed according to the cross–sections predicted by the program. The comparison showed that the main features of the dijet–plus–muon sample are well reproduced by the MC mixture of signal and background. The HERWIG Monte Carlo gives also a good description of the data.

The PYTHIA MC predicts the background to be composed by 57% of muons from charmed-hadron decays and 43% of non–prompt muons from light–flavours, mostly due to in-flight decays of π and K, with a small amount (5% of the LF component) from muons produced in secondary interactions.

The p_T^{rel} distribution for the background, was obtained from the p_T^{rel} distribution of inclusive tracks, in a dijet sample of data selected without muon requirements, times the probability that a track is (mis–)identified as a muon taken from the MC. This probability was obtained from the ratio of the Monte Carlo distributions for muons and for inclusive tracks. PYTHIA underestimates the p_T^{rel} tail by $\sim 25\%$ (at 3 GeV), the difference being larger at low track p_T and in the barrel region.

Figure 1.12 shows the result of the p_T^{rel} fit for muons in the Rear, Barrel and Forward regions. The two components are able to reproduce the data reasonably well. The total fraction of b in the dijet–plus–muon sample is $0.224 \pm 0.017(\text{stat.})$.

The measured cross–sections are defined for dijet events with $p_T^{j1,j2} > 7,6$ GeV, $|\eta^{j1,j2}| < 2.5$, $Q^2 < 1$ GeV ^{2} and $0.2 < y < 0.8$. The first set of measurements are beauty cross–sections for muons passing the cuts defined in

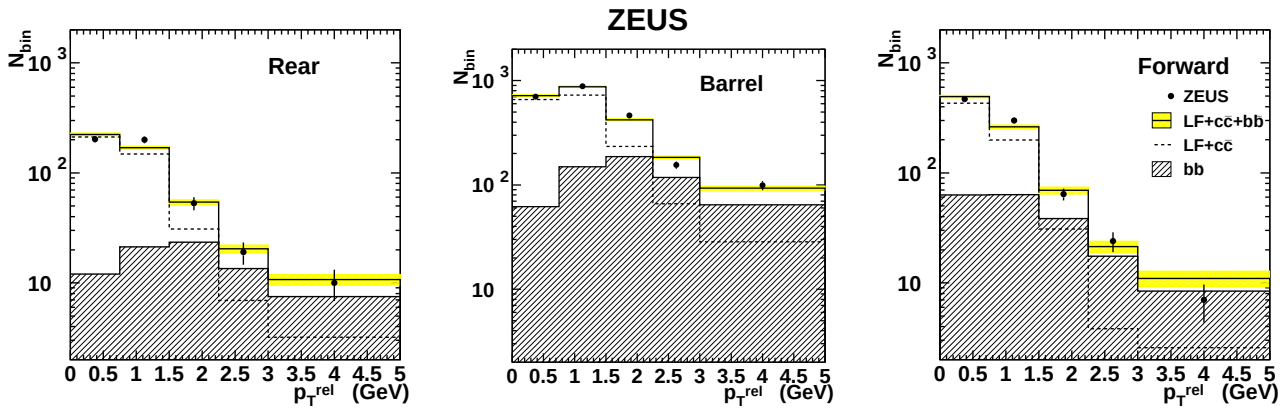

Figure 1.12: *The p_T^{rel} distribution for events with muons in the Forward, Barrel and Rear regions. The data (points) are compared to the mixture of beauty and charm+LF background obtained from the p_T^{rel} fit (full line). The shaded band shows the uncertainty from the Monte Carlo statistics. The hatched histogram represents the beauty component while the dashed–line histogram is the background.*

Equations 1.33. The result for the Forward, Barrel and Rear regions are shown in the Left hand plot in Figure 1.13 and compared with NLO prediction and MC models. Both the NLO and the MC models are in agreement with the data in the Barrel and Rear regions but are somewhat below the data in the Forward region where the measured cross–section is 1.8 (1.4) standard deviations above the nominal (upper) value of the NLO prediction after the hadronisation correction.

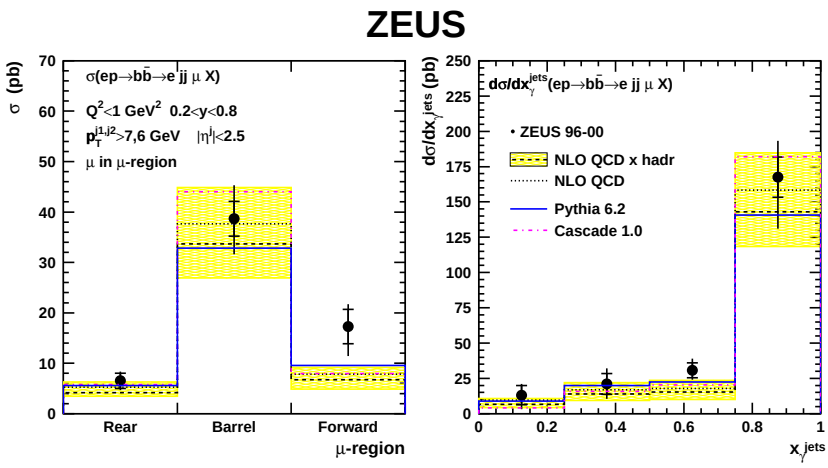

Figure 1.13: *Beauty cross sections for events with two jets and a muon, in the Forward, Barrel and Rear regions (Left plot), and differential cross–section as a function of x_{obs}^{γ} (Right plot). The data (dots) are compared to the predictions of NLO QCD (dashed line: parton–level jets, solid line: jets corrected to the hadron–level). The full error bars are the quadratic sum of the statistical (inner part) and systematic uncertainties. The band around the NLO represents the variation on the theoretical predictions obtained by varying the b–quark mass and μ_R and μ_F as explained in the text. The data are also compared to the predictions of* PYTHIA *(solid line histogram) and* CASCADE *(dot–dashed line histogram) Monte Carlo models.*

The acceptances were calculated using the PYTHIA Monte Carlo, in which the distribution of the transverse momentum of the b–quark was reweighted to agree to that of the NLO calculations. The reconstructed jets were corrected to jets made of stable hadrons, where the weakly-decaying B hadrons were considered stable. The acceptances for the visible cross–sections obtained in this way vary from 10% to 20%.

The measured cross–sections were compared to NLO QCD predictions based on the program FMNR by Frixione et al. [23, 24]. The parton distribution functions used for the nominal prediction were GRV–G HO for the photon and CTEQ5M for the proton. The b–quark mass was set to $m_b = 4.75$ GeV, and the renormalisation and factorisation scales to the transverse mass, $\mu_R = \mu_F = m_T = \sqrt{\frac{1}{2}(p_T^{b2} + p_T^{\bar{b}2}) + m_b^2}$, where $p_T^{b(\bar{b})}$ is the transverse momentum of the $b(\bar{b})$ quark. Jets were reconstructed by running the k_T algorithm on the four momenta of the b and $\bar{b}$ quarks and of the third light parton (if present) generated by the program. The fragmentation of the b quark into a B hadron was simulated by rescaling the quark momentum (in the frame in which $p_z^b = -p_z^{\bar{b}}$, obtained with a boost along z) according to the Peterson fragmentation function with $\epsilon = 0.0035$. The muon momentum in the B hadron rest frame was then extracted from the decay spectrum given by PYTHIA.

To evaluate the uncertainty on the NLO calculations, the b–quark mass and the renormalisation and factorisation scales were varied simultaneously from $m_b = 4.5$ GeV and $\mu_R = \mu_F = m_T/2$ to $m_b = 5.0$ GeV and $\mu_R = \mu_F = 2m_T$. The effect on the cross–section of a variation the Peterson parameter from 0.002 to 0.0055 and of a change of the fragmentation function from the Peterson to the Kartvelishvili parametrisation [48] was within $\pm$ 3%. The hadronisation correction needed to correct the partonic jets produced by the NLO to jets made of stable hadrons was obtained from the MC. The average between the corrections obtained from PYTHIA and HERWIG was taken as the central value and their full difference as the uncertainty. The hadronisation correction factors range from $-20 \pm 6\%$ in the rear region to -3.0 ± 0.3 % at large p_T^μ. The cross–sections measured from data collected at two different center–of–mass–energies, $\sqrt{s} = 300$ GeV and $\sqrt{s} = 318$ GeV, were corrected to $\sqrt{s} = 318$ GeV using the NLO QCD prediction. The size of this correction is 2%.

The measured cross–sections were also compared to the absolute predictions of two MC models, PYTHIA 6.2 and CASCADE 1.0. The predictions of PYTHIA 6.2 were obtained following the prescriptions of [49], namely mixing direct–($\gamma g \rightarrow b\bar{b}$) and resolved–photon ($gg \rightarrow b\bar{b}$, $q\bar{q} \rightarrow b\bar{b}$) flavour–creation processes calculated using massive matrix elements, with the flavour–excitation (FE) processes ($bg \rightarrow bg$, $bq \rightarrow bq$) in which a heavy quark is extracted from the photon or proton parton density. The FE processes contribute to 27% of the total $b\bar{b}$ cross–section from PYTHIA. The small (5%) contribution from gluon splitting in parton showers ($g \rightarrow b\bar{b}$) was not included. The parton density CTEQ4L was used for the proton and GRVG–LO for the photon; the b–quark mass was set to 4.75 GeV and the b-quark string fragmentation was performed according to the Peterson function with $\epsilon = 0.0041$ [50].

The uncertainty related to the p_T^{rel} shape of the LF and charm background was evaluated by varying the jet-track association in the inclusive track sample and alternatively, by reweighting the tracks in the inclusive track sample according to a p-dependent MC parametrisation of the probability to be identified as a muon. It was then tried to vary the p_T^{rel} shape of the charm component of the background between the prediction from PYTHIA and the value obtained from the inclusive track sample, taking the average as the nominal value. The relative charm to LF fraction in the background sample was also varied from -50% to +100%. Finally HERWIG instead of PYTHIA was used to simulate the background. The total uncertainty from these sources is 10%.

The plots in Figure 1.13 show the differential cross–section $d(ep \rightarrow b\bar{b}X \rightarrow jj\mu X')/dx_{obs}^\gamma$ for muons in the range defined by Equation 1.33. The sample is clearly dominated by the high-x_{obs}^γ peak but a low–x_{obs}^γ component is clearly present. The NLO describes well this distribution. PYTHIA is also able to give a good description of the data thanks to the large contribution from flavour–excitation at low–x_{obs}^γ. CASCADE, which generates low–x_{obs}^γ jets events from initial–state radiation without any parton density in the photon, is in reasonable agreement as well. The differential cross–sections in the muonic variables were measured for $p_T^\mu > 2.5$ GeV to get an uniform acceptance in all the three regions of Equations 1.33.

Differential cross–sections in the muon pseudorapidity η^μ and transverse momentum p_T^μ were measured. The NLO and the MC models describe well $d\sigma/d\eta^\mu$. In the last η^μ bin the excess in the forward region is still present after the requirement $p_T^\mu > 2.5$ GeV but with lower statistical significance. The p_T^μ distribution is well reproduced by the NLO while the p_T^μ slope tends to be too soft in CASCADE and PYTHIA. The jet associated to the muon ($\mu - jet$) reproduces the kinematics of the b (or $\bar{b}$) quark with a good degree of approximation. The $\mu - jet$ distributions in η and p_T have been corrected for the inclusive $b \rightarrow \mu$ branching ratio, including direct and indirect decays, and for the full muon phase–space to obtain the cross–sections for b(or $\bar{b}$) jets in dijet events: $\sigma(ep \rightarrow e'jjb(\bar{b})X)$.

The plots in Figure 1.14 show the differential cross–sections $d\sigma/d\eta^{j_{b(\bar{b})}}$ and $d\sigma/dp_T^{j_{b(\bar{b})}}$. The b–jet distributions are again reasonably well described by the NLO and by the MC models. It should be noted that the hadronisation corrections in the first two $\eta_{b(\bar{b})}^j$ bins are large (-20%) because for negative pseudorapidities most of the jets are close to

the minimal $p_T^{j1,j2}$ allowed by the dijet selection. Since the NLO QCD describes well the data in the central region, it was used to extrapolate the dijet cross–section to the inclusive b-quark cross–section ($\sigma(ep \to bX)$) allowing for a direct comparison with other measurements given at the b–quark level.

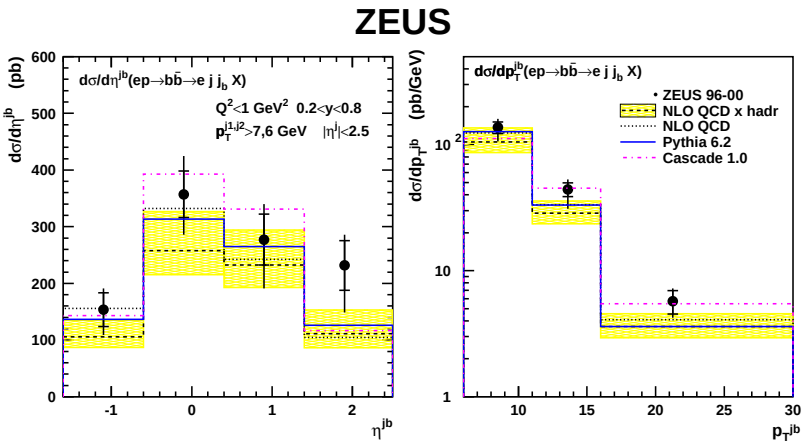

Figure 1.14: *Beauty differential cross sections as a function of the pseudorapidity, η^{jb} and transverse momentum p_T^{jb} of the jet containing the B hadron for events with two jets. The data (dots) are compared to the predictions of NLO QCD (dashed line: parton–level jets, solid line: corrected to hadron–level jets). The full error bars are the quadratic sum of the statistical (inner part) and systematic uncertainties. The band around the NLO represents the variation on the theoretical predictions obtained by varying the b–quark mass and μ_R and μ_F as explained in the text. The data are also compared to the predictions of* PYTHIA *(solid line histogram) and* CASCADE *(dot–dashed line histogram) Monte Carlo models.*

The b-quark inclusive cross–section for quark transverse momentum $p_T^b > 7$ GeV and for pseudorapidity $|\eta^b| < 2$ was obtained from the dijet crosssection for events with a b–jet within $|\eta^{j_b(\bar{b})}| < 2$ and then extrapolated to the b–quark using the NLO program. As a cross–check the measurement was corrected to the b–quark level using the MC, giving a result in agreement within 6%. The result is shown in Figure 1.14, compared with the previous ZEUS measurement [51]. The two independent measurements are consistently above but agree with the NLO QCD predictions within experimental and theoretical uncertainties

The NLO is in good agreement with the data within the experimental and theoretical uncertainties in all the differential distributions with the only exception of the muons in the forward direction, which are 1.8 (1.4) standard deviations above the nominal (upper) NLO prediction. The MC models CASCADE and PYTHIA are also able to give a reasonable description of the differential cross–sections, with the possible exception of the high–p_T^μ bin that is too low in PYTHIA and of the muons in the forward direction that are slightly above all the predictions. The beauty production in ep collisions appears therefore reasonably well understood both in terms of NLO QCD and in terms of MC models that include a substantial flavour excitation component (PYTHIA) or k_T –factorisation effects (CASCADE). This result is consistent with the previous ZEUS measurements using B decays into electrons [51] and for larger Q^2 [52] that were also found to be compatible with the NLO QCD within the experimental and theoretical uncertainties. The large excess over the NLO QCD prediction reported by the first measurements of beauty production at HERA [39] is much reduced.

ZEUS beauty photoproduction results with semi–leptonic electrons

The ZEUS Collaboration also published results on beauty photoproduction with semi–leptonic decay into electrons [51]. We will briefly summarise the results of this analysis which are important being complementary and independent to the one with muons.

The data sample used corresponds to ~ 38 pb^{-1} collected during 1996–97 data–taking. Events were selected by requiring the presence of at least two jets in the final state, reconstructed by the k_T–algorithm [46], having transverse energy $E_T^{jet1(2)} > 7(6)$ GeV, in the angular region defined by $|\eta_{jet1,2}| < 2.4$. DIS background was rejected by removing events with a well reconstructed positron in the CAL and by cutting on the inelasticity, y_{JB}, measured using

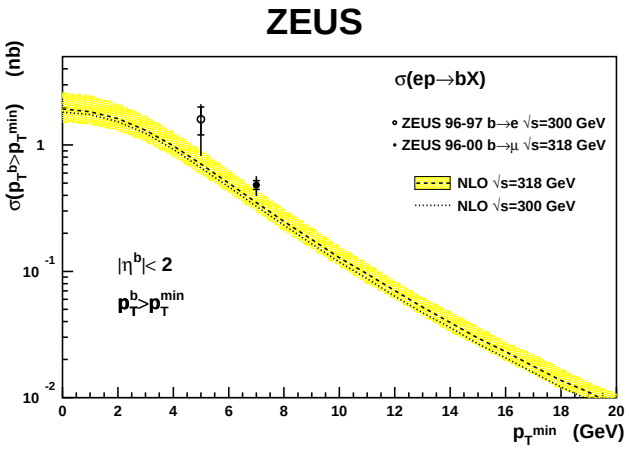

Figure 1.15: *The b-quark cross section for b-quark transverse momentum larger than p_T^{min} , for b–quark pseudorapidity $|\eta_b| < 2$, compared to the predictions of NLO QCD. The full error bars are the quadratic sum of the statistical (inner part) and systematic uncertainties. The band around the NLO represents the variation on the theoretical predictions obtained by varying the b–quark mass and μ_R and μ_F as explained in the text. The result is compared to the previous ZEUS measurement in the electron channel [51].*

the Jacquet–Blondel method [47]. The inelasticity was asked to be in the range $0.2 < y_{JB} < 0.8$. These cuts limit the data sample to $Q^2 < 1$ GeV^2.

Electrons were identified in the Central Tracking Detector (see Section 2.2.2) from the dE/dx of the charged tracks, using a method of statistical subtraction. The identified electrons were asked to have $p_T^e > 1.6$ GeV and to be in the angular region defined by $|\eta_e| < 1.1$.

The differential cross sections $d\sigma/dp_T^{rel}$ and $d\sigma/dx_\gamma^{OBS}$ for events with a semi–leptonic decay of a heavy quark into an electron were calculated in the kinematic region defined by $0.2 < y < 0.8$, $Q^2 < 1$ GeV^2 , $E_T^{jet1(2)} > 7(6)$ GeV, $|\eta_{jet1,2}| < 2.4$, $p_T^e > 1.6$ GeV and $|\eta_e| < 1.1$. The obtained distributions are shown in Figure 1.16. The data are compared to the expectations of the HERWIG [53] Monte Carlo simulation, which has been area normalised to the data for a comparison of shape; the scaling factor was 3.8.

In the $d\sigma/dp_T^{rel}$ differential cross section, the peak at low values is consistent with predominant semi–leptonic decays of charm quark, whereas the tail at high p_T^{rel} values is consistent with a significant contribution from b decays. The contribution from light flavours, essentially coming from decays, was estimated to be less than 3%.

In the $d\sigma/dx_\gamma^{OBS}$ distribution a peak at high values is observed, consistent with the dominance of direct photon processes, but the tail at low–x_γ^{OBS} values cannot be explained by direct processes alone. HERWIG predicts a contribution of 35% from resolved processes to the total cross section, giving a distribution in good agreement with the data. From the fit of the shape of the direct and resolved components to the data distribution, the resolved photon component is estimated to give a 28 ± 5 (stat.)% contribution to the total cross section. Therefore, LO Monte Carlo models require resolved photon processes to describe heavy quark production, as was already observed for charm production in [54]. The p_T^{rel} distribution of the data was fitted to the sum of the contributions from beauty and charm, including the cascade decay $b \to c \to e$ in the background expected for charm. The fitted beauty percentage, $f_b = 14.7 \pm 3.8$ (stat.), was used to determine the cross section for beauty production in the kinematic region defined above. The result was:

$$\sigma^{b\to e^-}_{e^+p\to e^+ + \text{dijete}^- \text{X}} = 24.9 \pm 6.4^{+4.2}_{-7.3} \text{ pb} \tag{1.34}$$

This cross section was extrapolated to the parton level in a restricted range of the transverse momentum and pseudorapidity of the b–quark, defined as $p_T^b > 5$ GeV, $|\eta_b| < 2$. The kinematic region was also defined by $Q^2 < 1$ GeV^2 and $0.2 < y < 0.8$. The extrapolation factor evaluated by the HERWIG Monte Carlo was 6.8, with a large uncertainty due to the hadronisation model, quantified in 26% by using the PYTHIA [55] Monte Carlo to extrapolate (PYTHIA uses the Lund model while HERWIG uses the cluster model for the hadronisation). To correct to the full beauty cross section

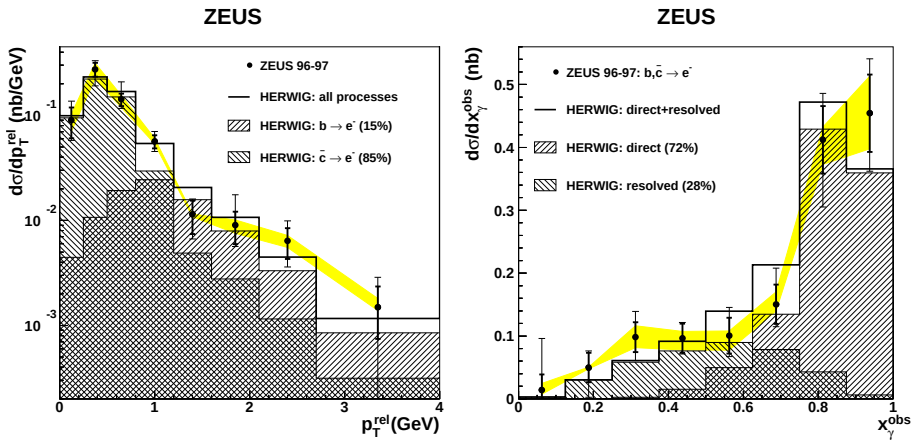

Figure 1.16: **Left**: *differential cross section $d\sigma/dp_T^{rel}$ for heavy flavour production. The shaded band represents the effect of the uncertainty on the calorimeter energy scale. The experimental data are compared to the* HERWIG *Monte Carlo prediction (solid line) for all quark flavours, fitted to the data and scaled up by a factor 3.8. The contributions from beauty (forward–diagonally hatched histogram) and from charm processes (backward–diagonally hatched histogram) predicted by the Monte Carlo model are shown separately.* **Right**: *differential cross section $d\sigma/dx_\gamma^{OBS}$ for heavy quark decays. The direct (forward–diagonally hatched histogram) and resolved photon components (backward–diagonally hatched histogram) are shown separately. From Reference [51].*

the branching ratio for the process $b \to e = (10.73 \pm 0.35)\%$ [56] was used. The extrapolated cross section was found to be:

$$\sigma^{ext}_{ep\to e^+bX} = 1.6 \pm 0.4(\text{stat.})^{+0.3}_{-0.5}(\text{syst.})^{+0.2}_{-0.4}(\text{ext.})\ \text{nb} \tag{1.35}$$

The cross section extrapolated in this way was compared to the NLO QCD predictions by Frixione et al. [28, 57]. The parton densities used for the proton and the photon were MRST99 [58] and GRV–G HO [34], respectively; the renormalisation and factorisation scales were set to the transverse mass, $\mu_R = \mu_F = m_T = \sqrt{m_b^2 + p_T^2}$, using for the mass of the b–quark the value $m_b = 4.75$ GeV. The predicted beauty cross section with the above settings was 0.64 nb. To estimate the uncertainty on the theoretical calculation the b–quark mass and the scales were changed simultaneously in order to obtain the maximum upper and lower variation of the predicted cross section. The obtained result is shown in Figure 1.15 (hollow bullet): the extrapolated cross section lies somewhat above the central NLO prediction.

H1 beauty electroproduction results

It is interesting to see if the discrepancy between data and theoretical predictions is observed also in the deep inelastic scattering regime, since in this case the production mechanism of heavy quarks is quite different than in the photoproduction case (see Section 1.3.3).

The H1 Collaboration has presented preliminary results [59] on beauty production in the high–Q^2 region. The analysed sample corresponds to 10.5 pb^{-1} of data collected during 1997. The analysis is very similar to that of the PHP regime, reported in [41], but in this case the scattered positron had to be observed in the detector, having a polar angle $\theta^e < 177^o$ and an energy $E_e > 9$ GeV. The cross section was determined in the kinematic range $2 < Q^2 < 100$ GeV^2 , $0.05 < y < 0.7$, $p_T^\mu > 2$ GeV and $35° < \theta^\mu < 130°$. The beauty fraction in the data was determined by a fit to the two dimensional (δ, p_T^{rel}) distribution, as for the photoproduction analysis. The resulting beauty fraction in the data was $f_b = 43 \pm 8\%$. From this value the beauty production cross section in the DIS regime could be extracted:

$$\sigma_{vis}(ep \to bX \to \mu X) = 39 \pm 8(\text{stat.}) \pm 10(\text{syst.})\text{pb} \tag{1.36}$$

The NLO QCD prediction was obtained using the HVQDIS program [25]. The Peterson function was used to describe the b fragmentation. The proton parton densities chosen were GRV98 [60]; the renormalisation and factorisation scales were $\mu_R = \mu_F = \mu = \sqrt{Q^2 + 4m_b^2}$, with the b–quark mass set to $m_b = 4.75$ GeV. The value found was (11 ± 2) pb, well below the experimental result.

ZEUS beauty electroproduction results

The ZEUS experiment also has presented preliminary results [52] on beauty production in the DIS regime. The analysed sample corresponds to 60 pb^{-1} of data collected during 1999–2000 running period. DIS events were selected by requiring a well reconstructed positron with $E_e > 10$ GeV, $Q^2 > 2$ GeV^2 and $0.05 < y < 0.7$. At least one jet reconstructed in the Breit frame was required, having transverse energy $E_T^{jet} > 6$ GeV, in the pseudorapidity range $2 < \eta^{lab} < 2.5$, where η^{lab} is the pseudorapidity measured in the laboratory frame. The muon, reconstructed in the region $30^o < \theta^{\mu} < 160^o$, and with $p_T^{\mu} > 2$ GeV, had to be included in one jet having $E_T > 4$ GeV in the Breit frame. The Monte Carlo used to simulate signal and background events was RAPGAP [61]. The fraction of beauty in the data was determined by a fit to the p_T^{rel} variable, mixing the charm and light flavour components according to their relative luminosities, since the shape of their p_T^{rel} distribution was very similar and cannot be distinguished by the fit. The fraction of beauty events in the data was $f_b = 25 \pm 5\%$ (stat.), and the corresponding beauty cross section was:

$$\sigma_{b\bar{b}}(e^+p \rightarrow e^+b\bar{b}X \rightarrow e^+\text{jet}\mu^{\pm}\text{X}) = 38.7 \pm 7.7(\text{stat.})^{+6.1}_{5.0}(\text{syst.})\text{pb} \tag{1.37}$$

The biggest contribution to the systematic uncertainty comes from the muon reconstruction efficiency and from the p_T^{rel} fit procedure.

The LO QCD prediction folded with the DGLAP evolution (RAPGAP Monte Carlo) underestimates the measured cross section. CASCADE is in good agreement with the data (35 pb). The NLO QCD predictions were determined using the HVQDIS [25] program. The Peterson function with $\epsilon = 0.002$ was used to describe the b fragmentation into hadrons, and the semi–leptonic decay of b–hadrons was modelled using a parametrisation of the muon momentum spectrum extracted from the Monte Carlo. The proton parton densities used were CTEQ5F4 [62], the b–quark mass was set to $m_b = 4.75$ GeV, and the renormalisation and factorisation scales to $\mu = \sqrt{Q^2 + 4m_b^2}$. The resulting value was $28^{+5.3}_{-3.5}$ pb, which is somewhat below but in agreement within the experimental and theoretical uncertainties with the measured value.

Differential cross sections were also calculated in the same restricted kinematical range as for the total visible cross section by repeating the fit of the p_T^{rel} distribution in each bin. The two plots in Figure 1.17 show the differential cross sections as a function of x and Q^2 compared to the NLO predictions.

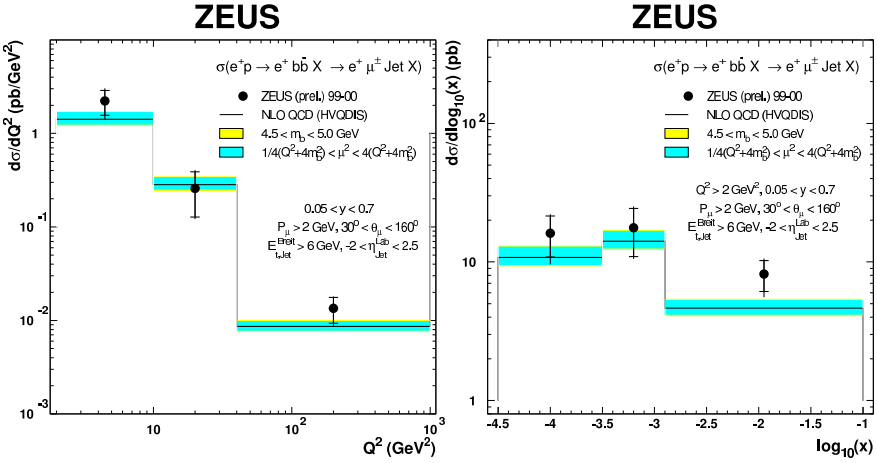

Figure 1.17: *Differential beauty cross section as a function of Q^2 (Left) and x (Right) for events with at least one jet reconstructed in the Breit frame and a muon, compared to the NLO QCD calculations. The error bars on the data points correspond to the statistical uncertainty (inner error bars) and to the statistical and systematic uncertainty added in quadrature (outer error bars). The shaded bands show the uncertainty of the theoretical prediction coming from the variation of the renormalisation and factorisation scale, μ, and the b-quark mass.*

1.4.1.2 D^* inclusive photoproduction

At HERA, large statistical samples are available for the analysis of charm events. Open charm production has been studied via the semileptonic decays into electrons or via D^* meson production. We will focus on this last channel

which has the advantage of having a quite clear experimental signature. Preliminary results published by ZEUS ([63]) in D^* photoproduction will be presented first.

The analysis was based on an integrated luminosity of 78.7 pb^{-1}. The measured differential cross sections were compared with perturbative QCD predictions which incorporate mass effects up to next-to-leading order and the resummation of transverse-momentum logarithms up to the next-to-leading-logarithmic level (NLL).

Charm production was tagged by identifying $D^*(2010)$ mesons in the final state via their charged decay products:

$$D^{*+} \rightarrow D^0 \, \pi_s^+ \rightarrow (K^- \, \pi^+) \, \pi_s^+ \tag{1.38}$$

and the charge conjugated processes. The small mass difference $\Delta m = m(D^*) - m(D^0) = 145.42 \pm 0.02$ MeV [64] yields a low momentum pion, referred to as the soft pion, π_s , from the D^* decay, and a large signal just above the threshold of the $\Delta m = m(K\pi\pi_s) - m(K\pi)$ distribution, where the phase space contribution is highly suppressed. These features of the events are used to discriminate the signal from the background. The Δm distribution for the final data sample is shown in Figure 1.18.

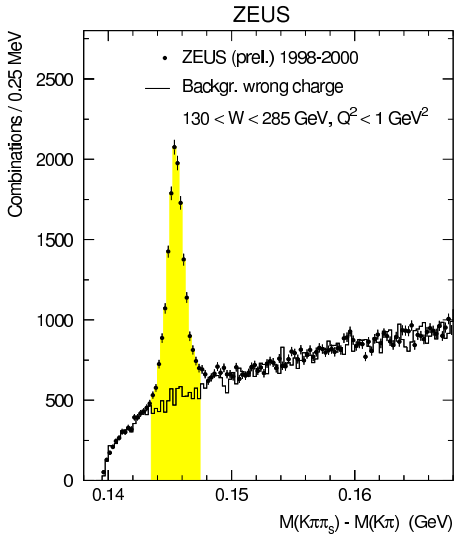

Figure 1.18: *The distribution of the mass difference, $\Delta m = m(K\pi\pi_S) - m(K\pi)$, for $D^{*\pm}$ candidates (solid dots). The histogram shows the Δm distribution for wrong charge combinations.*

The Monte Carlo samples of charm and beauty events used for the acceptance calculations were produced with the HERWIG 6.301 and PYTHIA 6.156 generators. The generation included direct photon processes, in which the photon couples directly to a parton in the proton, and resolved photon processes, where the photon acts as a source of partons, one of which participates in the hard scattering process. The latter contribution is the most sizeable for positive $\eta(D^{*\pm})$ values, i.e. in the forward (proton) direction, and at low $z(D^{*\pm})$ values. The CTEQ5L [65] and GRV LO [66] parametrisations were used for the proton and photon structure functions, respectively. The quark masses were set to the values $m_c = 1.5$ GeV and $m_b = 4.75$ GeV. All components were generated proportionally to the predicted MC cross sections.

The HERWIG simulation reproduces the data reasonably well; it was used as the reference MC to calculate the acceptances. The PYTHIA simulation (not shown), predicts too soft a $p_T(D^{*\pm})$ distribution and too backward an $\eta(D^{*\pm})$ distribution. This simulation was used as a systematic check after reweighting the $p_T(D^{*\pm})$ and $\eta(D^{*\pm})$ distributions to describe the data.

Differential cross sections of the inclusive $D^{*\pm}$ production for the process $ep \rightarrow D^{*\pm}X$ were measured in the kinematic region $Q^2 < 1$ GeV^2, $130 < W < 285$ GeV, $1.9 < p_T(D^{*\pm}) < 20$ GeV and $-1.6 < \eta(D^{*\pm}) < 1.6$. They were determined as a function of $p_T(D^{*\pm})$, $\eta(D^{*\pm})$, W and $z(D^{*\pm})$ [9].

[9] $z(D^{*\pm}) \equiv \frac{(E-p_Z)^{D^*}}{E-p_Z}$. In the proton rest–system $z(D^*)$ is the fraction of the photon energy carried by the D^* meson.

The four Left hand plots in Figure 1.19 show the differential cross-sections $d\sigma/dp_T$, $d\sigma/d\eta$, $d\sigma/dW$ and $d\sigma/dz$. The $d\sigma/dp_T$ distributions for four intervals of $\eta(D^{*\pm})$ are shown in the Right hand part of Figure 1.19. The $d\sigma/d\eta$ distributions for four intervals of $p_T(D^{*\pm})$ are shown in the four Left hand plots in Figure 1.20. The four Right hand plots in Figure 1.20 show the $d\sigma/dp_T$ and for four intervals of $z(D^{*\pm})$. The $d\sigma/d\eta$ cross–sections in z bins are shown in the Left hand part of Figure 1.21. The $d\sigma/dz$ distributions for four intervals of $p_T(D^{*\pm})$ are shown in the Right hand part of Figure 1.21. The measured cross sections are consistent with previous measurements based on data taken in 1996-1997 [54].

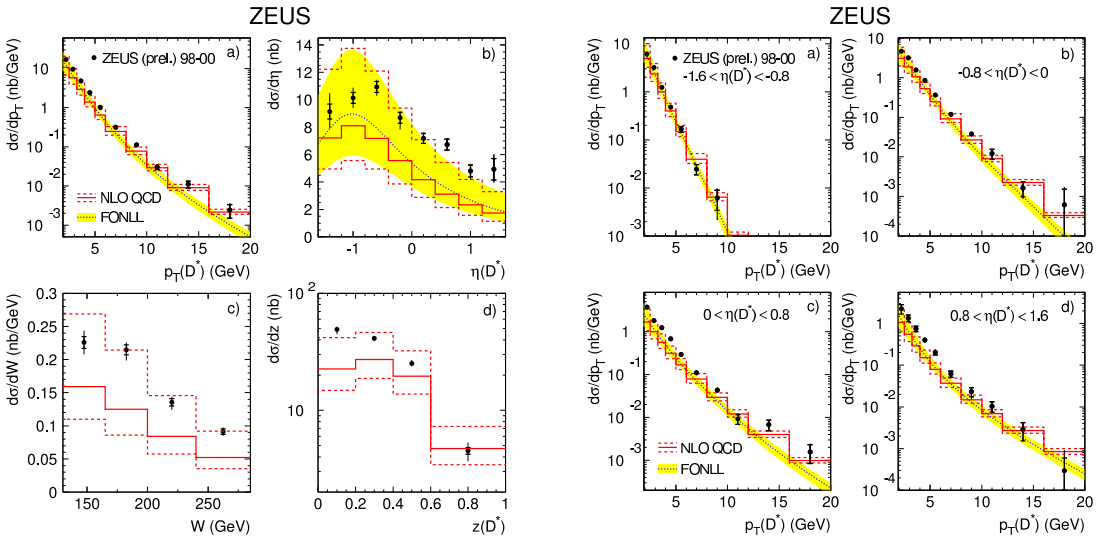

Figure 1.19: **Left** *part: Differential cross sections for inclusive $D^{*\pm}$ production in the in the kinematic region defined in the text. a) $d\sigma/dp_T$, b) $d\sigma/d\eta$, c) $d\sigma/dW$ and d) $d\sigma/dz$. The inner error bars represent statistical uncertainties and the outer bars show statistical and systematic uncertainties added in quadrature. The predictions of NLO calculations with the central choice of parameters are given by the solid histograms. The upper (lower) dashed histograms correspond to the upper (lower) bounds of the predictions. The FONLL predictions, whenever available, are shown as dotted curves and their uncertainties are given by the shaded bands. The parameters used for the NLO and FONLL calculations are described in the text.* **Right** *part: $d\sigma/dp_T(D^*)$ in bins of $\eta(D^*)$*

A detailed study of possible sources of systematic uncertainty was performed for the measured differential cross sections. Uncertainties originating from the signal extraction procedure, the modelling of the MC simulation, the CAL energy simulation and the tracking simulation were considered. Contributions from the different systematic uncertainties were calculated and added in quadrature for each bin of the differential cross sections. The statistical and systematic errors were added in quadrature. The overall normalisation uncertainties due to the luminosity measurement ($\pm 2.2\%$) and to D^{*+} and D^0 decay branching ratios ($\pm 2.3\%$) were not included in the systematic errors.

The measured differential cross sections were compared to the NLO [67] and FONLL [68] calculations. The structure-function parametrisations used in both calculations were CTEQ5M1 [65] for the proton and AFG [21] for the photon. The fraction of c quarks hadronising as D^{*+} mesons was set to $f(c \to D^{*+}) = 0.235$ [69]. The Peterson parametrisation [69] was used for the charm fragmentation in both calculations. For the NLO calculations, the Peterson parameter, ϵ, was set to the value 0.035 obtained in an NLO fit [70] to ARGUS data [71]. For the FONLL calculations, $\epsilon = 0.02$ in accord with a NLL fit [5] to e^+e^- data [71, 72]. Figures 1.19, 1.20, 1.21 compare the NLO calculations to the differential cross sections. The solid histograms correspond to the central NLO predictions with the renormalisation and factorisation scales $\mu_R = \mu_F = m_T = \sqrt{m_c^2 + p_{c,T}^2}$ and $m_c = 1.5$ GeV, where m_c and $p_{c,T}$ are the pole mass and transverse momentum of the charm quark, respectively. The theoretical uncertainties were estimated by simultaneous varying the renormalisation scale and the mass of the charm quark. The upper (lower) dashed histograms show the NLO predictions obtained with $\mu_R = 0.5 m_T$ ($\mu_R = 2 m_T$) and $m_c = 1.3$ GeV ($m_c = 1.7$ GeV).

The NLO predictions reproduce the shape of the $d\sigma/dW$ distribution and the general trends of the $d\sigma/dp_T$ distributions. However, the central NLO predictions significantly underestimate the data over almost the whole kinematic range. The largest disagreements are seen for medium $p_T(D^{*\pm})$ values, for positive $\eta(D^{*\pm})$ values (i.e. in the

forward or proton direction) and for low $z(D^{*\pm})$ values. For these regions, even the upper bounds are below the data. By contrast, the central NLO predictions describe the data well, both in shape and normalisation, for the range $0.6 < z(D^{*\pm}) < 1$.

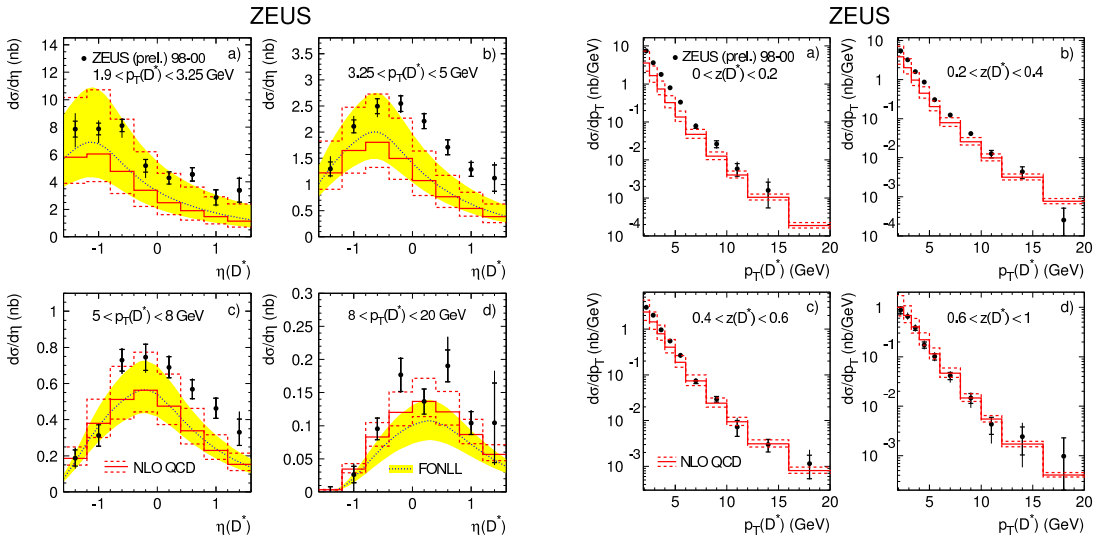

Figure 1.20: **Left** *part:* $d\sigma/d\eta(D^*)$ *in bins of* $p_T(D^*)$ **Right** *part:* $d\sigma/dp_T(D^*)$ *in bins of* $z(D^*)$

The FONLL predictions obtained with $\mu_R = \mu_F = m_T$ and $m_c = 1.5$ GeV are shown in Figures 1.19 and 1.20 as the dotted curves. The shaded bands indicate the uncertainties of the FONLL predictions. The upper (lower) limits were calculated by adding linearly the effects of varying the renormalisation scale μ_R to $0.5m_T$ ($2m_T$) and m_c to 1.2 GeV (1.8 GeV) [73]. As expected [68], for low $p_T(D^{*\pm})$ values the FONLL predictions are very close to the central NLO predictions, the small excess being explicable due to the smaller value of the Peterson parameter used. The FONLL predictions do not give a better description of the data than NLO. For large $p_T(D^{*\pm})$, the FONLL predictions are below the NLO calculations, considerably underestimating the data.

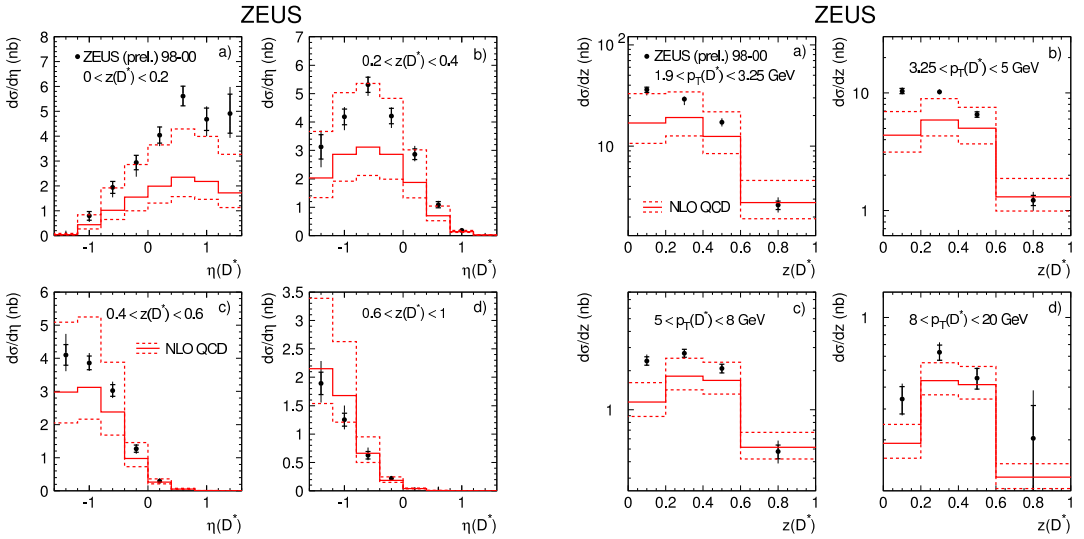

Figure 1.21: **Left** *part:* $d\sigma/d\eta(D^*)$ *in bins of* $z(D^*)$ **Right** *part:* $d\sigma/dz(D^*)$ *in bins of* $p_T(D^*)$

1.4.1.3 Charm electroproduction at HERA

It is a firm observation how copiously charm quarks are produced in deep–inelastic scattering at HERA. At sufficiently high photon virtualities, Q^2, the production of charm quarks constitutes up to 30% of the total cross section [74, 75]. We will here briefly review some recent results by the ZEUS collaboration on charm production in DIS [76].

Inclusive production of $D^{*\pm}$ mesons in deep–inelastic scattering has been measured with the ZEUS detector at HERA using an integrated luminosity of 81.9 pb^{-1} (1998–2000 data taking, 16.7 ± 0.3 pb^{-1} with e^-p collisions and 65.2 ± 1.5 pb^{-1} with e^+p collisions). The decay channel $D^{*+} \to D^0\pi_s$ with $D^0 \to K^+\pi^-$ and corresponding antiparticle decay were used.

Figure 1.22 shows the ΔM distribution for the D^* candidates together with the background from the wrong–charge combinations. For the range $0.143 < \Delta m < 0.148$ GeV, a clear signal of D^0 candidates is also shown in the same Figure. The number of D^* candidates determined in the two signal regions and after subtracting the background estimated from the wrong–charge sample was 5545 ± 129.

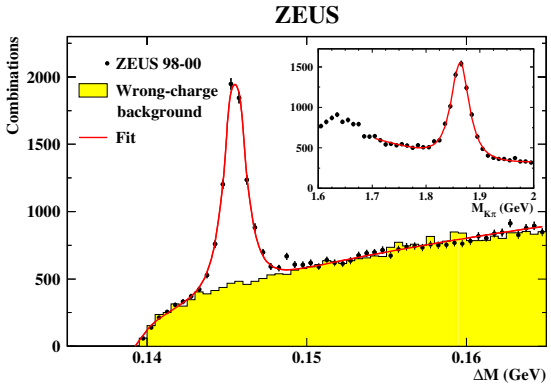

Figure 1.22: *The distribution of the mass difference, $\Delta m = (m_{K\pi\pi_s} - m_{K\pi})$, for D^* candidates (solid dots). The Δm distribution from wrong-charge combinations, normalised in the region $0.15 < \Delta M < 0.165$ GeV, is shown as the histogram. The $m_{K\pi}$ distribution for the D^0 candidates in the range $0.143 < \Delta M < 0.148$ GeV is shown as an inset. The fit is the sum of a modified Gaussian to describe the signal and a second-order polynomial to describe the background.*

The overall acceptance after applying the selection criteria for $1.5 < Q^2 < 1000$ GeV^2 , $0.02 < y < 0.7$, $1.5 < p_T(D^*) < 15$ GeV and $|\eta(D^*)| < 1.5$ calculated with RAPGAP is 31%, both for e^-p and e^+p data. The total cross sections in the same region are $\sigma(e^-p \to e^-D^*X) = 9.37 \pm 0.44(\text{stat.})^{+0.59}_{-0.52}(\text{syst.}) \pm 0.23(\text{BR})$ nb; are $\sigma(e^+p \to e^+D^*X) = 8.20\pm0.22(\text{stat.})^{+0.39}_{-0.36}(\text{syst.})\pm0.20(\text{BR})$ nb where the final uncertainty arises from the uncertainty on the branching ratios for the D^* and D^0. The cross section obtained from the combined sample is: $\sigma(e^\pm p \to e^\pm D^*X) = 8.44 \pm 0.20(\text{stat.})^{+0.37}_{-0.36}(\text{syst.}) \pm 0.21(\text{BR})$ nb.

The NLO predictions for $c\bar{c}$ cross sections were obtained using the HVQDIS program [25] based on the so-called fixed–flavour–number scheme (FFNS). In this scheme, only light quarks (u,d,s) are included in the initial state proton as partons whose distributions obey the DGLAP equations [77], and the $c\bar{c}$ is produced via the BGF mechanism [78] with NLO corrections [79]. The presence of the two large scales, Q^2 and m_c^2 , can spoil the convergence of the perturbative series because the neglected terms of orders higher than α_s^2 contain $log(Q^2/m_c^2)$ factors which can become large. Therefore, the results of HVQDIS are expected to be most accurate at $Q^2 \sim m_c^2$ and to become less reliable when $Q^2 >> m_c^2$. The prediction from the HVQDIS program is $8.41^{+1.09}_{-0.95}$ nb, in good agreement with the data. The renormalisation and factorisation scales were set to $\mu = \sqrt{Q^2 + 4m_c^2}$.

The uncertainty in the HVQDIS prediction is about 2.5 times the size of the uncertainty in the measurement. A contribution to the total cross sections arises from D^* mesons produced in $b\bar{b}$ events. The D^* cross section arising from $b\bar{b}$ production was estimated, to be 0.17 nb for $Q^2 > 1.5$ GeV^2. The measured differential cross sections include a component from beauty production. Therefore, all NLO predictions include a $b\bar{b}$ contribution calculated in each bin.

The differential D^* cross sections as a function of Q^2, x, $p_T(D^*)$ and $\eta(D^*)$ for the combined e^-p and e^+p data samples are shown in Figure 1.23. The number of D^* was determined for each bin in order to calculate the differential

cross sections using the wrong charge background–subtraction method. The cross sections in Q^2 and x both fall by about four orders of magnitude in the measured region. The cross–section $d\sigma/dp_T(D^*)$ falls by two orders of magnitude with increasing $p_T(D^*)$. The cross–section $d\sigma/d\eta(D^*)$ rises with increasing $\eta(D^*)$.

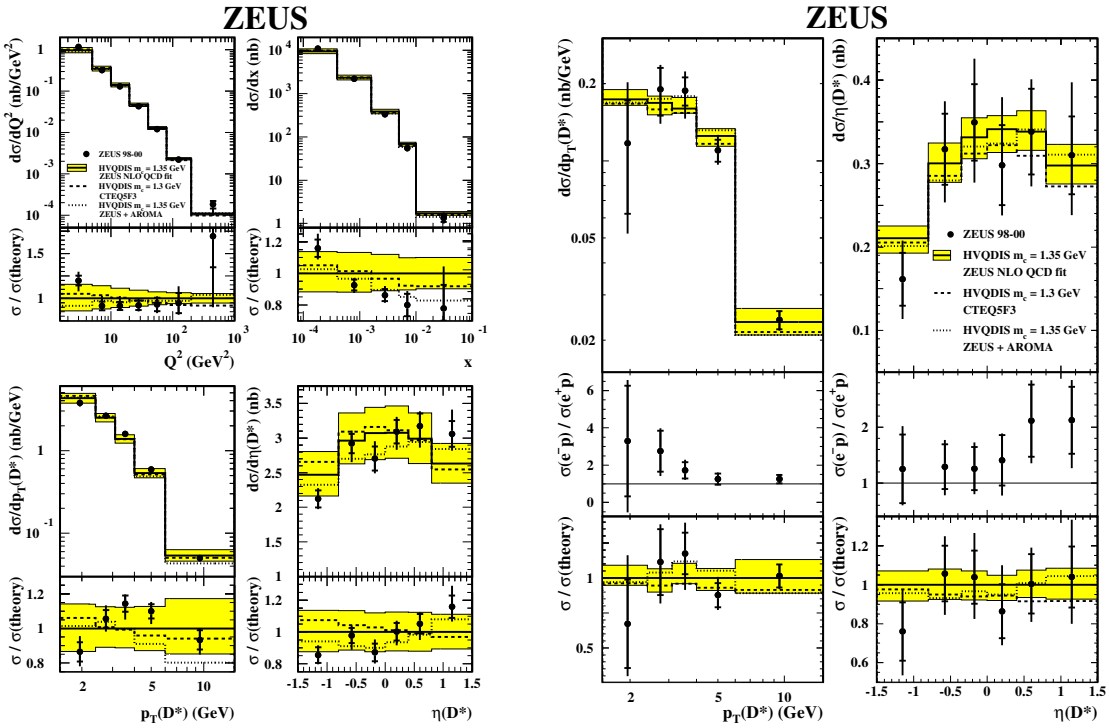

Figure 1.23: **Left**: *Differential D^* cross sections, for e^-p and e^+p data combined, as a function of Q^2, x, $p_T(D^*)$ and $\eta(D^*)$ compared to the NLO QCD calculation of* HVQDIS. *The inner error bars show the statistical uncertainties and the outer bars show the statistical and systematic uncertainties added in quadrature. Predictions from the ZEUS NLO QCD fit are shown for $m_c = 1.35$ GeV (solid line) with its associated uncertainty (shaded band) as discussed in the text. Predictions using the CTEQ5F3 PDF (dashed-dotted line) and an alternative hadronisation scheme (dotted line) are displayed. The ratios of the cross sections to the central* HVQDIS *prediction are also shown beneath each plot.* **Right** *As for the Left plots but for $Q^2 > 40$ GeV^2.*

The data in Figure 1.23, have been compared with the NLO calculation implemented in the HVQDIS program. The predictions used the default parameter settings. Predictions using an alternative PDF, CTEQ5F3, and an alternative hadronisation scheme, from AROMA, are also shown. The differences between the predictions, which are comparable to the uncertainties in the data, demonstrate the sensitivity of this measurement to the gluon distribution in the proton. The ratio of data to theory is displayed for each variable. For the cross sections as a function of Q^2 and x, the NLO predictions give a reasonable description of the data over four orders of magnitude in the cross section. For $d\sigma/dQ^2$, the description of the data is similar over the whole range in Q^2, even though HVQDIS is expected to be most accurate when $Q^2 \sim m_c^2$. The NLO calculation, however, exhibits a somewhat different shape, particularly for $d\sigma/dx$, where the NLO is below the data at low x and above the data at high x. The predictions using CTEQ5F3 instead of the ZEUS NLO fit, or using AROMA for the hadronisation instead of the Peterson function, give better agreement with the data for the cross–section $d\sigma/dx$.

The cross sections as a function of $p_T(D^*)$ and $\eta(D^*)$ are also reasonably well described by the NLO calculation. The prediction using the ZEUS NLO QCD fit gives a better description than that using CTEQ5F3 (and also better than the prediction using GRV98-HO, not shown), especially for the cross–section $d\sigma/d\eta(D^*)$. A better description of $d\sigma/d\eta(D^*)$ is also achieved [85] by using AROMA for the hadronisation, although, in this case, $d\sigma/dp_T(D^*)$ is not so well described. It should be noted that previous publications [74, 75] revealed discrepancies in the forward $\eta(D^*)$ direction. This region can now be reasonably well described by a recent fit to the proton PDF as shown in the (d) plot in the Left part of Figure 1.23. The data presented here are practically independent of the data used in the ZEUS NLO PDF fit to inclusive DIS data. Further refinement of NLO QCD fits and even the use of these data in future fits may achieve a better description.

Cross sections as a function of $\eta(D^*)$ and $p_T(D^*)$ were also measured for $Q^2 > 40$ GeV^2. The combined e^-p and e^+p data samples are shown in the Right part of Figure 1.23 compared with the HVQDIS predictions. Although the HVQDIS calculation is not thought to be applicable at high Q^2, the data are well described.

The same data in Figure 1.23 have also been compared compared with predictions (not shown) from the MC generators AROMA and CASCADE. The prediction from AROMA is generally below the data, particularly at low Q^2 and medium to high $p_T(D^*)$. In contrast, the prediction from CASCADE agrees at low Q^2, but generally lies above the data. Both MC predictions describe the shapes of the cross–sections $d\sigma/dx$ and $d\sigma/d\eta(D^*)$ reasonably well. The uncertainties in these MC predictions are difficult to estimate and may be large.

The open-charm contribution, $F_2^{c\bar{c}}$, to the proton structure-function F_2 can be defined in terms of the inclusive double-differential $c\bar{c}$ cross section in x and Q^2 by

$$\frac{d^2\sigma^{c\bar{c}}(x,Q^2)}{dxdQ^2} = \frac{2\pi\alpha^2}{xQ^4}\{[1+(1-y)^2]F_2^{c\bar{c}}(x,Q^2) - y^2F_L^{c\bar{c}}(x,Q^2)\}. \quad (1.39)$$

The $c\bar{c}$ cross section is obtained by measuring the D^* production cross section and employing the hadronisation fraction $f(c \to D^*)$ to derive the total charm cross section. Cross sections in the measured D^* region and in the Q^2 and y were extrapolated to the full $p_T(D^*)$ and $\eta(D^*)$ phase space using HVQDIS. Typical extrapolation factors are between 4.7 at low Q^2 and 1.5 at high Q^2.

The beauty contribution was subtracted from the data using the theoretical prediction At low Q^2 and high x, this fraction is small but it increases with increasing Q^2 and decreasing x. For the lower x point at highest Q^2, the contribution from beauty production is about 7% of that due to charm production.

The measured x dependence of $F_2^{c\bar{c}}$ in bins of Q^2 is shown in the Left hand plot of Figure 1.24. Data are compared with the previous measurement [74] and with the ZEUS NLO QCD fit. The two sets of data are consistent[10]. The prediction describes the data well for all Q^2 and x except for the lowest Q^2, where some difference is observed. The uncertainty on the theoretical prediction is that from the PDF fit propagated from the experimental uncertainties of the fitted data. At the lowest Q^2, the uncertainty in the data is comparable to the PDF uncertainty shown. This implies that the double–differential cross sections could be used as an additional constraint on the gluon density in the proton.

The values of $F_2^{c\bar{c}}$ are presented as a function of Q^2 at fixed values of x and compared with the ZEUS NLO QCD fit in the middle plot in Figure 1.24. The data rise with increasing Q^2, with the rise becoming steeper at lower x, demonstrating the property of scaling violation in charm production. The data are well described by the prediction. The Right hand plot in Figure 1.24 shows the ratio $F_2^{c\bar{c}}/F_2$ as a function of x at fixed values of Q^2. The ratio $F_2^{c\bar{c}}/F_2$ rises from 10% to 30% as Q^2 increases and x decreases. This asymptotic contribution at high Q^2 is consistent with the picture in which the c quark can be treated as any other massless quark ($Q^2 >> m_c$), the relative contribution following just from a simple charge counting rule. The drop of F_2^c/F_2 at high x is related to the steep decrease of the proton gluon density with x leading to a suppression of gluon initiated processes.

1.4.2 Heavy quark production results at fixed–target experiments

The beauty quark was discovered in 1977 as being the constituent of the Υ meson which manifested itself as a bump at about 9.5 GeV in the invariant mass spectrum of di-muons (Left two plots in Figure 1.25) produced in a famous fixed target experiment directed by Lederman at Fermilab [86]. Subsequently the open-b[11] production cross section was measured first in $p\bar{p}$ collisions at CERN [87] and at Tevatron [88], in fixed target experiments [3] and more recently in $\gamma\gamma$ interactions at LEP [89] and, as we have already seen, ep scattering at HERA [39, 41, 59, 52, 43].

Heavy quark production has been studied extensively at fixed target experiments. Since the typical centre–of–mass energy is between 10 and 40 GeV, where the beauty cross section is quite small, most of the available data are for charm production. Because of the small value of the c–quark mass, the perturbative expansion may not be reliable due to higher–order terms and to the non–perturbative contributions. This fact has to be kept in mind while comparing experimental results and theoretical predictions. The production of $c\bar{c}$ pairs in γN collisions has been studied in

[10] The first three points of the previous data were measured at $Q^2 = 1.8$ GeV^2 and not at 2 GeV^2, so they have been shifted to 2 GeV^2 using the ZEUS NLO QCD fit. All other points were measured at the same Q^2 values.

[11] We denote as "open" production the case in which each b quark in the produced pair hadronises separately into different hadrons without forming a bound $b\bar{b}$ state

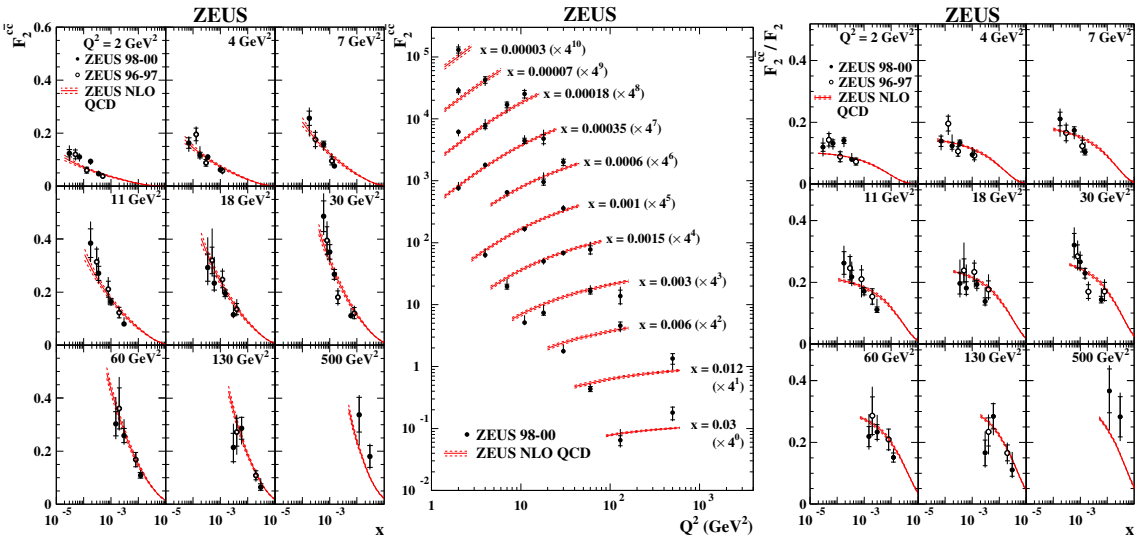

Figure 1.24: **Left** *The measured $F_2^{c\bar{c}}$ at Q^2 values between 2 and 500 GeV^2 as a function of x.* **Middle** *The measured $F_2^{c\bar{c}}$ at x values between 0.00003 and 0.03 as a function of Q^2.* **Right** *The measured ratio $F_2^{c\bar{c}}/F_2$ at Q^2 values between 2 and 500 GeV^2 as a function of x. The current data (solid points) are compared with the previous ZEUS measurement (open points). The data are shown with statistical uncertainties (inner bars) and statistical and systematic uncertainties added in quadrature (outer bars). The lower and upper curves show the fit uncertainty propagated from the experimental uncertainties of the fitted data.*

various experiments [3]. The experimental results in comparison with NLO QCD predictions are shown in Figure 1.8. The theoretical uncertainties found in photoproduction, shown here, are smaller than in hadroproduction [90]. In the Figure, the bands are obtained by varying the renormalisation scale between $m_c/2$ and $2m_c$, while the factorisation scale has been kept fixed to $2m_c$. The data are consistent with a charm mass of 1.5 GeV, but some of the experimental results are incompatible with one another so that no final response could be obtained.

The most recent measurement (2002) of the total beauty production cross section in a fixed target experiment was performed by the HERA–B collaboration. Events coming from $b \to J/\psi \to l^+l^-$ decays were identified in a sample

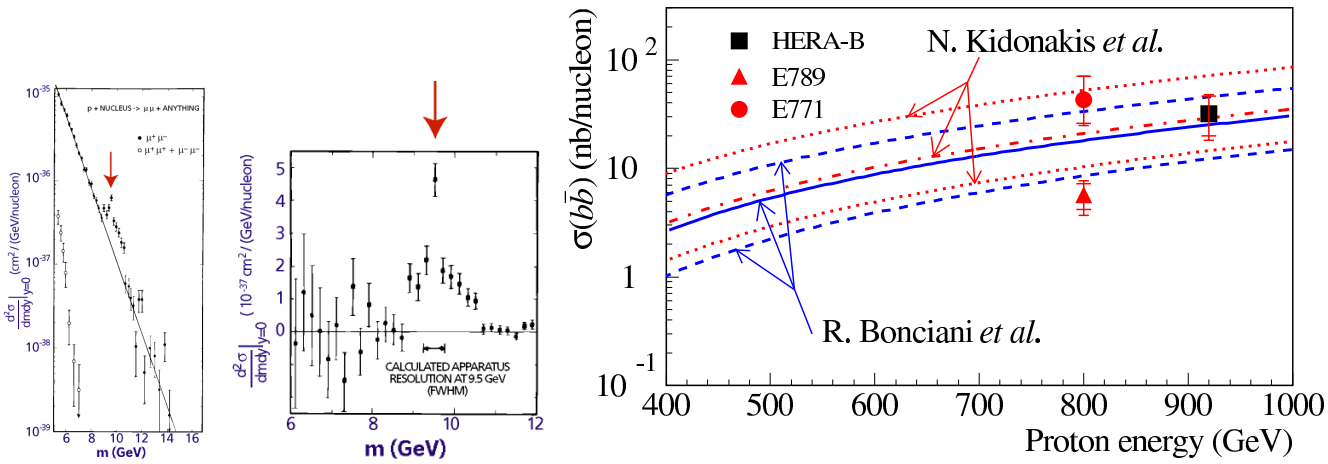

Figure 1.25: **Left***: Υ discovery in 1977 at Fermilab [86]* **Right***: The comparison of the HERA–B $\sigma_{b\bar{b}}$ value with other experiments and with the theoretical predictions of R. Bonciani et al. [91] updated with the NNLL parton distribution function in [92] (solid line: central value, dashed lines: upper and lower bounds) and N. Kidonakis et al. [93] (dot–dashed line: central value, dotted lines: upper and lower bounds).*

of 1.35 million dilepton triggered events. The data analysis which uses a detached vertex technique, resulted in the

identification of $1.9^{+2.2}_{-1.5}$ $b \to J/\psi \to \mu^+\mu^-$ candidates and $8.6^{+3.9}_{-3.2}$ $b \to J/\psi \to e^+e^-$ candidates.

From these candidates, the $b\bar{b}$ production cross section was computed by normalizing to the known prompt J/ψ cross section. In the J/ψ kinematic range $-0.25 < x_F < 0.15$[12], the measured cross section was $\sigma_{b\bar{b}} = 16^{+18}_{-12}$ nb/nucleon and $\sigma_{b\bar{b}} = 38^{+18}_{-15}$ nb/nucleon in the muon and electron channels, respectively. Within statistical errors, the two results are compatible. The combined result of the $b\bar{b}$ production cross section measured by HERA–B at 920 GeV using pC and pTi interactions in the defined x_F range was found to be $\sigma_{b\bar{b}} = 30^{+13}_{-11}(\text{stat}) \pm 6(\text{sys})$ nb/nucleon. Extrapolating this measurement to the full x_F range, the total $b\bar{b}$ production cross section result is : $\sigma_{b\bar{b}} = 32^{+14}_{-12}(\text{stat})^{+6}_{-7}(\text{sys})$ nb/nucleon. This determination is compatible with the existing measurements [94] [95] and in agreement with the most recent QCD predictions [91] [93] beyond NLO (see Figure 1.25).

1.4.3 Beauty production results at e^+e^- colliders

We will not deal here with the results at the beauty factories (CLEO, BABAR, BELLE) since in that case the main focus is on the decay of the B hadrons rather than on their production which is essentially equivalent to the production of the $\Upsilon(4S)$ resonance. For analogous considerations we will not cover in this review the LEPI results since in this case large samples of beauty events have been collected coming essentially from the decay of the Z^0 boson ($Z^0 \to b\bar{b}$).

In the previous cases a big role is played by the decay $B^0 \to D^* l\nu_l$ which has a favourable branching ratio and is experimentally relatively easy to study. It is employed to measure the $|V_{cb}|$ and $|V_{ub}|$ terms in the Cabibbo-Kobayashi-Maskawa matrix by measuring the lepton spectrum distribution, $B^0\bar{B}^0$ oscillations and CP violation. As we will see the bulk of beauty events collected with our selection comes also from this decay. Nevertheless this kind of measurements which concentrate on the B meson decay require a sizeable statistics and the knowledge of the original B meson direction of flight (i.e. by reconstructing the neutrino direction measuring the missing energy in the event). The fact that the $B\bar{B}$ system is produced almost at rest is also an important ingredient at the beauty factories. Since we are focusing on the production rate and due to limitation in statistics, calorimetry and vertex tagging information we will not describe further the analysis techniques adopted in these measurements.

We will instead concentrate on open beauty production in the so–called continuum–region explored by LEP II, ($\sqrt{s} = 189 - 209$ GeV) for which OPAL [96], DELPHI [97] and L3 [98] produced some recent measurements.

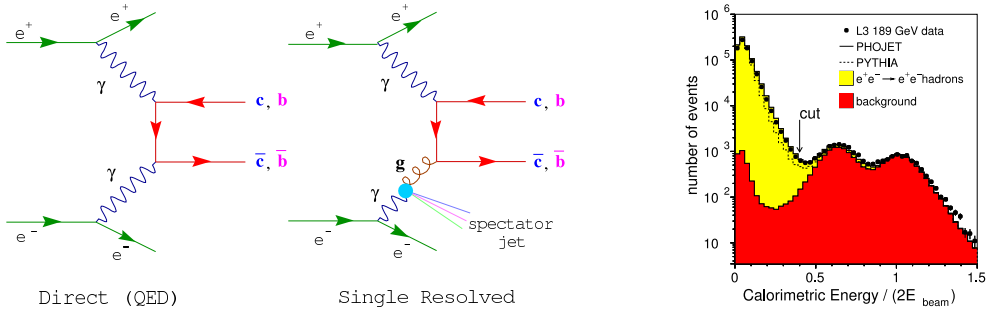

Figure 1.26: **Left***: HF production diagrams in $\gamma\gamma$ collisions.* **Right***: Energy cut used in the $\gamma\gamma$ sample selection.*

In this regime the main hadron source in e^+e^- collisions is given by the so–called $\gamma\gamma$ processes (see Figure 1.26 (Left) for the corresponding diagrams). Due to the involved centre–of–mass energies and the fact that the photons have typically very low virtuality, this environment is not so different from the photoproduction regime at HERA. In this case, if both the photons behave hadronically, the possibility arises of *double resolved* processes.

$\gamma\gamma$ events are selected by requiring the absence of scattered electrons in the main calorimeter (anti-tag) and by requiring the visible energy to be only a small fraction of the available $\sqrt{s}$ (due to the fact that the electrons are scattered at low angles down into the beam–pipe). This kind of cut is illustrated in Figure 1.26 (Right). As it can be seen it reduces efficiently the background from other sources ($e^+e^- \to e^+e^-\tau^+\tau^-$, $e^+e^- \to Z/\gamma \to q\bar{q}$, $e^+e^- \to \tau^+\tau^-$, $e^+e^- \to W^+W^-$). Further cuts on the minimal number of tracks further reduce some of these background components.

[12] With x_F we denote the J/ψ x-Feynman variable

Signal extraction is performed on a semi–leptonic b decay subsample with the standard p_T^{rel} technique. Both electrons and muons were used with momentum above 2 GeV. Jets were reconstructed with the Jade algorithm ($y_{cut} = 0.1$) explicitly excluding the lepton contribution to the deposited energy. An example of the final p_T^{rel} distribution obtained by DELPHI [97] is shown in Figure 1.27 (Left). The various components as determined by the fit are shown separately (the $b\bar{b}$, $c\bar{c}$, uds are fitted while the small component due to other background is fixed according to the Monte Carlo expectation). The main systematic uncertainty comes form the selection procedure. The NLO calculation to which

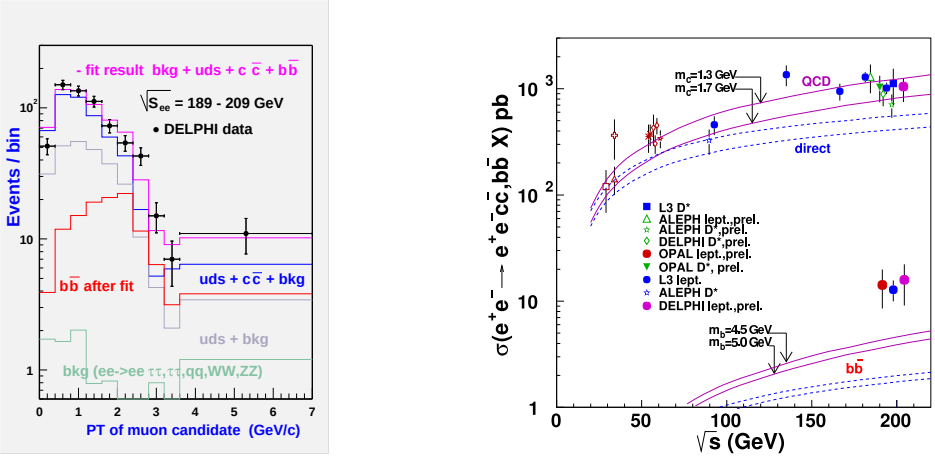

Figure 1.27: **Left** *: DELPHI fit to the p_T^{rel} distribution.* **Right***: LEP heavy quark cross sections compared to theory expectations.*

measurements have been compared can be found in reference [99]. The beauty mass has been varied between 4.5 and 5 GeV. The measured $b\bar{b}$ cross section in $\gamma\gamma$ collisions is generally found to be a factor about 3 higher than NLO expectations. In the case of L3 the significance is of about 4 standard deviations (see the LEPII summary plot in Figure 1.27).

1.4.4 Beauty production results at hadron colliders

We will first describe the early results of UA1 at the $Sp\bar{p}S$ collider at CERN ($\sqrt{s} = 630$ GeV) dating back to the first years of the nineties and then the more recent results from the Tevatron experiments ($\sqrt{s} = 630 - 1800$ GeV).

1.4.4.1 Beauty production at the $Sp\bar{p}S$

The first measurements of the beauty production cross section at a hadron collider were performed by the UA1 collaboration [100]. The analyses used semi–leptonic beauty decays to muons to measure the integrated bottom quark cross section for $p_T^b > p_T^{min}$ at $\sqrt{s} = 630$ GeV (see Left hand plot in Figure 1.28). The analyses showed a slight excess of the measurements relative to the NLO QCD prediction, but were consistent with the theory within its systematic uncertainties.

1.4.4.2 Beauty production at the Tevatron: CDF and D0

The analyses on beauty production in $p\bar{p}$ collisions at the Tevatron [102] have shown that the b–quark production cross section is higher than the theoretical predictions (obtained with the standard choice of the input parameters) by a factor of 2 to 3. One of the most recent publications by the CDF Collaboration [103] is of particular interest, since it has been investigated by M. Cacciari and P. Nason in order to make clearer some aspects of the NLO calculations. In Reference [103] the B^+ total cross section and the differential cross section $d\sigma/dp_T^{B^+}$ were measured, using fully reconstructed B mesons decaying into the exclusive final state $J/\psi K^{\pm}$. The measurement used a data sample of 98 pb^{-1} collected from 1992 to 1995 by the CDF experiment from $p\bar{p}$ collisions at a centre–of–mass energy of 1.8 TeV. The whole data sample is divided into two sub–samples, treated in different ways in the analysis: the run 1A sample consists of 19.3

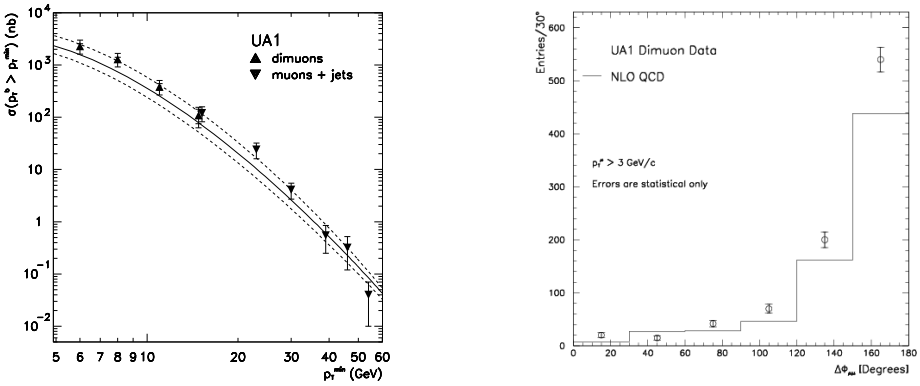

Figure 1.28: *Bottom production measurements at the SppS ($\sqrt{s} = 630$ GeV)* **Left***: UA1 measurements [100] of b quark integrated crosssection.* **Right***: UA1 $\Delta\phi$ measurement [101] using μ–μ*

pb^{-1} of data used for a previous analysis on B^+ production [104], while the rest of the sample is referred to as run 1B. The J/ψ coming from the B^+ decay was reconstructed by measuring both muons coming from its decay with the silicon vertex detector. For run 1A data, the transverse momentum of each muon was asked to be $p_T^\mu > 1.8$ GeV, with one of the muons having $p_T^\mu > 2.8$ GeV, while for run 1B data both muons were asked to have $p_T^\mu > 2$ GeV. The two muons had to have opposite sign, and to be less than 5.0 cm far to each other at the point of closest approach to the vertex. They were then constrained to come from a common point in space. The width of the reconstructed J/ψ peak was 16 MeV, the signal region being defined as that with dimuon candidates with reconstructed mass within 3.3 σ of the known J/ψ mass. To reconstruct the B candidate, each charged particle in an event was combined with the two muons if the z coordinate of the track at the point of closest approach to the beam line was within 5 cm of the z position of the J/ψ candidate decay vertex. Since kaons from B decays have much harder transverse momentum spectrum than K coming from background events, a cut was imposed on p_T^K , requiring $p_T^K > 1.25$ GeV. The p_T of each B candidate was required to be $p_T > 6.0$ GeV, and the proper decay length to be greater than 100 μm, to suppress background from prompt J/ψ mesons. The differential cross section $d\sigma/dp_T^{B^+}$ was determined by dividing the full B candidate sample into four p_T ranges, and in each range the invariant mass distribution was fitted using an unbinned maximum likelihood fit, to determine the number of B candidates. The value of the cross section in each $p_T^{B^+}$ bin was then given by:

$$\frac{d\sigma(B^+)}{dp_T^{B^+}} = \frac{N_{sig}/2}{\Delta p_T^{B^+} \mathcal{L} \mathcal{A} \mathcal{B}} \tag{1.40}$$

where N_{sig} is the number of B in each p_T^B bin as given by the fit, p_T^B is the width of the bin, $\mathcal{A}$ is the acceptance, which also includes trigger and reconstruction efficiency, $\mathcal{B}$ is the product of the branching ratios $BR(B^\pm \to J/\psi K^\pm) \cdot BR(J/\psi \to \mu^+\mu^-)$. The factor 1/2 keeps into account the fact that both B^+ and B^- mesons are detected, while the cross section is reported for B^+ mesons, assuming charge invariance in the production process. The differential cross section $d\sigma/dp_T^{B^+}$ is shown in the Left hand plot of Figure 1.29, compared to NLO QCD predictions. In the theoretical calculation the proton parton densities used were MRST [58] and the renormalisation and factorisation scales were set to $\mu_R = \mu_F = \mu = m_T = \sqrt{m_b^2 + p_T^2}$. The fragmentation of b–quarks into hadrons

was modelled using the Peterson fragmentation function, with $\epsilon = 0.006$, as obtained from a fit to data collected at e^+e^- colliders [106]. The uncertainties on the NLO predictions were estimated by varying the mass of the b–quark from 4.5 to 5.0 GeV, and the renormalisation and factorisation scales from $m_T/2$ to $2m_T$. The ratio between the measured values and the NLO QCD predictions was calculated in the four p_T bins, and then fitted by a line. The value found by the fit, corresponding to the mean data to theory ratio, was 2.9. Recently, the results obtained by the CDF Collaboration in Reference [103] have been analysed by M. Cacciari and P. Nason [105] to see how the big discrepancy between the data and the NLO predictions could be explained. They focused their attention on the implementation of the hadronisation effects in the NLO QCD calculations, which is a non–perturbative issue. The non–perturbative hadron–formation effect is usually introduced by writing the hadron–level cross section for B mesons as:

$$\frac{d\sigma_B}{dp_T} = \int d\hat{p}_T dz \frac{d\sigma^b}{d\hat{p}_T} D(z) \delta(p_T - z\hat{p}_T) \tag{1.41}$$

where the function $D(z)$ is a phenomenological parametrisation of hadronisation effects. Usually, the Peterson [107] form of the $D(z)$ function is used, and the quark cross section is given by a shower Monte Carlo program; the

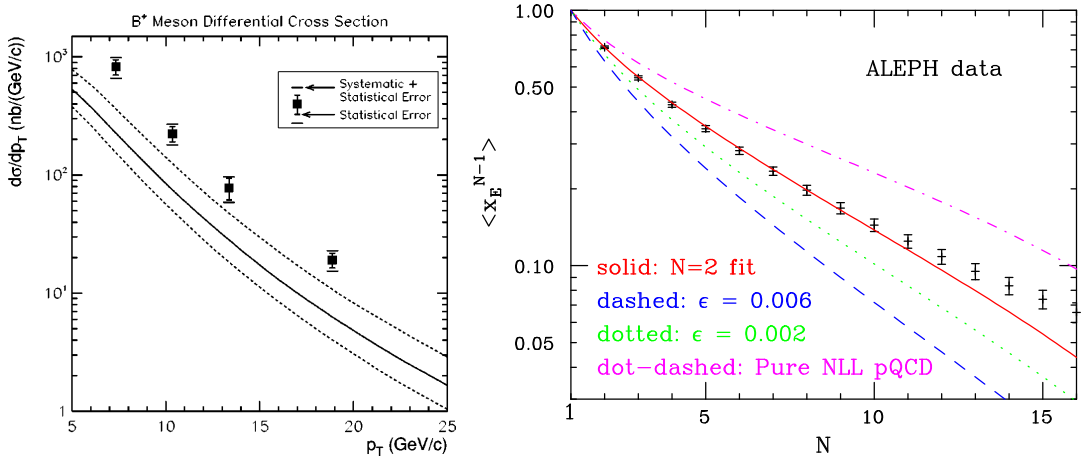

Figure 1.29: **Left**: *Differential cross section $d\sigma/dp_T^{B^+}$ compared to NLO QCD prediction. The solid curve represents the theoretical prediction for $m_b = 4.75$ GeV, $\mu_R = \mu_F = \mu = \sqrt{m_b^2 + p_T^2}$, while the dashed curves are obtained by setting $m_b = 4.5$ GeV, $\mu_R = \mu_F = \mu/2$, and $m_b = 5.0$ GeV, $\mu_R = \mu_F = 2\mu$ (from Reference [103]).* **Right**: *Moments of the measured B meson fragmentation function compared with the perturbative NLL calculation supplemented with different non–perturbative fragmentation forms $D(z)$. The solid line is obtained using a one–parameter form fitted to the second moment. section is influenced by this effect since the transverse momentum spectrum of the b–quark is steeply falling. In Reference [105]*

parameter is taken from e^+e^- data. The effect of the fragmentation is to reduce the momentum of the B meson with respect to that of the b–quark of roughly 10%. Nevertheless, the value of the cross section is influenced by this effect since the transverse momentum spectrum of the b–quark is steeply falling.

In Reference [105] the NLO QCD predictions for the $d\sigma/dp_T^{B^+}$ were recalculated by correctly implementing the effect of heavy quark fragmentation. To this aim, a complete resummation of large transverse momentum logarithms at the next–to–leading level (NLL) [108] was needed, and a formalism for merging the NLL resummed results to the fixed order (FO) NLO calculation had to be used (FONLL) [109]. In Reference [110] the fact is pointed out that the value $\epsilon = 0.006$ is appropriate only when a leading–log (LL) calculation of the spectrum is used, while when NNL calculations are used, smaller values of are needed to fit the data. Another fact has to be noticed, that, rather than the knowledge of the whole spectrum of $D(z)$ for $z \in [0, 1]$, the knowledge of some specific moment of the fragmentation function

$$D_N = \int D(z) z^N \frac{dz}{z} \tag{1.42}$$

is sufficient to calculate the hadronic cross section, assuming the power law behaviour of the differential cross section as a function of the transverse momentum of the B meson, $d\sigma/dp_T \propto 1/p_T^n$. It is, in fact:

$$\frac{d\sigma}{dp_T} = \int dz d\hat{p}_T D(z) \frac{A}{\hat{p}_T^N} \delta(p_T - z\hat{p}_T) = \frac{A}{p_T^N} D_N \tag{1.43}$$

Therefore, the hadronic cross section is the product of the partonic cross section and the n^{th} moment of the fragmentation function. The value of n for the p_T spectrum in the region of interest ranges from 3 to 5. It is thus clear that having a good determination of the moments of the fragmentation function, when fitting to e^+e^- data, is more important than describing the whole $D(z)$ spectrum. In the Right hand plot of Figure 1.29 the moments of the fragmentation function are shown, calculated from the distribution of the B meson energy fraction with respect to the beam energy, xE , published by the ALEPH collaboration [111]. The dot–dashed line is the pure perturbative part, while the dotted and the dashed lines represent the convolution of the perturbative part with a Peterson function with $\epsilon = 0.002$ and $\epsilon = 0.006$, respectively. It is clear from the Figure that the parametrisation with $\epsilon = 0.006$ does not describe the data. In order to give a good description of the low moments, a one–parameter form of the non–perturbative fragmentation function was used, its free parameter being fixed by fitting the $N = 2$ point in moments space. The results are shown by the solid line in the Right hand plot of Figure 1.29. The description of the data is good up to $N \simeq 10$. Therefore, this "$N = 2$" fit is a good candidate for the calculations of the hadronic cross sections according to Equation1.43. The theoretical prediction of the differential cross section $d\sigma/dp_T^{B^+}$ was re–calculated using this form of the fragmentation

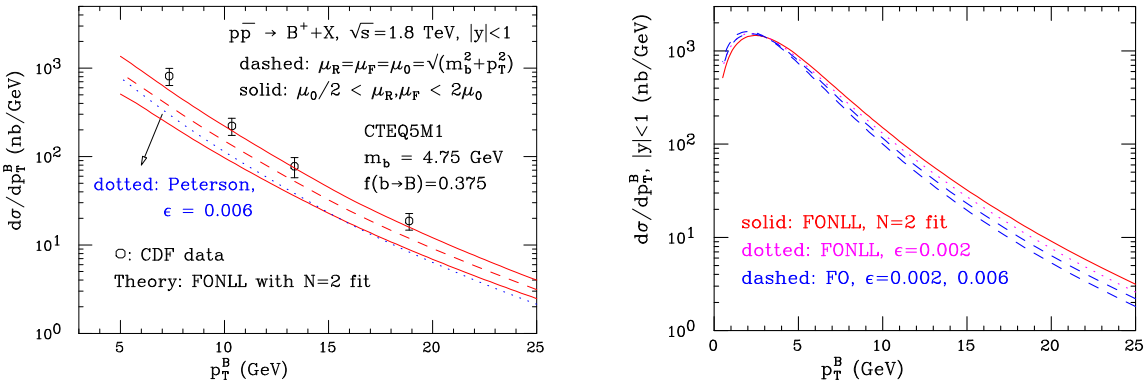

Figure 1.30: **Left***: Prediction for the B cross section obtained using the calculation in [109], supplemented with the $N = 2$ fit of the non–perturbative fragmentation function, compared to the CDF data in Reference [103].* **Right***: Theoretical prediction of the differential cross sections $d\sigma/dp_T^B$, calculated with different schemes and forms of the fragmentation function.*

function, and then compared to the results obtained by the CDF Collaboration (Left plot in Figure 1.30). In the Figure, also the NLO QCD prediction obtained using the Peterson fragmentation with $\epsilon = 0.006$ is shown, and it can be clearly seen that this choice underestimates the B cross section at large p_T values. The ratio between the measured values and the theoretical predictions has in this case a mean value of 1.7, to be compared to the 2.9 obtained with the previous choice of the fragmentation function. It is also interesting to see a comparison of the different theoretical predictions as a function of the p_T of the B meson. This is reported in the Right hand plot in Figure 1.30, where the results obtained using a fixed–order NLO QCD calculation are shown, together with the FONLL calculation with $\epsilon = 0.002$ or with the "$N = 2$" fit. It is clear from the Figure that the difference is more evident for high–p_T values, whereas it is much smaller at low p_T.

1.4.4.3 $b\bar{b}$ correlations at hadron colliders

We will conclude this review by outlining some results on $b\bar{b}$ correlations since this topic has some implications in the analysis presented in this work which uses a double tag technique.

Studies of the one–particle inclusive distributions are a benchmark test of QCD. However, these tests do not probe all of the important features of the production mechanism. In several cases the correlations between the quark and the antiquark can provide additional important information. In the case of fixed–target $c\bar{c}$ production, the shape of the azimuthal correlations between the c and $\bar{c}$ quarks is sensitive to the amount of intrinsic p_T carried by the partons in the hadron. Given the large mass of the b quark and the large p_T values at which b's are probed in hadronic collisions, these effects should be negligible. However, one could observe similar behaviours induced by the build–up of large transverse momentum due to the perturbative evolution of the initial state (i.e. multi–gluon emission). This phenomenon would be even more pronounced at small p_T and in the presence of important small–x effects. The knowledge of heavy–quark correlations is also an important element in the study of detector acceptances and detection systematics. For example, in studies of b tagging in samples where both b's have been tagged, it is important to know what the correlations between the b and $\bar{b}$ momenta are, since the tagging efficiency depends on the b momentum. These studies have implications on the determination of tagging efficiencies for a multitude of important measurements, from the study of top production [112] to the study of R_b [113].

The study of $b\bar{b}$ correlations in hadronic collisions was pioneered by UA1 [114, 115, 116]. For these measurements they used their sample of high–mass and non–isolated dimuon events. The shapes of the $\Delta\phi_{\mu\mu}$ and $\Delta R_{\mu\mu}$ distribution for the data are both in good agreement with the theoretical expectations [115]. The rate is approximately 30% higher than the central value of the theoretical predictions, a result consistent with the UA1 determination of the inclusive cross section (see Right hand plot in Figure 1.28). They also separated the sample of dimuon events into two classes, defined by two–body and three–body topologies. Contributions to the three–body topology come from events with hard–gluon bremsstrahlung, and are therefore proportional to α_S^3 . Two–body final states, with the b and the $\bar{b}$ almost back–to–back, are dominated by Born–like processes, and their rate is of $O(\alpha_S^2)$. A comparison between the two

samples, carried out as a function of the p_T of the b quark, allowed UA1 to study the dynamical evolution of $b\bar{b}$ correlations and to extract the value of $\alpha_S(M_Z) = 0.113^{+0.007}_{-0.006}\,(\mathrm{exp})^{+0.008}_{-0.009}\,(\mathrm{th})$ [116]. The same study led to a 3σ evidence for the running of α_S.

CDF presented their first study of $b\bar{b}$ correlations using a sample of $e\mu$ pairs [117]. Once again, good agreement was found between the shape of the data and the QCD expectations. A second measurement has been recently reported by CDF, using muons plus tagged b jets [118]. The shape of the $\Delta\phi$ distribution is in reasonable agreement with QCD, while the distributions of the jet E_T and of the muon p_T are not (see Figure 1.31).

Contrary to the case of $c\bar{c}$ correlations measured in fixed–target experiments, the measurement at hadron colliders is sensitive to the modelling of the heavy–quark fragmentation, because of possible trigger biases. A harder (softer) fragmentation function would enhance (decrease) the efficiency for the detection of the softest of the two b quarks. These effects could have an impact on the distributions reported in this study by CDF. This collaboration explored the effects of changes in the ϵ_b parameter within the Peterson fragmentation model, finding them negligible. As we argued earlier, it cannot be excluded that a systematic study of other possible parametrisations for the fragmentation modelling could lead to significant effects. Also the possible effects of the k_T kick have been studied by CDF [118], with the conclusion that not even an average k_T as large as 4 GeV could improve the agreement between theory and data for the measurements considered.

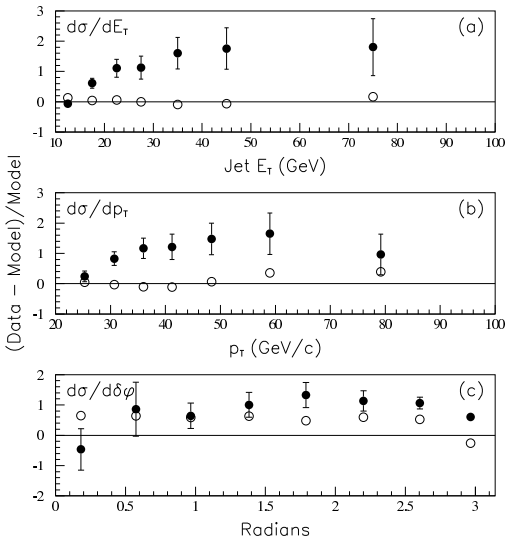

Figure 1.31: *CDF results on the $b\bar{b}$ correlations using μ + b–tagged jet final states [118], compared to NLO QCD. Solid points correspond to the default theoretical prediction, with scales $\mu = \mu_0$, empty circles correspond to the difference between the choice $\mu = \mu_0/2$ and $\mu = 2\mu_0$. Top figure: tagged–jet E_T distribution. Central: muon p_T spectrum. Bottom: azimuthal correlations.*

Both CDF and D0 recently presented studies based on samples of high–mass dimuons [119] . The shapes for both $\Delta\phi$ and p_T^b for a given $p_T^{\bar{b}}$ are well reproduced by theory, within the large uncertainties, while there is a normalisation discrepancy relative to the central predictions (Figure 1.32). In conclusion we can say that, overall, there are good indications that NLO QCD correctly describes the correlations between b pairs produced in hadronic collisions. Most of the large theoretical systematics present in the case of fixed–target charm production are not relevant here. The discrepancies observed in the CDF measurement using the muon+tagged–jet final states, however, indicate that there is still a possible interplay between the theoretical and experimental systematics, which is not entirely understood as yet.

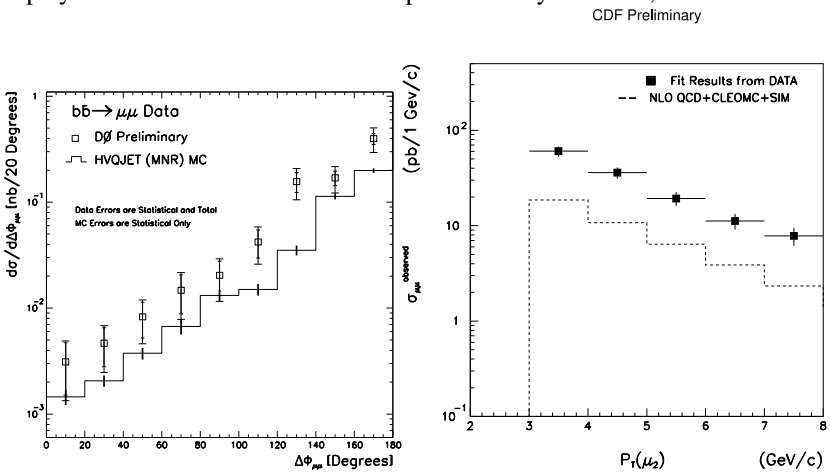

Figure 1.32: *Results on $b\bar{b}$ correlations using dimuon final states, compared to NLO QCD. Left: azimuthal–correlation results from D0. Right: p_T distribution of the slowest muon from CDF.*

Chapter 2

Experimental setup

In this Chapter a brief description of the HERA ep collider and ZEUS detector is presented with a specific attention to the components that are more relevant for the analysis presented in this thesis. A detailed description of the ZEUS detector can be found in [120].

2.1 The HERA collider

The Hadron Electron Ring Accelerator (HERA) [121] located at the DESY (Deutsches Elektronen-SYnchrotron) laboratory in Hamburg (Germany) is the first, and so far only, electron (positron)-proton collider. It operates since autumn 1991. The tunnel in which it resides was built 10 to 25 m under the earth surface and it has a circumference of 6.3 Km. The storage ring consists of four circular arcs (with a radius of 779 m) and four straight segments (each 360 m long) as shown in Figure 2.1. Four interactions points (IP) are placed in the straight segments, where the experiments H1, ZEUS, HERMES and HERA–B are located.

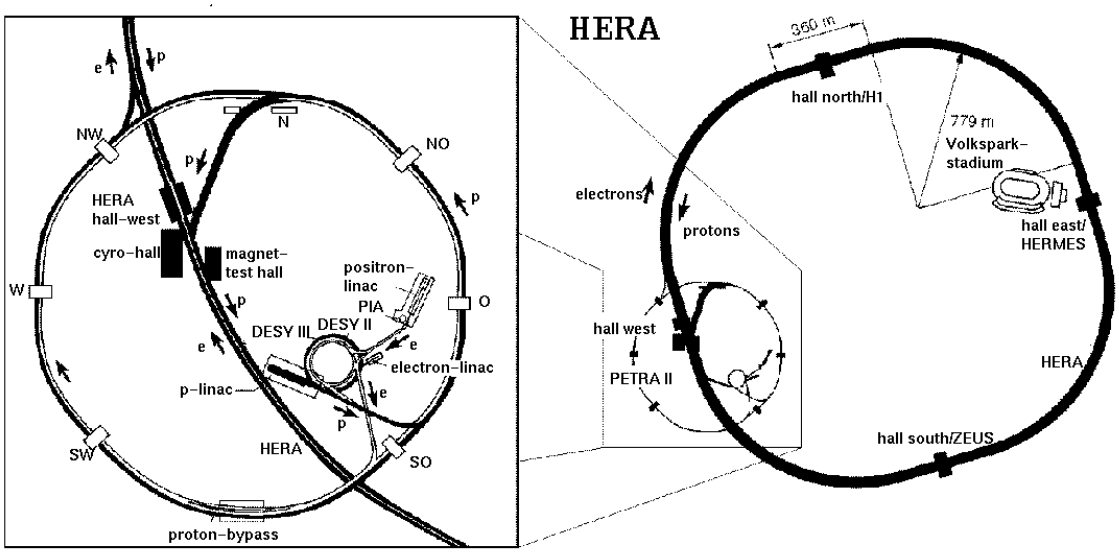

Figure 2.1: *Schematic view of the HERA storage ring and of its injection system.*

One of the remarkable features of HERA, which distinguishes it from a "classical" collider, is the asymmetry between the two beam energies. HERA was designed to collide electron (positron) and protons with nominal energies of 27.5 GeV and 820 GeV respectively, resulting in a center-of-mass energy of $\sqrt{s} \sim 300$ GeV.

	p		e
Nominal energy (GeV)	920		27.5
Luminosity (cm^{-2} s^{-1})		1.5 10^{31}	
Polarisation time (min)			15
Interaction regions		4	
Circumference (m)		6436	
Curvature radius (m)	588		608
Magnetic field (T)	4.65		0.165
Energy at injection (GeV)	40		14
Energy interval (GeV)	300-820		10-33
Circulating currents (mA)	163		58
Number of bunches		210	
Total number of particles	2.1 10^{13}		0.8 10^{13}
Crossing interval (ns)		96	
beam dimension σ_x (mm)	0.29		0.26
beam dimension σ_y (mm)	0.07		0.07
beam dimension σ_z (cm)	11		0.8
Energy loss/turn (MeV)	1.4 10^{-10}		112
Filling time (min)	20		15

Table 2.1: *Nominal parameters of the HERA storage ring.*

Beam injection is performed by a procedure involving several preaccelerators (see Figure 2.1). Electrons are initially accelerated up to 200 MeV in the electron linear accelerator LINAC II, and then in the DESY II synchrotron up to an energy of 7.5 GeV. Afterwards, the electrons are injected into PETRA, where their energy is increased up to 14 GeV, before they are finally transferred to HERA. The protons start as H^- ions in the proton LINAC and are accelerated up to 50 MeV. After acceleration in DESY III (to 7.5 GeV), the electrons are stripped off and the protons are injected in PETRA, where their energy increases up to 40 GeV, before injection into HERA.

While the high momentum of the proton beam requires superconducting magnets, the electrons are controlled using conventional magnets. The HERA proton ring consists of 422 main dipoles delivering a bending field of 4.7 T and 244 main quadrupoles. Standard cells of 47 m length combining 4 dipoles, 4 quadrupoles, 4 sextupoles and correction magnets are installed in the arcs of the proton ring and are cooled down to 4.2 K. The conventional electron ring consists of 456 main dipoles of 0.17 T and 605 main dipoles grouped in 12 m long magnet modules which contain one dipole, one quadrupole, one or two sextupoles and several correction dipoles. The energy loss due to synchrotron radiation is compensated by 500 MHz copper cavities installed in the straight segments of HERA. In addition, 16 superconducting 4-cell cavities with an electric field gradient of 5 MV/m are used to accelerate the electrons from 14 GeV (the energy they have when they are injected from PETRA to HERA) to the maximum energy.

The electrons and protons are stored in separated bunches with a distance of 28.8 m between two successive bunches. This distance corresponds to a bunch crossing time of 96 ns. In order to maximise the luminosity, up to 210 bunches of particles can be stored for each beam. Unpaired bunches with only protons or electrons as well as completely empty bunches are used to estimate the number of background events coming from interactions with the residual beam gas in the storage ring, events produced by cosmic rays or other "non-ep"events.

Close to the interaction region, protons and electrons have to run in the same orbit in order to collide at zero angle. The distance of about 81 cm between the electron and the proton rings has to be traversed. A total of 123 guiding magnets are used to deflect the protons until they run in the same vacuum pipe as the electrons. After passing the interaction point they are brought back to the level of the proton ring.

From the 1994 running period it was decided to accelerate positrons instead of electrons in order to achieve longer lepton-beam lifetime. Interactions with almost stationary positive charged particles, most likely originated from the ion getter pumps of the HERA vacuum system, tend to defocus the electron beam. For a positron beam the pile-up of the ions is avoided due to the repulsive electromagnetic force between the positrons and the positively charged ions. During some part of the '98 and '99 running periods the machine accelerated electrons. From that moment till September 2000, positrons were collided with protons. Since then, HERA and the experiments have been involved in

a long shutdown to improve the performance and increase the luminosity. From 1998 the proton beam has an energy of 920 GeV, which yields to an increase of 5% in the center-of-mass energy.

In addition to the available center-of-mass energy, another important quantity that characterises the performance of a collider is the luminosity. This quantity determines the rate at which interactions occur. From the luminosity ($\mathcal{L}$) and the cross section for a given process (σ) the number of events observed is given by

$$N = \mathcal{L} \cdot \sigma$$

The luminosity $\mathcal{L}$ is controlled by several parameters: the number of bunches, the number of particles per bunch, the geometrical properties of the bunches and the crossing time. Figure 2.2 shows the luminosity delivered by HERA from 1993 up to the end of the 2000. The time evolution of the beam currents during a typical fill is illustrated in Figure 2.3.

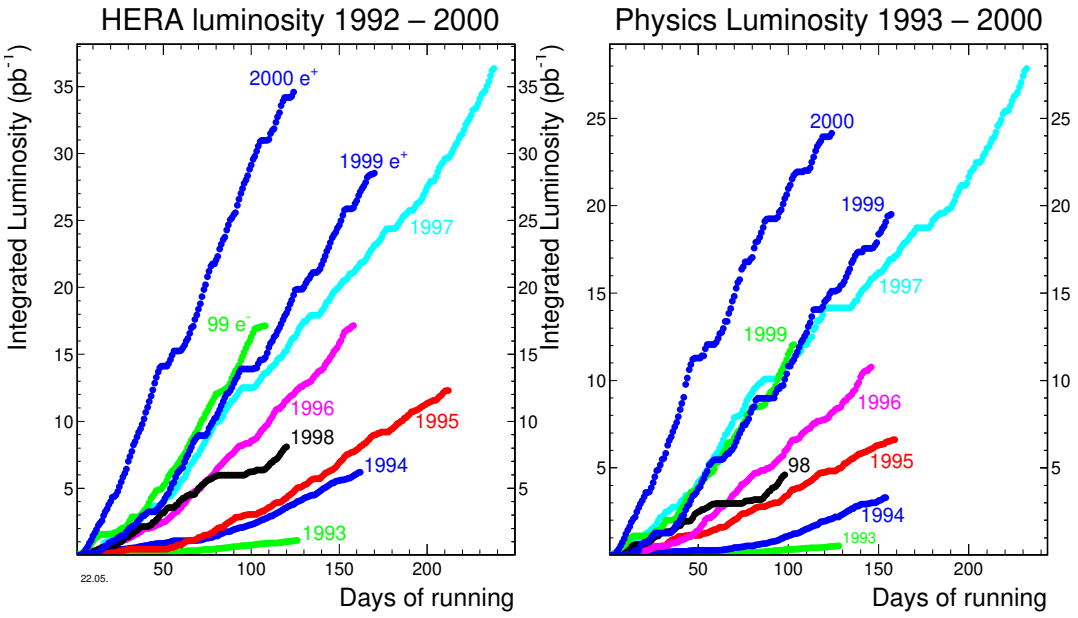

Figure 2.2: *The trend of integrated luminosity as a function of time in days is shown for years 1993 to 2000. On the* **Left** *the HERA delivered luminosity is presented while the faction used by ZEUS is on the* **Right**.

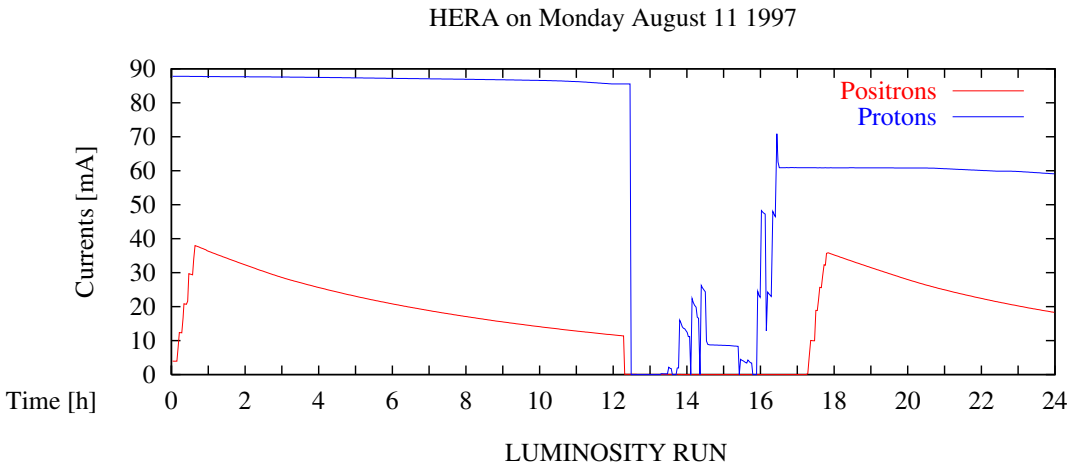

Figure 2.3: *Beam currents intensity development during a run taken in 1997.*

2.2 The ZEUS detector

The ZEUS detector [120] [1] is one of the currently four experiments at the HERA collider. It is a large multipurpose detector designed to study the wide spectrum of HERA physics. The ZEUS Collaboration consists of around 330 physicists belonging to more than 50 institutes from 12 different nations. The detector is located 30 m underground in the South Hall of the HERA tunnel outside of the DESY site and has a size of 12 m $\times$ 11 m $\times$ 20 m and weights 3600 ton.

The original form of the detector was driven by the different processes that can be observed at HERA. The detector can measure energies from few MeV to hundreds of GeV in the forward region. For low-momentum particles the tracking on a magnetic field is very precise (the resolution behaves as $\sigma(p_T)/p_T \sim p_T$) , while high energy particles are well measured by the calorimetric system (resolution goes as $\sigma(E)/E \sim \sqrt{E}/E$). Particle identification is needed in a wide momentum range: in Neutral Current (NC) DIS events the scattered lepton has to be identified and measured with high precision; the identification of electrons, positrons and muons is needed in order to study the semileptonic decay of heavy quarks and exotic processes involving leptons. In Charged Current (CC) DIS processes a hermetic detector is needed in order to reconstruct the missing transverse momentum carried by the outgoing neutrino. In this kind of events and also in untagged photoproduction events the precise reconstruction of the final state energy is important in order to determine the event kinematic.

As it is evident from Figure 2.4, the detector is asymmetric to comply with the fact that the big difference in momentum between the protons and the electrons projects the most of the final state particles in a tight cone along the proton direction. Furthermore the detector needs to cope with high particle densities and small time intervals between subsequent bunch crossings (96 ns) in presence of high backgrounds coming from both beams.

The ZEUS geometry (Figure 2.4) is described by a right-handed coordinate system with its origin at the nominal interaction point. The z-axis is pointing along the incoming proton direction and the x-axis horizontally towards the center of HERA.

2.2.1 Overview of the main components

The main components which are found starting from the inner part of the detector and going outside are the following:

- The system of inner tracking detectors. The main constituent is a big cylindric drift chamber (CTD) which was built to measure charged particle trajectories in the central angular region. The device is complemented by other detectors which measure the forward emitted tracks, the FTD and an analogous one, the RTD, in the rear region. In between the FTD planes a transition radiation detector, the TRD, is located. It is used to improve the electron identification power in the forward region. In Figure 2.4 the FTD and RTD are collectively denoted as FDET.
- The small-angle rear track detector (SRTD) is situated behind the RTD and covers the face or the RCAL to a radius of 34 cm around the center of the beam-pipe hole.
- A super conductor solenoid containing the above mentioned tracking detectors is able to generate a 1.8 T magnetic field. Due to the addition of iron to shield the photo-multipliers, the mechanical stress on the solenoid supports, arising from the asymmetric position of the solenoid within the detector, reaches the tolerance limit at 1.43 T which is then the used value in place of the design value of 1.8 T. The coil has an overall length of 2.46 m and an inner diameter of 1.91 m. A high field solenoid (5 T) situated behind the RCAL compensates the effect or the main solenoid on the electron beam. The axial field produced by the solenoid is used to measure the momentum of the charged particles.
- An intrinsic compensation calorimeter composed by alternate layers of depleted Uranium and scintillator (CAL) divided in three modules: the FCAL (Forward calorimeter), BCAL (Barrel calorimeter) and RCAL (Rear calorimeter).
- At a longitudinal depth of 3 radiation lengths in the RCAL the Hadron-Electron Separator (HES) is located. It consists of 3 $\times$ 3 cm^2 silicon-diodes and provides a better discrimination power between electromagnetic and hadronic showers originating from low energetic particles ($<$ 5 GeV).

[1] ZEUS stands for the Greek expression for *Search to Elucidate the Underlying Symmetry*

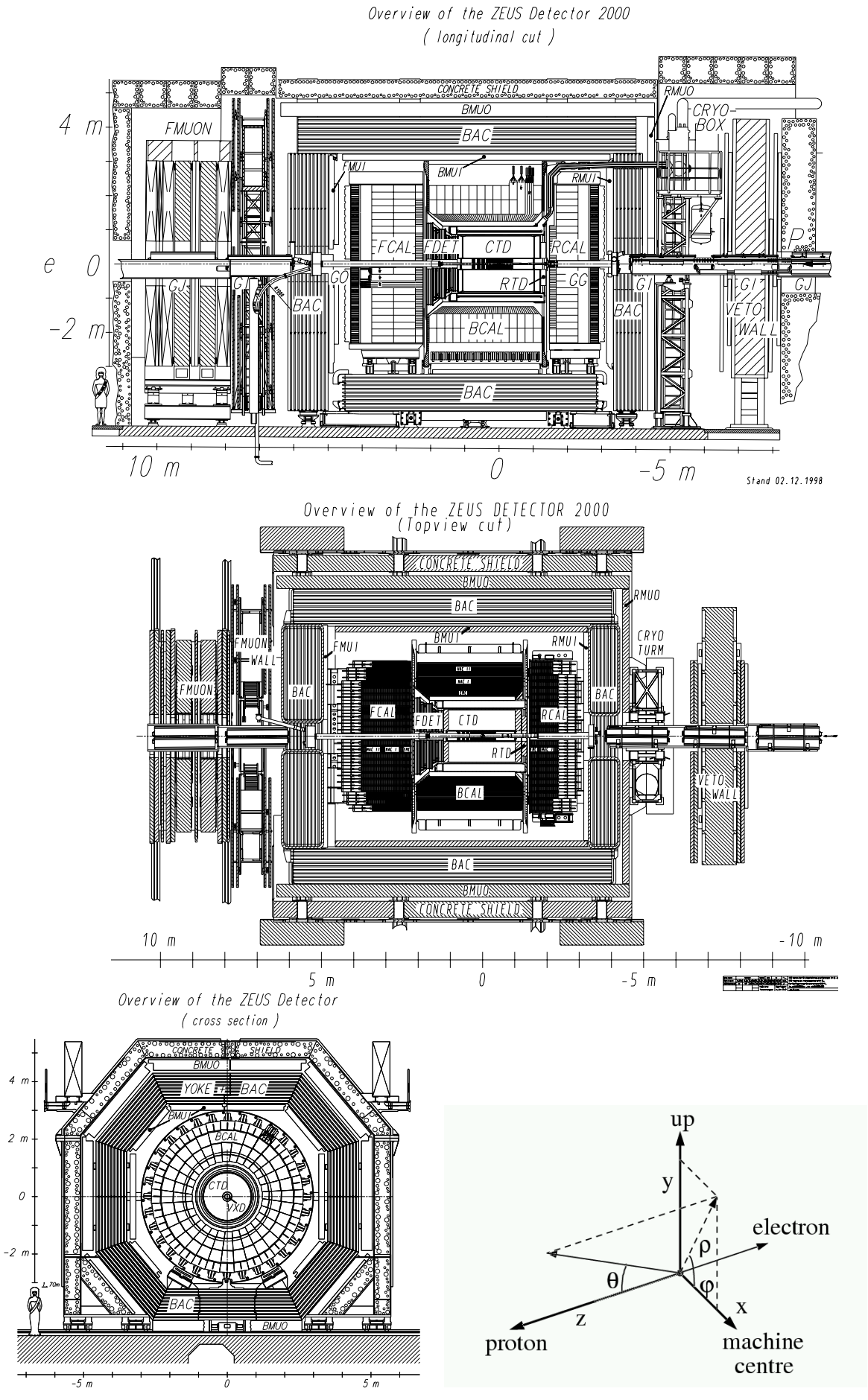

Figure 2.4: *Cross section of the ZEUS detector in the vertical plane: side view (top), top view (middle). Cross section in transverse plane containing the nominal interaction point (bottom left)). The ZEUS reference frame (bottom Right)*

- A moderate resolution second calorimeter (BAC) which is intended to complement the hadronic jets energy measurement in the CAL by measuring the energy leakage. The BAC is made of 7.3 cm thick iron plates and also serves as the return yoke for the magnetic flux from the solenoid.
- Muon detectors placed both in the inner part of the iron yoke (FMUI, BMUI and RMUI) and in the outer of it (FMUO, BMUO, RMUO). The toroidal magnetic field in the yoke, generated by a suited coil system, allows a measurement of the muons' momentum independent from the one provided by the inner tracking detectors.
- In the rear part or the main detector, at 7.5 m upstream of the interaction point, a veto detector (VETOWALL) is installed to suppress the interactions of the proton beam upstream of the main detector.
- A small lead-scintillator counter (C5), located around the beam pipe at $z = -3.15$ m, monitors the synchrotron radiation accompanying the beams and the timing and longitudinal structure of the proton and electron bunches.
- At $\sim\ 20 - 90$ m downstream in the proton-beam direction the Leading-Proton Spectrometer (LPS) and the Forward Neutron Calorimeter (FNC) detect protons and neutrons scattered elastically through small angles, respectively.
- The Proton-Remnant Tagger (PRT) is a lead-scintillator counter located at $z = 5.1$ m around the beam pipe and covers the pseudorapidity range $4.3 < \eta < 5.8$.
- The system is completed in the electron beam direction, by two small lead-scintillator calorimeters which are installed at $z = -30$ m and $z = -104$ m for the measurement of outgoing electrons and photons, respectively, at low scattering angles. They are used for the determination of the luminosity and and to detect $Q^2 \sim 0$ events (photoproduction regime) and radiative events.

In the next sections a brief description is given of the components which were more relevant to our analysis.

2.2.2 The Central Tracking Detector (CTD)

The CTD [122] is a cylindrical wire chamber with nine superlayers of eight sense wire layers each, as shown in Figure 2.5, covering the polar-angle range of $15^\circ < \theta < 164^\circ$. The inner radius of the chamber is 16.2 cm, while its outer radius is 85 cm. The longitudinal length is 241 cm. Five of the superlayers have wires parallel to the chamber axis and are called *axial superlayers*. The remaining four layers are *stereo superlayers*: the wires are tilted by a small angle (5° or 6°) with respect to the beam, as displayed in the Right part of Figure 2.5. Stereo superlayers can thus provide information on the z-coordinate of the hits.

The CTD is filled with a gas mixture of Argon (Ar), carbon dioxide (CO_2) and ethane (C_2H_6) (in the ratio 83:5:12) which is bubbled through ethanol.

A charged particle, traversing the CTD, ionises the gas, creating electron-ion pairs along its trajectory. Under the action of the electric-field, the free electrons drift towards the positive sense wires (with an approximately constant velocity of 50 μm/ns), whereas the positive ions are accelerated towards the negative field wires. In the field of the sense wires, avalanche-like multiplication of the electron occurs, being the amplification factor about 104. The produced sizable pull is read out and digitised by 8-bit flash ADCs. For trigger purposes, the three inner layers are additionally equipped with a z-by-timing system which determines the z-position of the hit from the difference in arrival times of a pulse at both end of the chamber.

After the final offline reconstruction, the r - ϕ hit resolution is 200 μm (depending slightly on the polar angle). The resolution in z using the axial and stereo superlayers is 2 mm and when using z-by-timing is 4 cm. The relative transverse momentum resolution of the CTD is

$$\frac{\sigma_p}{p} = 0.005\, p \oplus 0.007 \oplus \frac{0.001}{p} \tag{2.1}$$

for particles transversing all 9 superlayers and with p in GeV. The actual numbers in this parametrisation have been obtained running the detector simulation (tuned with data) on generated tracks coming from the $D^* \to K\pi\pi$ channel (Figure 2.6). The first term correspond to the resolution of the hit positions, the second term to smearing from multiple scattering within the CTD and the last term to multiple scattering before the particle enters into the CTD [123]. In the

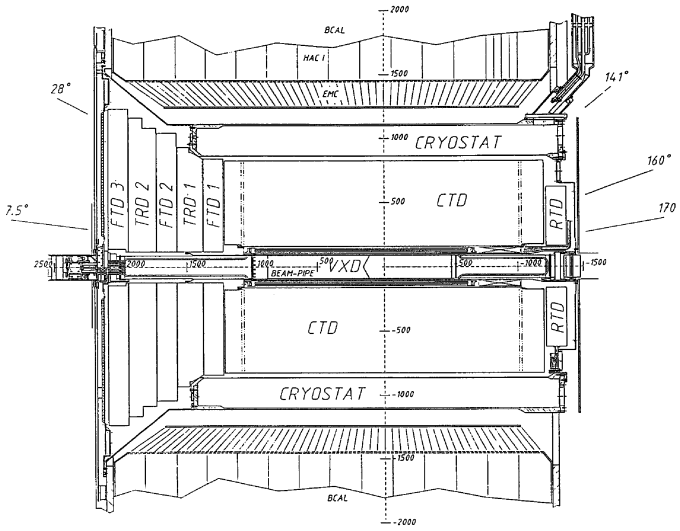

Figure 2.5: **Left***: Cross section of the inner tracking detectors along the beam plane.* **Right***: Layout of a CTD octant in the transverse plane. The wires of the four superlayers with even numbers are slightly tilted with respect to the beam (stereo superlayers). The value of this angle is displayed below the corresponding superlayer in the figure.*

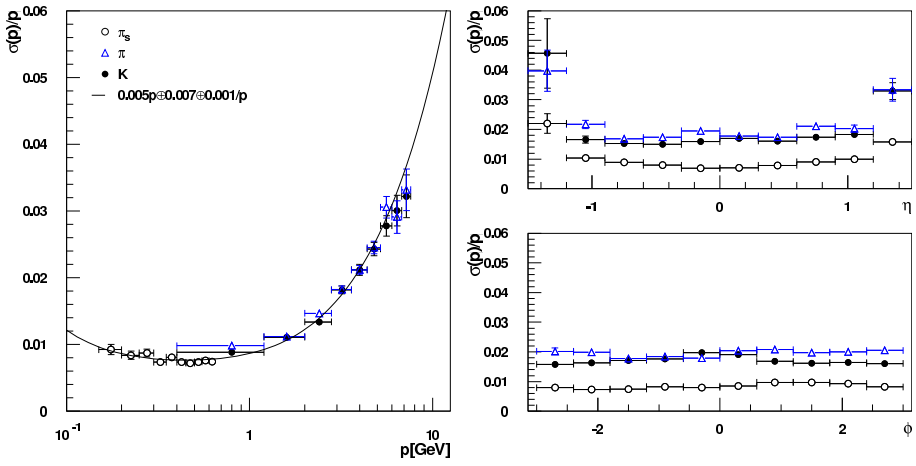

Figure 2.6: **Left***: Momentum resolution as a function of the track's momentum.* **Right***: Momentum resolution as a function of the track's η and ϕ.*

forward region the acceptance of the CTD is extended by the FTD, a system of three planar drift chambers. Between the three FTD chambers, the modules of a Transition Radiation Detector (TRD) designed to enhance hadron-electron separation in the forward region, are positioned. FTD and TRD together form the Forward Detector FDET. In the rear direction, a single chamber (RTD) of identical design of those of the FTD extends the CTD acceptance to polar angles between 160° and 170°.

The information used to determine the spatial position of a particle, needed for the track reconstruction, come from the time of arrival of the ionisation electrons on the sense wire. If the drift velocity is approximately constant and equal to u_d , the relation between the drift time, t_d , and the distance from the sense wire, d_s, is given by: $d_s \simeq u_d \cdot t_d$ where t_d is defined as the difference between the time t_f at which the pulse appears on the sense wire, and the time t_i of passage of the charged particle, calibrated for every wire, $t_d = t_f - t_i$. However, this kind of information is not sufficient to determine from which side of the wire the particle comes, therefore a Left-Right ambiguity is still present. The 45° tilt of the sense wires can solve this ambiguity, since tracks coming from the interaction point tend to pass the boundary of adjacent cells within a superlayer. The pattern recognition of the track begins looking for a seed, a group of hits in the outermost superlayer (SL9). To these hits a virtual hit at $X = Y = 0$ is added, keeping into account the transverse dimension of the beam as an error on this hit. The two hits are enveloped with a circle arc, and inner hits on the axial superlayers are added on the way, updating the circle parameters and refining the trajectory determination. Once the trajectory spans several axial superlayers, the arc in the XY plane is used for the stereo pattern recognition: stereo hits are selected that match with the arc after being rotated. The pattern recognition begins with the longest tracks, those going from SL9 to SL1, then continues with shorter tracks, reaching inner superlayers (SL7, SL5...), and finally includes tracks with no hits in the innermost superlayer, that can come from the decay of long lived particles. When the pattern recognition is done, all the candidate tracks are fitted with a helix, starting with the innermost superlayer and adding the outer ones on the way. The five helix parameters are :

- $a_1 = \phi_H$, the angle tangent to the helix in the XY plane;
- $a_2 = Q/R$, where Q is the charge and R the radius of the helix;
- $a_3 = Q \cdot D_H$, where D_H is the distance of the helix from the origin;
- $a_4 = z_H$, the z position of the point of closest approach;
- $a_5 = cot\ \theta$, where θ is the polar angle.

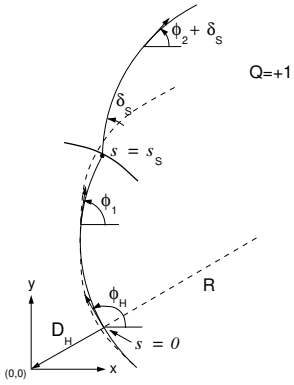

The track helix in the XY plane.

The event vertex is then reconstructed from the information on the fitted tracks. Tracks too far from the determined vertex are discarded, the surviving tracks are constrained to the vertex and the fit parameters recalculated.

2.2.3 The Small-angle Rear Tracking Detector (SRTD)

The Small Angle Rear Tracking Detector (SRTD) [124] is a scintillator strip detector located at $z = 148\ cm$ on the face of the RCAL covering 68 $\times$ 68 cm^2 around the rear beam hole. The active part of the SRTD consists of two layers of orthogonally arranged (x,y) strips with a 1 cm pitch. Each plane is subdivided into four quadrants. The strips provide a position and pulse height measurement for charged particles via an optical fiber photo-multiplier readout. The SRTD supplies additional tracking (to the CTD) to measure low-angle scattered electrons hitting the RCAL near the beam pipe. The SRTD is also used as a presampler in order to correct for energy losses due to inactive material (mostly cables and tracking detector end-plates) in this detector region. Electrons preshower in these materials and the energy deposit of the preshowers in the SRTD can be used to correct for these energy losses. Complementing the calorimeter information on the scattered electron is important for an accurate reconstruction of the event kinematics at low Q^2.

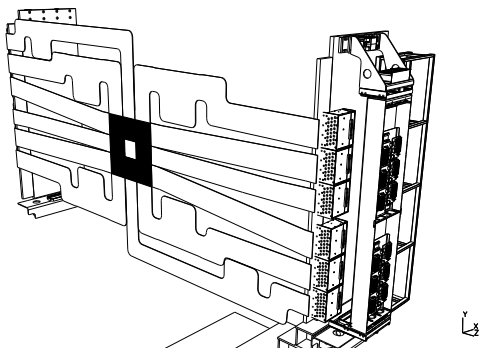

Layout of the SRTD.

2.3 The ZEUS Uranium-scintillator calorimeter (UCAL)

The ZEUS calorimeter [125] is a sampling calorimeter with almost equal response to electrons (positrons and photons) and hadrons ($e/h \simeq 1$). This important property, often referred as *intrinsic compensation*, allows a good resolution in the determination of both the electromagnetic and the hadronic energy. It is achieved by the use of a sandwich of absorber plates of depleted Uranium and plastic scintillator layers as active plates with tuned thickness.

The basic design parameters which are fulfilled with the choice of this technology, are the following:

- Hermetic coverage over a large solid angle (99.7%) and uniform response
- High energy resolution for both hadrons and electrons.
- Calibration of the absolute energy scale up to the 1% level
- Fine segmentation for precise angular resolution ($\lesssim$ 10 mrad);
- Longitudinal segmentation for hadron-electron separation;
- Short signal-processing time at the ns level (no dead-time, rejection of cosmic and beam-gas events - interaction of p with residual gas in the beam-pipe).
- Containment for hadronic showers with energy up to 400 GeV in the proton direction
- Radiation damage resistance up to doses of 20 rad/day

2.3.1 Energy resolution and compensation

The energy resolution in non homogeneous calorimeters is determined by two dominant effects :

- the event by event fluctuations in the shower development
- the fluctuations of energy losses in the various materials of which the calorimeter is made

For electromagnetic showers produced by high energy electrons, positrons or photons the intrinsic resolution is ruled by the fluctuations of the energy losses in the various layers of absorber and sensitive material of the inhomogeneous calorimeter. Typical resolutions in this case are of order $\sigma(E)/E \sim 10\ \%/\sqrt{E}$.

For hadronic showers the resolution depends instead also on the relative response of the calorimeter to hadrons and electrons. A generic hadronic shower has an electromagnetic component (mostly from $\pi^0 \rightarrow \gamma\gamma$) which varies stochastically in each event. These fluctuations associated to an unequal response to hadronic and electromagnetic energy ($e/h \neq 1$) lead to a much worsened resolution: $\sigma(E)/E \sim (50-60)\ \%/\sqrt{E}$.

An adequate choice of material and thickness allow to bring the e/h ratio to unity thus obtaining resolutions $\sigma(E)/E \sim (30-35)\ \%/\sqrt{E}$. In such a structure the visible energy corresponds to the energy released by the shower in the various scintillator planes.

In the case of an electromagnetic shower the energy released in the absorber is unseen since the electrons, positrons and photons are completely adsorbed without secondary visible effects. On the other hand, in the case of an hadronic shower, the charged pions and protons induce the Uranium fission with the consequent production of nuclear fragments and neutrons. A fraction of these secondaries exit from the Uranium absorber and interact elastically with the protons in the scintillator producing a visible energy. With this mechanism part of the energy lost by an hadronic shower in the absorber is recovered via the Uranium fission. A further contribution comes from the photons coming from the de–excitation of nuclear fragments coming from the Uranium fission. By exploiting these reactions compensation can be achieved.

Computer simulations and tests on prototypes showed that 3.3 mm thick depleted Uranium interleaved with 2.6 mm scintillator (SCSN 38) allow to achieve intrinsic compensation. These resolutions were measured on these prototypes for hadrons:

$$\frac{\sigma(E_{had})}{E_{had}} = \frac{35\ \%}{\sqrt{E_{had}}} \oplus 2\%$$

and for electrons:

$$\frac{\sigma(E_{e.m.})}{E_{e.m.}} = \frac{18\ \%}{\sqrt{E_{e.m.}}} \oplus 1\%$$

2.3.2 Mechanical structure and readout

The depleted Uranium plates have a composition of 98.1% U_{238}, 1.7% Nb and less than 0.2% U_{235}. The optical readout is performed via plastic wavelength shifters (WLS), light-guides and photo-multipliers.

The solenoid and the tracking chambers are completely enclosed by the Uranium calorimeter, except in the region around the beam-pipe. The UCAL is constructed in three main parts, the hollow cylindrical central part of BCAL with a polar angle acceptance of $36.7° < \theta < 129.1°$ and the two end caps FCAL and RCAL, which cover the polar angle of $2.2° < \theta < 36.7°$ and $129.1° < \theta < 176.2°$, respectively (see Left part of Figure 2.7) (Left). The inner radius of

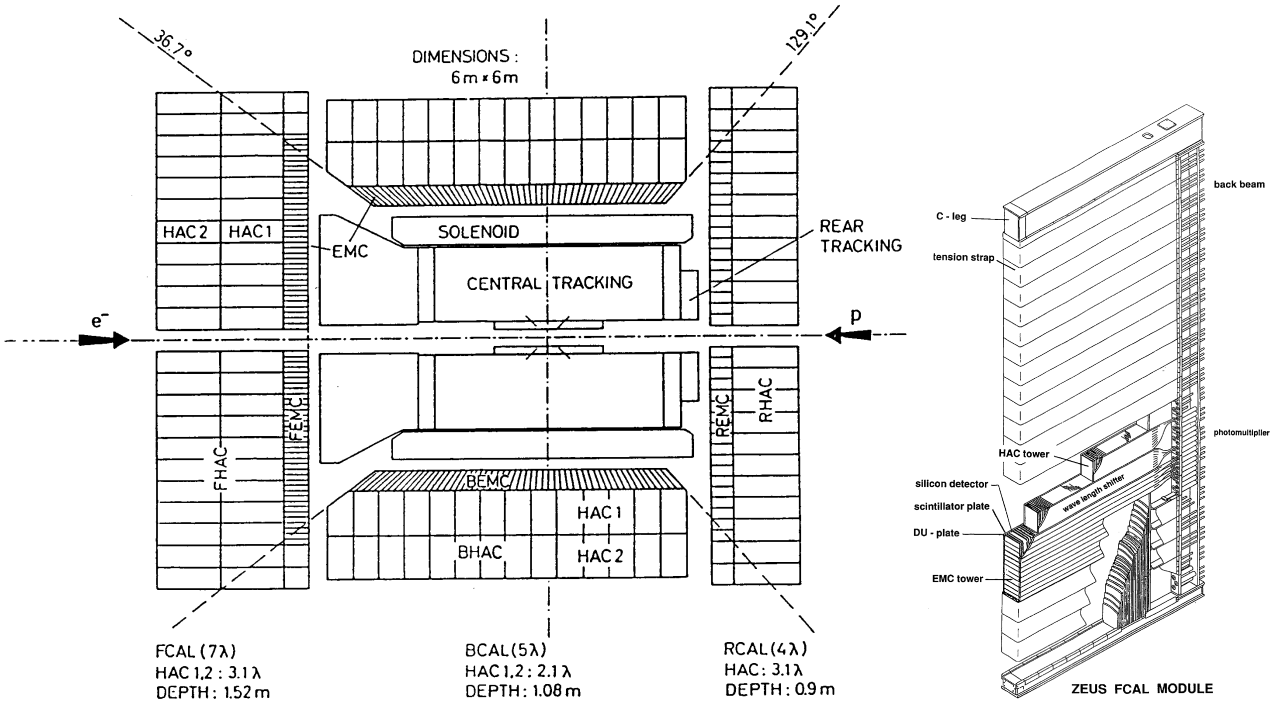

Figure 2.7: **Left***: Layout of the ZEUS high resolution Uranium-scintillator calorimeter. The picture shows the three sections of the UCAL and the polar-angle acceptance of each section.* **Right***: Internal structure of an FCAL module. The RCAL modules are very similar but they contain only two EMC cells instead of the four in FCAL and BCAL. One module in BCAL follows the same distribution as in FCAL but its geometry is adapted to the barrel requirements.*

the BCAL is 134.5 cm, while the FCAL and RCAL face closer to the interaction point are located perpendicular to the z-axis at the position 234.4 cm and -160.2 cm, respectively, along that axis whose origin is in the nominal interaction point.

The total depth of the three different calorimeter sections takes into account the Lorentz boost and reflects the maximum energy deposition of scattered particles. The FCAL has a maximum depth of 7.1 interaction length (λ_{int}), while BCAL has 5.3 λ_{int} and RCAL 4 λ_{int}. Each section is divided into modules and further subdivided into towers which provide granularity for position reconstruction.

The three calorimeter components have similar structures and are subdivided longitudinally into an electromagnetic calorimeter (FEMC, BEMC, REMC) with a depth of 1 λ_{int}, which is sufficient to fully contain the electromagnetic showers, and a hadronic calorimeter (HAC). In FCAL and BCAL the HAC section is divided into two subsections HAC1 and HAC2, while the RCAL has only one HAC section.

The whole calorimeter has a modular structure. The FCAL and RCAL calorimeters consist of 23 modules which follow the same construction principles, as shown in Figure 2.7 (Right), where an isometric view of a FCAL module is presented. The FCAL and RCAL modules have the same width of 20 cm and have a height varying from 2.2 m to 4.6 m so that roughly a cylindrical structure with a radius of $\sim$ 2.3 m can be built. The depth varies from 7.1 λ_{int} in the central region to 5.6 λ_{int} in the outer horizontal regions for FCAL. For RCAL the depth is smaller ($\sim$ 4 λ_{int}) since momentum conservation does not allow very high energy particles going into the rear direction of the detector.

The centered module of the FCAL and RCAL calorimeter are composed of separate upper and lower parts leaving a hole in between to allow the beam-pipe crossing through the detector. The horizontal segmentation is determined by the width of the modules. The transverse segmentation depends on the height of the wavelength shifters which collect the scintillator light. Each longitudinal section (EMC, HAC1, HAC2) is read out in both sides by wavelength shifters. For the FCAL the segmentation of the EMC section is 5 $\times$ 20 cm, and for RCAL 10 $\times$ 20 cm. These sections are called EMC cells. The hadronic cells of FCAL and RCAL have a segmentation of 20 $\times$ 20 cm.

The BCAL modules [120] present a similar distribution than of FCAL, but the geometrical design is slightly different to adapt to the barrel-shape requirements of this calorimeter part. Each module consists of 14 towers parallel to the z-axis. The 32 modules complete the circle around the z-axis containing the interaction point. In the BCAL, each tower is similar to one tower in FCAL except that the depth is around 5 λ_{int}. The first (last) tower in each module contains only 3 (2) electromagnetic cells. To increase the efficiency for detecting electromagnetic showers, the first and the last towers have their electromagnetic cells oriented towards the interaction point.

Due to the optical read-out combined with photo-multipliers a fast readout processing can be performed which allows the determination of the arrival times of incoming particles at the ns level. The timing resolution for each calorimeter cell is $\sigma_t = 1.5/\sqrt{E} \oplus 0.5$ ns, where E (GeV) is the energy deposited in the cell [125]. The timing information from the calorimeter is useful to remove both beam-gas and cosmic ray related backgrounds. The time $t = 0$ ns is defined to be the time at which the particles originating from ep collisions at the interaction point arrive at the calorimeter.

When particles from beam-gas interactions which occur behind the RCAL, deposit energy in the RCAL, this time is negative. Therefore, a cut on the RCAL time can remove beam-gas events. In addition, the "up-down" time difference should be zero for deposits related to an ep collision. However, for cosmic rays, this time difference is greater than 10 ns. Therefore, cosmic rays events can also be removed with the calorimeter time information. The vertex position along the the z-axis can also be measured using calorimeter time information. The time t at which energy is deposited in the FCAL near the beam-pipe from an ep collision will depend on the vertex position along the z-axis (z_{vtx}). The correlation between the z_{vtx} measured using the tracking detectors and the FCAL timing information can also be used to remove beam-gas interactions.

The readout of the calorimeter cells is fast enough to avoid mixing the information of two successive bunch crossings, but since the trigger decision about each event is slower (see Section 2.5.1), the information has to be stored waiting for it. This is done by means of a pipelined readout [127]. Each of the channels stores the information in a system of capacitors which delays the transmission of the read values during the time the trigger system takes a decision about the event. This system can store up to a maximum of 58 events, which means that the information is kept $\sim 5.6\ \mu s$ after the event occurs. This time delay is enough to take a fairly good decision about the usefulness of the event.

The calibration of the calorimeter is performed using several redundant tools, which are described in [126]. The main calibration source is the use of the natural Uranium radioactivity, the so-called Uranium noise (UNO), which produces a low background current in the photomultiplier. This current is statistically very stable and the deviations from the expected value allow the detection of problems in the operation of the photomultiplier. On the other hand, to calibrate the electronic system reading the information for each channel, injectors of charge are used to simulate the signal coming from the photomultiplier. Since the quantity of charge is known, the returned value given by the complete readout system is used to calibrate the effects of the electronics, after subtraction of the noise contribution. All these tools provides a stable diagnostic tool for monitoring and calibration.

2.4 Muon detectors

The main aim of these detectors is the measurement of the tracks coming from the interaction region (pointing tracks) and that are able to cross the whole calorimeter and the iron yoke (penetrating tracks). This behavior is characteristic of muons, that can cross large amount of material without being absorbed since, being much heavier than the electrons and not interacting strongly, they lose their energy just by ionisation. The muon detection system, as the other detectors in ZEUS, has to keep into account the boost of the particles in the forward direction. The momenta of the muons can be very different depending on their polar angle: in the forward region muons with more than 10 GeV momentum are easily found, whereas in the barrel and rear regions the average momentum of the muons is much smaller. Therefore the muon detection system is split into two detectors, designed and realised in different ways: the Forward Muon Detector (FMUON) and the Barrel and Rear Muon Detector (BMUON and RMUON).

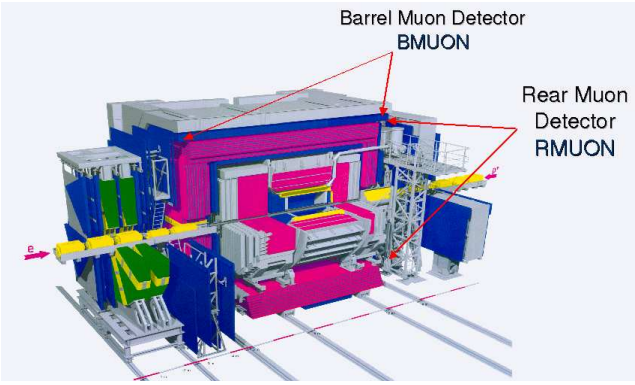

Figure 2.8: *Location of the barrel and rear muon chambers within the ZEUS detector.*

2.4.1 The Barrel and rear muon chambers (BRMUON)

The Barrel and Rear Muon Detector [129] has to cover a very large area, of the order of 2000 m^2. So far, it is the largest system of this kind ever built. This constraint led to the choice of the *Limited Streamer Tubes* (LST) [128] technology. This kind of detector is particularly suited when a large coverage is needed since it has the advantage of providing good resolution ($\sim 1\ mm$) and efficiency with relatively low costs. For the same reason a modular structure was conceived.

The basic element is denoted as *chamber*. The chambers covering the inner barrel part, between the CAL and the iron yoke, are called BMUI, whereas the chambers situated in the outer barrel part, outside the yoke, are denoted as BMUO. In a similar way, in the rear region the detector is divided into RMUI and RMUO chambers. In Figure 2.9 the layout of BRMUON is schematically shown. The chambers have different shapes and dimensions depending on

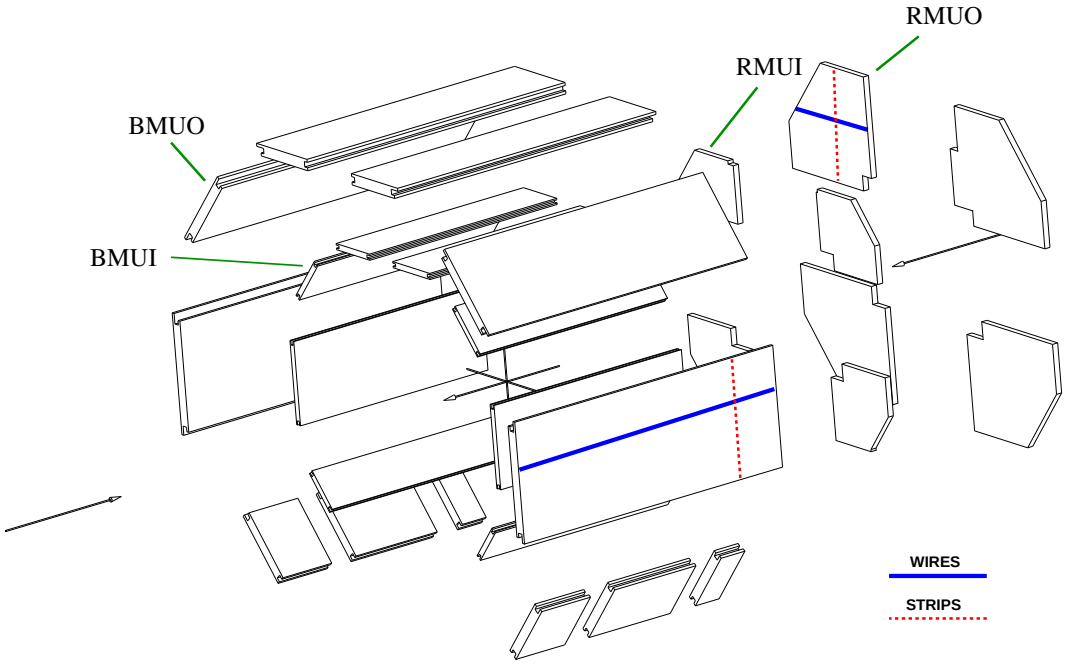

Figure 2.9: *Three dimensional exploded view of the barrel and rear muon chambers.*

where they are located, but their internal structure is the same: the element bearing the weight of the chamber is an aluminum honeycomb structure, 12.7 cm thick in the rear and inner barrel chambers, 30.4 cm in the outer barrel ones.

On both sides of the honeycomb a couple of planes of limited streamer tubes (LST) [128] is placed (see Figure 2.10). Each tube contains eight cells, each with one sense wire; the distance between two sense wires is 1 cm. During the

data-taking the sense wires are brought to $\sim$ 4500 V so that they behave as anodes, while the inner cell walls, covered by graphite, act as cathodes. The cells are filled with a mixture of carbon dioxide (CO^2), Argon (Ar) and Isobuthane (C_4H_{10}).

On one of the outer wall of the LST plane conductive strips orthogonal to the wires are placed. The distance between two adjacent strips is 1.5 cm. The signal read by the wires is also induced on the strips, so that a single plane of wires and strips is sufficient to determine the particle position. For redundancy each chamber has two LST planes on each side. The cells in one plane are displaced with respect to those in the other plane by half cell, in order to have good acceptance also for the particles passing near the boundary of two cells in a plane. In the BMUI and BMUO chambers the LST are parallel to the beam direction, whereas in RMUI and RMUO they are horizontal (parallel to the ZEUS x direction) (see Figure 2.9).

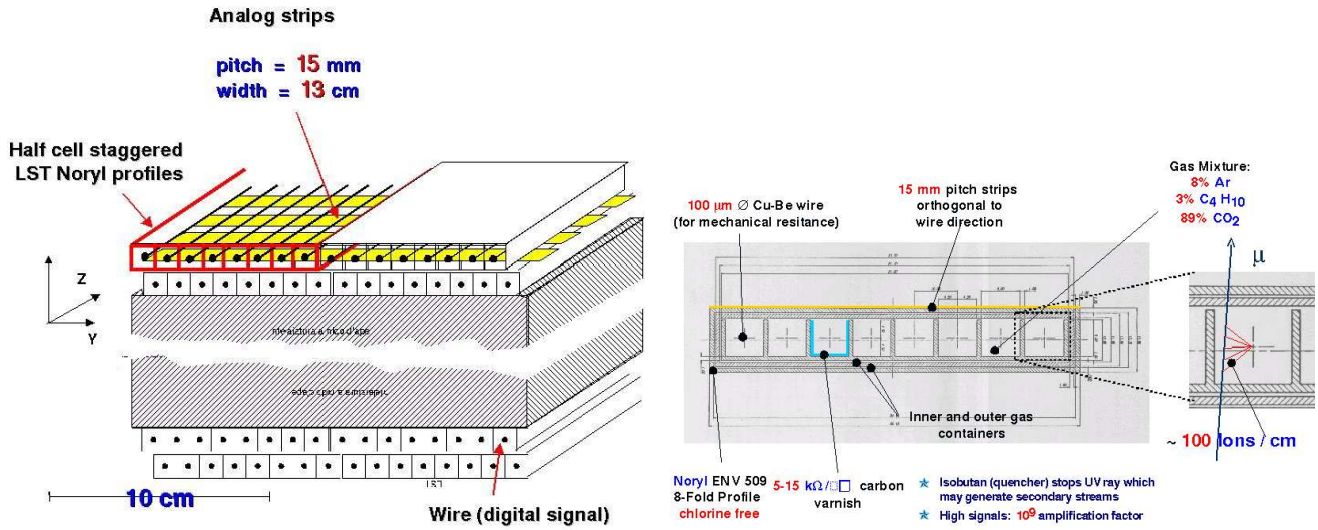

Figure 2.10: **Left***: Cross section of a barrel-rear muon chamber in the transverse plane.* **Right***: Cross section of an LST tube used in the BRMUON chambers.*

The determination of the position of a particle passing through the muon chambers proceeds by collecting the information coming from the wires, read by electronic cards called SGS, and from the strips, with readout cards named STAR. The reading of the cards depends on the presence of a trigger signal in the event. There are two types of trigger signals in an event: when the muon chambers identify a penetrating track, giving activity in the inner and outer muon chambers, and pointing to the central tracking devices, the trigger signal is called *strong* ; on the other hand, if the muon chambers find activity in at least one of the inner chambers, the trigger signal is called *weak*.

The trigger signal is determined by the analysis of the wires and strips hit in the event. First of all, the adjacent wires in the same LST plane are OR'ed in groups of 16, and the same is done with the strips. The signal obtained from these groups is further analyzed in order to obtain information on the polar and azimuthal position of the wires and strips that have been hit. Coincidence matrices designed for this purpouses analyse the information coming from the inner and the outer muon chambers, and select configurations generated by tracks coming from the volume specified by the inner tracking detectors (pointing tracks). In the case of positive response by the matrices, a strong trigger signal is present.

When there is a strong or weak trigger signal in the event the following information are recorded: the addresses of the hit wires, the drift distance wire by wire, the addresses of the hit strips and the charge collected by each strip (analog readout). With the analog readout the achievable spatial resolution on the coordinate orthogonal to the wires is 200 μm, while it is 700 μm for the coordinate parallel to the wires. If there is no trigger signal in the event, the recorded information are the addresses of the hit wires and of the OR of four adjacent strips, called quadruplets (digital readout). In this case the resolution on the single hit is $1/\sqrt{12}$ cm in the direction orthogonal to the wires, $6/\sqrt{12}$ cm along the wires.

2.4.1.1 Segment reconstruction and momentum measurement

The final parameters of the reconstructed tracks in the barrel and rear chambers are collected in a table of the ADAMO database (MBXYSG). The $MBXYSG_X(3)$ contains the position of the segment in the inner chambers in the ZEUS reference frame while in $MBXYSG_DirCos(3)$ the segment director cosines are stored. If the muon was energetic enough to traverse the whole iron yoke and reach the outer chambers ($p \gtrsim 2-3$ GeV) the measurement of the momentum becomes possible ($1/MBXYSG_InvP$) by considering the curvature introduced by the yoke magnetic field. A scatter-plot showing the correlation between the signed momentum as measured in the BRMUON chambers and that measured in the CTD is presented in Figure 2.11. A good correlation is observed. The systematic difference between the two measurements ($\sim 1-2$ GeV) illustrates the energy loss of the muon in the UCAL.

The $MBXYSG_Chi2$ variable (matching χ^2) represents the probability that the segments in the inner and outer chambers to actually come from the passage of the same particle.

Variable	*Description*
`X(1)`	x coordinate
`X(2)`	y coordinate
`X(3)`	z coordinate
`DirCos(3)`	Director cosines
`Invp`	Inverse of the track momentum
`R`	Sector
`Cov(15)`	Covariance matrix
`Chi2`	χ^2 of matching

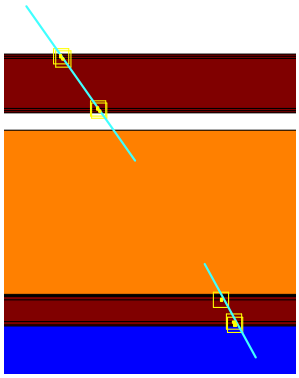

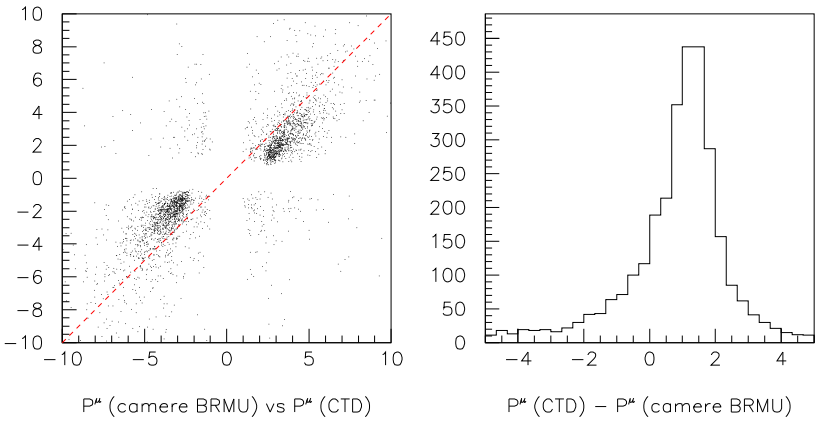

Figure 2.11: *Correlation between the momentum of the muon as measured in the CTD and in the BRMUON chambers. Distribution of the difference between the momentum measured in the CTD and the muon chambers. The systematic shift is due to energy loss in the dead material).*

2.4.2 The Forward muon chambers (FMUON)

The Forward Muon Detector is made of two modules (Figure 2.12): one is located between the FCAL and the BAC (inner detector, FMUI), the other is positioned outside the BAC (outer detector, FMUO). The FMUON detector consists of:

- a system of four limited streamer tubes [128] trigger planes (LST1 LST4), with digital ρ and ϕ readout;

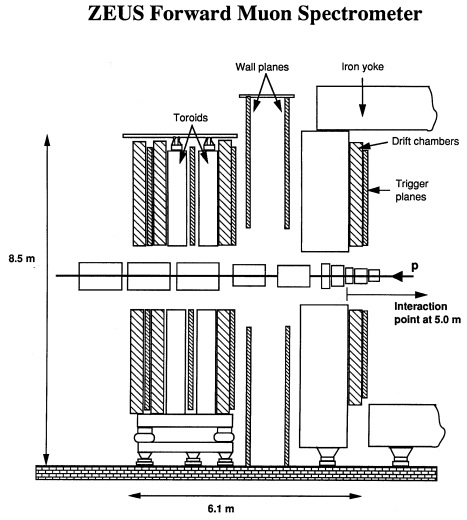

Figure 2.12: *Layout of the FMUON detector.*

- two coverage planes of limited streamer tubes with digital (ρ, ϕ) and analog ρ readout, in the large polar angle region (LW1, LW2);
- four planes of drift chambers (DC1$\div$DC4);
- two large toroidal iron magnets providing a magnetic field of 1.7 T for the momentum separation and measurement in the angular region $5^\circ < \theta < 16^\circ$.

The first LST plane and the first drift chamber make up the FMUI detector, while the FMUO detector consists of the rest of the system.

2.4.2.1 The Limited Streamer Tubes (LST) Planes

The aim of the limited streamer tubes (LST) planes is to trigger on muon candidates and to reconstruct their position in terms of the azimuthal and radial coordinates of the track. A trigger plane is made of four LST chambers, grouped by two in two half-planes. A quadrant consists of two layers of LST, positioned horizontally inside a plastic sheet. The tubes of the two planes are slightly displaced (0.5 cm) in order to achieve a complete geometrical acceptance. Each quadrant is contained in an aluminum air tight box. The signals generated by the LST are induced on copper strips with polar geometry, glued on the outer side of the plastic sheet. The number of radial ρ strips, 1.9 cm wide, is 132, and they are divided along the bisector of the quadrant so that the simplest unity of the trigger plane to be read is the octant. The last 64 strips far away from the beam line are OR'ed two by two since as θ becomes larger a coarser resolution is needed.

Therefore the number of channels needed for each octant is 96. The number of ϕ strips is 32 per octant: each covers a 1.4° interval in azimuth.

2.4.2.2 The drift chambers (DC)

The drift chambers are needed in order to obtain a good momentum resolution. Each plane consists of four chambers, grouped two by two in two half planes, fixed on a sustain panel. The basic constituent of the chamber is the cell, made of four sense wires and of the layers needed to generate the appropriate electric field. The four sense wires measure the radial coordinate. The information gathered by the wires are sent to a TDC, which converts them into a time distance, connected to the space distance by a known relation.

2.4.2.3 The Large Angle Wall Planes (LW)

The two large angle coverage planes (LW) are needed in order to achieve the desired geometrical acceptance also in the region left uncovered by the toroids ($16^\circ < \theta < 32^\circ$).

Each plane consists of eight aluminum tight wrappings that contain a LST layer. The LST signal is induced on copper strips with radial geometry, spaced of 0.7° in the ϕ coordinate and of 1.8 cm in the ρ coordinate. The number of ϕ strips is 64 per octant, while the ρ strips are 192 per octant. The achieved resolution in the ρ coordinate, using a charge barycenter method, is $\sim$ 1 mm.

2.4.3 The backing calorimeter (BAC)

The main purpose of the Backing Calorimeter (BAC) (see Figure 2.4) is to measure the energy leakage out of the main calorimeter. In addition, it is used to detect muons from ep interactions and cosmics.

In order to measure energy of hadron shower leakages out of the central Uranium calorimeter and to correct jet energy measurement, the BAC was equipped in an analog readout, giving precise information on the deposited energy but only approximate deposit position. On the other hand, in order to enable muon tracking in the iron yoke a complementary digital readout was designed, giving basically no information about the deposited energy, but exact position in two dimensions (XY plane). This information can be also used for better positioning of shower leakages and for discrimination between leaking hadron cascades and muons.

The BAC totally covers the UCAL using as absorber material the 7.3 cm thick iron plates of the yoke. The iron yoke for the return of the magnetic field has the shape of an octagonal prism which is closed by end-caps on both sides. It can be magnetised by copper coils, in order to create a magnetic field for an independent measurement of the momentum of muons in the barrel muon chambers. It consists of slabs of iron separated by 3.7 cm gaps instrumented with several proportional tubes (up to ten).

2.5 Luminosity measurement

The physical process being used at HERA to measure the luminosity is the ep–*bremsstrahlung* in which the electron interacts elastically with the proton electromagnetic field via the emission of one high energy photon:

$$e + p \rightarrow e' + \gamma + p$$

Its cross section is fairly large, so that a short measurement time is needed for a reasonably accurate estimate of the instantaneous luminosity , and its cross section is calculable to a high degree of accuracy.

The outgoing electron and the photon are measured in coincidence in the so–called luminosity monitor (LUMI). An important constraint come from the fact that the scattered electron and photon energies must add up to the electron beam energy: $E_{e'} + E_\gamma = E_e$.

The cross section for this process is given semi–classically by the Bethe–Heitler formula[130]:

$$\frac{d\sigma_{BH}}{dE_\gamma} = 4\alpha r_c^2 \frac{E'_e}{E_\gamma E_e}\left(\frac{E_e}{E'_e} + \frac{E'_e}{E_e} - \frac{2}{3}\right)\left(ln\frac{4E_pE_eE'_e}{mME_\gamma} - \frac{1}{2}\right)$$

where E_γ is the photon energy, E_e, E'_e are the energies of the initial and final electrons, E_p is the proton energy, M (m) is the proton (electron) mass, α is the fine structure constant and r_c is the classical electron radius.

It has been shown that, within the experimental conditions, this cross section agrees excellently with QED calculations [131]. The radiative corrections to this process have been calculated and amount to -0.3% within the measurable region of phase space.

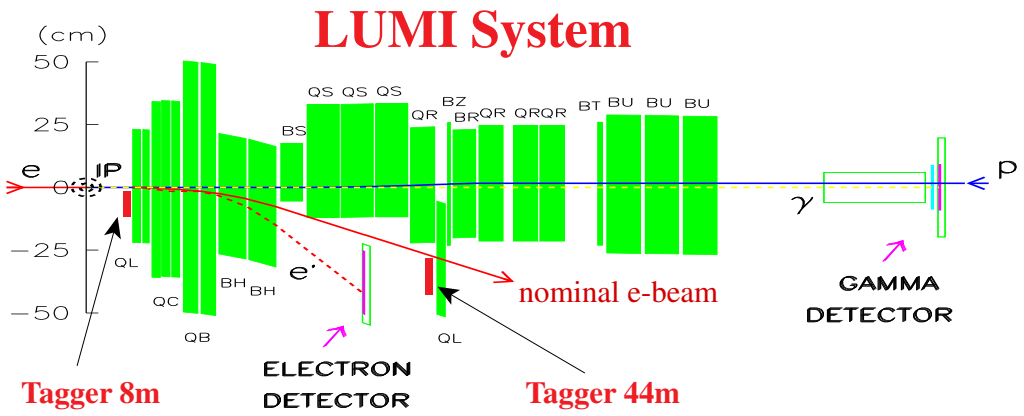

Figure 2.13: *Positions of the electron and photon taggers along the beam–line.*

The ZEUS luminosity monitor [132] consists of two separate detectors, one for the photon branch and one for the electron branch. The layout of the luminosity monitor components is shown in Figure 2.13.

Photons emerging from the bremsstrahlung process at scattering angles $\theta_\gamma \lesssim 0.5$ mrad leave the beam pipe through a window located at a distance of 92.5 m from the interaction point, and are measured in a lead-scintillator electromagnetic calorimeter at 107 m from the interaction point. In front of the photon calorimeter, a 2 radiation length carbon filter absorbs the large flux of synchrotron radiation photons, which typically have low energy ($\sim$ KeV), whereas the bremsstrahlung photons used for the luminosity measurement have energies well above 1 GeV. A Čerenkov counter placed between the filter and the calorimeter detects events in which the photon has been converted in the filter in an e^+e^- pair. The energy resolution of this calorimeter under test beam conditions is $18\%/\sqrt{E(GeV)}$, although in practice is slightly worse ($25\%/\sqrt{E(GeV)}$) due to the filters. The acceptance for bremsstrahlung photons is about 98%, independent of energy.

Electrons scattered at angles $\theta_{e'} \lesssim 6$ mrad, and with energies $0.2\ E_e \lesssim E_{e'} \lesssim 0.9\ E_e$ are deflected by the beam magnets away from the nominal electron beam orbit. They leave the electron beam line through a window at 27.5 m from the interaction point, and hit the electron calorimeter located at 34.7 m from the interaction point. The acceptance is measured to be above 70 % and flat for scattered electrons with energies in the range $0.35\ E_e \lesssim E_{e'} \lesssim 0.65\ E_e$. This is the region used in the luminosity measurement. In addition, the electron calorimeter of the LUMI can be used to tag electrons scattered at very small angles. In this case, no coincidence with the photon calorimeter is required. This electron–tagger covers the Q^2 range between 10^{-7} and $2 \cdot 10^{-2}$ GeV^2.

The luminosity value is easily obtained from the observed ep-bremsstrahlung rate R_{ep} by $\mathcal{L} = R_{ep}/\sigma_{obs}$, where σ_{obs} is the ep-bremsstrahlung cross section corrected for detector inefficiencies and acceptances. The uncertainty in σ_{obs} is small and, therefore, the error in the luminosity measurement is largely dominated by the uncertainty in R_{ep}.

The luminosity measurement suffers from a number of background processes. By requiring a coincidence between a high-energy electron and photon, this background is dominated by interactions of electrons with the remaining gas in the beam pipe. The most problematic contribution is the beam-gas bremsstrahlung process in which the positron interacts with a nucleus (Z),

$$e\ Z \rightarrow e'\ Z\ \gamma$$

which is in principle indistinguishable from the process of interest. Its contribution to the total counting rate of the luminosity monitor has to be estimated by using the pilot electron bunches. Let the fully measured counting rate of the luminosity detector be R_{tot}, the rate of the pilot bunches be R_{pilot}, the total current in the electron ring be I_{tot}, and the current in the pilot bunches be I_{pilot}; the actual ep-bremsstrahlung rate for the luminosity measurement can be estimated as:

$$R_{ep} = R_{tot} - R_{pilot} \cdot \frac{I_{tot}}{I_{pilot}}$$

The luminosity can then be extracted form this corrected rate (R_{ep}) using the Bethe-Heitler expression corrected for the acceptance of the LUMI detector. For the determination of the luminosity photons with energies in the range 10-16 GeV are used. However, these cut values are varied for systematic checks.

The ZEUS integrated luminosity available for physics analysis is listed in Table 2.2 for the 1993-2000 running periods. In these years the average ZEUS efficiency was around 70%.

Period	HERA delivered (pb^{-1})	ZEUS on-tape(pb^{-1})	ZEUS physics (pb^{-1})	ZEUS physics (10^6 events)
e- 93-94	2.17	0.99	0.82 (+-1.5%)	8.34
e+ 94-95	17.42	10.57	9.64 (+-1.2%)	29.98
e+ 96-97	53.51	40.54	38.62 (+-1.6%)	50.58
e- 98-99	25.2	17.78	16.67 (+-1.8%)	23.57
e+ 99-00	94.95	73.37	66.04 (+-2.25%)	66.76

Table 2.2: *Luminosity collected by ZEUS in 1993-2000. The difference between "on-tape" and "physics" comes from the rejection of data considered not useful for analysis by the offline data quality monitoring.*

2.5.1 Trigger and data acquisition

The rate of photoproduction and deep inelastic ep collisions is at a level of 1-100 Hz, which is several orders of magnitude smaller than the rate for background events (10-100 kHz), which mainly come from proton interactions with the residual gas molecules upstream of the detector. The raw data information from the roughly 250.000 detector channels has a size of about 0.5 Mb. Since the writing speed is limited to 0.5 Mb/s, it is essential to select the small fraction of interesting physics events and reduce redundancies in the data online at an early stage of the data acquisition.
This reduction is accomplished by a three level trigger system, as illustrated in the Figure on the Right. Each detector component has its own custom built front-end and read-out electronics and a local first level trigger (FLT) which provides a first decision based on a subset of the data by means of very fast hardware as, e.g., programmable gate arrays, look-up tables etc. The global first level trigger (GFLT) synchronises the component triggers with the HERA clock. Each bunch crossing is identified by a number (BCN) which is used for keeping the entire system in phase.

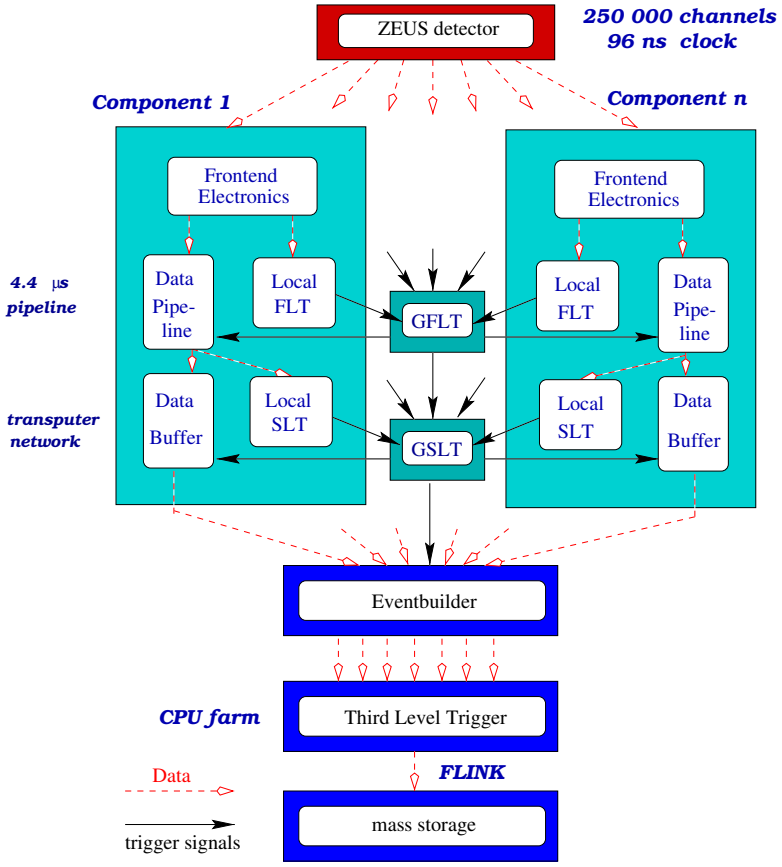

Schematic view of the ZEUS trigger system.

The GFLT expects the FLT decisions from the sub-detectors 31 clock cycles after the bunch crossing, and needs additional 15 clock cycles until an accept signal is generated from the logical OR of 64 logical trigger slots. Since it can take additional cycles until the accept signal has been propagated, components like the calorimeter keep their signals in data pipelines, which are 58 bunch crossings (5.5 μs) deep. The GFLT is supposed to reduce the rate below 1 kHz.

Accepted events are fully digitised and copied to the second level trigger (SLT), which again is local to most of the components. This step typically takes 30 μs and thus creates $\sim$ 3 % dead time (considering the average GFLT rate of

$\sim$ 1 kHz). On the SLT level, objects like track momenta, the event vertex and calorimeter clusters are reconstructed, permitting a more restrictive trigger decision. The result is sent to the global SLT (GSLT) together with the reconstructed variables for an overall evaluation. Like many of the SLTs, the GSLT is based on a Transputer network. Each Transputer is devoted to a particular task such as general vetoing or the recognition of certain event signature, leading to a further reduction down to the level of 50-100 Hz. For each event that passes the GSLT, the data from the various components are handed over to the event builder (EVB), which is a network of custom made Transputer models with triple-ported memory (TPM). It combines all the data of an event in to a single record of ADAMO [134] database tables. This is the data structure used at all subsequent levels up to the physics analysis programs, and distributes the assembled events over the processor nodes of the third level trigger (TLT).

The TLT is a computer farm of 36 Silicon Graphics (SGI) workstations. Each workstation individually analyses an classifies a single event with a custom version of the offline reconstruction software, which uses the full event information. The accepted event pass the TLT at a rate of $\sim$ 5 Hz with a size of $\sim$ 150 Kb each and are written onto a data summary tape (raw-DST) which is sent to the on-line cluster for monitoring and to the event repository, which is a tape robot in the DESY computing center.

Later, a complete and final reconstruction of the events is performed offline, with filter programs provided by the ZEUS physics groups serving as a fourth level trigger. A preselection bit-pattern is assigned to every event, where each bit is associated with a group of selection criteria. Based on the raw-DST, so called mini-DST are written, which contain the event data in a condensed form and reconstructed objects, e.g. the tracks of scattered electrons found by the offline software. In general these mini-DST are the input files for physics analysis programs, whereas the raw-DSTs are used for background studies and data quality monitoring.

Chapter 3

Physics simulation

The use of simulation programs is essential in physics analyses. In fact, a better understanding of the data and of the detector behaviour can be achieved by simulating the detector response to physics events. Moreover, the theoretical models implemented in the simulations can be tested by comparisons to real data.

The simulation of physics events at HERA is done in two main steps. First, the ep scattering process is simulated using an event generator. This program, following the prescriptions of the theoretical models implemented in it, provides the complete list of the four–momenta of the final state particles. In the second step, all the detector and the trigger system are simulated, in order to determine their response to the particles produced in the physical process.

These simulations are based on Monte Carlo (MC) techniques, which turn out to be an essential tool to understand the complexity of high energy physics processes and of particle detectors.

3.1 General structure of an event generator

The factorisation theorem for hard processes [138] is the main theoretical justification for QCD Monte Carlo event generators. Following the prescriptions of the theorem, an ep scattering process characterized by a hard scale μ can be factorized into the following separate stages (Figure 3.1):

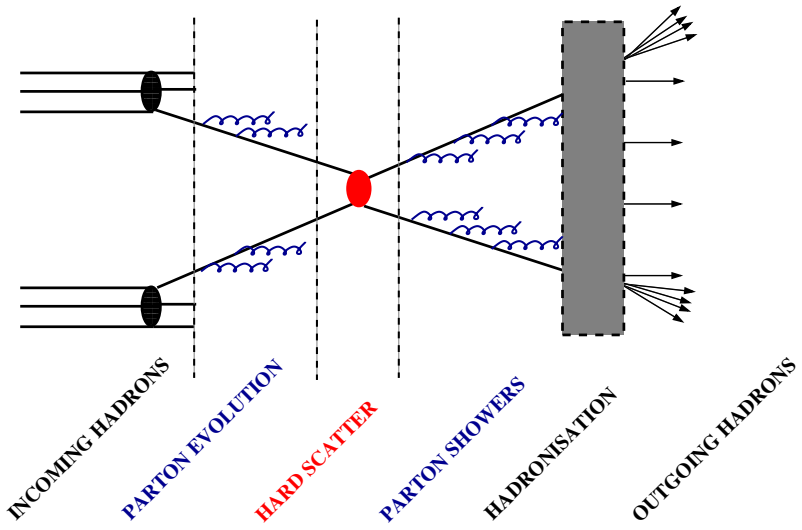

Figure 3.1: *Schematic representation of the processes involved in a typical hard QCD interaction.*

- *hard sub–process*: it is the main feature of the event, the interaction between a parton, extracted from the proton, and the photon, or a photon constituent in resolved photon events. This process can be calculated in a fixed order perturbative expansion since it involves a hard scale μ
- *initial and final state radiation*: in processes involving charged and coloured objects the topology of an event can be strongly influenced by the emission of gluons and photons in the initial or final state. These perturbative corrections are usually modeled by the so called *parton shower* method: the radiation is simulated by an arbitrary number of branchings of one parton into two, like $e \to e\gamma$, $q \to qg$, $q \to q\gamma$, $g \to q\bar{q}$. The kernel $P_{a\to bc}(z)$ of a branching gives the probability distribution of the energy sharing, with daughter b taking a fraction z and daughter c the remaining $)1-z$ of the initial energy E_a. The two daughters may branch in turn, producing other partons, and so on. Via the initial state radiation a parton, constituent of the incident hadron (photon), having low space–like virtuality, radiates time–like partons, increasing its space–like virtual mass. On the other hand, via the final state radiation an outgoing virtual parton with large time–like mass generates a shower of partons having lower virtuality. The shower evolution stops at some fixed scale μ_0, typically of the order of 1 GeV;
- *hadronisation*: it is the process in which colourless hadrons are formed starting from coloured partons. It is a non–perturbative phenomenon and is still not completely understood. Therefore simulation programs model the hadronisation process using phenomenological inputs. The main hadronisation models now available are the cluster model, implemented in the HERWIG Monte Carlo (see Sect. 3.2) and the string model, implemented in the PYTHIA Monte Carlo program (see Sect. 3.3);
- *beam remnant*: in ep interactions, the simulation programs reconstruct the particles that have gone through the initial state radiation and have then generated the partons involved in the hard sub–process. These initial particles, one from each beam, are a parton extracted from the proton and a photon or, in resolved photon processes, a parton from the photon. They carry only a fraction of the initial beam energy, the rest is taken by the beam remnant. If the shower initiator is coloured, also is the beam remnant, that is therefore connected to the rest of the event and has to be fragmented and reconstructed coherently.

3.2 The HERWIG Monte Carlo

The HERWIG (*Hadron Emission Reactions With Interfering Gluons*) [176] Monte Carlo program is a general–purpose particle physics event generator which can simulate lepton–lepton, lepton–hadron and hadron–hadron interactions. It has a relatively small number of free parameters, a large predictive power, and is as independent as possible of non–perturbative parameters.

The initial and final state radiation are factorized as successive branching processes in which the energy fractions are distributed according to the Altarelli–Parisi splitting functions. The full available phase–space is restricted to an angular ordered region, as a result of interference, and leading infrared singularities are correctly kept into account. In the case of final state radiation, at each branching the angle between the two emitted partons is smaller than that of the previous branching.

In the case of initial state radiation, the angular ordering applies to the angle θ_i between the incoming hadron and the emitted partons i. The scale of α_s at each branching is set at the relative transverse momentum of the two emitted partons. In the case of heavy flavour production, the mass of the quark modifies the angular–ordered phase–space so that the soft radiation in the direction of the heavy quark is depleted. The emission within a cone with an opening angle m_Q/E_Q , where m_Q and E_Q are the mass and the energy of the heavy quark, vanishes. This angular screening determines the shape of the heavy flavour jet.

A large variety of electroweak and QCD processes can be simulated using HERWIG. The factorisation scale μ^2 of the hard subprocess is given by:

$$\mu^2 = \frac{2\hat{s}\hat{t}\hat{u}}{\hat{s}^2+\hat{t}^2+\hat{u}^2} \tag{3.1}$$

where $\hat{s}$, $\hat{t}$ and $\hat{u}$ are the Mandelstamm variables. The resulting cross section for light flavour production diverges in the limit $p_T \to 0$, therefore a cut on the minimum transverse momentum of the produced partons has to be applied.

HERWIG uses the Equivalent Photon Approximation (EPA) [135] to generate the spectrum of the photons radiated from the incoming lepton in an ep scattering. The boson–gluon fusion process in heavy flavour production uses the

exact cross section of the process $ep \to Q\bar{Q}X$ as fully computed by Schuler [139]. In the case of resolved photon processes, the program allows at each branching the possibility for a dynamical $\gamma \to q\bar{q}$ anomalous splitting.

In the hadronisation process, three types of non–perturbative contributions have to be considered: the representation of the incoming partons as constituents of the incoming particles, the conversion of the outgoing partons into hadrons, and the description of the soft underlying event due to the presence of spectator partons.

The incoming parton treatment is related to the factorisation theorem of collinear singularities. A phenomenological input structure function describes the distribution of the partons longitudinal momentum fractions, while the transverse momentum distribution is characteristic of the size of the hadron.

Regarding the formation of hadrons from the outgoing partons below the time–like cutoff scale Q_0, perturbative QCD predicts [140] that in hard processes the confinement of partons is local in colour and independent of the hard scale μ. The cluster hadronisation model used in HERWIG is assumed to satisfy these requirements. After the perturbative parton branching process, all the outgoing gluons are splitted non–perturbatively into light (u or d) quark–antiquark or diquark–antidiquark pairs, the splitting into diquarks being suppressed with respect to that into quarks. Quarks are then combined with their nearest neighbours to form colour singlet clusters, whose mass distribution is peaked at low values and falls rapidly for large masses. The clusters formed in this way are fragmented into hadrons following some prescriptions. If a cluster is too light to decay into two hadrons, it is taken to represent the lightest single hadron of its flavour, and its mass is shifted to the right value by an exchange of momentum with a neighbouring cluster. The clusters which are massive enough decay isotropically into pairs of hadrons, following some rules that bring to the formation of an unbiased selection of decay products conserving flavour. The small fraction of clusters having too high masses for isotropic two–body decay are fragmented using an iterative fission model, until the masses of the products are below the fission threshold. The mechanism is not unlike string fragmentation (see Sect. 3.3).

The spectators extracted from the incoming particles in hadron–hadron and lepton–hadron collisions are included into beam clusters. In the formation of those clusters, the colour connection between the spectators and the initial state parton shower is cut by the forced emission of a quark–antiquark pair. In a lepton–hadron collision, the soft underlying event is represented by a soft collision between the beam cluster and the adjacent cluster, produced in the forced emission mentioned above.

3.3 The PYTHIA Monte Carlo

The PYTHIA [55] Monte Carlo is a general–purpose event generator, sharing many common features with HERWIG, but having also some significant differences, in particular in the treatment of the non–perturbative processes. The PYTHIA philosophy, in fact, is to describe also the hadronisation processes in as much detail as possible.

PYTHIA and HERWIG are slightly different also in the description of the hard sub–process. In particular, in photo-production events PYTHIA uses the Weizsäcker and Williams [141] approximation to generate the spectrum of the photons radiated from the incoming lepton, whereas HERWIG uses the equivalent photon approximation. Another difference is the scale of the hard scattering, μ^2; PYTHIA sets μ^2 to the transverse mass of the two outgoing partons, m_T :

$$\mu^2 = \frac{1}{2}(m_3^2 + p_{T3}^2 + m_4^2 + p_{T4}^2) = \frac{1}{2}(m_3^2 + m_4^2) + \frac{\hat{t}\hat{u} - m_3^2 m_4^2}{\hat{s}} \tag{3.2}$$

whereas the scale used by HERWIG is given by the Formula 3.1. The parton shower processes implementation is similar to that of the HERWIG Monte Carlo, but in PYTHIA the parton emissions are ordered only according to the virtuality of the radiated partons. The perturbative parton radiation is stopped at some cut–off scale Q_0^2 , of the order of 1 GeV^2 . The main difference between PYTHIA and HERWIG is the hadronisation model. In PYTHIA fragmentation is performed by the JETSET program [142][143], which implements the string fragmentation or Lund model [144]. The string model is based on the starting assumption of a linear confinement picture. According to this model, the energy stored in the colour dipole field between a charge and an anticharge increases linearly with the separation between the charges. This assumption is supported by lattice QCD studies performed on one of the simplest possible systems, the colour–singlet $q\bar{q}$ 2–jet event. As q and $\bar{q}$ move apart from their common production vertex, the physical picture is that of a colour flux tube, with transverse dimensions of the typical hadronic sizes (1 fm), being stretched between the q and the $\bar{q}$. If the tube is uniform along its length, this leads to a confinement picture with a linearly rising potential. The simplest way to obtain a Lorentz covariant and causal description of the energy flow due to this confinement is

the use of the dynamics of the massless relativistic strings with no transverse degrees of freedom. Coming back to the fragmentation process, as q and $\bar{q}$ move apart the potential energy stored in the string increases, and the string may break producing a new $q'\bar{q}'$ pair. The original system therefore splits into two colour–singlet systems $q\bar{q}'$ and $\bar{q}q'$. Further breakings may occur if the invariant mass of either of these string pieces is large enough. The string break–up process proceeds until only on–mass–shell hadrons remain. In the generation of quark–antiquark pairs from string break–ups quantum mechanical tunneling is used, leading to a flavour–independent Gaussian spectrum for the transverse momentum p_T of the $q'\bar{q}'$ pair. Since the string has no transverse excitation this p_T is locally compensated between the quark and the antiquark of the pair. The p_T of a hadron is made up of the p_T of the quark and antiquark forming it. The tunneling picture also implies a suppression of heavy quark production so that charm and heavier quarks are not expected to be produced in the soft fragmentation, but only in perturbative parton shower branchings $g \to q\bar{q}$. A tunneling mechanism can also be used to explain the production of baryons. The different string breakings are causally disconnected. This means that, for example, starting from a system made up of a quark moving in the $+z$ direction and an antiquark moving in the z direction, the formation of mesons can be described in the following way: by a string break–up, the production of a $q_1\bar{q}_1$ pair brings to the formation of a $q\bar{q}_1$ meson, leaving behind an unpaired quark q_1. A second pair $q_2\bar{q}_2$ may now be produced, to give a new meson with flavours $q_1\bar{q}_2$, etc. This process can be iterated until all energy is used, with some modifications near the q end to make the total energy and momentum consistent. The case of several partons moving apart from a common origin is more complicated. For a $\bar{q}qg$ event, a string is stretched from the q to the $\bar{q}$ end via the gluon, so that the gluon has two string pieces attached. The string fragments into two $\bar{q}q$ pairs, boosted with respect to the centre–of–mass frame of the original $q\bar{q}g$ system, and into one hadron straddling both string pieces.

3.4 The RAPGAP Monte Carlo

The RAPGAP Monte Carlo [149, 150] simulates the deep inelastic scattering as well as the photoproduction regime. In our analysis it will be used for the DIS subsample. Events were generated in our sample with a preselection cut at $Q^2 > 0.6$ GeV. Diffractive contributions are also taken into account. RAPGAP implements initial and final state parton shower and uses the Lund string fragmentation model as PYHTIA does. QED radiative effects, i.e. real photon emission from both the incoming and the scattered electron, can have large effects on the reconstruction of the DIS kinematic variables. These processes are simulated in RAPGAP through the HERACLES package [151, 152]. Both resolved and direct photon processes were included in the simulation. Resolved diagrams in DIS can play a role when the scale μ^2 of the hard subprocess is larger than Q^2, the inverse size of the photon.

3.5 The detector simulation

All the event generators supported in ZEUS, like PYTHIA and HERWIG, are gathered in a software program called AMADEUS. The user can choose the event generator, which gives as output all the four–momenta of the particles produced in the hard scattering process and all the relevant kinematic variables. The data produced by an event generator are the input to the ZEUS detector and trigger simulation program, MOZART[1] [145]. MOZART is based on the GEANT [146] package, whose kernel contains a description of all the detector components, including the material they are made of, their shapes and positions. The program traces the particles through the whole detector, simulating its response and keeping into account physics processes such as energy loss, multiple scattering and particle decays in flight. The events pass then through the CZAR [2] [147] package, that simulates the trigger logic as implemented in the data taking. As a final step, the generated sample is processed by the ZEUS reconstruction program, ZEPHYR[3]. This program reconstructs the event variables, like particle momenta and energies, treating the data and the Monte Carlo in the same way. All the information coming from the different detectors making up ZEUS are taken as inputs by ZEPHYR. All the ZEUS data are organized using the ADAMO [4] [148] data management system, used for the data storage in memory or on external media and for their documentation. The access to the data by the users is done with the EAZE program; the LAZE program generates bi–dimensional graphical representation of the real or simulated events. A diagram of the ZEUS reconstruction scheme for data and Monte Carlo is shown in Figure 3.2

[1] MOnte Carlo for Zeus Analysis Reconstruction and Triggering.
[2] Complete Zgana Analysis Routine.
[3] ZEus PHYsics Reconstruction.
[4] Aleph DAta MOdel.

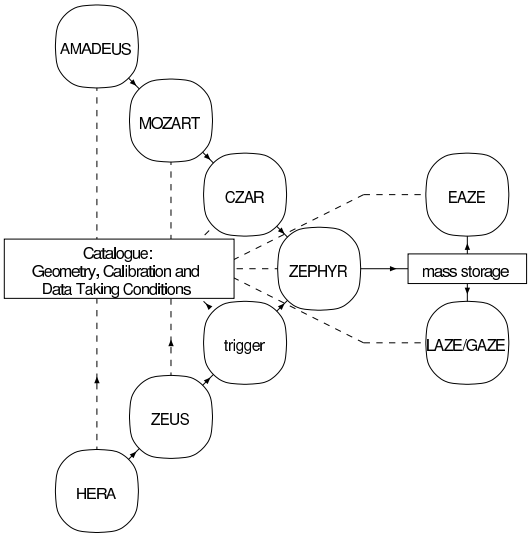

Figure 3.2: *A schematic diagram of ZEUS data and Monte Carlo reconstruction chain.*

3.6 Monte Carlo samples used for the analysis

In this Section, a brief description of the Monte Carlo samples generated for the simulation of the data used in this work will be given. Due to the fact that the HERA centre–of–mass energy was changed in 1998 from $\sim$ 300 to $\sim$ 320 GeV, and to account for small modifications of the detector and the trigger logic, different Monte Carlo samples were generated for the various years of data taking proportionally to the relative luminosity of the homogeneous data samples. The statistic significance of the employed Monte Carlo samples is expressed in terms of the *equivalent luminosity* $\mathcal{L}$. This quantity is the ratio between the total number of generated events before any preselection normalised over the cross section of the process. These values are summarised in Table 3.1 for the beauty and charm Monte Carlo used in the analysis.

The central Monte Carlo used in this analysis (general D–meson Monte Carlo) has been particularly tuned to have a realistic description of $f(c \to D^{*+})$ and other hadronisation fractions. Relevant masses, widths, life times and branchings have been set to the measured values. In particular the relative yield of D mesons with different spins and angular momenta was tuned (for example the P_V parameter ruling the relative probability to form a D^0 or a D^* meson). The events were generated with no requirements on the presence of muons. The presence of interesting D mesons was required with p_T thresholds which were chosen differently depending on the decay modes according to the following Table:

Mode	p_T *cut*
$D^{*+} \to (D^0 \to K^-\pi^+)\pi_s^+$	$p_T(D^{*+}) > 1.25$ GeV
$D^{*+} \to (K_s^0\pi^+\pi^-)\pi_s^+$	$p_T(D^{*+}) > 1.35$ GeV
$D^{*+} \to (D^0 \to K^-\pi^+\pi^-\pi^+)\pi_s^+$	$p_T(D^{*+}) > 2.3$ GeV
$D^0 \to K^-\pi^+$	$p_T(D^0) > 2.6$ GeV
$D_s^+ \to (\phi \to K^+K^-)\pi^+$	$p_T(D_s^+) > 1.7$ GeV
$D^+ \to (\phi \to K^+K^-)\pi^+$	$p_T(D^+) > 1.7$ GeV
$D^+ \to K\pi\pi$	$p_T(D^+) > 2.8$ GeV
$\Lambda_c^+ \to Kp\pi$	$p_T(\Lambda_c^+) > 2.8$ GeV

In addition a selection of main non–flat backgrounds was performed. These are backgrounds which arise from other decay modes of the same D–mesons and "similar" decay modes of other D–mesons. This preselection is compliant with the minimal requirement which are required in each mode in order to be reconstructed and the cuts at trigger level.

The CTEQ5L and GRV-G LO parton densities were used for the proton and photon respectively (from PDFLIB 8.04 [153]).

Charm and beauty hadrons were decayed at generator level (AMADEUS 2.03) while long-life strange hadrons were kept as stable to be tracked and decayed in the detector simulation package MOZART. The same is true for neutral pions.

3.6.1 Beauty events simulation

The production of beauty quarks in an event proceeds through different sub–processes. The main contribution to the cross section is given by the direct photon process, which at LO reduces to the boson–gluon fusion: $\gamma g \rightarrow Q\bar{Q}$. Other lower but still significant contributions to the cross section come from resolved photon processes. Other processes leading to the production of beauty quarks are the beauty excitation phenomena, in which a beauty quark is extracted from the photon or from the proton. Monte Carlo samples simulating all these sub–process have been generated. The beauty events generated by PYTHIA have been used to determine the central values of the cross sections, whereas beauty samples generated by HERWIG have been used to determine the systematic uncertainties, mainly related to the different hadronisation models used by the two generators. The sub–processes simulated in the PYTHIA sample were:

- b in direct γ: $\gamma g \rightarrow b\bar{b}$
- b in resolved γ: $q\bar{q} \rightarrow b\bar{b}$, $gg \rightarrow b\bar{b}$
- b excitation γ: $bq \rightarrow bq$, $bg \rightarrow bg$
- b excitation in p: $b\gamma \rightarrow b\gamma$, $bg \rightarrow bg$, $bq \rightarrow bq$, $b\bar{b} \rightarrow b\bar{b}$

The Feynman diagrams for these processes have already been presented in Section 1.3.4. The relative contributions of the processes given above are predicted to be 71 %, 12 %, 16 %, 1 % respectively.

In the case of beauty excitation in the proton, both direct and resolved processes are involved. Two samples were generated using the HERWIG Monte Carlo, one simulating all the direct γ processes (boson–gluon fusion, direct processes of beauty excitation in the proton) the other including all the resolved photon processes (qq and gg interactions, and beauty excitation in the photon). The relative importance of direct and resolved component is estimated in HERWIG to be 80% and 20% respectively. In the event generation, the b–quark mass was set to $m_b = 4.5$ GeV.

3.6.2 Charm events simulation

Monte Carlo samples simulating charm photoproduction have been generated using PYTHIA. The production mechanisms of $c\bar{c}$ quark pairs are identical to those of $b\bar{b}$. Charm excitation in the photon and in the proton gives indeed a relatively higher contribution to the cross section. Resolved processes are in fact more important for lower masses of the produced quarks. The relative importance of charm in direct γ, charm in resolved γ, charm in γ and p are 46 %, 4 %, 31 %, 18 % respectively. In the event generation the mass of the c quark was set to $m_c = 1.35$ GeV.

Monte Carlo	$\mathcal{L}$ (pb^{-1})
PYTHIA 6.156	515
HERWIG 6.301	1250
RAPGAP 2.08/18	619

Table 3.1: *Equivalent luminosities of the beauty and charm Monte Carlo samples for the year 1996-2000 used in the analysis.*

Chapter 4

Event selection and reconstruction

In this Chapter we will describe the various steps which led us to our final data sample. The aim was to select, in an efficient manner, events with a D^* and a muon in the final state. In Section 4.1 we will illustrate the employed trigger logic and present some studies on the time stability of the selection. Section 4.2 is dedicated to the reconstruction of the kinematic variables y and Q^2 and to the separation of the deep inelastic and photoproduction samples. Sections 4.3 and 4.4 will deal with the offline D^* and μ reconstruction algorithms, respectively. Section 4.5 summarises the final cuts for our D^* μ sample. A series of Monte Carlo studies on resolutions on important variables will close the Chapter (Section 4.6).

4.1 Data selection at trigger level

The whole data sample collected by the experiment in the years is quite large. For this reason in practice one needs to run the analysis on a subsample which has to be of a reasonable size in order to be used efficiently. A very effective way of preselecting data is provided by the ZES [154][155] tool. It consists in a relational database written in C++ collecting all the events and a quite large set of variables associated to each event. It is possible to provide an arbitrarily complex combination of requirements on the available variables (*predicate string selection*) thus selecting only a set of interesting events on which the user code will be run.

In our case we required the presence of at least one $D^* \rightarrow (K\pi)\pi_s$ or $D^* \rightarrow (K\pi\pi\pi)\pi_s$ candidate[1] in the event. The code defining these candidates is the same which will be used in the final analysis. The muon matching code was subsequently run on this sample of data. Only events with at least a muon candidate were finally stored.

In this work we analyse the data collected by ZEUS detector in the year from 1996 to 2000. This final sample was depurated by all those runs which did not fulfill the standard ZEUS or BRMUON data quality [156] requirements. The integrated luminosity corresponding to this sample amounts to 114 ± 2 pb^{-1} [157].

4.1.1 Description of the trigger selection

A proper trigger logic was chosen in order to maximize the number of final events. The characteristics of the events we are interested in is such that a redundancy of triggers is available based on the presence of both the μ and D^* (and the scattered electron in the case of deep inelastic scattering events, e'). We built a "trigger branch" by requiring the presence in the event of a trigger signal consistently at each level of the ZEUS trigger scheme: FLT, SLT and TLT (see Section 2.5.1) . The global trigger logic on the basis of which the event is kept or rejected is an "*or*" of the following five branches:

[1] Predicate string selection example for the $K\pi$ channel: $ZeusIO - Variable\ ((Kpi_pt > 1.5) and (Kpi_eta < 1.5) and (Kpi_eta > -1.5))$

branch	*description*	*FLT*		*SLT*		*TLT*
1	*isolated inner* μ	10 *or* 11	*and*	MUO1	*and*	MUO3
2	*non–isolated outer* μ	14 *or* 15	*and*	MUO2	*and*	GLOEXO
3	*"old"* D^* *chain*	42	*and*	HPP1	*and*	HFL10 (11)
4	*"new"* D^* *chain*	42 *or* 59	*and*	HFL1	*and*	HFL10 (11)
5	*DIS chain*					(DIS03 *and* DSTbit 14) *or* DIS27

4.1.1.1 Muon chain

The muon trigger chains used in the analysis are here schematically written:

1 : (FLT 10 *or* FLT 11) *and* SLT MUO1 *and* TLT MUO3

2 : (FLT 14 *or* FLT 15) *and* SLT MUO2 *and* TLT GLOEXO

The first chain triggers on muons detected by the inner muon chambers. It imposes loose isolation criteria at the first level by requiring a rough coincidence between a muon signal in the chambers and a deposit in the calorimeter with a minimum ionizing particle (*m.i.p.*) topology. The second chain is instead suited for non isolated higher momentum muons reaching the outer chambers. We will now go a little more into the detail of what each single trigger slot means in terms of physics requirements.

FLT 10 and FLT 11

These slots were designed to keep events with at least one isolated track reaching any of the barrel inner muon chambers BMUI (FLT 10) or rear inner muon chambers RMUI (FLT 11). The isolation requirement is done by associating to the track a muon-like energy deposit in the CAL: rather compact and not too high. The logic is based on coincidence matrices whose positive response ensures the observed pattern in the calorimeter and inner muon chambers to be consistent with the crossing of a charged particle with muon characteristic energy deposit.

Additional requirements implicit in this slot are: a minimal CTD activity, corresponding roughly to at least one track coming from the interaction point and the absence of veto signals from the C5 counter, the Veto Wall inner and outer planes, the CTD and SRTD.

FLT 14 and FLT 15

These slots (FLT 14 for the barrel and FLT15 for the rear) are similar to the previous ones (FLT 10 and 11) but they require a pattern of hit wires and strips present in both B(R)MUI and B(R)MUO chambers being consistent with a track pointing towards the volume defined by the inner tracking detectors. Furthermore a minimal CTD activity, and the absence of veto signals from the C5 counter and CTD are required. In this case the isolation requirement has been dropped. The only request is the presence in any calorimeter tower of at least 464 MeV deposit (this is the minimal measurable energy due to the discretisation of the electronics read-out). In the case of FLT 15 this requirement is restricted to the rear calorimeter towers.

SLT MUO1 and MUO2

The SLT branch MUO1 selects only events coming from FLT slots 10, 11 and 8 (designed to trigger on elastic dimuons). Two additional requirements are then applied:

- the timing of any significant energy deposit in BCAL is required to be consistent with the nominal bunch crossing time. More precisely if more than one photomultiplier (PMT) fires and the total energy is above 1 GeV, then the energy weighted mean of all the PMT timings has to be less than 10 ns from the closest bunch crossing. If only one PMT fires or the energy is less than 1 GeV the event is kept anyway.
- p_z/E, where $p_z = \sum_i E_i \cos\theta_i$ and $E = \sum_i E_i$ (E_i and θ_i being the energy and polar angle of the geometric centre of the i–th CAL cell above threshold), is required to be less than 0.96. This cut removes mainly halo–muon events [2] and proton beam gas collisions.

[2] These events are characterised by high momentum muons traveling horizontally, in the beam-line direction. They originate in the interactions of protons with residual molecules in the beam pipe very upstream of the detector.

The SLT branch MUO2 selects only events coming from FLT slots 14 and 15. Due to the much lower rate of these slots (with respect to 10, 11, 8) only the additional requirement of a good BCAL timing, as explained above, was applied.

TLT MUO3 and GLOEXO

These physics filters at the third level trigger fire in presence of a matching between a reconstructed segment in the inner muon chambers and a vertex track in the central drift chamber. The matching parameter includes the angles between the segment and the linear extrapolation of the CTD track to the inner surface of the calorimeter, as well as the angle between the extrapolated track an the segment linking the BRMUI hits with the end of the track swim. In the case of the GLOMU filter the matching also requires the presence of a m.i.p. deposit in the calorimeter. Its position is included in the evaluation of the matching parameter. Track candidates are preselected requiring a minimal (transverse) momentum of 1 GeV in the (Barrel) Rear region and a polar angle $\theta > 20°$. In order to discard cosmics only track helices whose distance of closest approach to the vertex is $D_H < 10$ cm and having $z_H < 15$ cm are considered. The GLOEXO filter, which was designed for exotic searches, differs from GLOMU since it drops the m.i.p. requirement in the matching and uses a tighter preselection of inner tracks requiring $p_T > 5$ GeV. Further details can be found in Reference [158].

4.1.1.2 D^* chain

The D^* trigger chains used in the analysis are composed according to the following logic:

3 : FLT 42 *and* SLT HPP1 *and* TLT HFL10

4 : (FLT 42 *or* FLT 59) *and* SLT HFL1 *and* TLT HFL10

As we did for muons we will describe the physical cuts implied by this trigger choice.

FLT 42 and 59

In the first level trigger the calorimeter cells are combined to define regional and global sums which are required to exceed some thresholds. The FLT42 slot requires:

$$\begin{gathered}(E > 15 \text{ GeV } \textit{and } (\ E^{RCAL}_{emc} > 10 \text{ GeV } \textit{or } E^{BCAL}_{emc} > 3.5 \text{ GeV})) \\ \textit{or} \\ (E > 2 \text{ GeV } \textit{and } E_{FCAL}/E < 0.65)\end{gathered}$$

In addition, at least one CTD track coming from the ep interaction region is required. Events with timing measured by the veto counters, inconsistent with an ep interaction, are removed. The FLT59 slot is similar to FLT42 but uses different energy thresholds:

$$\begin{gathered}(E > 2 \text{ GeV } \textit{and } (\ E^{RCAL}_{emc} > 0.5 \text{ GeV } \textit{or } E^{BCAL}_{emc} > 2 \text{ GeV})) \\ \textit{or} \\ (E > 8 \text{ GeV } \textit{and } E_{FCAL}/E < 0.65)\end{gathered}$$

SLT HPP1 and HFL1

In the second level trigger beam-gas events are rejected by exploiting the excellent timing resolution of the calorimeter. Also events are rejected in which the vertex determined by the CTD was not compatible with the nominal ep interaction region. The HFL1 in particular consists of the following requirements:

- FLT 42 *or* FLT 59
- $E - p_z > 7$ GeV
- $E_T > 6$ GeV (calculated excluding the two inner rings of FCAL)

- $p_z/E < 0.96$
- number of vertex tracks ≥ 3 and number of found tracks ≥ 5
- number of found tracks ≥ 16 *or* sum of two highest–p_T tracks > 1.2 GeV

while the HPP1 requirements are:

- FLT: 40 *or* 41 *or* 42 *or* 43
- at least one good track
- $E - p_z > 8$ GeV
- $E_T > 8$ GeV (calculated excluding a box around the beam–pipe in FCAL)
- $E - p_z > 12$ GeV *or* $p_z/E < 0.95$

TLT HFL 10 ($D^* \to (K\pi)\pi$) and TLT HFL 11 ($D^* \to (K\pi\pi\pi)\pi$)

At the third level trigger (TLT) the full event information is available and a full D^* reconstruction algorithm similar to the one used in the offline environment is run. Calorimeter timing cuts are tightened for further rejection of the remaining beam-gas events.

The HFL 10 TLT filter requires:

- $|z_{vtx}| < 50$ cm
- $3 < N_{trks} < 100$
- $p_T(K), (\pi), (\pi_s) > 0.35,\ 0.4,\ 0.1$ GeV
- $p_T(D^*) > 1.8$ GeV
- $1.4 < m_{D^0} < 2.2$ GeV
- $\Delta m < 0.17$ GeV

HFL11 is the analogous of HFL10 for the channel $D^* \to (K\pi\pi\pi)\pi_s$. The cuts are the same as for HFL10 except for:

- $5 < N_{trks} < 100$
- $p_T(\pi_s) > 0.15$ GeV
- $m_{D^0} < 2.2$ GeV
- $\Delta m < 0.16$ GeV
- $p_T(D^*) > 3.6$ GeV

In the deep inelastic scattering regime the cuts on the D^* transverse momentum are lowered to $p_T(D^*) > 1.35$ GeV and $p_T(D^*) > 2.8$ in the case of HFL10 ($D^* \to K\pi$) and HFL11 ($D^* \to K3\pi$) respectively. The DIS requirements include a $E - p_z$ of the event above 30 GeV and a candidate electron found by at least one electron finder algorithm having $E_e > 4$ GeV and hitting the RCAL calorimeter outside of a 6×12 cm fiducial region around the beam axis.

4.1.1.3 DIS chain

The cuts performed by the various filters are in this case similar to those already described in the previous paragraph. Electron finder algorithms are run at the third level trigger and at least a candidate with energy greater than 4–5 GeV is required. Other cuts involve the calorimeter energy and $E - p_z$ of the event which has to be typically above 30–35 GeV. Furthermore electrons hitting the RCAL in a rectangle around the beam pipe are rejected since in this region the electron could not be reconstructed properly due to imperfect containment of the electromagnetic shower.

We have verified that the trigger logic so far described is able to trigger on almost the totality of the events selected inclusively, i.e. with all the final analysis cuts except for trigger requirements.

The importance of each of the defined branches is shown in Figure 4.1 for an event selection close to the final one which we will adopt. The results for both data (bullets) and Monte Carlo (hatched histograms) are presented in the $K\pi$ mode. The Monte Carlo reproduces the relative importance of each trigger branch as it is found in the data.

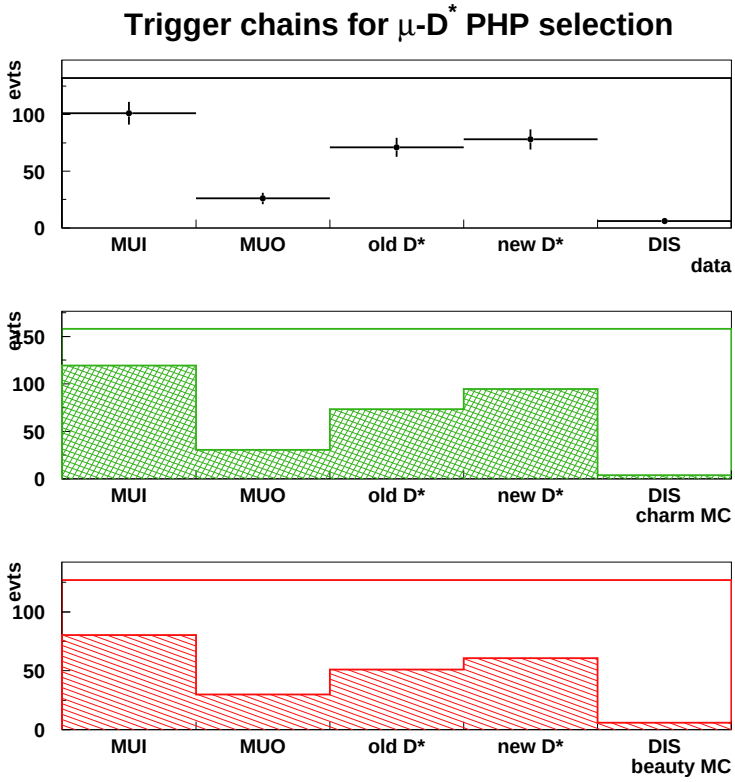

Figure 4.1: *Trigger chain distribution for the photoproduction selection in data (bullets), charm Monte Carlo (middle histogram) and beauty Monte Carlo (bottom histogram).*

4.1.2 Time stability of the selection

In order to check the time stability of the previously described data selection and the accuracy of our Monte Carlo in describing the data we subdivided our preselected data sample in smaller subsamples by choosing run intervals in such a way that each subsample had a comparable integrated luminosity of about 1 pb^{-1}. Each interval contains then homogeneous data, recorded in more or less the same data taking period. For each trigger requirement under test we divided the number of events satisfying the trigger over the interval luminosity. We expect the rate of events over luminosity to be constant apart from changes in the definition of the trigger which are documented and, in principle, reproduced by the Monte Carlo. Degradation in the efficiency of the detector components could in principle also play a role.

To have a visual impression of whether or not the Monte Carlo describes the rates in different years we roughly ordered the files according to the data taking periods and repeated the procedure. Instead of dividing by the luminosity in this case we took the ratio on all the simulated events with a proper normalisation factor. This procedure is somewhat approximate since in between each Monte Carlo file events are not chronologically order so that only the information averaged over each period is meaningful.

The rate of selected events normalised to the luminosity in each interval is plotted against the interval number in Figures 4.2 and 4.3 for data and Monte Carlo respectively. Since the intervals are ordered with increasing time this plot shows the evolution of the selection power imposed by the trigger requirements. The trigger branches which were previously discussed are treated separately in each plot and the global *or* is also shown (labeled "total"). They are named according to the convention set in the Table of Section 4.1.1. The data pattern is shown with bullets while the Monte Carlo pattern is visualised as the filled histogram.

The rates of the inner and outer muon branches (1,2) are reasonably flat. This indicate that the muon chamber performance was stable during the four years of data taking. The same is true for the first D^* trigger chain except for an

increase in the rate from 1998 onward (3). The second D^* branch exhibits this change even more markedly. These are due to changes in the energy thresholds. The DIS (5) also shows some structures while the "total" chain, defined by the *or* of the previous ones, is flat to a good approximation. The Monte Carlo is in general able to reproduce the major features which are observed in the data.

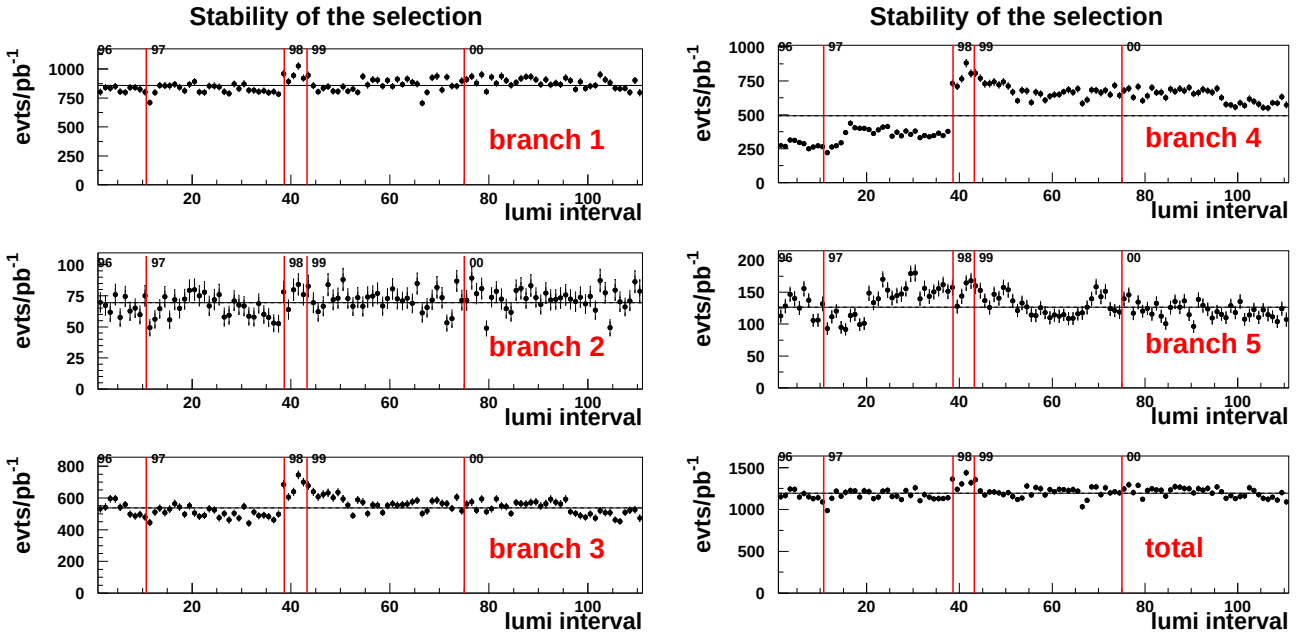

Figure 4.2: *Check on the stability of the trigger selection with time. For each interval in integrated luminosity ($\sim$ 1 pb^{-1}) the ratio between the number of selected data events and the luminosity of the interval is plotted (bullets).*

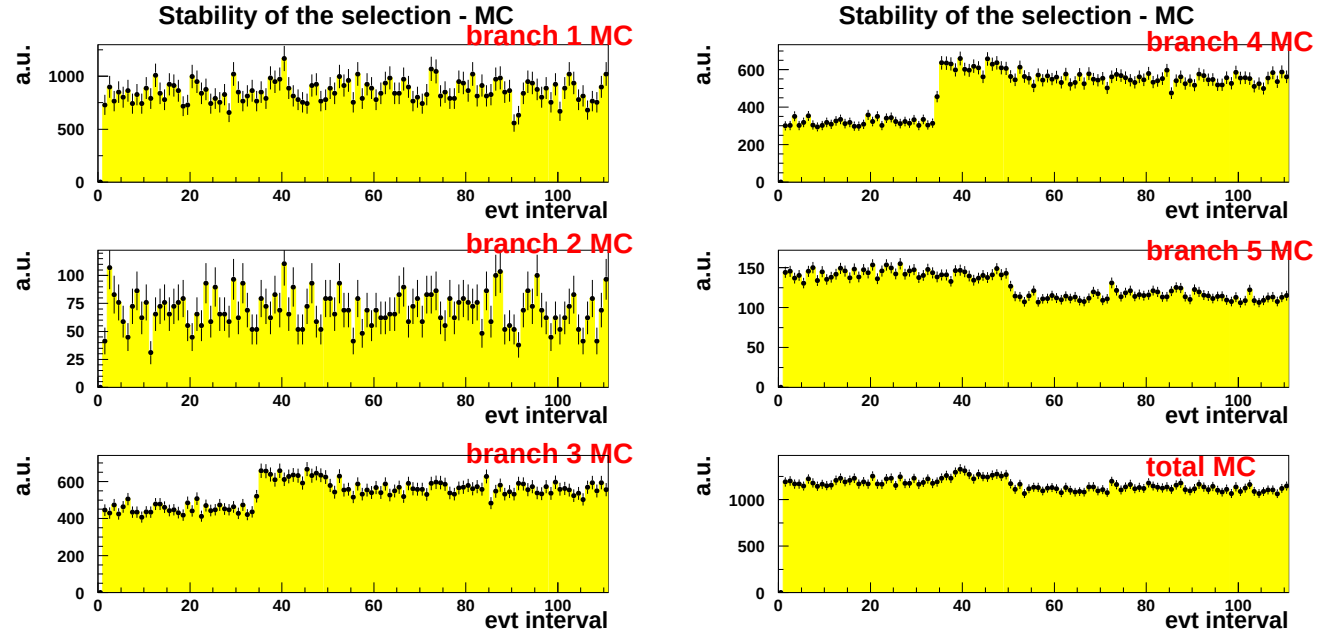

Figure 4.3: *The filled histogram shows the fraction of selected events over the number of analysed events for a beauty DIS Monte Carlo with an arbitrary normalisation factor.*

4.2 Separation of deep inelastic scattering and photoproduction events

4.2.1 y and Q^2 reconstruction

Several reconstruction techniques exist for the inelasticity y and the square of the momentum transfer at the leptonic vertex Q^2. We will illustrate those which will be used in this analysis.

4.2.1.1 The electron method

If the energy and direction of the scattered electron are measured in the main calorimeter, the y and Q^2 of the event can be easily reconstructed by applying the definitions given in Section 1.1:

$$y_e = 1 - \frac{E'_e}{2E_e}(1 - \cos\theta_e) \tag{4.1}$$

$$Q^2_e = 2E_e E'_e(1 + \cos\theta_e) \tag{4.2}$$

where we indicate with E_e and E'_e the energies of the incoming and scattered electron respectively and with θ_e the polar angle of the scattered electron in the ZEUS frame.

In the case of photoproduction events, where the momentum transfer is low, the electron almost keeps its original direction unaltered ($\cos\theta_e \approx -1$). With this approximation it becomes clear from Equation 4.1 that the y variable can be interpreted as the fraction of the electron energy transferred to the photon.

$$y \approx \frac{E_e - E'_e}{E_e} = \frac{E_\gamma}{E_e}$$

4.2.1.2 The Jacquet-Blondel method

The so–called Jacquet-Blondel [47] method allows the measurement of the y of the event from the characteristics of the hadronic final state. It is applied in photoproduction when the interacting electron is undetected being scattered at low angle down into the beam pipe. The difference between the energy (E) and the longitudinal momentum (p_z) summed over all the final state particles, is barely sensible to the fact that the detector is not completely hermetic:

$$\delta = \sum_f (E_f - p_{z,f}) \tag{4.3}$$

By introducing the p_z term the contribution arising from the unmeasured particles escaping in the beam–pipe (*proton remnant*) is strongly reduced. The δ quantity is expected to be, with a good approximation, within the experimental error a conserved quantity:

$$\sum_f (E_f - p_{z,f}) = \sum_f E_f(1 - \cos\theta_f) \approx \sum_{i=e,p} E_i(1 - \cos\theta_i) = 2E_e \tag{4.4}$$

The f and i indexes run respectively on final and initial state particles. The estimator of y in the Jacquet–Blondel method is defined as:

$$y_{JB} = \frac{\sum_{f\neq e}(E_f - p_{z,f})}{2E_e} \tag{4.5}$$

If the scattered electron is included in the sum it follows from 4.4 that $y_{JB} \simeq 1$ while if it is not measured the y_{JB} variable provides an estimate of the y of the event. This becomes evident if we rearrange Equation 4.4 in the following way:

$$\sum_{f\neq e}(E_f - p_{z,f}) + E'_e(1 - \cos\theta_e) = 2E_e \tag{4.6}$$

$$\frac{\sum_{f\neq e}(E_f - p_{z,f})}{2E_e} = 1 - \frac{E'_e}{2E_e}(1 - \cos\theta_e) = y_e \tag{4.7}$$

4.2.2 Definition of deep inelastic scattering and photoproduction events

In the present analysis the following cuts are applied to select a sample of neutral current DIS events:

- A well reconstructed vertex reconstructed from the central drift chamber's tracks having a Z coordinate within ± 50 cm from the nominal interaction point.
- $40 < (E - p_z)_{cal} < 65$ GeV. As discussed previously in this Section for well contained DIS events $\delta = 2E_2 = 2 \cdot 27.52$ GeV (*kinematic peak events*). The lower cut rejects photoproduction while the upper cut is introduced to remove residual cosmic ray background.
- At least one electron candidate found by the SINISTRA [159] electron finder algorithm with probability $\mathcal{P} > 0.9$.
- To ensure high purity the electron candidate is required to have an energy $E_e > 10$ GeV.
- $Q^2_{el} > 2$ GeV^2. In this region the acceptance and reconstruction is well under control.
- $y_{el} < 0.7$. DIS events have a distribution in y behaving like y^{-2}. Events with $y_{el} > 0.7$ are mostly photoproduction events with electromagnetic activity from neutral pions.
- $y_{JB} > 0.05$. This cut requires the presence of a minimal hadronic activity.
- In addition a fiducial cut is applied to the electron position. When the scattered electron hits the RCAL surface too close to the detector edge the electromagnetic shower is not fully contained in the active volume of the calorimeter. As a consequence, the measured energy of these electrons is systematically lower than the true one. Events are therefore rejected if the position of the scattered electron at the RCAL surface is contained in a box defined by $|x_e| < 13$ cm and $|y_e| < 7$ cm where the response is uniform.
- When the SRTD position was not available the calorimeter information has been used. In this case, if the scattered electron is reconstructed in the RCAL towers surrounding the beam pipe hole. For these hits the y-position is not correctly reconstructed by the calorimeter and it is always equal to the middle point of the cell.

Photoproduction was selected by requiring the absence of a good DIS candidate according to the above defined cuts an that

$$(E - p_Z)_{cal} < 34 \text{ GeV} \sim y_{JB} < 0.62 \tag{4.8}$$

In this way DIS events populating the kinematic peak are efficiently rejected. As it can be seen from the upper Left plot in Figure 4.13 that the imposed cut is equivalent to a cut at $y_{true} \simeq 0.85$.

4.3 D^* reconstruction

Both for photoproduction and DIS events, two different decay chains of the $D^{*\pm}$ meson have been used

$$D^{*+} \to D^0 \pi_s^+ \to (K^- \pi^+) \pi_s^+ \qquad (K\pi \quad \textit{mode}) \tag{4.9}$$

$$D^{*+} \to D^0 \pi_s^+ \to (K^- \pi^+ \pi^+ \pi^+) \pi_s^+ \qquad (K3\pi \quad \textit{mode}) \tag{4.10}$$

to reconstruct the produced D^* from their decay products. Use of the mass difference technique has been made [160], which is based on the small difference between the D^* and D^0 masses ($m(D^*) - m(D^0) = 145.421 \pm 0.010$ MeV according to [161]). The mass difference is just above the pion mass and thus the phase space available for combinatorial background is severely limited. The pion coming from the D^* decay has 40 MeV in the D^* rest frame, and is therefore denoted as "slow (soft) pion" (π_s).

The used algorithm [162] combines the reconstructed tracks in each event to form D^* candidates assuming the decay channels $D^* \to (K\pi)\pi$ or $D^* \to (K\pi\pi\pi)\pi$. The following requirements have been applied to all particles entering these combinations.

- the track must be associated to the reconstructed event vertex
- tracks are demanded to extend at least up to superlayer 3.
- the track must be in the pseudorapidity region $|\eta| < 1.75$, which corresponds to a polar angle in the range $20^\circ < \theta < 160^\circ$
- it must have a transverse momentum above 200 MeV.

4.3.1 $D^* \to (K\pi)\pi$ channel

At least three tracks with the previous properties are required. Each track with $p_T > 0.35$ GeV is assigned the kaon mass and is then combined with all other tracks with $p_T > 0.35$ GeV. For each pair the invariant mass is calculated assuming the other track to be a pion. No particle identification is used, so kaon and pion masses were assumed in turn for each particle in the pair. Each pair with an invariant mass between 1.4 and 2.2 GeV is considered as a D^0 (or $\overline{D^0}$) candidate. To each one of these candidate track pairs a third track is combined, the so–called slow pion, π_s. The sign of the third track is required to be opposite to the kaon one. In this way the following combinations are rejected: $((K\pi)\pi_s)$: $((++)+)$, $((--)-)$, $((+-)+)$, $((-+)-)$ and only the combinations in which the sum of charges equals ± 1 are retained. These are in indeed not allowed in the Cabibbo favoured channels:

$$D^{*+} \to D^0 \to (K^-\pi^+)\pi_s^+$$

$$D^{*-} \to \overline{D^0} \to (K^+\pi^-)\pi_s^-$$

for which the sign of the slow pion (= the sign of the D^*) is always opposite to the one of the kaon. If the difference between the pair and pair+slow pion track ($\Delta m = m(K\pi\pi_s) - m(K\pi)$) is less than 0.17 GeV or if it is less than 0.15 GeV and the the pair mass is between 1.78 and 1.95 GeV than the three tracks are considered to be a D^* candidate. Combinations in which the D^0 tracks have the same sign and the D^* has charge ± 1 are kept as a separate sample (*wrong charge* combinations). This sample proves to be useful in order to simulate the combinatorial background contribution to the signal peak. The preselected D^*s are then required to have $p_T > 1.5$ GeV and $|\eta| < 1.5$.

4.3.2 $D^* \to (K\pi\pi\pi)\pi$ channel

At least five preselected tracks are required. A first loop on all tracks having a $p_T > 0.18$ GeV is performed. These tracks are assigned the kaon mass and combined to all tracks having $p_T > 0.18$ GeV which are assigned the pion mass. The pairs having an invariant mass lower than $2.2\ \mathrm{GeV} - 2\mathrm{m}_\pi$ are further associated as pions with the other remaining tracks with $p_T > 0.18$ GeV. If the 3–track invariant mass is lower than $2.2\ \mathrm{GeV} - 3\mathrm{m}_\pi$ another track with $p_T > 0.18$ GeV is combined (with pion mass assignment). At this stage combinations with 4 positive $(++++)$ or 4 negative $(----)$ charges are rejected. These combinations are required to have an invariant mass between 1.4 and 2.2 GeV to be considered a $D^0 \to K\pi\pi\pi$ ($\overline{D^0}$ candidate). The soft pion track is then associated. Only D^* candidate combinations having charge ± 1 are kept at this stage. Combinations in which the D^0 has zero charge and the kaon and π_s have the same sign are rejected. If the $\Delta m = m(K\pi\pi\pi\pi_s) - m(K\pi\pi\pi)$ is less than 0.165 GeV or if it is less than 0.15 GeV and the the pair mass is between 1.68 and 2.05 GeV than the five tracks are considered to be a D^* candidate. The preselected D^*s are then required to have $p_T > 3$ GeV and $|\eta| < 1.5$. The wrong charge sample is built by considering the combinations with a total charge of ± 2 for the reconstructed D^0 candidate and ± 1 for the D^* candidate.

4.3.3 Kinematical correlations and background studies

The kinematical correlations existing between the reconstructed D^* meson and the decay products ("daughter tracks") are shown in Figure 4.4. The slow pion and D^* directions are highly correlated as well as for their transverse momenta. This is due to the fact that, because of the limited phase space, the slow pion is produced almost at rest in the D^* rest frame. This behaviour is even more strongly present when the D^* has higher transverse momentum as in the case of the $K3\pi$ mode (Right side plots). The correlation with the D^0 decay products is less marked.

The combinatorial D^* background is known to be efficiently suppressed by cutting on the transverse momentum of the D^* meson. This is due to the fact that tracks from the decay of a real D^* have on average higher transverse momentum than random tracks which happen to fall in the signal invariant mass region. Another, correlated variable which helps in reducing the combinatorial background is the ratio of the transverse D^* momentum and the total transverse energy of the event as measured by the main calorimeter. We have studied how the signal/background ratio varies for different cuts on the slow pion p_T[3] and $p_T^{D^*}/E_T$. In Figure 4.5 the Δm distributions obtained for different set of cuts on real data are shown. The wrong charge D^* sample is presented as the hatched histogram. It nicely reproduce the the right charge (bullets) combinatorial background. The first lower plot shows the dependence of the number of signal and

[3] As we have seen a cut on this variable is an effective cut on the D^* p_T

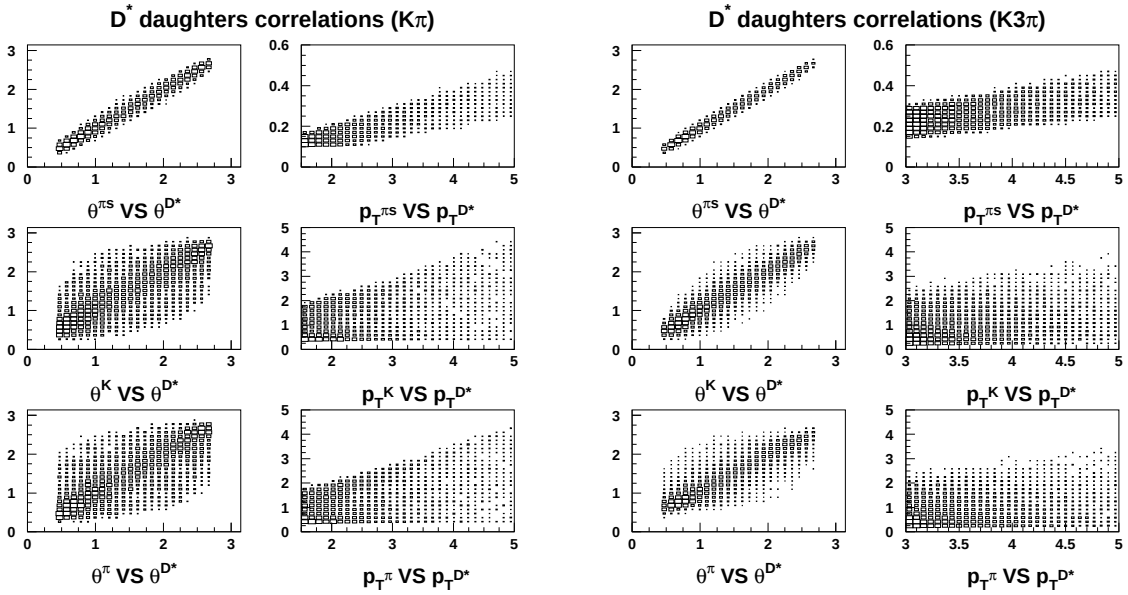

Figure 4.4: **Left***: Correlation plots between the p_T and θ of the D^* reconstructed in the $K\pi\pi$ mode and the daughter π_s, K, π tracks (from top to bottom).* **Right***: the same for D^* decaying in the $K3\pi$ channel. A beauty DIS Monte Carlo has been used.*

combinatorial candidates in the signal region as the cuts are varied while the bottom one displays the trend of the signal/background ratio under the peak. This ratio is rapidly enhanced as the cuts are tightened, especially for the $p_T^{D^*}/E_T$ cut. Analogous results for the $K3\pi$ mode are shown in Figure 4.6. In this case the wrong charge sample had to be reweighted by a factor 0.82 to reproduce the combinatorial D^* background. Since statistics is a major issue in the present analysis a compromise was chosen between the combinatorial background suppression and the need to retain as many events as possible. In particular instead of using a cut on $p_T^{D^*}/E_T$ in our analysis we cut on the $p_T^{D^*+\mu}/E_T$. The cuts which were finally chosen will now be reported.

4.3.4 D^* final cuts

The final offline cuts applied in this analysis on D^* mesons in the $K\pi$ mode are here listed:

- $1.81 < m_{D^0} < 1.92$ GeV
- $0.1435 < \Delta m < 0.1475$ GeV
- $p_T^{D^*} > 1.9$ GeV, $|\eta^{D^*}| < 1.5$
- $p_T^K > 0.5$ GeV
- $p_T^\pi > 0.5$ GeV
- $p_T^{\pi_s} > 0.125$ GeV

In deep inelastic scattering the combinatorial background is lower so the $p_T^{D^*}$, $p_T^{\pi_s}$, p_T^π, p_T^K were lowered to 1.5, 0.12, 0.4, 0.4 GeV respectively. The $K3\pi$ mode, involving the reconstruction of five tracks, is characterised by a higher level of combinatorial background. To cope with this tighter cuts were imposed on the p_T of the tracks. Other cuts are unchanged.

- $p_T^{D^*} > 3.8$ GeV
- $p_T^{\pi_s} > 0.15$ GeV
- $p_T^K > 0.35$ GeV
- $p_T^\pi > 0.4$ GeV

The applied cuts have chosen to be tighter or at most equal to the corresponding ones at trigger level (see Section 4.1.1) where the precision with which the tracks are measured is lower.

The Δm and m^{D^0} invariant mass plots obtained after the D^* preselection described in Section 4.1 and after the requirement on the presence of at least a muon candidate with loose quality cuts are shown for the $K\pi$ and $K3\pi$ channels in the Left side plots of Figure 4.7. The same plots after the above outlined D^* cuts are shown in the Right

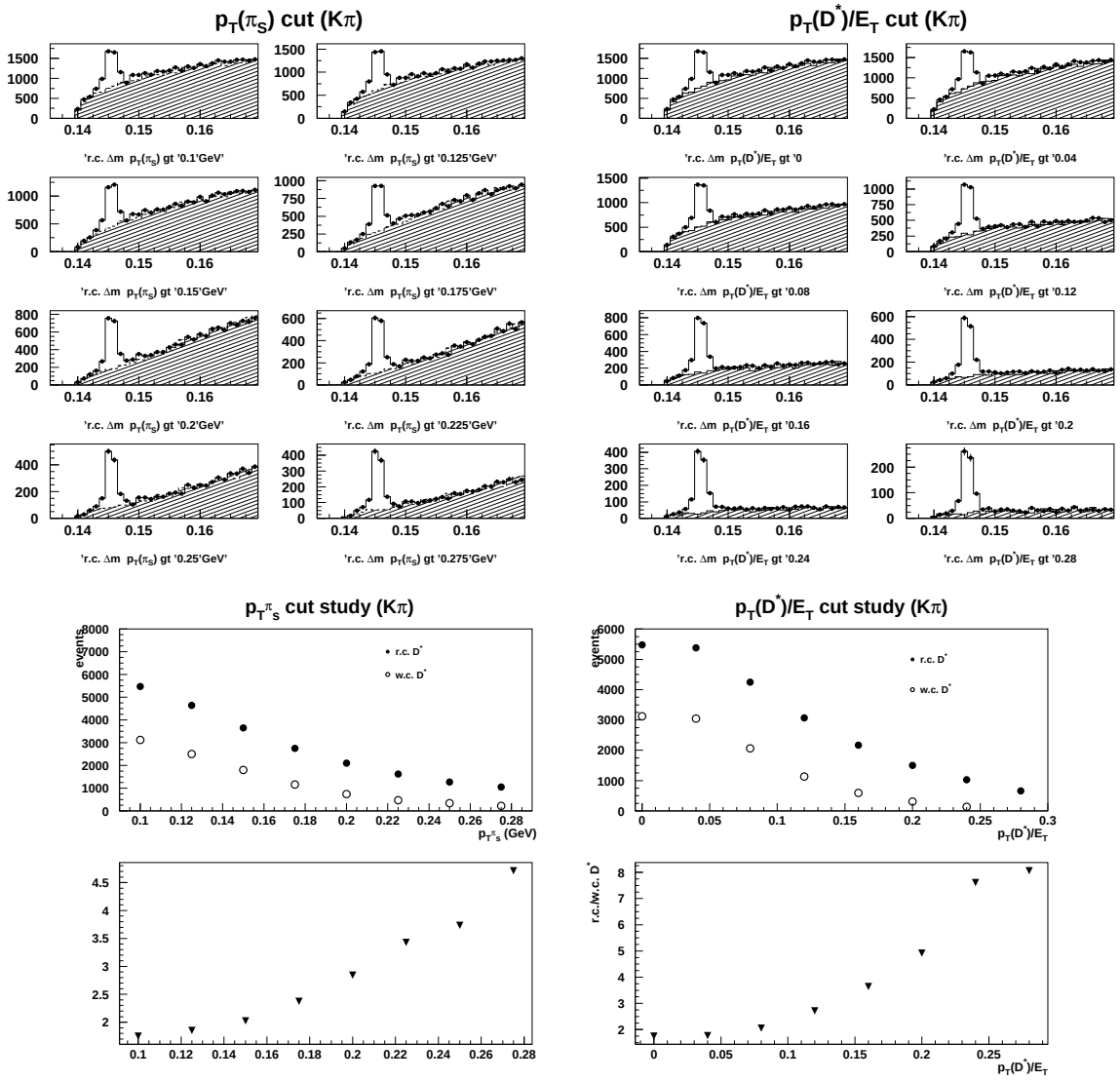

Figure 4.5: *Signal to background ratio dependence on the $p_T^{\pi_s}$ and $p_T^{D^*}/E_T$ cuts for $D^* \to K\pi$ in real data.*

side of the same Figure. The excess seen in the $m(K\pi)$ in the right charge sample with respect to the wrong charge is due to $D^0 \to K\pi\pi^0$ decays. The missing contribution to the invariant mass due to the undetected π^0 broadens and shifts the distribution to lower values.

In the calculation of acceptance we had to recognise the presence of a particular decay mode at true level, from the final state particle listing in the Monte Carlo. We cross checked the correctness of the algorithm which we developed for this purpouse by plotting the Δm and $m(D^0)$ distributions when asking for a particular decay channel to be present. The results of this check are shown in Figure 4.8. The Left side plots refer to the $K\pi$ channel, the Right ones to the $K3\pi$ channel. From top to bottom the following requirements were made on the presence in the event of one true level: D^*, $D^* \to K\pi$ $D^* \to K3\pi$, $D^* \to (K\pi\pi^0)\pi_s$. As expected, in the presence of a certain decay at true level, the corresponding reconstructed decay is enhanced and the combinatorial background decreases. If the decay is absent the peak also disappears. It is nice to notice the appearance of the above–described bump in the $m(D^0)$ distribution in presence of the $D^* \to (K\pi\pi^0)\pi_s$ at true level.

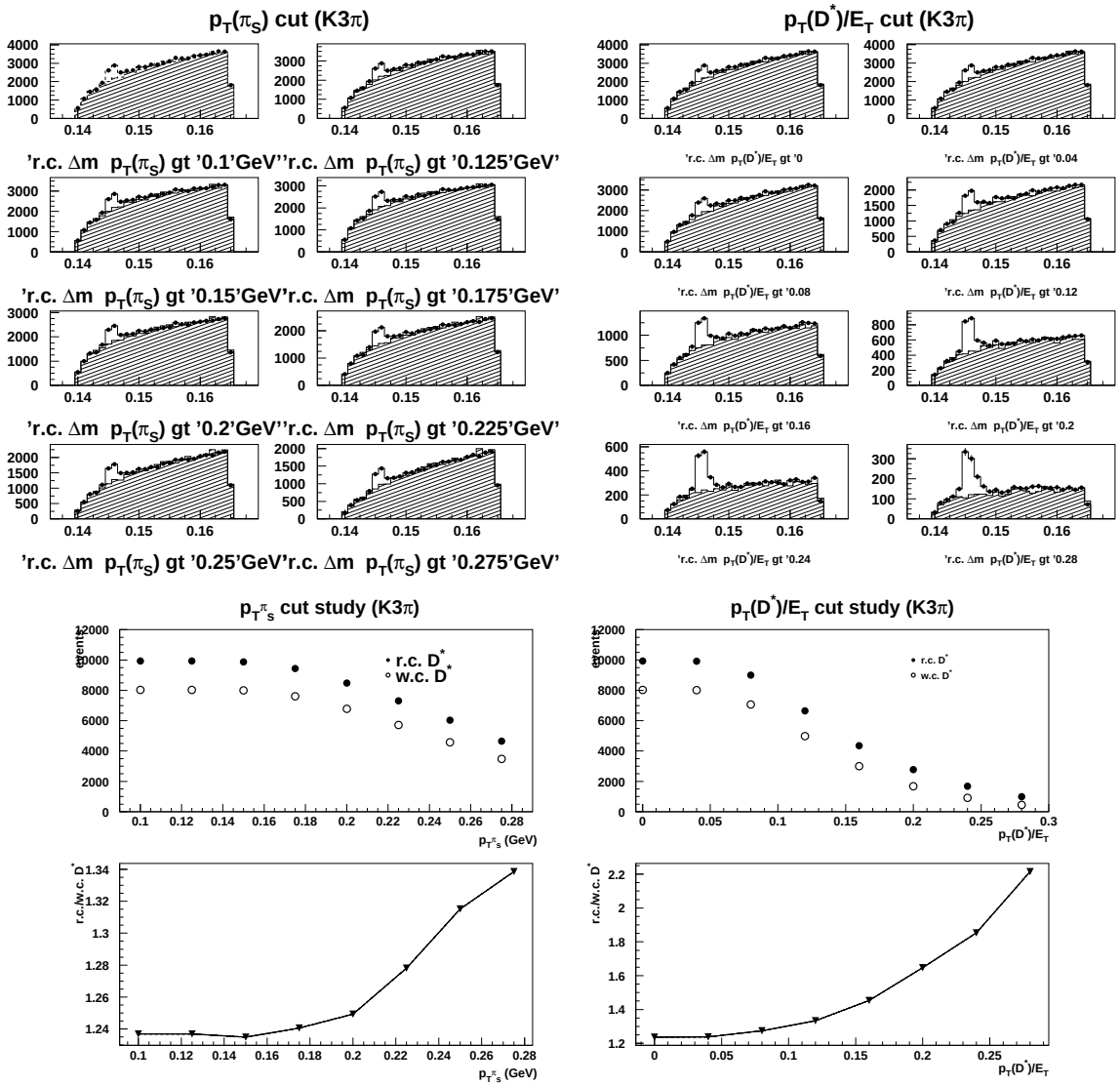

Figure 4.6: *Signal to background ratio dependence on the $p_T^{\pi_s}$ and $p_T^{D^*}/E_T$ cuts for $D* \rightarrow K3\pi$ in real data.*

4.4 Muon reconstruction: the BREMAT matching package

The Barrel and Rear Extrapolation MATching package, BREMAT [163], is used to match segments reconstructed in the barrel and rear muon detectors to tracks measured in the inner tracking detectors, mainly the central drift chamber (CTD Section 2.2.2). The limited streamer tubes, and the associated strips, used in the BRMUON detector have a resolution of the order of ~ 1 mm on both the coordinates they measure, x and y (see Section 2.4.1) but the momentum resolution for most of the muons is dominated by multiple scattering in the iron yoke placed between the inner and the outer chambers. The most powerful way to reconstruct muons in this context requires that measurement errors, multiple scattering and energy losses are correctly taken into account. This is the technique used by the BREMAT code.

The main purpouse of the algorithm is to find out candidate muons, associating inner detector tracks to segments in the muon chambers and providing the resulting matching χ^2 . The main input to the algorithm is the MBXYSG table , containing the information on the reconstructed segments in the BRMUON chambers, and the VCTRHL table, containing the parameters of the tracks reconstructed by the inner detectors. When an entry in MBXYSG is found, i.e. a segment in the muon chambers, BREMAT looks for candidates to be associated to it in the VCTRHL table, i.e. between all the tracks reconstructed by the inner drift chamber. A loose preselection is done on VCTRHL tracks to be associated to MBXYSG segments:

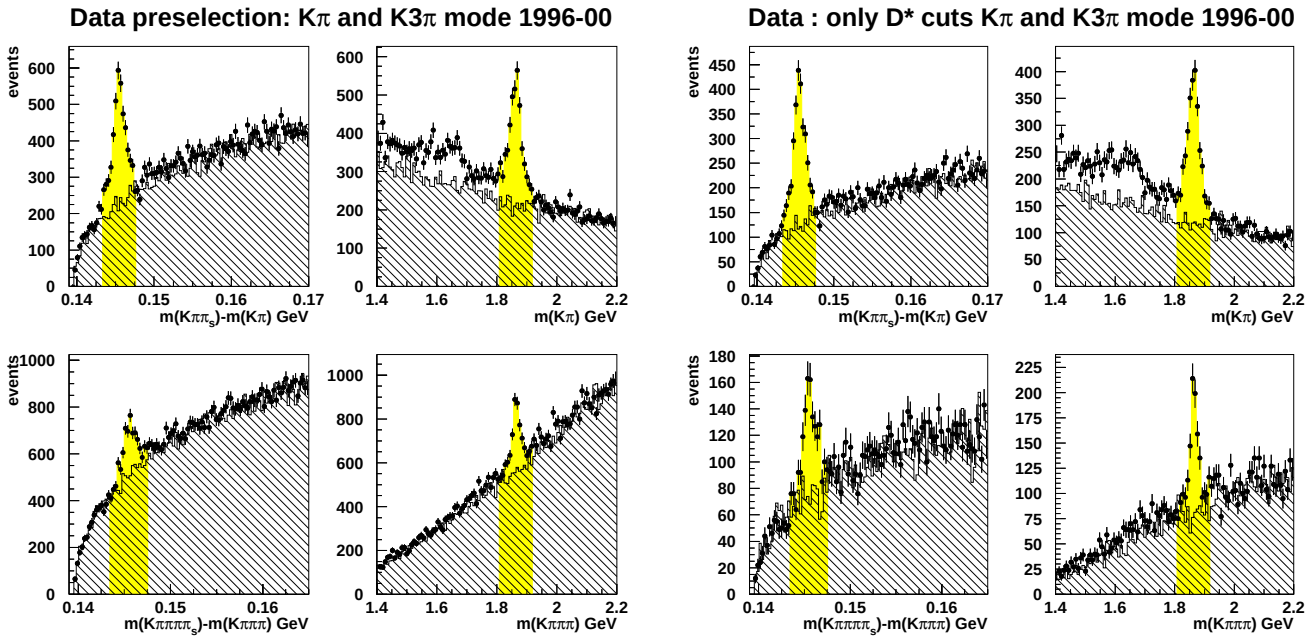

Figure 4.7: **Left**: *D^* invariant mass peaks for the 1996-2000 data with a loose preselection on muon candidates and no trigger requirements. The upper histograms refer to the $K\pi$ mode, the lower ones to the $K3\pi$ mode. The right charge sample is represented with bullets while the wrong charge one is represented by the hatched histogram. The shaded area show the selected D^* signal region.* **Right**: *The meaning is the same as for the Left plots but these histograms after applying the cuts described in Section 4.3.4.*

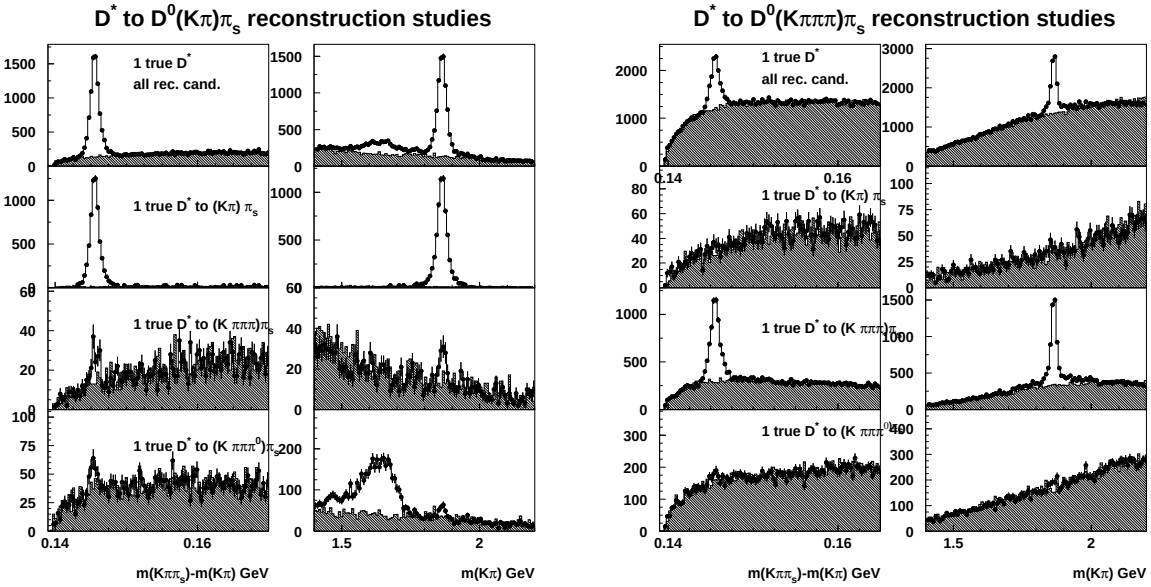

Figure 4.8: *The* **Left** *hand plots refer to $D^* \to (K\pi)\pi$ while those on the* **Right** *to $D^* \to (K\pi\pi\pi)\pi_s$. Each panel shows the reconstructed Δm and $m(K\pi)$ ($m(K\pi\pi\pi)$) distributions in the Monte Carlo under different assumptions. From top to bottom the following requirements were imposed at true level: 1) at least one D^*, 2) at least one $D^* \to (K\pi)\pi_s$, 3) at least one $D^* \to (K\pi\pi\pi)\pi_s$, at least a $D^* \to (K\pi\pi^0)\pi_s$.*

- the momentum p of the track has to be $p > 1$ GeV; this is a minimal request for tracks that have to cross all the calorimeter before being identified by the chambers;
- the polar angle θ of the track has to be $\theta > 20^\circ$ (better acceptance of the tracking detectors, mainly CTD; rejection of forward tracks);
- the track has to start from CTD superlayer 1 and to extend at least to superlayer 3 (see Section 2.2.2);
- the impact parameter of the track, D_H, has to be $|D_H| < 10$ cm;
- the z coordinate at the point of closest approach has to be $|z_H| < 75$ cm;
- $\chi^2_{track}/n.d.f. < 5$;
- $\Delta \leq 150$ cm, Δ being the distance between a central point on the BRMUON segment and the straight line obtained by extrapolating the CTD track at the calorimeter entrance.

Tracks passing the preselection are extrapolated through the calorimeter using the GEANE [164] package. The extrapolation of the parameters and error matrix of the candidate track proceeds from the outer surface of the inner tracking devices, through the calorimeter up to a reference surface on the inner muon chambers, where matching is done. This surface is shaped as a prism, having one base on the rear chambers plane at $z = -310.53$ cm, the other base lying on the forward end of the barrel chambers, at $z = 450.0$ cm, and the side faces corresponding to the barrel sectors (see Section 2.4.1). The track extrapolation is done outward, starting from the inner region, for the best treatment of the low–momentum muons, which suffer big energy losses compared to their initial energy. With the GEANE package also tracks that completely loose their energy before reaching the chambers are simulated.

The output track parameters and error matrix at the reference surface are usually referred to as predictions. The predicted variables and error matrix are obtained in a convenient Cartesian parametrisation, related to the local coordinate frame of each sector. The slopes of the track x' and y' are also given in order to determine the predicted direction of the particle. The fifth coordinate is the momentum of the particle Q/p, that can be measured by the BRMUON detector just in the case the muon reaches the outer chambers.

Naming ξ_{M_i} and ξ_{P_i} , respectively, the measured and the predicted track parameters at the reference surface, the residuals are defined as $\delta_i = \xi_{M_i} - \xi_{P_i}$. If the coordinate of the Cartesian parametrisation are written as $(x, y, x', y', Q/p)$ the matching χ^2 is given by:

$$\chi^2 = \sum_{i,j} S^{-1}_{ij} \delta_i \delta_j$$

where the sum goes from 1 to $n = 4$ or 5, depending whether the momentum is included or not in the χ^2 , and S^{-1}_{ij} is the inverse of the covariance matrix of the residuals:

$$S_{ij} = \sum_{kl} T_{ik} (\sigma^2_{\rm track})_{kl} T^T_{lj} + (\sigma^2_{\rm random})_{ij} + (\sigma^2_{\rm BRMU})_{ij}$$

with $k, l = 1,\ldots,n$, T is the transport matrix, between the start and the stop of the swim, $\sigma^2_{\rm track}$ is the error matrix of the inner detector track,$\sigma^2_{\rm random}$ the error matrix due to multiple scattering and energy loss, and $\sigma^2_{\rm BRMU}$ the error matrix of the BRMUON segment from the MBXYSG table. The first two terms are calculated by steps during the GEANE extrapolation using the detailed geometry of the ZEUS detector and the magnetic field map. BREMAT makes a loose cut on the matched tracks, considering as matching the tracks having $\chi^2 < 100$.

4.4.1 Matching algorithm tests

A good Monte Carlo description of the matching procedure is important for example in the calculation of acceptance corrections. If the Monte Carlo properly reproduces the matching parameters we can be more confident that the contaminations to a true muon sample are well taken into account. As a first check we will compare the shape of the difference between the measured and predicted values normalised over their expected error (*pulls*):

$$\text{pull}_i \equiv \frac{\delta_i}{\sqrt{S_{ii}}} \tag{4.11}$$

If the errors have been correctly estimated the distributions of the pulls should be gaussians with unitary width. Possible shifts of the observed distributions would denote misalignments between the real and simulated detector (in the case of x, y, x', y') or systematic differences between the true and simulated magnetic field (in the case of Q/p). This comparison in shape is shown in the Left hand plots of Figure 4.9. The only significant deviation between data and Monte Carlo appears in the Q/p pull. It will anyhow not be used in the present analysis since we will consider the high statistic sample of muons reaching the inner muon chambers only. In this case, as we saw, the matching is based on the position and slope of the muon segment.

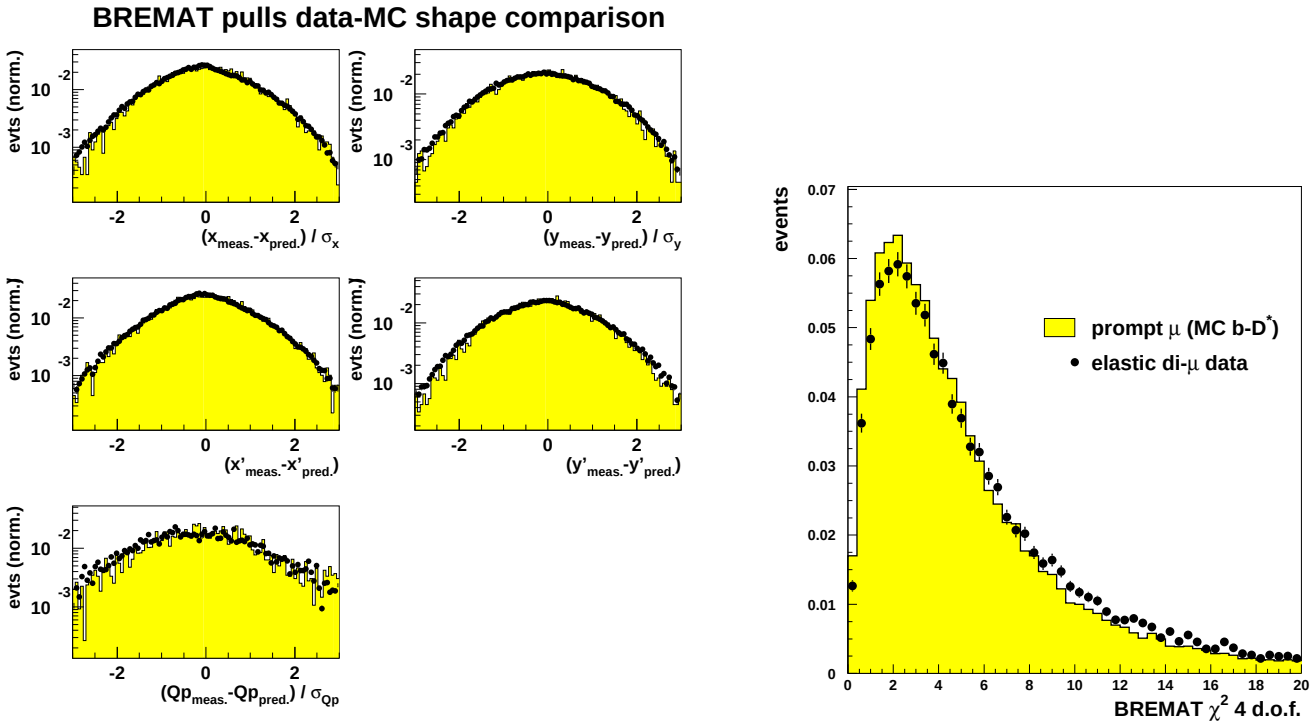

Figure 4.9: **Left***: Data–Monte Carlo shape comparison of the* BREMAT *pulls.* **Right***: Shape comparison of the normalised distributions in the* BREMAT *4 d.o.f.* χ^2*, for an elastic dimuon sample and a beauty Monte Carlo true–muons sample. Data are shown as bullets while the (beauty) Monte Carlo is shown as the plain filled histogram.*

We then compared the shape of the 4 d.o.f. matching χ^2 in data and Monte Carlo for a sample of true muons. The used data sample consists of elastic dimuon events while in the Monte Carlo only matching tracks corresponding to prompt muons at true level were selected. The shape of χ^2 agrees well (Right side plot of Figure 4.9). Possible deviations in the data towards higher values might be due to contaminations in the data sample. We will verify that the same conclusion holds in the case of fake muons in Appendix A.

A dedicated study in the Monte Carlo shows how the χ^2 parameter is partially sensitive to the differences between the various categories of muon candidates. This is shown in the Right hand plot of Figure 4.9. The shape of the χ^2 is shown separately for prompt muons and other categories of muon candidates which will be described later in this work and extensively in Appendix A (pion or kaon sail through, punch-through, secondary muons from K, π in flight decays). The correct description of the matching parameters distribution thus provides some control on the fake muon background.

4.4.2 Muon final cuts

In the present analysis muon candidates were accepted if they fulfilled the following requirements:

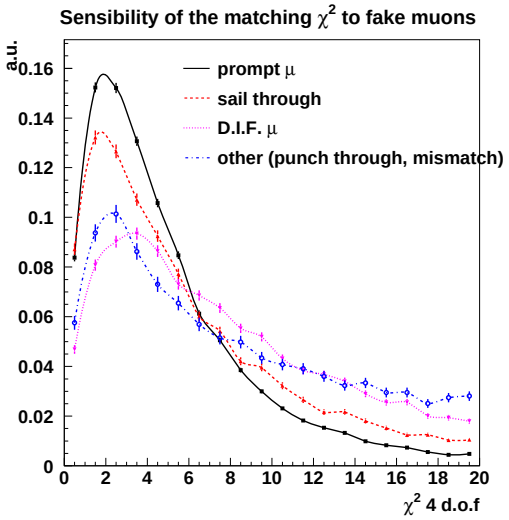

Figure 4.10: *Shape comparison of the normalised distributions in the* BREMAT *4 d.o.f.* χ^2 *for* BREMAT *matching candidates. The true muon, sail–through, decay in flight and other cases are shown separately. Charm Monte Carlo has been used.*

- $\mathcal{P}_{4\ d.o.f} > 0.01$ [4]
- $p_T^{\mu} > 1.4$ GeV
- $-1.75 < \eta^{\mu} < 1.3$ (approximately equivalent to $30^{\circ} < \theta < 160^{\circ}$)

The cut in the probability of the matching at 0.01 was chosen since matchings with lower probabilities are dominated by fake muons. The reduction power introduced by this cut has been been studied on a sample enriched of fake muons in Appendix A.

The cut on the transverse momentum is motivated by the fact that low–p_T muons arise mostly from secondary or fake muons while prompt muons, especially from beauty, have a much harder p_T spectrum. This will be explicitly shown in the next Chapter 5. Furthermore it is clearly seen from dimuon samples that at lower values of p_T, due to the dead material absorption, the efficiency is rather low.

The angular cut instead almost coincides with the geometrical coverage of the BRMUI detector. The requirements on matched tracks are those imposed by the BREMAT algorithm in Section 4.4. In addition, in order to suppress the occurrence of matches from secondary muons, we required the candidate tracks to be refitted to the vertex (VCTPAR ADAMO table [180]).

The Right hand plots of Figure 4.11 show the distributions in p_T, η, $\mathcal{P}_{4\ d.o.f.}$ and p_T vs η of all the BREMAT matching candidates. The corresponding distributions are shown in the Left part of the same Figure after the cuts in 4.4.2 have been applied. A big fraction of the initial candidates, especially at low p_T, is concentrated at negative pseudorapidities (rear region). This region is more affected to muon background due to the reduced thickness of the rear calorimeter with respect to the barrel one. Furthermore only a small fraction of the beauty signal is expected at these values in pseudorapidity (the distribution of the pseudorapidity for muons from beauty is shown for example in the next Chapter in Figure 5.25). The bump at pseudorapidity $\eta \simeq$ -0.7 arise from tracks passing through the crack between the barrel and rear calorimeters. After the matching and p_T cuts have been applied a dip in the pseudorapidity distribution appears due to the gap between the barrel and rear muon chambers. The lines in the p_T vs η scatter plots indicate the values of the applied cuts.

[4] The probability that a random variable having a χ^2 distribution with $N \geq 1$ degrees of freedom assumes a value which is larger than a given value $\chi^2 \geq 0$ ($\mathcal{P}(\chi^2, N)$) is given by the following relation: $\mathcal{P}(\chi^2, N) = \frac{1}{\sqrt{2^N}\Gamma(\frac{N}{2})} \int_{\chi^2}^{\infty} e^{-\frac{t}{2}} t^{\frac{N-1}{2}}\, dt$. A probability cut at 0.01 corresponds to a cut at $\sim$ 13 on the χ^2.

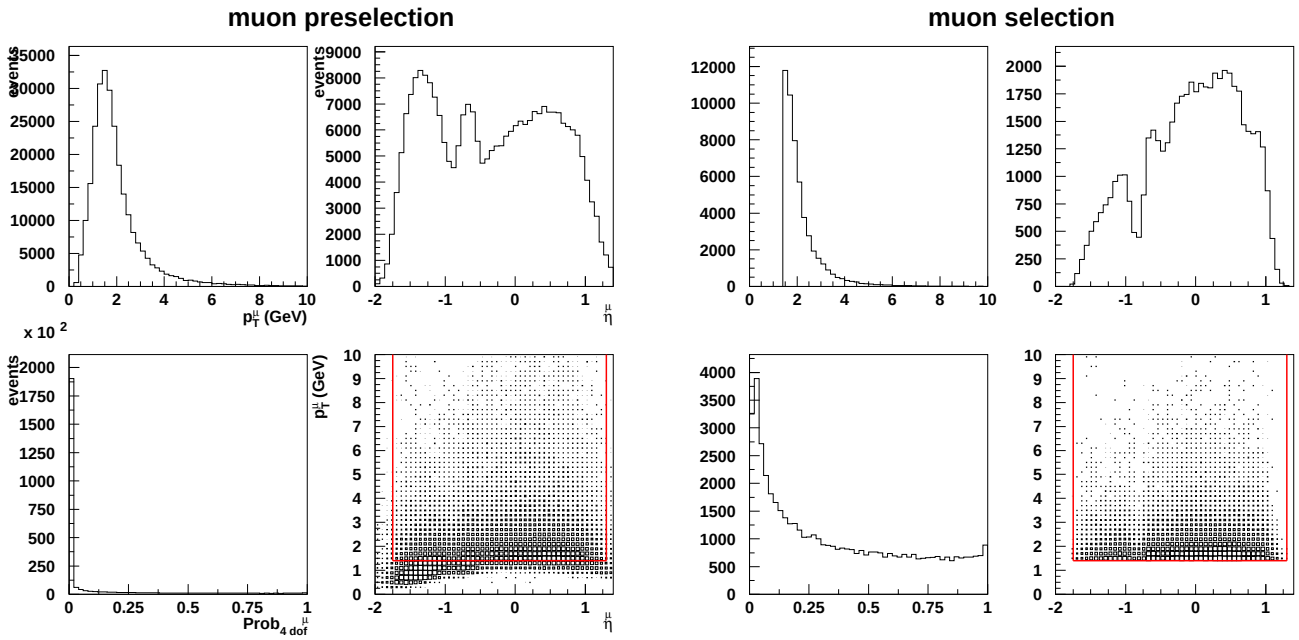

Figure 4.11: **Left***: from Top Left in counterclockwise order the p_T, η, $\mathcal{P}_{4\ d.o.f.}$ and p_T vs η for loose muon preselection.* **Right***: As for the Left plots but after applying the muon cuts outlines in Section 4.4.2.*

4.5 Muon + D^* final sample

We finally present in Figure 4.12 some relevant distributions (Δm, $m(D^0)$, p_T^μ, η^μ) for the sample in which both a good muon and a good D^* are present according to the requirements which we discussed (except for the trigger). It can be noticed how the invariant mass plots for the D^* in the $K\pi$ and $K3\pi$ modes have a somewhat improved signal to background ratio. This is expected since the requirement of a good muon enhances the heavy flavour component and suppress the light flavour one which is mainly responsible for the combinatorial background.

Except for other few additional cuts related with the muon–D^* relative properties which are meant to enhance the beauty component with respect to charm and combinatorial background, this is the starting sample which will be exploited for the measurements described in the next Chapters.

4.6 Resolution studies

In this section we will present a Monte Carlo study of the correlation existing between the values of the event variables as they are generated (*true* level) and the corresponding variables are they are finally measured (*reconstructed* level). This tells us how well we expect the quantities we are interested in to be accurately measured. Furthermore if systematic deviations show up because of the specific issues of the measurement, we can find appropriate parametrisations to correct a certain variable and bring it closer to the true value.

The correlation between the true inelasticity and the y_{JB} estimator is shown in the upper Left plot in Figure 4.13. y_{JB} calculated with calorimeter cells tends to underestimate systematically the true value due to the imperfect description of the final state given by the calorimeter in the presence of low momenta or minimum ionizing particles. Better estimators exist which use also the central drift chamber information. Anyhow for our purpouses y_{JB} from calorimeter cells can be fruitfully used. A constant correction factor puts the reconstructed and true values close as it can be seen in the lower Left plot of Figure 4.13. The remaining plots show the difference between the measured and true values as a function of the true value and the distribution of this difference before and after the correction has been applied.

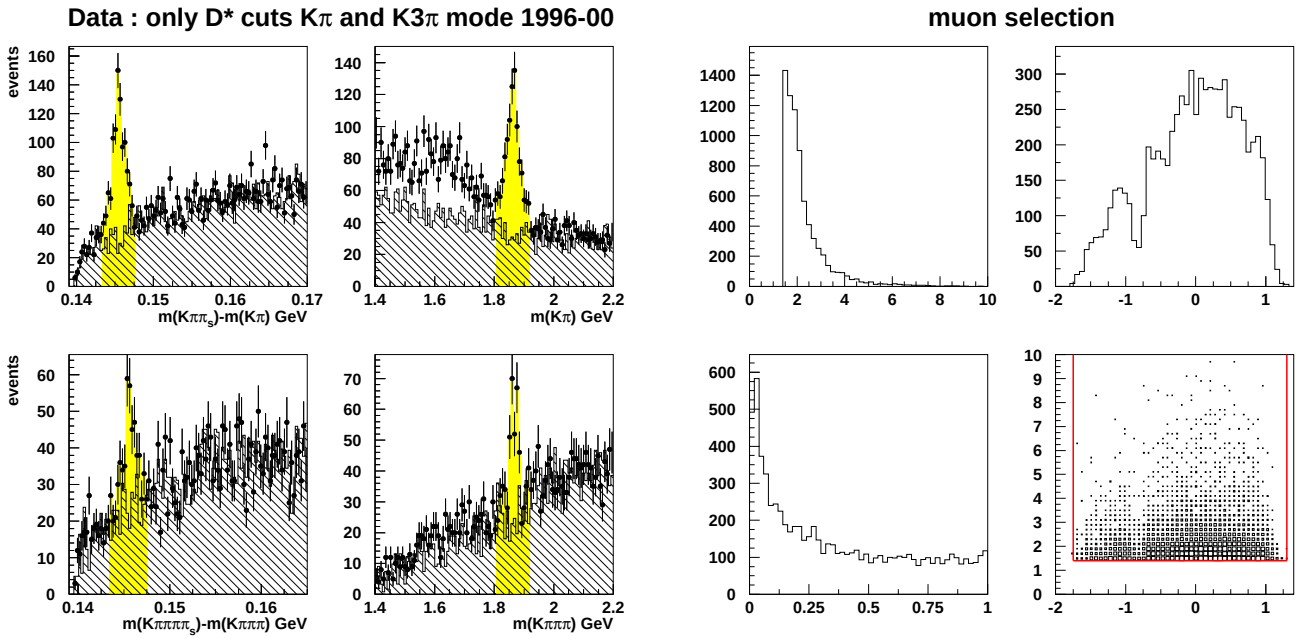

Figure 4.12: **Left** *: Distributions of Δm and $m(D^0)$ for events with at least a good D^* and a good muon candidate according to the cuts defined in Section 4.3.4 and 4.4.2. The upper plots refer to the $K\pi$ channel, the lower ones to the $K3\pi$ channel. The right charge sample is represented with bullets while the wrong charge one is represented by the hatched histogram. The shaded area show the selected D^* signal region.* **Right***: The distributions in p_T, η, $\mathcal{P}_{4\ d.o.f.}$ and p_T vs η for muons for the same sample used for the Left plots in this Figure.*

The electron method is more precise providing better resolutions ad smaller systematic deviations with respect to the true value. Analogous results shown for the Jacquet Blondel variables are shown for y_{el} and Q^2_{el} in the Right plots of Figure 4.13.

We have repeated the study of the resolutions which we already did for the global event variables y and Q^2 to the muon and D^* momentum and pseudorapidity. In order to restrict to the specific conditions that we will meet in the analysis, muons and D^* were required to have $p_T > 1.4$ and 1.9 GeV and η in [-1.75,1.3], [-1.5,1.5] respectively. A beauty Monte Carlo was adopted. In order to associate muons and D^* at generator and reconstructed level we used their distance in the η–ϕ plane. A cut at 0.02 units in this variable ensures to get an unambiguous association as seen in Figure 4.14. The plot shows the distribution of the distance in the η–ϕ plane of muons and D^* at true and reconstructed level. The tail at high values is due to the presence of more than one muon and one D^* satisfying the imposed cuts in the same event. The correlation plot between true and reconstructed level for the p_T and η of the muon and the D^* are shown in Figure 4.15. The correlation between the difference among true and reconstructed value and the true value is also displayed. The deviation is independent from the true value in both the η and p_T. Concerning the spread, it can be noticed that the distribution of the difference is broadened at higher values as expected.

Since the charge of muons and D^* is a relevant ingredient in our analysis, we have verified from the simulation that the probability for a muon to be reconstructed with the wrong momentum sign is negligible at least up to $\sim$ 10 GeV. The corresponding concern in the D^* case is even less serious since the curvature of the slow pion which determines the D^* charge is very well measured.

The resolution of variables related to the properties of the muon–D^* system which will be used later in the analysis have also been studied. The muon–D^* invariant mass, their distance in the η–ϕ plane and separation in azimuthal angle were considered. Figure 4.16 contains the scatter plots showing the correlation between the reconstructed and true values for these variables. Also in this case very good resolutions are achieved over all the interesting ranges.

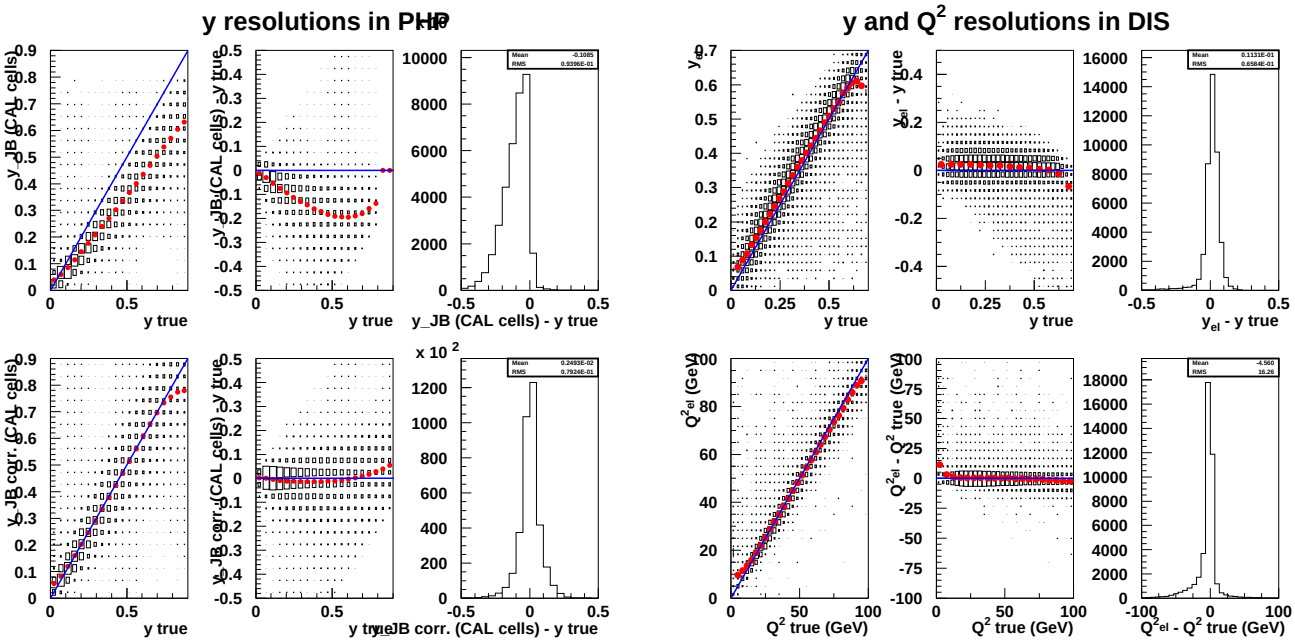

Figure 4.13: **Left**: y_{JB} *resolutions in photoproduction. The upper plots show, from Left to Right,* y_{JB} *vs* y_{true}*,* $y_{JB} - y_{true}$ *vs* y_{true}*, the distribution of* $y_{JB} - y_{true}$*. The same plots are shown in the lower plots after a constant correction has been applied.* **Right**: y_e *and* Q^2_{el} *resolutions in DIS. Upper plots:* y_{el} *vs* y_{true}*,* $y_{el} - y_{true}$ *vs* y_{true}*, distribution of* $y_{el} - y_{true}$*. Lower plots:* Q^2_{el} *vs* Q^2_{true}*,* $Q^2_{el} - Q^2_{true}$ *vs* Q^2_{true}*, distribution of* $Q^2_{el} - Q^2_{true}$

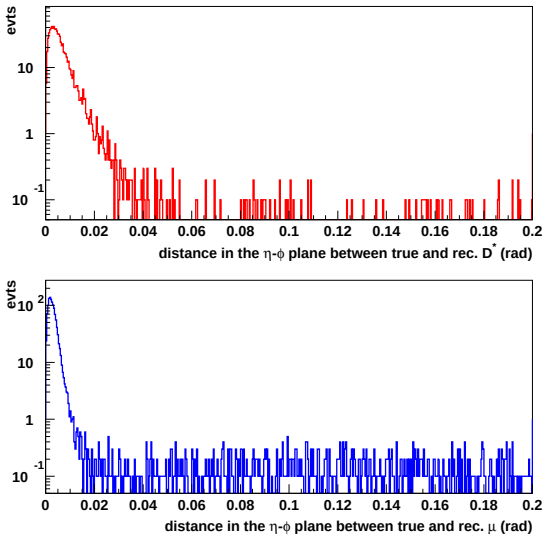

Figure 4.14: *Distance in the* $\eta - \phi$ *plane between the* D^* *(upper plot) and* μ *(lower plot) at true and reconstructed level.*

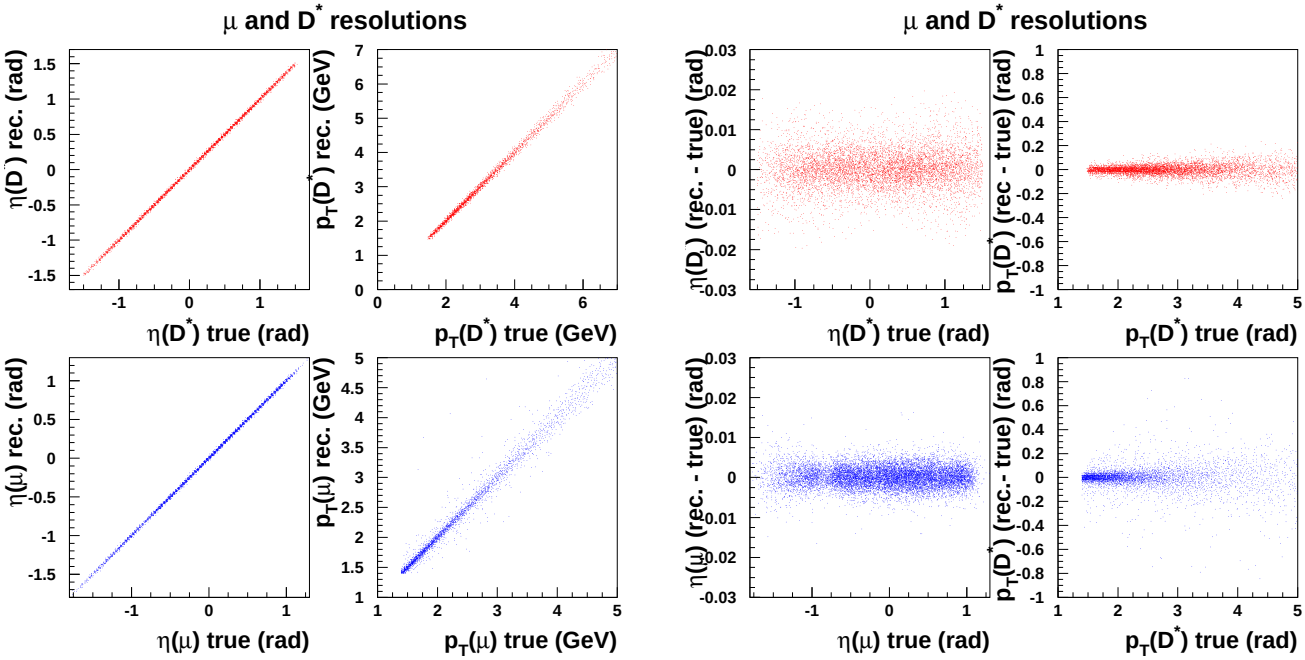

Figure 4.15: **Left**: *correlation between true and reconstructed values for the p_T and η of the muon and the D^*.* **Right**: *difference between the true and reconstructed values over the true value for the p_T and η of the muon and the D^**

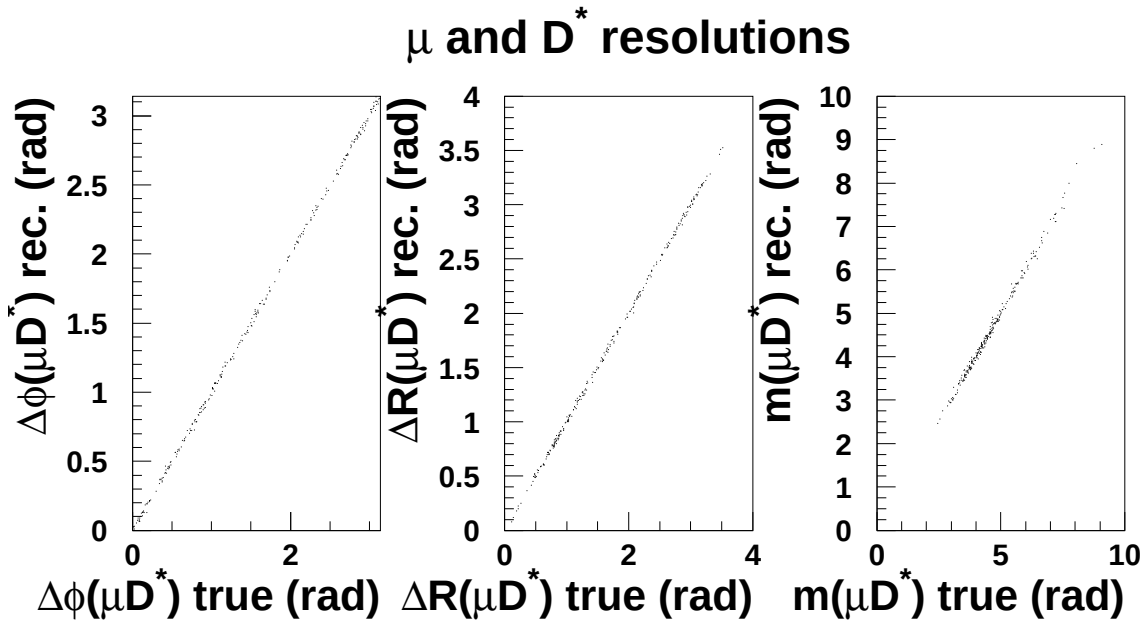

Figure 4.16: *Correlation between the true and reconstructed values for, from Left to Right, the μD^* angle in the azimuthal plane ($\Delta\phi(\mu D^*)$), the distance in the η–ϕ plane ($\Delta R(\mu D^*)$) and the invariant mass ($m(\mu D^*)$).*

Chapter 5

Cross section measurement

We will start this Chapter by describing the principle of the measurement and the strategy used to extract the beauty signal component in the final data (in Sections 5.1, 5.2, 5.4). The rest of the Chapter will deal with the experimental results on beauty visible cross sections in both deep inelastic scattering and photoproduction (Section 5.10). As a first step a comparison with the Monte Carlo predictions will be drawn. In the last part of the Chapter these results will be converted to a quark level cross section in order to perform a comparison with the more refined next–to–leading order calculations (Section 5.13.2).

5.1 Basic concepts and motivation

Beauty production has been studied at HERA in analyses based on the study of the transverse momentum of leptons with respect to the axis of associated jets (see Section 1.4.1.1). The analysis described in this thesis provides an independent way to measure the same process. It is based on a sample of events in which both a D^* and a muon have been produced. This final state offers the advantage of selecting a data sample enriched in b quarks and with strongly suppressed backgrounds from other processes, which allows low-p_T-threshold cuts to be applied on the muon and D^*. This possibility extends the sensibility towards b quarks produced down to transverse momenta close to zero. This analysis therefore complements measurements based on leptons with high transverse momentum which instead, due to the need to tag jets, are sensitive to b–production at higher transverse momenta. This is pictorially illustrated in Figure 5.1. The loss in statistics due to the exclusive final state is partially compensated by the fact that the bulk of the beauty cross section at HERA is expected to be concentrated at low momenta of the produced b–quark. The possibility to access a partially new kinematic region is also important since it is interesting to study whether the excess of data over theory which was observed in several previous measurements (Section 1.4) is reduced or enhanced.

In this analysis heavy quark production events are *double tagged* by the requirement of both a muon and a D^* in the final state. The presence of each of these particles is, by itself, a heavy flavour signature. On the other hand, in order to study beauty production neither a D^* nor a muon alone is sufficient since, lacking the information on possible detached vertices, it is not possible to separate the signal from other backgrounds which come essentially from charm and light quarks production. The presence of both these objects offers the possibility to have much more information to disentangle beauty from other backgrounds.

The idea is indeed to study the angular and charge correlations between the muon and the D^*. Of particular interest are events in which the muon and D^* originate from the same parent B meson, e.g. $B^0 \rightarrow D^{*-}\mu^+\nu$. These yield unlike sign D^*-muon pairs produced in the same hemisphere and constrained not to exceed the B-meson mass. Another important contribution arises from charm-pair production, where one charm quark fragments into a D^* and the other decays into a muon. This again yields unlike sign D^*-muon pairs. However, the D^* and the muon will be produced predominantly in opposite hemispheres. Furthermore, beauty-pair production in which the D^* and muon originate from different beauty quarks can yield both like and unlike sign D^*-muon combinations, depending on whether the muon is from the decay of the primary beauty quark, or from a secondary charm quark, and whether $B^0 - \bar{B}^0$ mixing has occurred. Beauty production is the only source of genuine like sign D^*-muon pairs. Background contributions to both like and unlike sign combinations include events with either fake D^* mesons, originating from combinatorial

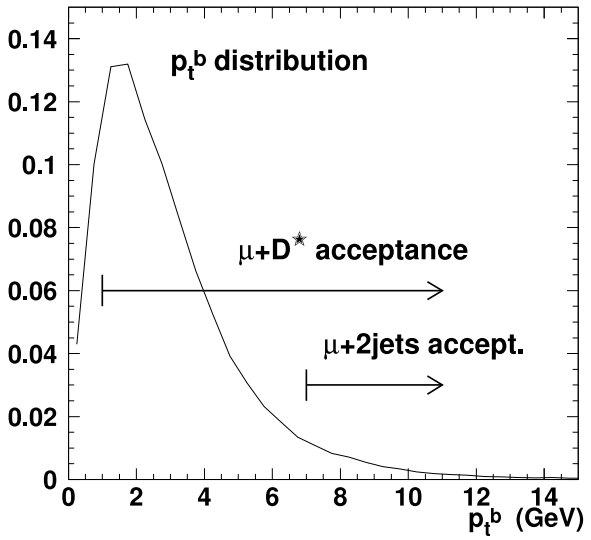

Figure 5.1: *The plots shows the distribution of the transverse momentum of the produced beauty quark (p_T^b). The arrows indicate roughly the sensibility achieved by the μD^* analysis and lepton+jets analyses.*

background, or fake muons. In this analysis, the signal is extracted from the unlike sign sample, while the like sign sample is used as a cross check.

We will now describe in more detail what we just anticipated by considering the possible topology of an event with a muon and a D^*. The most favourable configurations in terms of statistics and background will be pointed out.

5.2 Branching ratios

The $D^{*+}(2010)$ is a vector meson made up by a c and a light $\bar{d}$ quark. Since it decays through the mediation of strong interaction its lifetime is very short ($\sim 10^{-23}$ s). In this analysis we will use the decays of the charged D^* to a pion and a D^0 meson (Left diagram in Figure 5.2). The branching ratio for this decay is measured to be $\mathcal{B}(D^{*+} \rightarrow D^0\pi_s^+) = (67.7 \pm 0.5)$ % [161]. The D^0 meson decays on its turn to a pion and a kaon (see Right diagram in Figure 5.2) with a branching ratio of $\mathcal{B}(D^0 \rightarrow K^-\pi^+) = (3.80 \pm 0.09)$ %. We will use this decay mode as well as that into a charged kaon and three charged pions whose branching ratio is higher: $\mathcal{B}(D^0 \rightarrow K^-\pi^+\pi^+\pi^-) = (7.46 \pm 0.31)$ %. The global branching ratio for the complete decay chains are:

$$\mathcal{B}(D^{*+} \rightarrow D^0(\rightarrow K^-\pi^+)\pi_s^+) = (2.57 \pm 0.06)\ \% \quad (5.1)$$

$$\mathcal{B}(D^{*+} \rightarrow D^0(\rightarrow K^-\pi^+\pi^+\pi^-)\pi_s^+) = (5.1 \pm 0.3)\ \% \quad (5.2)$$

Measurements at e^+e^- experiments indicate that $f(c \rightarrow D^*) = 0.235$ [69] while for $f(b \rightarrow D^*) = 0.173$. Keeping this in mind we can express the combined branching ratios at quark level as:

$$\begin{aligned}
\mathcal{B}(c \rightarrow D^{*+} \rightarrow D^0(\rightarrow K^-\pi^+)\pi_s^+) &= 0.6\ \% \\
\mathcal{B}(c \rightarrow D^{*+} \rightarrow D^0(\rightarrow K^-\pi^+\pi^+\pi^-)\pi_s^+) &= 1.2\ \% \\
\mathcal{B}(b \rightarrow D^{*+} \rightarrow D^0(\rightarrow K^-\pi^+)\pi_s^+) &= 0.44\ \% \\
\mathcal{B}(b \rightarrow D^{*+} \rightarrow D^0(\rightarrow K^-\pi^+\pi^+\pi^-)\pi_s^+) &= 0.88\ \%
\end{aligned}$$

Semileptonic decays of heavy quarks are mediated by the weak interaction. A $c(\bar{c})$ quark can decay to an s or d quark ($\bar{s}$ or $\bar{d}$ anti–quark) via the emission of a W–boson, a positive muon (negative muon) and the corresponding neutrino (anti–neutrino). The c quark decays to an s quark and a muon with a probability of ~ 10 %. The decay to a d quark is instead heavily suppressed due to the fact that in the Cabibbo–Kobayashi–Maskawa matrix $|V_{cd}| << |V_{cs}|$. A $b(\bar{b})$

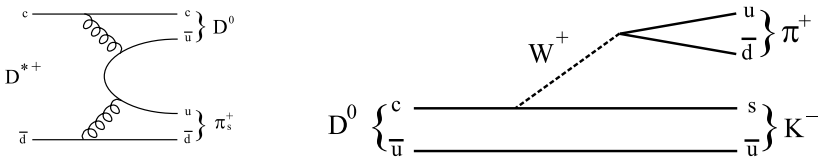

Figure 5.2: *Quark level cartoon for $D^{*+} \to D^0$ and $D^0 \to K^-\pi^+$ decay.*

quark decays to an c quark ($\bar{c}$ anti–quark) via an equivalent diagram. Furthermore the c quark coming from a b quark can in its turn lead to a $\mu\nu_\mu$ state. The global decay rate for b and c quarks to muons is then given by [161]:

$$\begin{aligned} \mathcal{B}(c \to \mu^+\nu_\mu X) &= (8.0 \pm 0.4)\,\% \\ \mathcal{B}(b \to \mu^+\nu_\mu X) &= (10.38 \pm 0.32)\,\% \end{aligned}$$

Experimentally, semi–leptonic decays have the advantage of large branching ratios and the characteristic signature of the energetic charged lepton. The neutrino, however, escapes undetected so a full reconstruction of the decaying B meson is in general not possible.

5.3 Sources of $D^*\mu$ events and $D^*\mu$ charge–angle correlations

We will here analyse the processes producing a final state containing both a $D^{*\pm}$ and a μ. If, for the time being, we exclude *c/b* production from gluon splitting ($g \to c(b)\bar{c}(\bar{b})$) which we will discuss later, the presence of the D^* restricts the possible configurations to events with primary $c\bar{c}$ or $b\bar{b}$ production. The muon can the be produced either from the decay of B, D or light mesons (K,π). We will first concentrate on muons from heavy mesons (*prompt muons*). The muon and the D^* can come from the same or different quarks. We will also restrict to D^* decaying to $(D^0 \to K\pi)\pi_s$ and in this way we exclude the cases in which the μ and the D^* come from the same c quark. The possible charge relations are fully determined if one considers that $c \to D^{*+}$, $c \to \mu^+$ and $b \to \mu^-$ and charge conjugate modes. We will also schematically assume that D^* and muons produced from different (the same) quarks lie in opposite (the same) hemisphere. This will be substantiated more quantitatively later in this Section.

Let's consider the case of $c\bar{c}$ production first. This case is illustrated in the upper Left diagram in Figure 5.3. The muon can come in this case only from the $c(\bar{c})$ quark which does not fragment into the D^*. Unlike sign μD^* pairs are thus produced lying in different hemispheres [1]:

$$\mu^- \quad \leftarrow \quad \bar{c}c \quad \rightarrow \quad D^{*+}$$

In $b\bar{b}$ production the spectrum of possibilities is enlarged since the muon can now decay directly from the B or from a D meson. Moreover the possibility for the μ and D^* to come from the same (b) quark is now allowed. The three possible configurations are shown in the upper Left and bottom plots in Figure 5.3.

If the μ and D^* come from the same b quark they will have opposite sign and will be in the same hemisphere. These events are produced from the $B^0 \to D^*\mu\nu_\mu$ decay.

$$X \quad \leftarrow \quad \bar{b}b \quad \rightarrow \quad \mu^- c\,(\sim D^{*+})$$

If the D^* and the muon derive instead from different quarks, we will end up with pairs lying in opposite hemispheres and having the same sign if the μ decays directly from the b quark which does not give the D^*

$$\bar{c}\mu^+ \quad \leftarrow \quad \bar{b}b \quad \rightarrow \quad c\,(\sim D^{*+})$$

or opposite sign if the muon is the decay product of D meson from b hadronisation.

[1] The charge conjugate modes are also implicitly assumed.

$$\mu^- \quad \leftarrow \quad \bar{c} \quad \leftarrow \quad \bar{b}b \quad \rightarrow \quad c\,(\sim D^{*+})$$

Concerning the last two sources, those producing μD^* pairs from different b quarks, we have to notice that $B^0_d - \overline{B^0_d}$ and $B^0_s - \overline{B^0_s}$ mixing can produce a migration of the two categories one into the other by flipping the charges of particles produced in one of the two quark branches. b quarks hadronise to a B^0 in about the 40 % of the cases and to a B^0_s in $\sim$ 10% [2]. The time integrated probability for a B^0 (B^0_s) to oscillate to a $\overline{B^0}$ ($\overline{B^0_s}$) is $\sim$ 16 % ($\sim$ 50%)[3]. Furthermore since the neutral B mesons are in general not produced in a quantum mechanically coherent state as in the beauty factories, the oscillation probabilities are independent. We then expect a migration between like sign and unlike sign μD^* events produced from different quarks in $\sim$ 11 % of the cases. If a double oscillation ($\sim$ 1%) happens than the initial configuration is restored so that the fraction is reduced to $\sim$ 10 %. We have verified directly that oscillations are simulated correctly in our central Monte Carlo by counting explicitly the number of times in which the B^0 gave "wrong charge" muons. The final effect on our measurement is rather small since, within the frame of the cuts which we imposed, the number of like sign and unlike sign muons in different hemispheres is very similar and this generates a compensation effect.

The possible μD^* correlations in charge and angle considered so far are summarised in the following Table:

	same hemisphere	*different hemispheres*
Unlike sign μD^*	same **b** quark	different **c** quarks different **b** quarks + μ from D meson different **b** quarks + OSCILLATION + μ from B meson
Like sign μD^*	/	different **b** quarks + μ from $\bar{B}$ meson different **b** quarks + OSCILLATION + μ from D meson

The relative importance of the various configurations can be estimated through the involved branching ratios. The combined branching ratios for the configurations for beauty which we have just discussed appear in the first three rows of Table 5.1. The rest of the rows refer to more "exotic" processes when more than one D^* or more than one muon might be produced. These cases occur with much lower probability. When a $\bar{b}$ quark produces a μD^* pair the b quark can produce a muon directly (4), a muon from c (5), both of them (6), a D^* (7), a D^* and a muon directly (8). When a $\bar{b}$ produces a D^* the b quark can produce (omitting the charge conjugates of cases already considered) a muon directly and indirectly (via a c quark) (9).

	b decay	b decay	$N(D^*)$	$N(\mu)$	$\mathcal{B}$ [%]
1	$b \rightarrow D^{*+}\mu^-$	X	1	1	$2.75 \cdot \mathcal{B}$
2	$b \rightarrow D^{*+}$	$\bar{b} \rightarrow \bar{c} \rightarrow \mu^-$	1	1	$1.4 \cdot \mathcal{B}$
3	$b \rightarrow D^{*+}$	$\bar{b} \rightarrow \mu^+$	1	1	$1.8 \cdot \mathcal{B}$
4	$b \rightarrow D^{*+}\mu^-$	$b \rightarrow \mu^+$	1	2	$0.3 \cdot \mathcal{B}$
5	$b \rightarrow D^{*+}\mu^-$	$\bar{b} \rightarrow \bar{c} \rightarrow \mu^-$	1	2	$0.22 \cdot \mathcal{B}$
6	$b \rightarrow D^{*+}\mu^-$	$\bar{b} \rightarrow \bar{c}\mu^- \rightarrow \mu^-\mu^+$	1	3	$0.023 \cdot \mathcal{B}$
7	$b \rightarrow D^{*+}\mu^-$	$\bar{b} \rightarrow D^{*-}$	2	1	$0.48 \cdot \mathcal{B}$
8	$b \rightarrow D^{*+}\mu^-$	$\bar{b} \rightarrow D^{*-}\mu^+$	2	2	$0.076 \cdot \mathcal{B}$
9	$b \rightarrow D^{*+}$	$b \rightarrow \bar{c}\mu^+ \rightarrow \mu^-\mu^+$	1	2	$0.15 \cdot \mathcal{B}$

Table 5.1: *All possible prompt muon + D^* configurations in $b\bar{b}$ events assuming that the D^* will not produce muons (i.e. $D^* \rightarrow K\pi\pi_s$ and $D^* \rightarrow K\pi\pi\pi\pi_s$). The following branching ratios have been adopted ([161]): $\mathcal{B}(\bar{b} \rightarrow D^{*-}\,\mathrm{X}) = (17.3 \pm 2)$ %, $\mathcal{B}(\bar{b} \rightarrow \mu^+\,\mathrm{X}) = (10.7 \pm 0.7)$ %, $\mathcal{B}(\bar{b} \rightarrow D^{*-}\,\mu^+\,\mathrm{X}) = (2.75 \pm 0.19)$ %. We have denoted with $\mathcal{B}$ in the last column the branching ratio (not taken in %) for the D^* decays to $K\pi\pi_s$ and $K\pi\pi\pi\pi_s$. They are given in Equations 5.1 and 5.2.*

[2] The relative yield of different B–hadrons from b quarks is the following: $\mathcal{B}(\bar{b} \rightarrow B^+) = \mathcal{B}(\bar{b} \rightarrow B^0) \simeq 40\%$ and $\mathcal{B}(\bar{b} \rightarrow B^0_s) = \mathcal{B}(b \rightarrow \Lambda_b) \simeq 10\%$.

[3] The time (t) dependent probability that a B^0 meson oscillates to a $\bar{B^0}$ meson is expressed as a function of the lifetime (τ) and the difference in mass between the two states (Δm_d) as : $\mathcal{P}(t)_{B^0 \rightarrow \bar{B^0}} = \frac{1}{2\tau} e^{-\frac{t}{\tau}}(1 - \cos(\Delta m_d t))$ with $\Delta m_d = 0.474\ \mathrm{ps}^{-1}$ and $\tau = 1.56$ ps. The time integrated probability (χ) is expressed in terms of the variable $x = \Delta m \cdot \tau$ as: $\chi = \int_0^\infty \mathcal{P}(t)dt = \frac{x^2}{2(1+x^2)}$ In the B^0_d system $x \simeq 0.7$ which gives $\chi \simeq 16\%$. In the case of the B^0_s system $\chi_s \simeq 0.5$ so the net effect is almost zero.

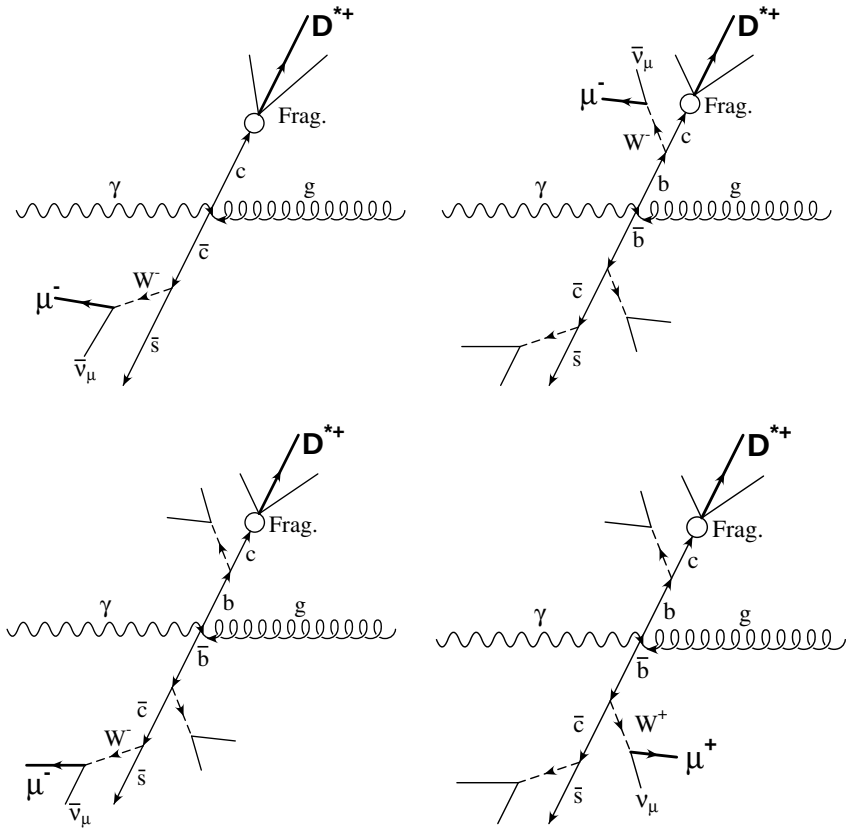

Figure 5.3: *Diagrams showing the physics configurations yielding events with a μ and a D^{*+}. The upper Left diagram refers to $c\bar{c}$ production, the upper Right and lower ones to $b\bar{b}$ production. For simplicity's sake the charge conjugate modes have been omitted. $c\bar{c}$ events produce unlike sign μD^* pairs in different hemispheres while $b\bar{b}$ events produce unlike sign μD^* pairs in both the same or different hemispheres and like sign μD^* pairs in different hemispheres. Full explanation can be found in the text.*

If we include in our considerations non prompt muons coming from K and π decay, the situation gets a bit more complicated to analyze. Yet we can take into account this effect with the Monte Carlo. Secondary muons are numerically dominant also in signal events but, on the other hand, they are heavily suppressed in the final selection being endowed with very low transverse momenta. This is illustrated in the Left hand histogram in Figure 5.4. The distribution in p_T of all muons coming from a B, C, or light (K, π) hadrons are plotted separately for an inclusive beauty in DIS Monte Carlo (RAPGAP). The corresponding distributions for muons which are also reconstructed in the central drift chamber and are able to reach the inner muon chambers are shown in the Right hand plot in the same Figure. The dead material between the interaction region and the muon chambers introduces a natural cut-off in the transverse momentum at about 1-1.5 GeV. It can also be noticed how the p_T cut efficiently suppress also the contribution from muons coming from D mesons thus enhancing the signal beauty with respect to charm events. The red vertical line in the plots marks the value at which we cut in p_T^μ in the analysis.

There is finally another process which we neglected up to now which can result into like sign μD^* pairs in different hemispheres. In the upper Right diagram of Figure 5.3 the W^+ emitted by the $\bar{b}$ quark can on its turn give origin to a $c\bar{s}$ pair the so called *upper vertex* charm. This contribution is also included in the Monte Carlo.

To corroborate the assumption that opposite quarks populate opposite hemispheres we have considered the kinematics of $b\bar{b}$ production via the boson–gluon fusion at HERA in beauty DIS Monte Carlo. The rapidity of the quark, defined in the usual way as:

$$y^b_{rap} = \frac{1}{2}\frac{E^b + p^b_z}{E^b - p^b_z} \tag{5.3}$$

is concentrated in the interval between -1 and 1 with a tail at higher values. This means that beauty quarks are generally produced in the central rapidity region which corresponds to the forward region in the laboratory due to the

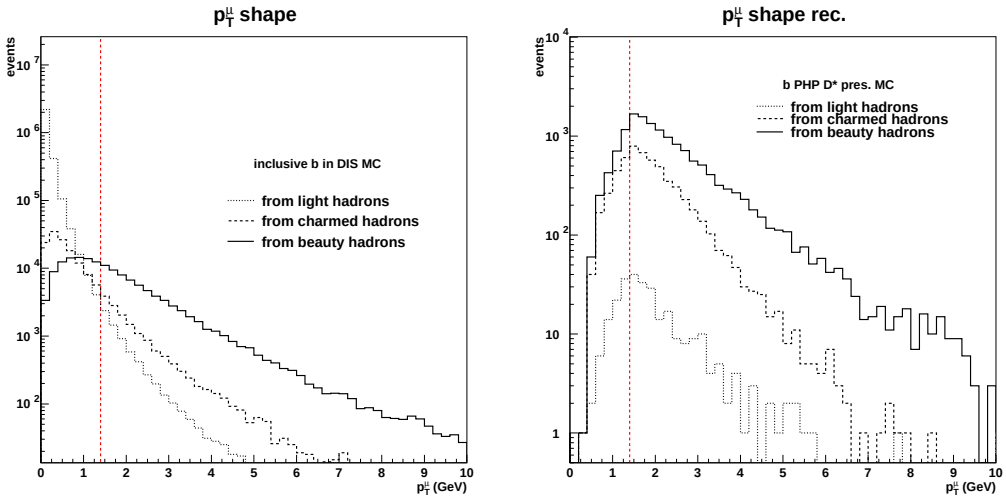

Figure 5.4: *Dependence of the p_T^μ distributions on the parent hadron. The* **Left** *plot shows the p_T^μ distributions at hadron level for an inclusive DIS beauty Monte Carlo. The* **Right** *plot instead refers to reconstructed muons (i.e. matched to a track by the* BREMAT *algorithm with a $\mathcal{P}_{4\ d.o.f.} > 0.01$). A beauty D^* Monte Carlo was used in this case.*

boost introduced by the asymmetric beam energies. The transverse momentum and rapidity are only mildly correlated (see Left plot in Figure 5.5), when the p_T is higher the quark tends to go forward. Concerning the correlations between the b and $\bar{b}$ it can be noticed in the Right hand plots of Figure 5.5 how the two quarks tend to be produced with similar p_T and y^{rap} (upper plots) and in a back–to–back configuration in the transverse plane (lower Left plot).

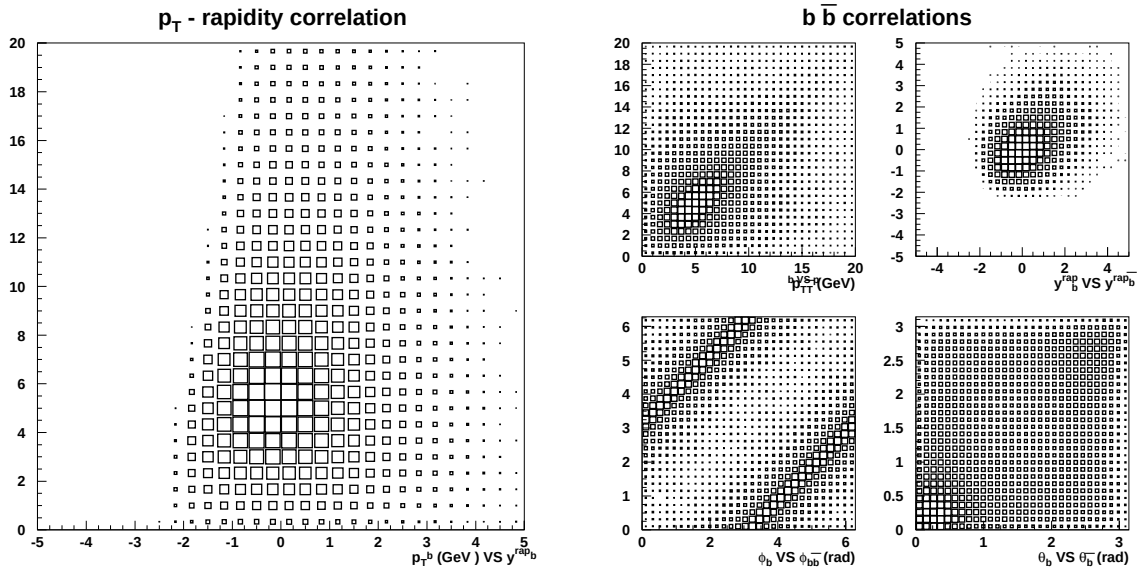

Figure 5.5: **Left***: Correlation between the rapidity and transverse momentum of b ($\bar{b}$) quarks produced via the dominant boson gluon fusion mechanism in DIS at HERA.* **Right***: Kinematical correlations between the p_T, y^{rap}, ϕ, and θ in the laboratory frame, of b and $\bar{b}$ quarks for the same process.*

5.4 μD^* variables and signal extraction

The angular correlations between the μ and D^* have been quantified by considering the μD^* azimuthal angle difference ($\Delta\phi_{\mu D^*}$), the distance in the $\eta - \phi$ plane ($\Delta R_{\mu D^*}$) and the invariant mass ($m_{\mu D^*}$):

$$\Delta\phi_{\mu D^*} = \mathrm{MIN}(|\phi_\mu - \phi_{D^*}|, 2\pi - |\phi_\mu - \phi_{D^*}|) \quad (5.4)$$

$$\Delta R_{\mu D^*} = \sqrt{\Delta\phi^2_{\mu D^*} + (\eta_\mu - \eta_{D^*})^2} \quad (5.5)$$

$$m_{\mu D^*} = \sqrt{m^2_\mu + m^2_{D^*} + 2(E_\mu E_{D^*} - \vec{p_\mu} \cdot \vec{p_{D^*}})} \quad (5.6)$$

In the following when referring to these variables we will often drop the μD^* subscript. These variables are not independent and express only slightly differently the angular topology of the μD^* pair. The opposite hemisphere configuration corresponds to high $\Delta\phi$ ($\sim \pi$), ΔR and invariant mass while the opposite is true in presence of collinear pairs. This kind of variables have been found to be the most effective in terms of separation power between signal and background as we will see in a while. Differences between the results obtained using different variables have been included in the signal extraction procedure systematic error.

The ΔR distributions at reconstructed level for beauty and charm Monte Carlo events surviving all the analysis cuts (which we will describe fully later in this Chapter) are shown in the Left part of Figure 5.6 for the unlike sign and like sign samples separately. Events in which the muon candidate is a prompt or fake are represented with different hatched styles (diagonal and vertical respectively).

The unlike sign sample in the beauty Monte Carlo exhibits a considerable enhancement at low ΔR arising from muon and D^* coming from the same b–quark [4]. The tail at high ΔR is instead mainly produced by muon and D^* coming from different b–quarks when the muon comes from a D meson decay. This contribution is statistically less important with respect to the one at low ΔR since the combined branching fraction is lower (compare the first two rows in Table 5.1) and muons from charm have softer p_T (Figure 5.4). On top of this the particular kinematic selection also plays a role as it will be later discussed. The like sign component at high ΔR comes from the same topology when instead the muon decays from b directly.

In the case of charm the main bump at high ΔR comes from muon and D^* pairs produced from different c quarks. The relative fraction of fake muons in the charm sample is higher than in the case of beauty due to the fact that, as we showed, beauty is more enriched in high-p_T muons than in the case of charm. This component accounts almost totally for the, otherwise unphysical, like sign μD^* charm sample. The small sample of events in this region associated with "prompt muons" are due to early decays (in the CTD) of secondary muons from light hadrons which, in this plot for technical reasons are treated as prompt muons.

By analysing the Left hand plots in Figure 5.6 it becomes clear that the sample in which a cleaner separation between signal and background can be achieved is the unlike sign μD^* sample. The like sign sample is in principle not affected by genuine charm background but unfortunately fake muons from charm populate a similar region in ΔR thus making the disentanglement of signal more difficult. Furthermore, within the frame of the applied experimental cuts, the statistic is lower and with current luminosity this is an important issue. The like sign sample on the other hand is an excellent control sample for the fake muon contamination and allows to have an internal control of this background.

In the unlike sign sample the contribution from μ and D^* in the same hemisphere sits in a ΔR region which is relatively free from charm background. The very low ΔR region is yet still affected by fake muon contamination.

This "D^*–collinear" fake muon component at low ΔR is more enhanced in the unlike sign sample since the (fake) muon and the D^* are leading hadrons by construction due to the D^* and muon p_T cuts so that the fake muon sign tends to be opposite to the sign of the D^* due to charge correlations in the fragmentation chain. Similar correlations but in the other direction exist if the muon is in the opposite hemisphere.

In order try and to suppress this low ΔR fake muon contamination it is interesting to look at the $m_{\mu D^*}$ distribution of this background component. The distributions of $m_{\mu D^*}$ are shown in the Right hand plots of Figure 5.6. It can be seen that, by requiring the μD^* invariant mass of unlike sign combinations to be above 3 GeV, the collinear fake muon component is effectively rejected. The signal is almost totally preserved. The invariant mass distribution of unlike sign μD^* pairs in the same hemisphere is indeed a broad peak ranging from the mass of the D^* and the B^0 mass (third upper plot in Figure 5.6), as expected due to undetected neutrino in the $B^0 \to D^* \mu \nu_\mu$ decay. For this reason we decided to put also an invariant mass upper cut at 5 GeV. This was applied only to the unlike sign sample when $\Delta R < 2$ to preserve the beauty and charm component in opposite hemispheres.

[4] Unless explicitly noted we will often use the collective name "b–quark" for b and $\bar{b}$ quarks.

- $3 < m_{\mu D^*} < 5$ GeV if $\Delta R_{\mu D^*} < 2$ (*signal enriched region*)
- no mass cut if $\Delta R_{\mu D^*} > 2$ (*charm enriched region*)

This cut is illustrated in the $m - \Delta R$ plane in the Left plots of Figure 5.7. The distribution of ΔR for the unlike sign sample for the charm and beauty after this cleaning cut is shown by the Right hand plots of the same Figure. We will use a fit to this variable as the central measurement of the beauty fraction by fitting the data with the Monte Carlo distributions. In this way the small contribution of charm in the low ΔR signal region and vice versa is taken into account. The m and $\Delta\phi$ distributions will be used as cross checks.

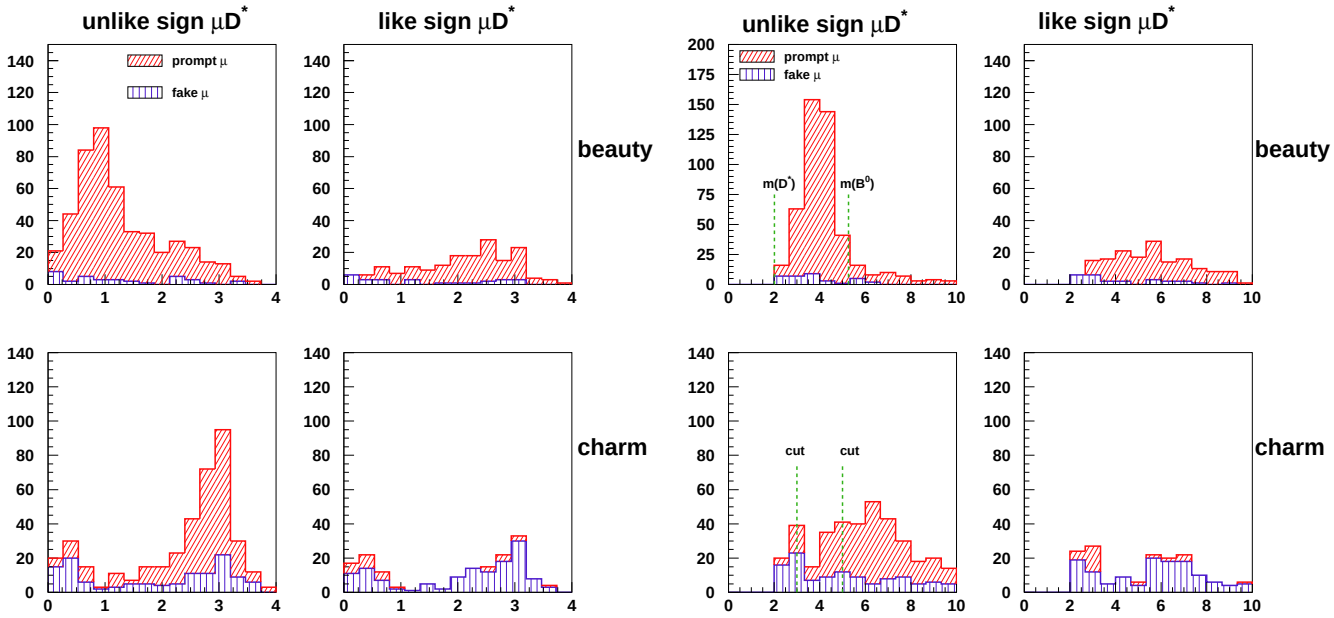

Figure 5.6: **Left**: *ΔR distributions at reconstructed level after the analysis cuts for the unlike sign and like sign samples in the beauty Monte Carlo (Left and Right upper plots), and in the charm Monte Carlo (Left and Right lower plots).* **Right**: *The same for $m_{\mu D^*}$.*

5.5 Background sources

The extraction of the signal from b–decays requires the correct evaluation of the background processes which survive the selection cuts. An exhaustive simulation of all those processes is crucial for the application of the statistical method which we will use.

The main backgrounds to our signal arise from charm and light flavour events. As we have seen charm constitutes a physical competing process producing genuine muons and D^* mesons. In the previous sections we have illustrated how, by exploiting the specific characteristics of charm production in terms of kinematics and charge, this kind of background can be relatively easily estimated and separated from the signal.

In addition to real muons and D^* from charm we must of course consider the contaminations from fake muons and/or fake D^*s.

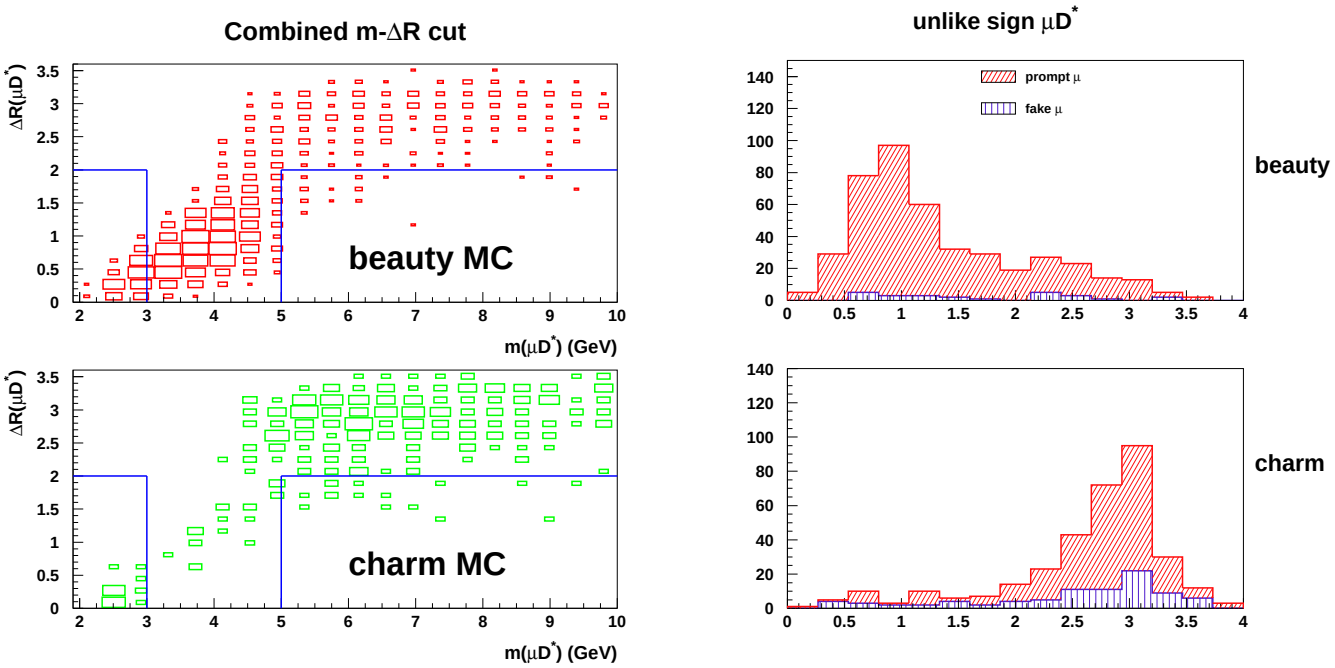

Figure 5.7: **Left**: *The bi-dimensional distributions of $m_{\mu D^*}$, $\Delta R_{\mu D^*}$, is presented for charm and beauty Monte Carlo. The cut in m between 3 and 5 GeV if $\Delta R < 2$ allows to reject a good fraction of fakes from charm without reducing the signal significantly.* **Right**: *The reconstructed ΔR distributions for beauty (top) and charm (bottom) after the cut outlined in the scatter plot on the Right.*

5.5.1 Fake muons

The phenomena which can lead to an incorrect muon identification can be classified under several categories. Fake muon signatures are typically produced by light hadron such as pions and kaons which are abundantly present in any high energy collision final state.

A first contribution which is often denoted as *sail– through* derives from the imperfect filtering operated by the dead material located between the interaction point and the muon detectors. This happen with a probability which depends on the transversed material d and the interaction length of the medium λ:

$$\mathcal{P}(d) = e^{-d/\lambda} \tag{5.7}$$

At ZEUS, the material in front of the Barrel and Rear muon chambers varies between 4λ in the RCAL and 5λ in the BCAL. Muons reaching also the outer muon chambers have to traverse an additional amount of material due to the BAC detector and the iron yoke, corresponding to $\sim 5\ \lambda$. This kind of background is of course enhanced in correspondence of cracks in the dead material i.e. between cells and the separation points between the different sections of the calorimeter.

Fake muon signals in the muon chambers can also be originated from the leakage of secondary particles produced in hadronic interactions in the calorimeter. This case will be denoted as *punch–through*.

Even secondary muons from *in-flight decays* of charged pions and kaons can be considered as further contribution to the background. We are in fact mostly interested in muons from B, D meson decays (*prompt muons*) since they more directly carry the interesting information about the produced heavy quarks. The decay of pions and kaons to muons happens with almost unitary probability according to an exponential law as a function of the distance d:

$$\mathcal{P}(d) = 1 - e^{-d/\beta\gamma c\tau} \tag{5.8}$$

where β is the particle velocity in units of c and γ is the ratio of its energy and mass. The decay muons are mostly characterised by low momenta and, therefore, highly rejected by the transverse momentum cut.

Due to the importance of this topic and its general interest for several analyses a detailed study of this background has been deferred to Appendix A. The level of description provided by the central Monte Carlo used in this analysis has been tested on real data for different particle species using large sample of pure hadrons from $K^0_S \to \pi^-\pi^+$, $\Lambda \to p\pi$, $\phi \to K^+K^-$ and $D^0 \to K\pi$.

As already noticed in the context of this analysis the like sign μD^* sample provides an additional handle to give control on this kind of background.

5.5.2 Fake D^*

The presence of fake D^* arise from the reconstruction procedure itself since random track combinations may happen to fulfill the correct invariant mass requirements imposed to D^* candidates. This *combinatorial* fake D^* background is evaluated from the data themselves using the classical "wrong sign D^*" method. We will start by considering the decay chain $D^{*+} \to D^0\pi^+_s \to K^-\pi^+\pi^+_s$. As we have seen, due to the very small available phase space the π^+_s decays almost at rest in the D^* rest system. In contrast, the K^- and π^+ from the D^0 decay will have almost symmetric properties.

In standard D^* analyses it turns out that the shape of the fake $D^{*+} \to K^-\pi^+\pi^+_s$ (charge $+1$) background is well simulated by taking "wrong sign" $K^-\pi^-\pi^+_s$ (charge -1) combinations instead, provided that multiple entries per event are allowed. Instead of requiring the D^0 candidate to be neutral, pairs of tracks with the same sign are also accepted if they have the right invariant mass. They are combined to a slow pion if its charge is opposite to the one of the pair (see also Section 4.3). Since there are no doubly charged D mesons, there is no significant bias from signal reflections. This sample reproduces the normalisation of the fake D^* combinatorial background typically to within 10 %. The alternative wrong sign combinations $K^+\pi^-\pi^+_s$ and $K^-\pi^+\pi^-_s$ are not useful because they are heavily affected by $D^0 \to K^-\pi^+$ or $\bar{D^0} \to K^+\pi^-$ events (from true D^*'s) where the π and K assignments have been interchanged.

With respect to the inclusive D^* case in the present analysis the complication of additional charge correlations with the muon arises. The classical "wrong sign" approach to the $K^-\pi^+\pi^+_s + \mu^-$ (neutral, unlike sign sample) and $K^-\pi^+\pi^+_s + \mu^+$ (charge $+2$, like sign sample) signal yields the combinations $K^-\pi^-\pi^+_s + \mu^-$ (charge -2) and $K^-\pi^-\pi^+_s + \mu^+$ (neutral). This is the naïve approach which one would use by taking the charge of the soft pion as the D^* charge also in the case of the wrong charge sample.

It turns out that neither of these two combinations yields a good description of the background shape of neither the unlike sign nor the like sign $D^* + \mu$ combinatorial background. Rather, the "muon charge blind" combination $K^-\pi^-\pi^+(\mu^+ + \mu^-)/2$. yields a good description for the shape of both backgrounds.

This is shown in Figure 5.8. The plots show the Δm reconstructed distributions for the unlike sign sample (Left side plots) and like sign sample (Right side plots) in the data for loose $p_T^{D^*}$ cuts (1.5 GeV) and standard muon cuts. In the upper plots the wrong charge sample is taken by simply replacing the right charge D^* (D^{*+}: $K^-\pi^+\pi^+_s$) with the corresponding wrong charge D^* ($K^-\pi^-\pi^+_s$) "of the same sign". As it can be seen with this choice the unlike sign sample combinatorial background is underestimated while the like sign sample is overestimated.

In the two lower plots instead the combinatorial background is taken as the sum of the two previous samples divided by a factor two. In this way the combinatorial D^* background normalisation is better reproduced in both cases. In some sense, by "neutralising" the muon the classical D^* case (without muon) is recovered. As a side effect, the statistical error of the background subtraction is reduced by a factor $\sqrt{2}$, at the price of a maximal correlation between the unlike sign and like sign $D^* + \mu$ background predictions.

Since we are interested in the shape of the ΔR distribution we have to choose a sample by which not only the normalisation but also the shape of the fake D^* background could be reproduced. This allows us to perform a proper subtraction in each bin of the measured distribution. In order to check that the wrong charge sample describes the combinatorial fake D^* background also in shape we restricted to the D^* sideband were only combinatorial background is present and compared the distribution of some test variables (ΔR, m, $\Delta\phi$). The sideband region is shown as the filled area in the $m(D^0)$–Δm plane in the plots of Figure 5.9 for the $K\pi$ (Left) and $K3\pi$ (Right) modes. The upper plots refer to the right charge sample while the lower ones to the wrong charge sample (which for convenience is displayed in the negative region of the plane). The rectangles indicate the signal mass window. The comparison in shape and normalisation between the wrong charge sample and right charge sample in the sideband is shown in the plots of Figure 5.10. The distributions of the right charge sample and wrong charge D^* sample taken regardless of the

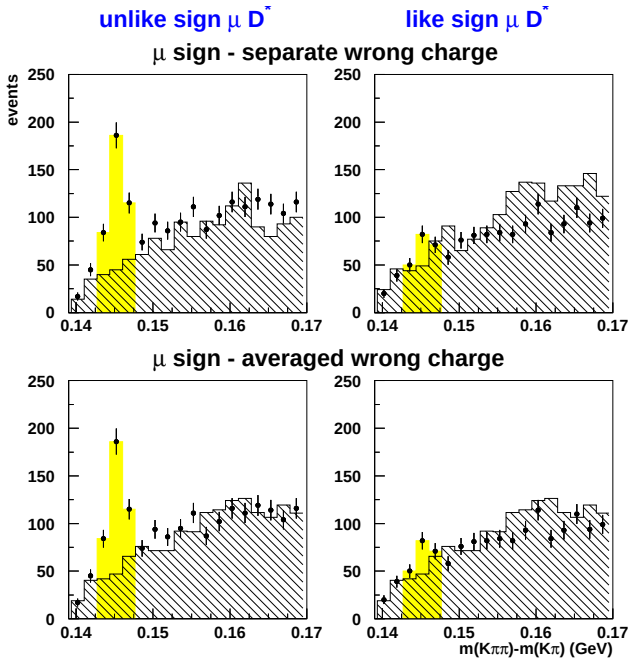

Figure 5.8: *Each plot shows the Δm reconstructed distribution for D^* in the $K3\pi$ mode for the unlike (Left side) and like sign (Right side) samples. The shaded histograms represent the wrong charge combinatorial D^* estimator under different assumptions (top and bottom) as explained in the text.*

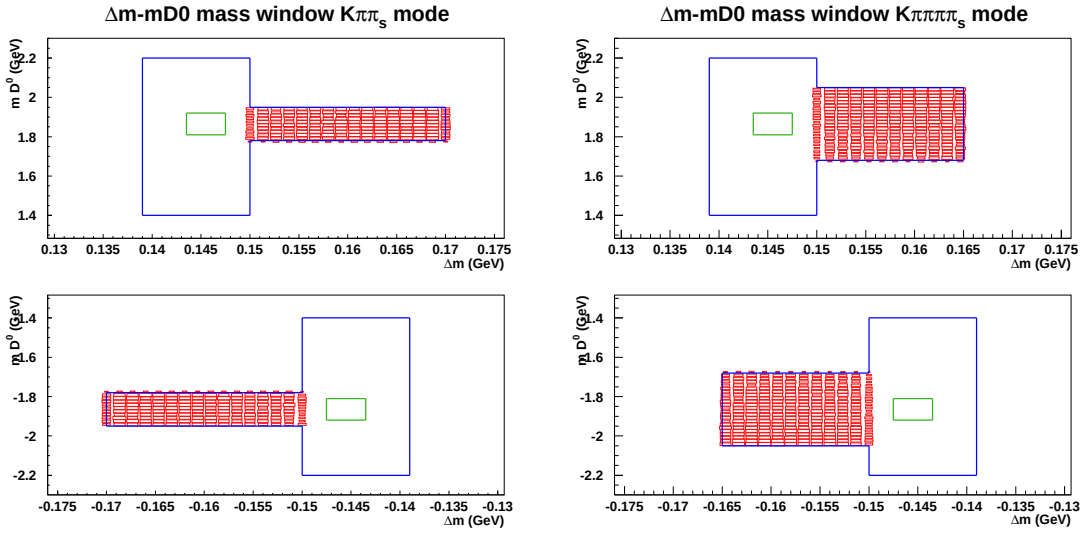

Figure 5.9: *Each plot shows the sideband region (filled area) in the $\Delta m - m(K\pi)$ plane for the right charge (upper histogram) and wrong charge combinations (lower histogram). The rectangle indicates the signal mass region while the other area is the region where preselected D^* data are available. The $K\pi$ channel is shown on the Left side while the $K3\pi$ channel on the Right one. The sideband is defined in the following intervals in $(m(D^0),\Delta m)$ for the $K\pi$ and $K3\pi$ channels respectively: ([1.78,1.95],[0.15,0.17]) GeV and ([1.68,2.05],[0.15,0.165]) GeV.*

muon charge are in good agreement especially for the unlike sign sample. The wrong charge sample taken separately for like and unlike samples suffers instead from normalisation problems similar to those already shown in the upper plots of Figure 5.8 (not shown).

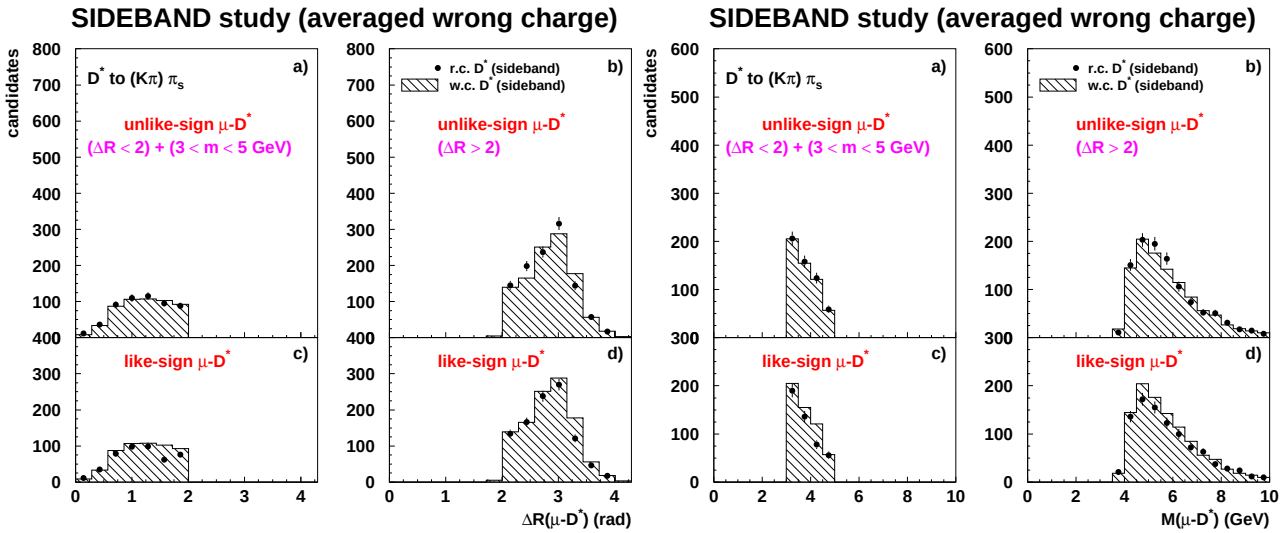

Figure 5.10: *The ΔR (**Left** plots) and m (**Right** plots) distributions in the right charge (bullets) and wrong charge (hatched histogram) sample in the sidebands have been compared for the $K\pi$ D^* mode. The wrong charge sample is taken averaging in the muon sign as described in the text. The unlike sign sample is shown in the upper plots, the like sign sample in the lower ones. The signal enriched region $\Delta R < 2$, $3 < m < 5$ GeV is shown in the Left column, the charm enriched region ($\Delta R > 2$) on the Right. All the analysis cuts have been applied. Both DIS and photoproduction have been included.*

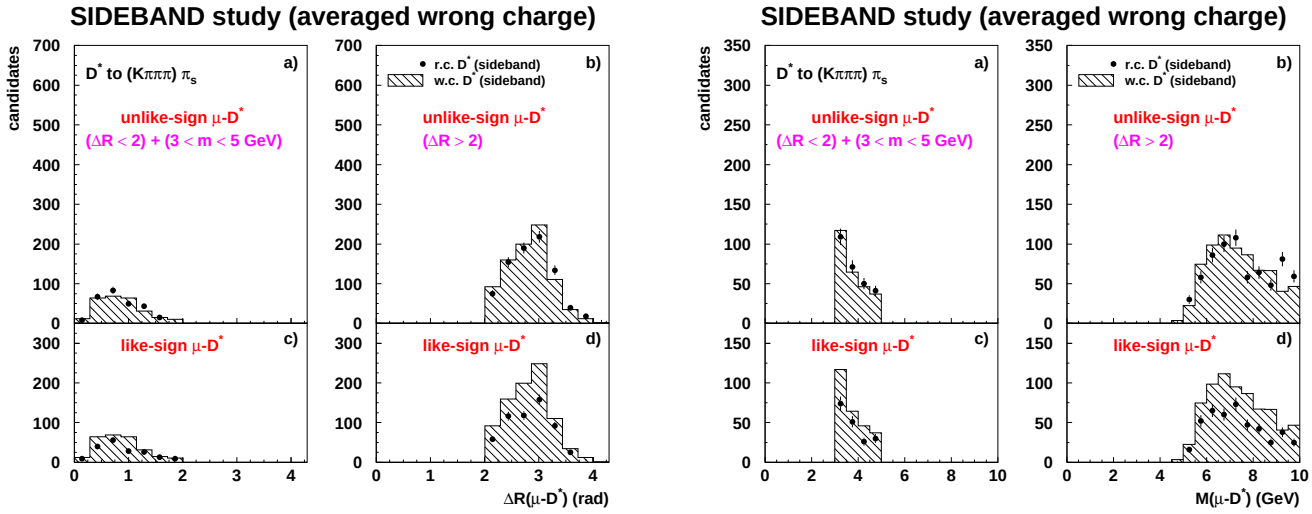

Figure 5.11: *The ΔR (**Left** plots) and m (**Right** plots) distributions in the right charge (bullets) and wrong charge (hatched histogram) sample in the sidebands have been compared for the $K3\pi$ D^* mode. The wrong charge sample is taken averaging in the muon sign as described in the text. The unlike sign sample is shown in the upper plots, the like sign sample in the lower ones. The signal enriched region $\Delta R < 2$, $3 < m < 5$ GeV is shown in the Left column, the charm enriched region ($\Delta R > 2$) on the Right. All the analysis cuts have been applied. Both DIS and photoproduction have been included.*

The $K3\pi$ wrong charge sample is given by combinations having a total charge of ± 2 for the reconstructed D^0 candidate and ± 1 for the D^* candidate. This means that the shape of the fake $D^{*+} \rightarrow (K^-\pi^+\pi^+\pi^-)\pi_s^+$ (charge $+1$) is simulated by taking the $(K^-\pi^-\pi^-\pi^+)\pi_s^+$ combinations (charge -1). Also in this case we compared the right and wrong charge samples in the sideband averaging on the relation between the muon and π_s sign. The result is shown in

Figure 5.11. The normalisation of the like sign is overestimated by the wrong charge sample taken in this way while the unlike sign sample is well reproduced in normalisation and shape. This was the adopted choice in the following.

The combinatorial D^* background can therefore be reliably predicted from the "wrong sign" D^*'s using the scheme defined above.

5.6 Final selection

In Chapter 4 we discussed already in detail the cuts on the muons and D^* mesons. For the latter a different set of cuts was used in the case of photoproduction and deep inelastic scattering. The requirements defining these kinematic regimes were also presented. Further cuts, which we did not describe up to now, and which directly concern the properties of the μD^* pair will be now described:

- The candidate muon track found by the BREMAT algorithm has to be different from one of the tracks composing the D^0 candidate[5].

  This requirement is needed to reject events in which the pion or the kaon from the D^0 decay is misidentified as being a muon. These events, if not rejected, generate a narrow bump at $\Delta R \sim 0$, $\Delta\phi \sim 0$, $m \sim m_{D^*}$ which disappears after requiring the D^0 and muon tracks to be different.

  Part of the cases in which the muon track coincides with the pion from the D^0 are due to real prompt muons from $D^0 \to K^-\mu^+\nu_\mu$ decays. The branching fraction of $D^0 \to K\mu\nu_\mu$ is of the same order of the $D^0 \to K^-\pi^+$ one. Even though heavily suppressed by both the $m_{K\pi}$ and Δm invariant mass cuts this component is of course enhanced by the requirement of a candidate muon in the event. This last source affects the like sign μD^* component only and it is expected, from the Monte Carlo[6], to amount to about 20-30 % of the events in which the pion is misidentified as a muon.

  In Appendix A we measured the probabilities for pions and kaons to yield a muon. In the data it is observed that kaons and pions are almost equally misidentified as muon while in the Monte Carlo it is more likely for a kaon to fake a muon than for a pions for about a factor two. The results obtained with kaons and pions from D^0 were cross checked with independent samples of pions from K^0_s and K from ϕ and found to be in good agreement.

  We have seen that, after requiring the muon and K or π tracks to be different and after applying the μD^* invariant mass cut described in Section 5.3, the fake muon contribution importance is much reduced in the final sample. For this reason, the limited differences which are observed between the fake muon probabilities in data and Monte Carlo (see Appendix A) have only a reduced influence on the final result. This effect will be included in the systematic error.

- The μD^* system is required to carry a significant fraction of the total transverse energy of the event. The ratio of the transverse energy of the μD^* over the total is asked to be above 10 % and 15 % for the $K\pi$ and $K3\pi$ channels in turn.

  This cut was introduced mainly to reduce the combinatorial background contamination. It is similar to the $p_T^{D^*}/E_T$ cut which we studied in Chapter 4. This is illustrated in the Left hand plot of Figure 5.12 in which the distribution for the unlike sign sample in the $K\pi$ mode is shown after all cuts but the one in $p_T^{\mu D^*}/E_T$. As it is visible the wrong charge component (hatched histogram, obtained as described in Section 5.5.2) is mainly concentrated at low values of the fractional p_T. The line marks the used cut value.

  Furthermore charm production, which is characterised by a back to back configuration between the muon and D^* ($\sim$ low transverse momentum of the μD^* system), is suppressed by this cut more than the beauty signal from the same quark to which we are particularly interested. The Right upper plot of Figure 5.12 shows that in the unlike sign sample charm is more peaked at low values of $p_T^{\mu D^*}/E_T$ than beauty, as expected. The lower Right plot shows that in the like sign sample beauty is also peaked at low values but this is less important since this component (μ and D^* from different b quarks) is less easily separated from other backgrounds.

We will now summarize the offline cuts which we imposed to get our final sample.

[5] It never happens the muon to be associated to the π_s track since it has typically too low momentum.

[6] In this context it becomes clear why we chose to use a complete charm Monte Carlo containing all the relevant decay modes rather than a Monte Carlo with a preselection on the reconstructed decay mode.

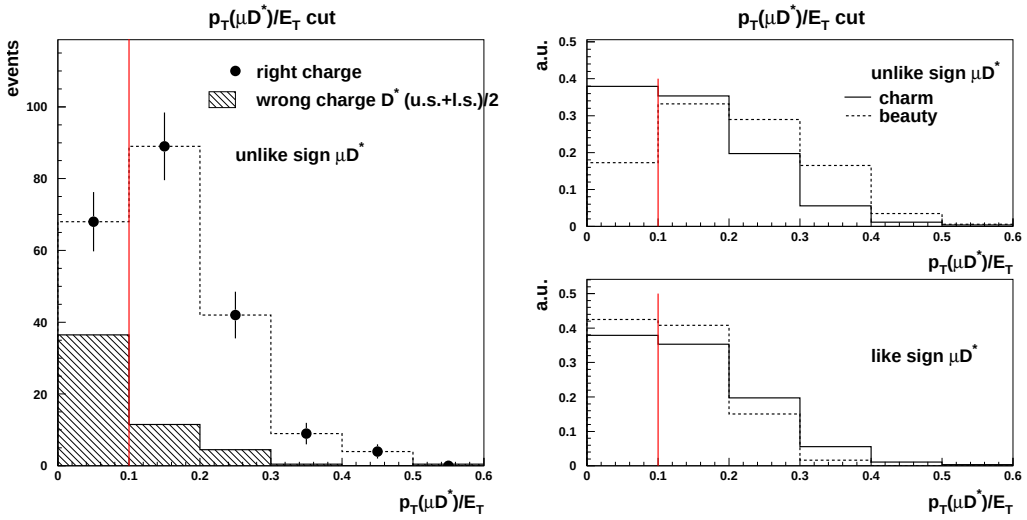

Figure 5.12: **Left**: *Distribution of $p_T^{\mu D^*}/E_T$ in the unlike sign sample for data in the $K\pi$ channel after all cuts except the cut on $p_T^{\mu D^*}/E_T$. The right (bullets) and wrong charge (dashed histogram) D^* samples are shown separately.* **Right**: *Distributions of $p_T^{\mu D^*}/E_T$ for charm (plain line) and beauty (dotted line) in the unlike (top) and like (bottom) sign sample. The vertical line indicates the value of the cut.*

Muons were reconstructed using the Barrel and Rear muon chambers and the BREMAT package. The muon trajectory is reconstructed in the CTD and extrapolated through the UCAL up to the surface of the inner muon chambers where the matching with the BRMUON reconstructed segments is done. Additional cuts on the muon candidate track were:

- $p_T^\mu > 1.4$ GeV
- $-1.75 < \eta^\mu < 1.3$
- BREMAT matching probability $\mathcal{P}_{4\ d.o.f} > 0.01$
- μ track $\neq$ (K or π) track

These cuts have been kept for both the $K\pi$ and $K3\pi$ D^* modes in deep inelastic scattering and photoproduction.

For D^* candidates in the $K\pi\pi_s$ channel we required:

- $1.81 < m_{D^0} < 1.92$ GeV
- $0.1435 < \Delta m < 0.1475$ GeV
- $p_T^{D^*} > 1.9$ GeV, $|\eta^{D^*}| < 1.5$
- $p_T^K > 0.5$ GeV
- $p_T^\pi > 0.5$ GeV
- $p_T^{\pi_s} > 0.125$ GeV
- $\frac{p_T^{\mu D^*}}{E_T^{cal}} > 0.1$

In order to suppress the combinatorial background D^* mesons in the $K\pi\pi\pi\pi_s$ decay channel require a tighter selections as far as the p_T of the D^* and daughter particles is concerned:

- $p_T^{D^*} > 3.8$ GeV
- $\frac{p_T^{\mu D^*}}{E_T^{cal}} > 0.15$
- $p_T^K > 0.35$ GeV
- $p_T^\pi > 0.4$ GeV
- $p_T^{\pi_s} > 0.15$ GeV

Other cuts are the same as for the $K\pi$ channel. In the following we will denote the sample obtained using the above cuts without specific requests on the event being in the photoproduction or deep inelastic scattering regime as *inclusive* sample.

Deep inelastic scattering events were selected by requiring the presence of at least an electron candidate found by the SINISTRA electron finder algorithm having a probability $\mathcal{P} > 0.9$. Other additional cuts on the scattered electron quality and general event kinematics were:

- $Q^2_{el} > 2$ GeV^2
- $E_e > 10$ GeV
- $y_{el} < 0.7$
- $y_{JB} > 0.05$
- $40 < (E - p_Z)_{cal} < 65$ GeV
- e' position: $|x_e| > 13$ cm, $|y_e| > 7$ cm

The complementary photoproduction (PHP) sample is defined by requiring the absence of good DIS candidates according to the given prescriptions and that the events are away from the kinematic peak:

- $(E - P_z)_{cal} < 34$ GeV

In the DIS regime the D^* cuts in the $K\pi$ mode were loosened profiting of the cleaner event topology which is found with respect to photoproduction.

- $p_T^{D^*} > 1.5$ GeV
- $p_T^{K} > 0.4$ GeV
- $p_T^{\pi_s} > 0.12$ GeV
- $p_T^{\pi} > 0.4$ GeV

The cut on the fractional transverse energy of the $D^*\mu$ system was also dropped, the other which we did not repeat are not changed with respect to the general case.

In the $K3\pi$ the DIS subsample alone was statistically too limited and still too affected by combinatorial D^* to be used as a standalone sample for a measurement even after loosening the cuts. The inclusive and photoproduction samples have been then used.

We also required the presence of a well reconstructed vertex having $|Z_{vtx}| < 50$ cm and a trigger signal as defined in Section 4.1. The display of a $b\bar{b}$ candidate event in DIS is shown in Figure 5.13.

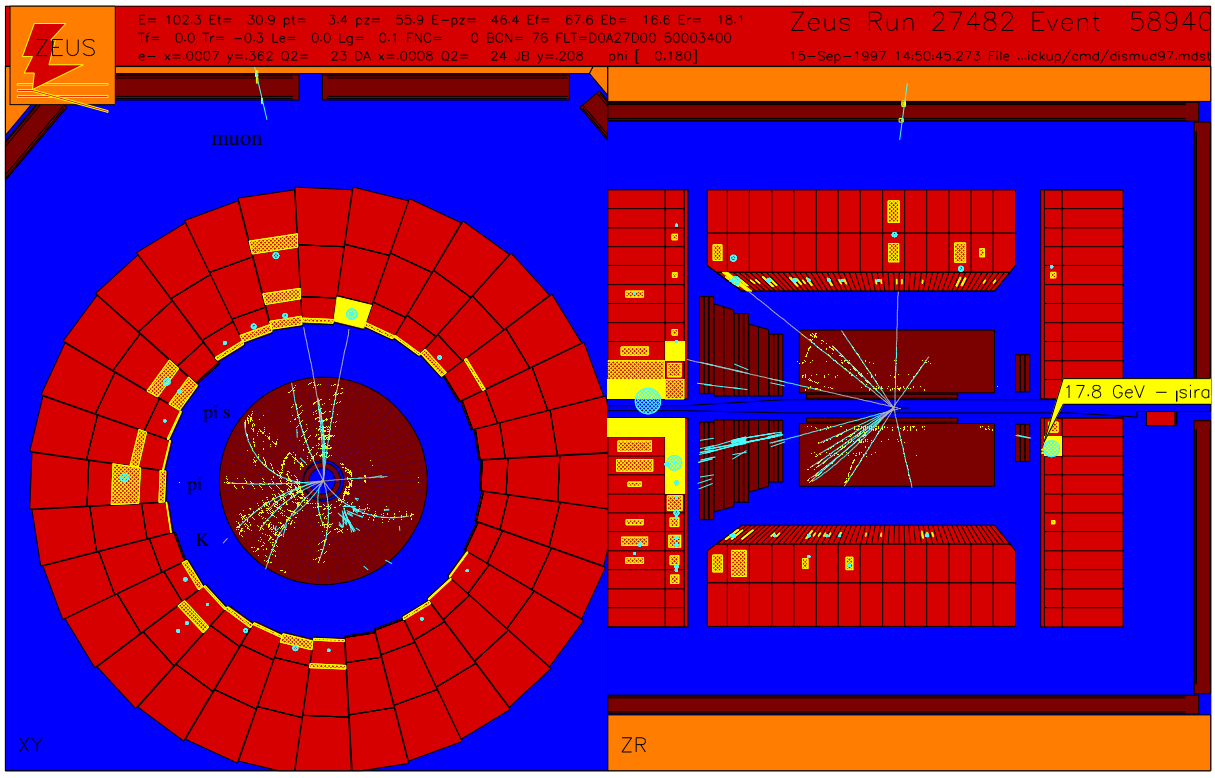

Figure 5.13: *Display of a candidate $ep \to b\bar{b}e'X \to \mu D^* X'$ event.* **Left***: view in the transverse plane.* **Right***: radial view in a plane parallel to the beam axis.*

5.7 Final data samples

D^* meson and muons satisfying all the above cuts, including the trigger requirements, were combined depending on their charge relation into like and unlike sign samples. Those cases in which more than one good muon and/or more than one good D^* were present in the event were treated by taking all possible muon–D^* combinations. This is not a concern in the $K\pi$ selection since, in practice, this situation never occurs. On the contrary, in the $K3\pi$ sample, two muon (D^*) events are found in $\sim$ 4 % (25%) of the cases. As we will see later in the Chapter this multiplicity is reproduced by the Monte Carlo.

The Δm and $m(D^0)$ distributions for the unlike and like sign μD^* combinations in the inclusive $K\pi$ sample are shown separately in the plots of Figure 5.14. The corresponding plots for the DIS subsample are instead presented in Figure 5.15. The Right charge sample is represented with bullets while the hatched histogram refers to the wrong charge sample. The shaded area indicates the D^* signal region.

The prescription described in Section 5.5.2 has been followed, i.e. the wrong charge sample is taken regardless of the muon sign and it is used as an estimator of the combinatorial background for both the unlike and like sign sample. As it is seen in Figures 5.14 and 5.15 even for the final sample the normalisation of the unlike and like sign combinatorial background is indeed well reproduced with this choice. The decrease in the level of this background with respect

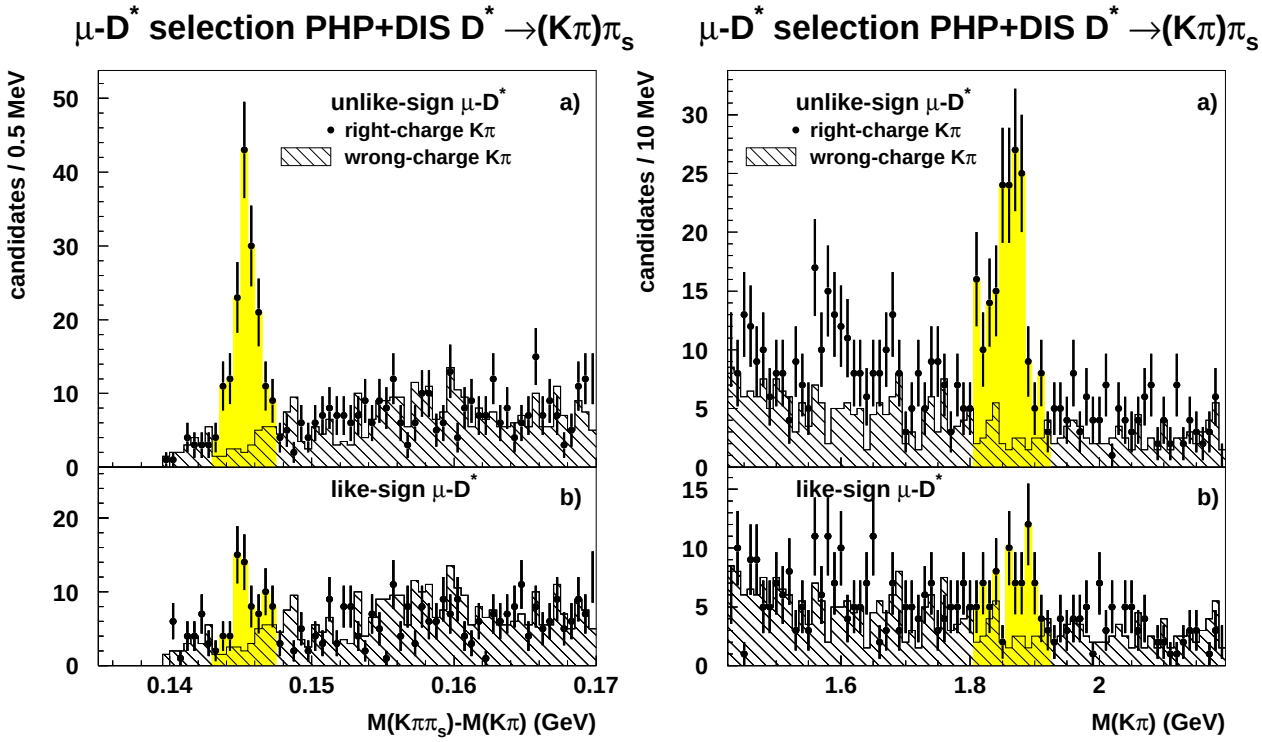

Figure 5.14: *Distribution of* $\Delta m(D^* - D^0)$ (**Left** *side) and* $m(D^0)$ *(* **Right** *side) for data (bullets), and combinatorial background (hatched histogram). The inclusive* $K\pi$ *data sample (PHP+DIS) has been used. The unlike sign (a)) and like sign (b))* μD^* *combinations are shown separately in the upper and lower plots respectively. The* D^* *signal region is indicated by the shaded area.*

to the plots shown previously in Section 4.5 depends mostly on the application of the $p_T^{\mu D^*}/E_T$ cut. The relative importance between the unlike and like sign samples reflects the presence of the different processes that we are about to study. The number of collected events at this stage in the $K\pi$ and $K3\pi$ modes is given in the following Table for the inclusive, photoproduction and DIS, samples:

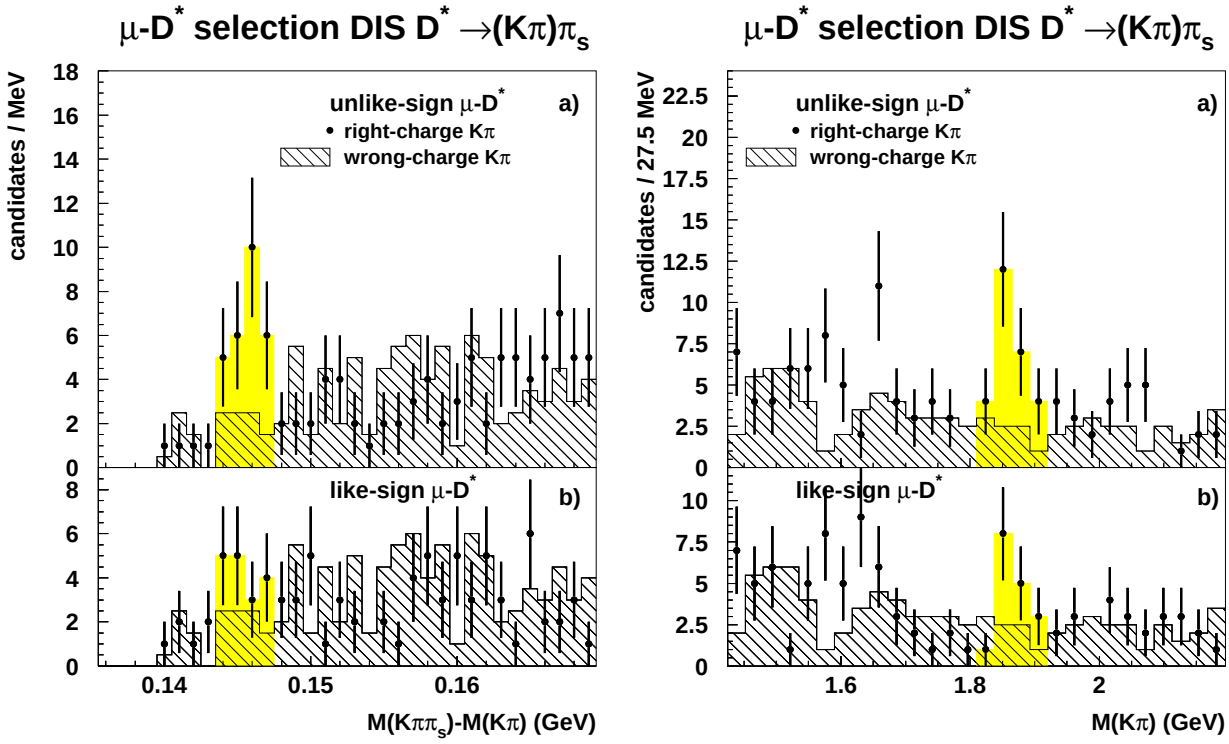

Figure 5.15: *Distribution of* $\Delta m(D^* - D^0)$ (**Left** *side) and* $m(D^0)$ *(* **Right** *side) for data (bullets), and combinatorial background (hatched histogram) for the* $K\pi$ *DIS sample. The unlike sign (a)) and like sign (b)) muon-*D^* *combinations are shown separately in the top bottom plots respectively. The* D^* *signal region is indicated by the shaded area.*

Channel	$K\pi$			$K3\pi$	
Regime	*PHP+DIS*	*PHP*	*DIS*	*PHP+DIS*	*PHP*
unlike sign μD^*	173	140	27	130	94
like sign μD^*	74	59	17	35	20
wrong charge D^*	0.5·(25+35)	0.5·(21+31)	0.5·(8+10)	0.5·(64+58)	0.5·(45+38)

The equivalent plots for the $K3\pi$ mode are shown in Figure 5.16 for the inclusive sample. The combinatorial D^* background in the unlike sign sample is correctly described by the average of the like sign and unlike sign sample as in the $K\pi$ case while the same sample overestimates the wrong charge combinations by a factor ~ 1.7. The wrong charge sample has been reweighted by this factor in order to reproduce the like sign fake D^* data in the lower plot of Figure 5.16. We chose then to consider the unlike sign sample only and to estimate the combinatorial background with the same procedure we used in the $K\pi$ channel.

5.8 Extraction of events from b decays

In the following, the signal extraction procedure is described for the inclusive sample in the $K\pi$ mode. The DIS sample, which has significantly less statistics, and the $K3\pi$ sample have been treated in an analogous way.

To distinguish the topologies of beauty decays from charm events, fake D^*'s and fake muons, we have proceeded in several steps.

First, events with a D^* and muon candidate according to all cuts outlined above except for the $\Delta m(D^* - D^0)$ mass cut were selected (Left plots in Figure 5.17). The side bands of the D^* peak provide the normalisation of the fake D^* contribution, obtained from the data. The distributions are shown for like and unlike sign μD^* events separately. The

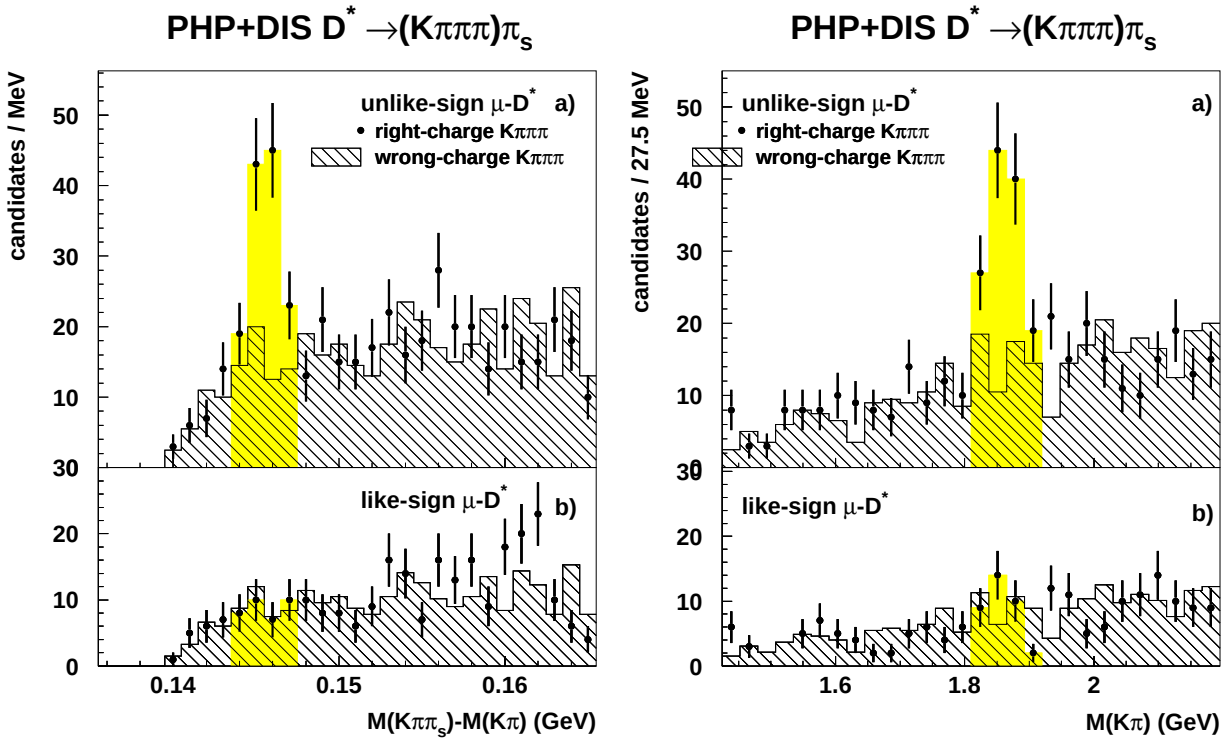

Figure 5.16: *Distribution of $\Delta m(D^* - D^0)$ for $K3\pi$ data (bullets), and combinatorial background (hatched histogram) for a) inclusive unlike sign b) inclusive like sign. In the like sign plot the wrong charge component obtained by averaging on the muon sign overestimates the like sign combinatorial background by a factor 1.7. The hatched histogram shown in the like sign plot has then been weighted accordingly in order to reproduce the like sign combinatorial background. The D^* signal region is indicated by the shaded area.*

expected signal and background contributions, normalised to the fractions determined later in the analysis, are also indicated cumulatively by the histograms with different hatch styles (see the legend).

Next, the Δm mass window cut was applied. The angular difference $\Delta R = \sqrt{\Delta\phi^2 + \Delta\eta^2}$ between the D^* and the muon after this cut is shown in the central plots of Figure 5.17. It becomes clear that, for unlike sign events, the region of $\Delta R > 2$ is dominated by events from charm (predominantly back-to-back configuration). In contrast, the region of $\Delta R < 2$ is enriched in beauty events in which in which the D^* and muon originate mainly from decays of the same parent B hadron.

This is illustrated further in the upper Right hand plot of Figure 5.17 which shows the μD^* invariant mass distribution for events in the beauty-enriched region ($\Delta R < 2$). A hump which can be attributed to the partial reconstruction of the decaying B meson is clearly visible. A comparison with the like sign sample shows that the low-mass edge of this peak is dominated by background. No hump is observed in the like sign sample, as expected. It becomes now clear from the data themselves the benefits of applying a cut at 3 GeV $< m_{\mu D^*} <$ 5 GeV to the $\Delta R < 2$ subsample in terms of background reduction (mainly from combinatorial D^* and fake muons).

The ΔR and $\Delta\phi$ distributions in the inclusive sample, after this additional cut and after subtraction of the fake D^* background, are shown in the two upper plots of Figure 5.18 together with a fit of the relative contributions from charm and beauty. The charm and beauty fitting histograms have also been subtracted of their wrong charge D^* component. The fake muon background (from charm) was fixed to the relative fraction predicted by the Monte Carlo simulation. The variation of this contribution within the limits allowed by the like sign sample (which is dominated by this background) is part of the systematic uncertainty quoted below. The beauty, charm (prompt μ and fake μ) contributions are shown cumulatively and are distinguished by different hatch styles (see the legend). The beauty histogram also includes a small component due to fake muons which, for graphical clearness, was not shown separately.

Since the background and signal components are well separated the signal extraction procedure is not particularly critical. A binned fit with the Monte Carlo histograms was used to estimate the signal fraction in the final sample (f_b).

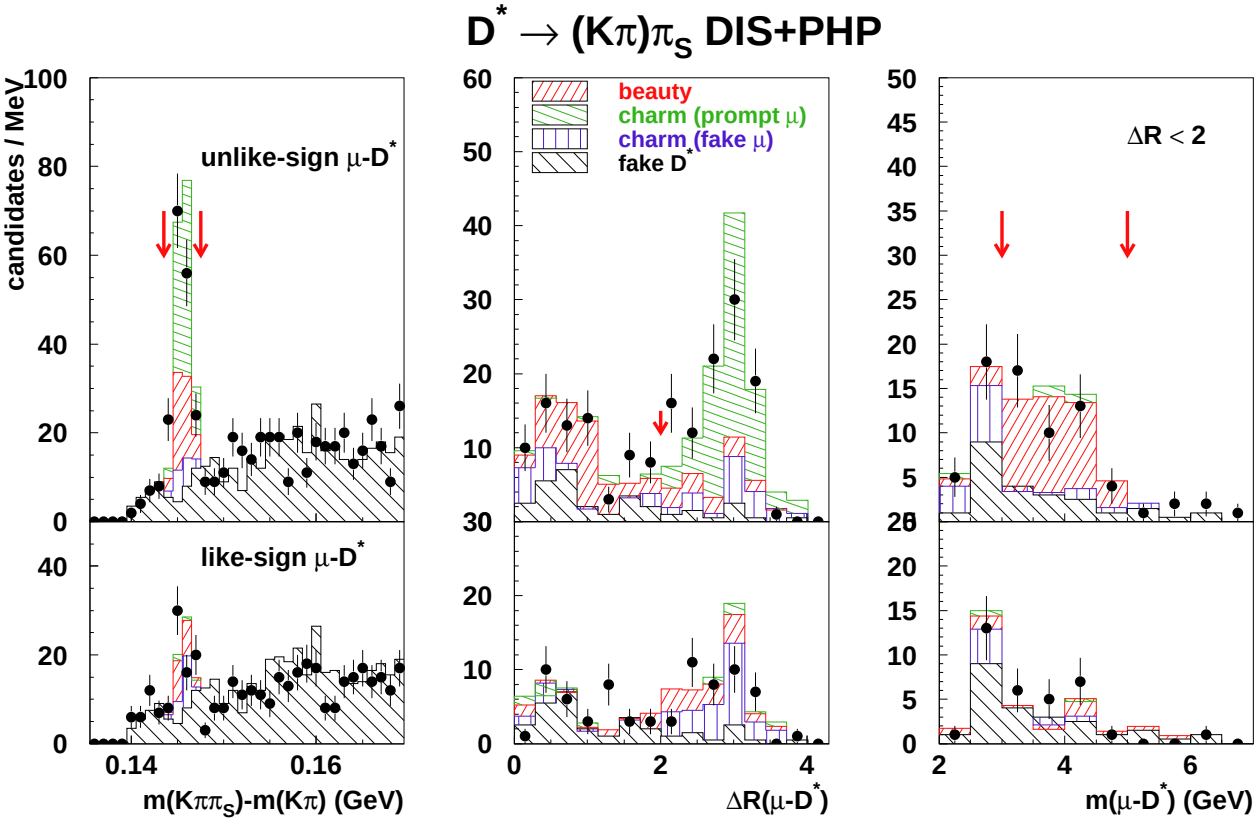

Figure 5.17: *Distribution of* $\Delta m(D^* - D^0)$ *(***Left***)* $\Delta R(D^* - \mu)$ *(***Center***) and* $m(D^* - \mu)$ *(***Right***) for data (bullets), heavy flavour signal (red hatched: beauty, green hatched: charm) and background (blue: fake* μ*, gray:* D^**). Cuts described in the text are indicated by red arrows.*

If we denote the normalised distributions of signal, background and data after wrong charge D^* subtraction as S_i, B_i, D_i ($i = 1, \ldots, N$ being the bin index) we can build a fitting function F_i as a linear combination of S_i and B_i:

$$F_i(\alpha) = \alpha \cdot S_i + (1 - \alpha) \cdot B_i \tag{5.9}$$

A first estimate of the beauty fraction was obtained by evaluating the value of the parameter α for which the χ^2 function meets its minimum:

$$\chi^2(\alpha) = \sum_{i=1}^{N} \frac{(D_i - F_i(\alpha))^2}{\sigma_i^2} \qquad \frac{\partial \chi^2}{\partial \alpha}\Big|_{\alpha = f_b} = 0$$

Binomial errors were used for low statistics bins. In this first approach the Monte Carlo statistical uncertainty is not taken into account. In order to properly treat this aspect we also used a more refine approach which minimizes a likelihood function expressed as the product of Poisson probabilities for data and Monte Carlo in each bin. The algorithm is implemented in the HMCMLL[165] CERN library routine. The two methods provide consistent values for the signal fraction. In the following the quoted statistical errors have been obtained from the HMCMLL program.

The results on the signal component as given by the ΔR fit after all the above described cuts will be now presented for the $K\pi$ and $K3\pi$ modes in the inclusive, photoproduction and (for $K\pi$ only) DIS samples.

5.8.1 Beauty signals in the $K\pi$ channel

The result for the fraction of beauty events in the final inclusive sample shown in the upper plots of Figure 5.18, using the shapes predicted by PYTHIA, is:

- $f_b^{PHP+DIS} = 0.363 \pm 0.084$ (stat.) from the $\Delta R_{\mu D^*}$ fit
- $f_b^{PHP+DIS} = 0.348 \pm 0.080$ (stat.) from the $\Delta \phi_{\mu D^*}$ fit

The ΔR result was chosen as the reference, and the $\Delta \phi$ result used as a systematic check. With these fitted fractions, the $\Delta m(D^* - D^0)$ distributions are shown separately for the signal enriched (Left plots) and charm enriched regions (Right plots) in Figure 5.19. The upper plots correspond to the unlike sign sample, the lower ones to the like sign sample. The corresponding number of beauty, charm, and fake muon candidates is indicated in each case. In the unlike sign part (upper plots), the beauty and charm contributions are well separated, with only small cross-contaminations. The low ΔR region in the like sign sample consists mainly in fake D^*s while at high ΔR we have a paritetic admixture of beauty (from different b quarks) and fake muons. Agreement is seen, even in the like sign part, which was not included in the fit. No independent normalisation was in this case introduced. This is an important cross check of the systematics of the signal extraction procedure. The fake muon component in particular is constrained by the like sign sample at high ΔR.

The fitted beauty fractions in the photoproduction subsample are:

- $f_b^{PHP} = 0.362 \pm 0.097$ (stat.) from the $\Delta R_{\mu D^*}$ fit
- $f_b^{PHP} = 0.336 \pm 0.085$ (stat.) from the $\Delta \phi_{\mu D^*}$ fit

Analogous results for the DIS sample are shown in Figure 5.18 and 5.19. In this case the charm component was not further subdivided into a fake and prompt muon component. The fitted beauty fractions, using the shapes predicted by RAPGAP, are

- $f_b^{DIS} = 0.51 \pm 0.25$ (stat.) from the $\Delta R_{\mu D^*}$ fit
- $f_b^{DIS} = 0.45 \pm 0.33$ (stat.) from the $m_{\mu D^*}$ fit

Again, the ΔR result is chosen as the reference, and the other as a cross check.

5.8.2 Beauty signals in the $K3\pi$ mode

The procedure outlined for the $K\pi$ channel has been repeated for the $K3\pi$ channel. The resulting ΔR and $\Delta \phi$ fits are shown for the inclusive sample, with the usual meaning of symbols, in Figure 5.20. The fitted b fraction for the inclusive sample is:

- $f_b^{PHP+DIS} = 0.368 \pm 0.08$ (stat.) from the $\Delta R_{\mu D^*}$ fit
- $f_b^{PHP+DIS} = 0.285 \pm 0.07$ (stat.) from the $\Delta \phi_{\mu D^*}$ fit

The final signal component in the photoproduction sample is instead determined as:

- $f_b^{PHP} = 0.286 \pm 0.09$ (stat.)
- $f_b^{PHP} = 0.205 \pm 0.085$ (stat.)

from a fit to the $\Delta R_{\mu D^*}$ and $\Delta \phi_{\mu D^*}$ respectively.

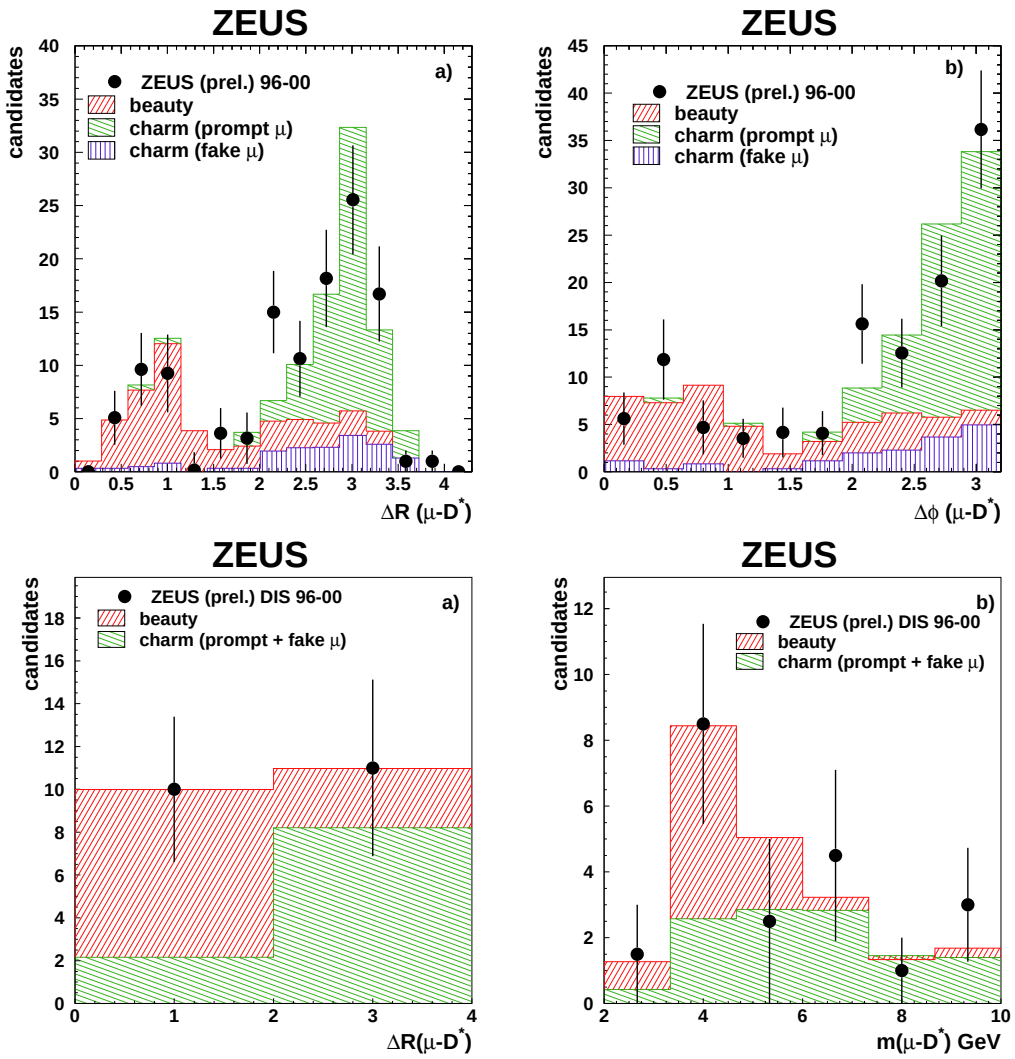

Figure 5.18: *a) ΔR and b) $\Delta\phi$ distributions of the μD^* system for inclusive unlike sign events, after subtraction of the fake D^* background. Data points (bullets) are shown together with the fitted contributions from beauty and charm, as indicated in the legend. The fake muon contribution from charm is shown separately, but fitted together with the charm contribution. The beauty contribution includes a very small fraction of fake muons from beauty.*

5.9 Data–Monte Carlo comparison: control plots

The extracted fraction of b events can be cross checked by comparing the measured kinematic distributions with those obtained by mixing the Monte Carlo histograms according to the fractions measured in the ΔR fits. In doing this comparison the normalisation of the Monte Carlo mixture has been fixed to be equal to that of the data. We considered the unlike sign sample. The data-Monte Carlo shape comparison has been performed for the photoproduction sample in the signal enriched region ($\Delta R_{\mu D^*} < 2$, $3 < m_{\mu D^*} < 5$ GeV) (Left side plots of Figure 5.21) and in the charm enriched region ($\Delta R_{\mu D^*} > 2$, no mass cut) (Right side plots of Figure 5.21). The expected fraction of beauty and charm is $\simeq 90$ %, $\simeq 10$ % and $\simeq 15$ % ,$\simeq 85$ % in the signal and background regions respectively. In these plots no distinction has been made between the fake an prompt muon component in the charm Monte Carlo. The hatch styles meaning follows the already used conventions.

The comparison between the muon and D^* transverse momentum, pseudorapidity, azimuthal angle have been considered. For the muon, in addition, the matching probability $\mathcal{P}_{4\ d.o.f.}$ and its "isolation" were also included. This last variable is constructed by counting the number of tracks with momentum above 1 GeV in a cone of 0.5 units in the

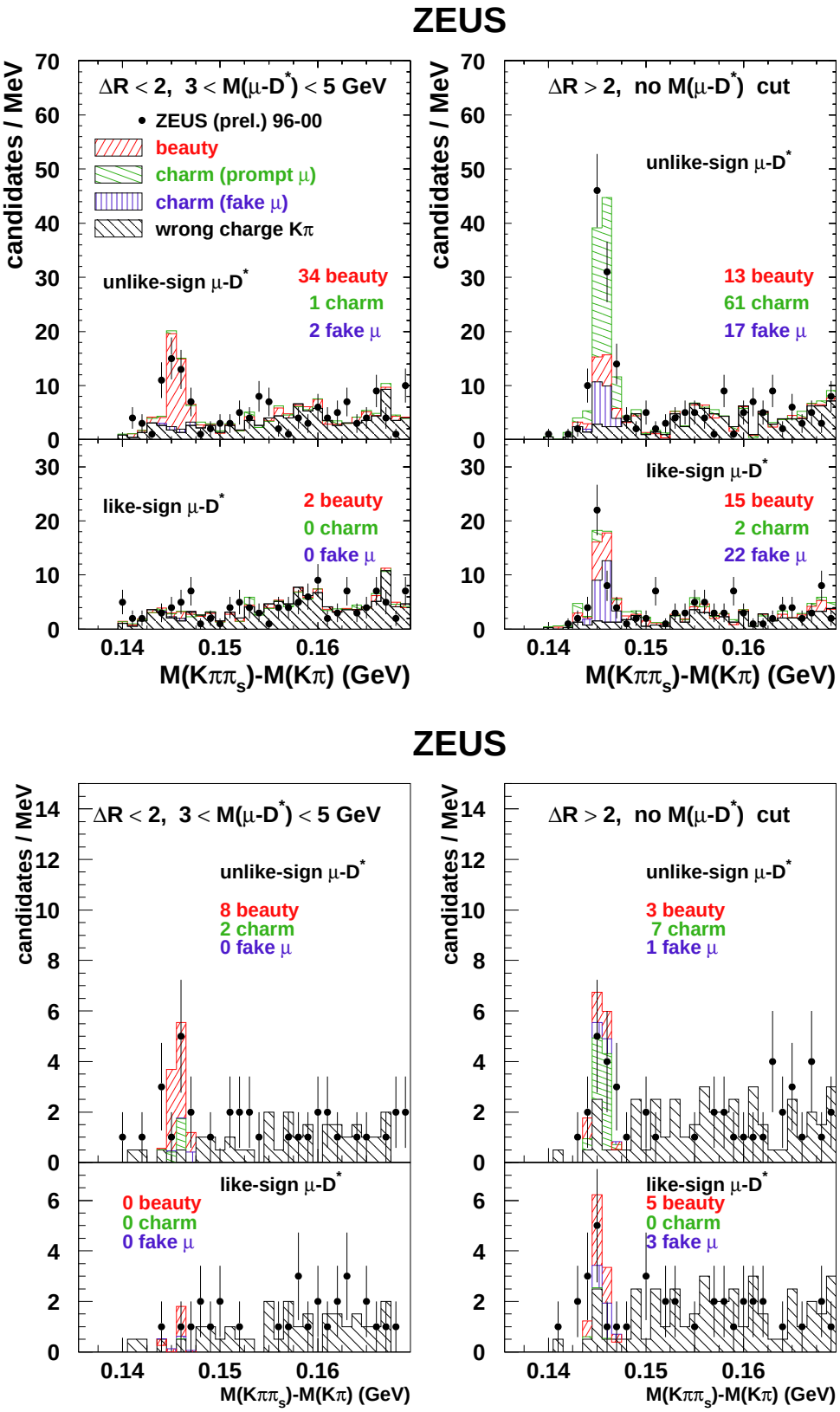

Figure 5.19: $\Delta m(D^* - D^0)$ *distributions for four different regions of inclusive phase space. The data are shown as full circles. The beauty and charm contributions, and the fake muon and combinatorial* D^* *backgrounds are indicated as shown in the legend. The number (rounded to the nearest integer) of beauty, charm and fake muon candidates is indicated in each figure.*

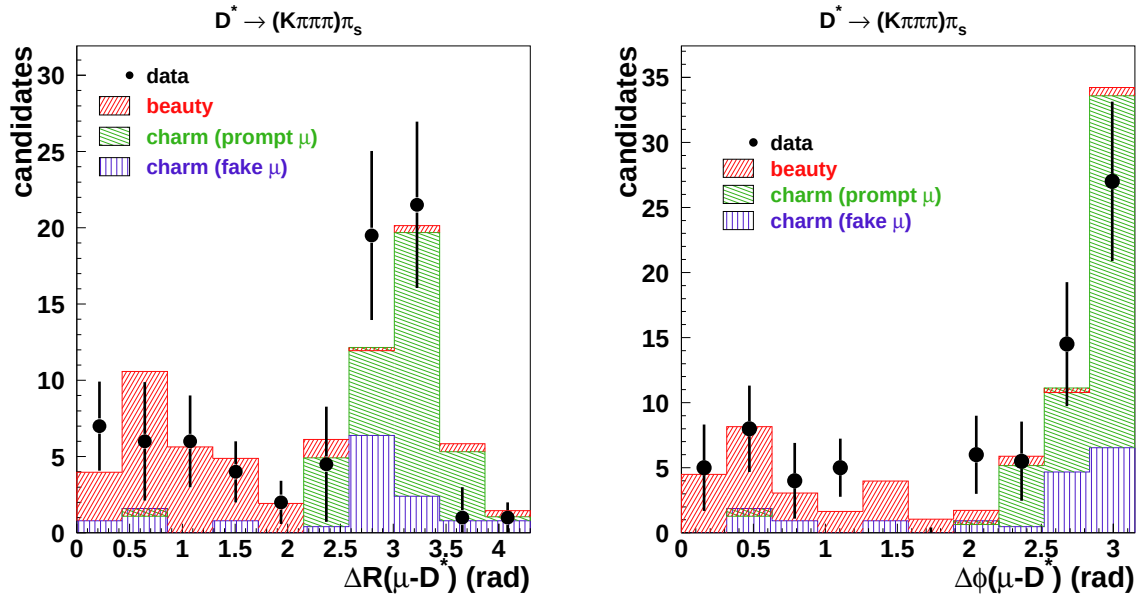

Figure 5.20: *a) ΔR and b) $\Delta\phi$ distributions of the μD^* system for inclusive unlike sign events, after subtraction of the fake D^* background. Data points (bullets) are shown together with the fitted contributions from beauty and charm, as indicated in the legend. The fake muon contribution from charm is shown separately, but fitted together with the charm contribution. The beauty contribution includes a very small fraction of fake muons from beauty.*

$\eta - \phi$ plane centered in the matched track. The overall description in the charm region is quite good. In the beauty enriched region the transverse momentum of the muon and the D^* tends to be harder in the Monte Carlo.

Several other variables have been included in the data–Monte Carlo comparison. The corresponding plots have been collected, for graphical convenience, in Appendix B. Here general event variables have been taken into account such as the $E - p_z$, Z_{vtx}, the total number of tracks and the number of vertex refitted tracks, the multiplicity of good muon and D^* candidates. These variables are generally well reproduced by the Monte Carlo in both regions. In addition to the already introduced ΔR, $\Delta\phi$ and m variables, other quantities related to the $D^*\mu$ system have been considered: the difference in polar angle ($\Delta\theta^{\mu-D^*}$), the angle in space between muon and D^* ($\Omega^{\mu D^*}$), the momentum, transverse momentum, polar angle and rapidity of the μD^* system, the relative transverse momentum of the muon with respect to the D^* ($p_T^{rel\ \mu D^*}$) and finally the fractional transverse energy ($p_T^{\mu D^*}/E_T$).

The description provided by the Monte Carlo is overall good with the possible exception of the $p_T^{\mu D^*}$ and $p_T^{\mu D^*}/E_T$ variables in the $K\pi$ channel and $p_T^{\mu D^*}/E_T$ in the $K3\pi$ channel for the beauty region. The observed distribution in the data appear to be somehow softer than in the Monte Carlo. This issue will be addressed extensively in the discussion of systematic uncertainties. Concerning other variables for which charm and beauty have different shapes, as $\Delta\theta^{\mu-D^*}$, $\Omega^{\mu D^*}$, $p_T^{rel\ \mu D^*}$, $\theta^{\mu D*}$ or the equivalent $y_{\mu D^*}^{rap}$ the observed correspondence between data and Monte Carlo provides support to the goodness of our signal extraction procedure. It must also be noted that the matching probability is nicely reproduced. As we have seen in Section 4.4.1 this variable provides a partial sensitivity to the relative importance of prompt and fake muons. This further indicates that this background is under control.

The data–Monte Carlo shape comparison has been repeated for the DIS subsample without separating the beauty and charm enriched regions to retain a statistically significant sample. The specific DIS variables were added: the Q^2 and the scattered electron energy E_{el}. The result is shown in Figure 5.22. The description of all variables is good. The histograms referring to the $K3\pi$ mode are shown in Figure 5.23. Both the charm and beauty regions are reasonably described.

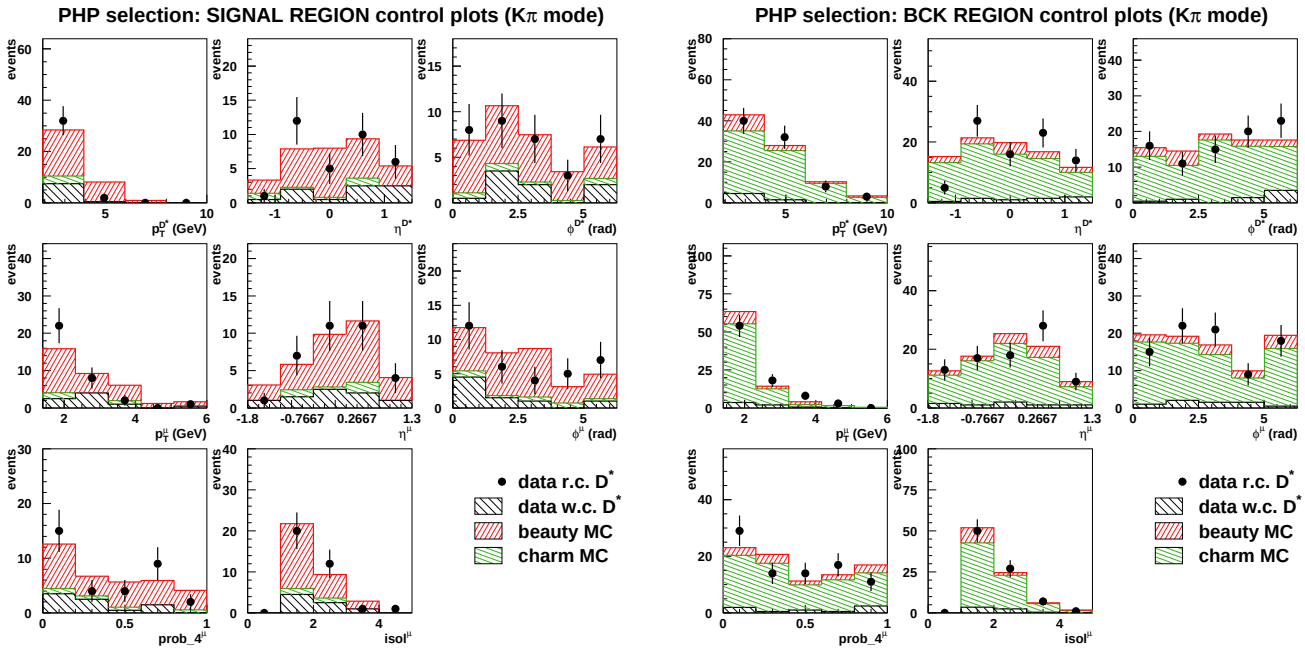

Figure 5.21: *Control plots for the photoproduction selection for events with a $D^* \to (K\pi)\pi_s$ in the beauty (***Left*** *plots) and charm (***Right*** *plots) enriched region. The beauty, charm and fake D^* components are indicated with different hatch styles (see legend).*

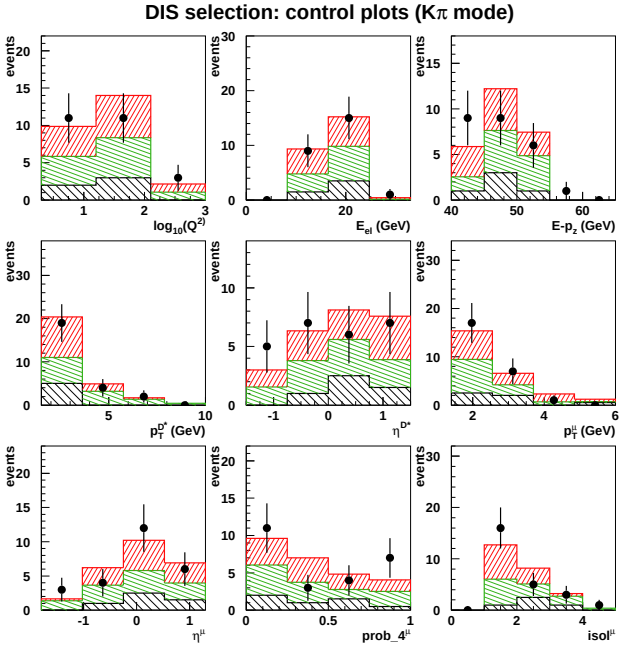

Figure 5.22: *Control plots for the DIS subsample in the $K\pi$ mode. The meaning of hatch styles is the same of Figure 5.21.*

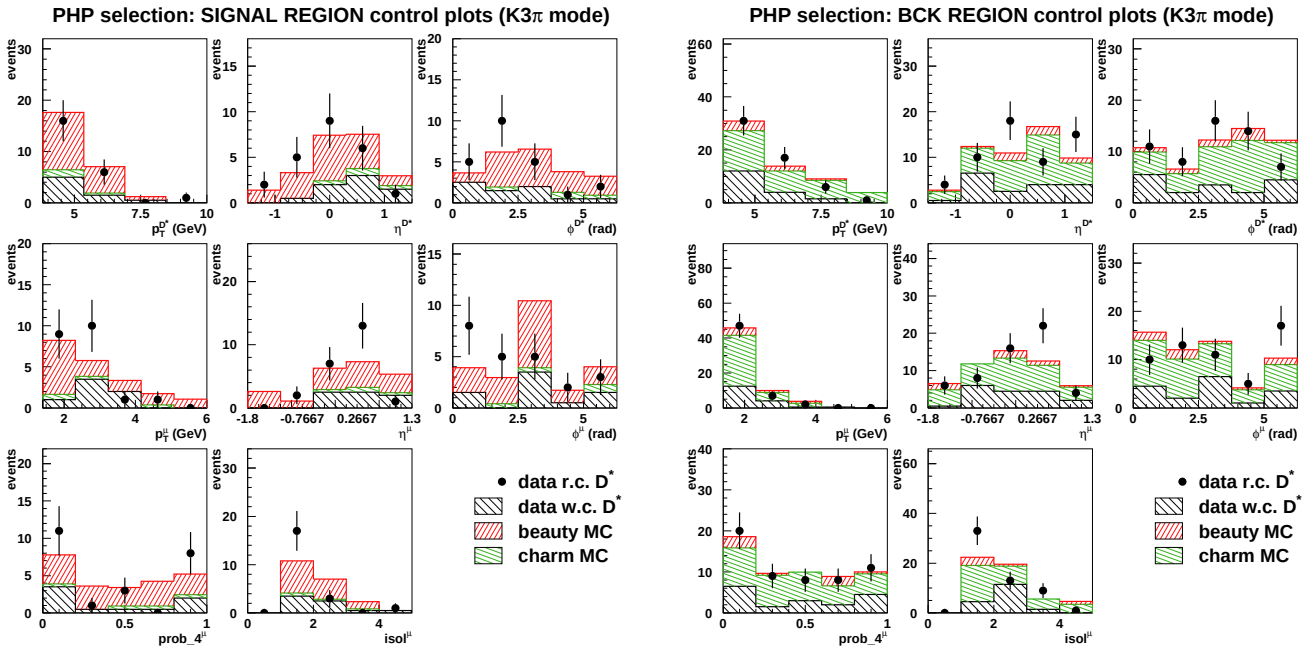

Figure 5.23: *Control plots for the photoproduction selection for events with $D^* \rightarrow (K\pi\pi\pi)\pi_s$ in the signal (***Left***) and background (***Right***) region. The beauty, charm and fake D^* components are indicated with different hatch styles (see legend).*

5.10 Visible cross section measurement

Having estimated the number of collected signal events and cross checked that the Monte Carlo provides a reasonable description of all the relevant observables, we will now calculate the cross section for the process

$$ep \rightarrow b\bar{b}X \rightarrow \mu D^* X' \tag{5.10}$$

in a kinematic region which we chose to be close to the one in which the measurement was performed (hence the adjective *visible*). The total visible cross sections have been derived according to the following formula:

$$\sigma_{vis} = \frac{f_b \cdot N^{u.s.}_{data}}{\mathcal{A} \cdot \mathcal{L} \cdot \mathcal{B}} \tag{5.11}$$

We indicate with $N^{u.s.}_{data}$ the number of (wrong charge D^* subtracted) unlike sign events in the data satisfying all the imposed selection cuts. f_b represents the fraction of these events being signal events according to the ΔR fit. $\mathcal{L}$ denotes the integrated luminosity of the used data sample (114 pb^{-1}) and $\mathcal{B}$ is the branching ratio of the used D^* decay mode.

With $\mathcal{A}$ we denote the *acceptance*. This quantity represents the reduction factor, evaluated on a signal Monte Carlo, which is needed to convert the number of events produced in the considered kinematic region at true level (N_{kin}) to the subsample of those, belonging to the unlike sign sample, which are experimentally measured ($N^{u.s.}_{b\ rec}$). As for $N^{u.s.}_{data}$, $N^{u.s.}_{b\ rec}$ in intended after the subtraction of the wrong charge D^* component.

In the definition of N_{kin}, we only counted those D^* decaying in the particular channel which was reconstructed [7]. Dividing by the branching ratio we extend the cross section to inclusive D^* production thus extrapolating for the experimentally observed decay channel. The used values for $\mathcal{B}$ are those in Equations 5.1 and 5.2.

[7] The selection of the interesting decay mode in the evaluation of N_{kin} is needed in order to avoid possible biases due to the D^* mode dependent generation cuts in the used Monte Carlo (see Section 3.6).

The acceptance evaluates the detector intrinsic and geometrical inefficiencies and the effect of the experimental cuts which are not taken into account in the definition of the kinematic regions (e.g. the muon probability cut).

$$\mathcal{A} \equiv \frac{N_{b\,rec}^{u.s.}}{N_{kin}} \tag{5.12}$$

A correct acceptance evaluation is an essential ingredient in the cross section calculation. Particular care is needed in the muon correction. The inefficiencies of the barrel and rear muon chambers are in fact not completely reproduced by the standard ZEUS Monte Carlo (MOZART). The simulation lacks the implementation of a complete list of dead limited streamer tubes (LST). In addition, during the data taking the bias voltage applied to the LST tubes was lower than the one corresponding to the efficiency plateau. At lower voltages a longer detector lifetime is expected. Still the inefficiency of the detector due to its geometrical acceptance (angular coverage, cracks between the chambers) is correctly implemented in the Monte Carlo.

In order to correct for the effect of non simulated inefficiencies dedicated studies have been performed based on real data. An excellent sample for these kind of studies comes from the decay in dimuons of diffractively produced J/ψ mesons as well as dimuon production in the *Bethe-Heitler*[8]. In a previous study [166] on this topic the efficiency has been evaluated by selecting the track which fired the muon trigger and taking the other one as an unbiased probe of the BRMUON response. The results obtained in this study have been used for our efficiency corrections. The ratio between the efficiency found in the data and in the Monte Carlo without the whole inefficiency treatment (δ *eff*) is shown as a function of p of the muon track for the rear region and as a function of p_T in the barrel region in Figure 5.24. This parametrisation has been chosen since the physically meaningful variable as far as the probability of traversing a certain amount of material is concerned, is the component perpendicular to the material itself. The Monte Carlo events were weighted according to the values of Figure 5.24 depending on the (transverse) momentum of the candidate muon track.

The kinematic regions in which we decided to measure our visible cross sections are close to the offline cuts. The definitions for the $K\pi$ channel are here given for the inclusive, photoproduction and DIS samples:

$K\pi$ *DIS+PHP*	$K\pi$ *PHP*	$K\pi$ *DIS*
$p_T^\mu > 1.4$ GeV, $-1.75 < \eta^\mu < 1.3$	$p_T^\mu > 1.4$ GeV, $-1.75 < \eta^\mu < 1.3$	$p_T^\mu > 1.4$ GeV, $-1.75 < \eta^\mu < 1.3$
$p_T^{D^*} > 1.9$ GeV, $\lvert\eta^{D^*}\rvert < 1.5$	$p_T^{D^*} > 1.9$ GeV, $\lvert\eta^{D^*}\rvert < 1.5$	$p_T^{D^*} > 1.5$ GeV, $\lvert\eta^{D^*}\rvert < 1.5$
	$0.05 < y < 0.85$, $Q^2 < 1$ GeV^2	$0.05 < y < 0.7$, $Q^2 > 2$ GeV^2

The corresponding kinematic regions for the inclusive and photoproduction $K3\pi$ samples are obtained from the ones in the $K\pi$ channel by raising the $p_T^{D^*}$ cut from 1.9 to 3.8 GeV.

The values of acceptances corrected for this effect are given in Table 5.2. They amount to $\sim$ 7-8 % up to $\sim$ 10 % if both like and unlike sign μD^* pairs are considered. For each region HERWIG was used as a systematic check of the PYTHIA/RAPGAP results. HERWIG predicts acceptances which, within the statistical error are compatible to the one predicted by the central Monte Carlo even if in general, except for the $K3\pi$ channel, they tend to be higher for about 5–10 %. This model dependence will be included in the systematic error.

To give an idea of the relative importance of the muon and D^* reconstruction in the global acceptance we have plotted the distributions in p_T and η for muons and D^*s at true and reconstructed level in the Left hand plots of Figure 5.25. The used cuts on muons and D^* mesons are those of the photoproduction selection except for the trigger requirements The dependence of the reconstruction efficiency as a function of the muon and D^* η and p_T is shown in the Right hand plots of Figure 5.25. The acceptance rise with the p_T and decreases at the limit of the considered pseudorapidity region. The structures seen in the muon plots are due to the geometry of the BRMUI detector. The muon reconstruction gives a contribution to the acceptance which is about 1.4 times the D^* one.

5.10.1 Visible cross sections in the $K\pi$ mode

The obtained beauty fraction in the inclusive sample was used to measure the cross section for the process $ep \to eb\bar{b}X \to eD^*\mu X$ in the kinematic range $p_T^{D^*} > 1.9$ GeV, $-1.5 < \eta^{D^*} < 1.5$, $p_T^\mu > 1.4$ GeV and $-1.75 < \eta^\mu < 1.3$. The final number of unlike sign events is made up of 135 μD^* pairs of which about 16 arise from D^* combinatorial

[8] di-lepton production via the QED diagrams involving two incoming photons, one from the proton and one from the electron (positron) are often referred as Bethe–Heitler processes.

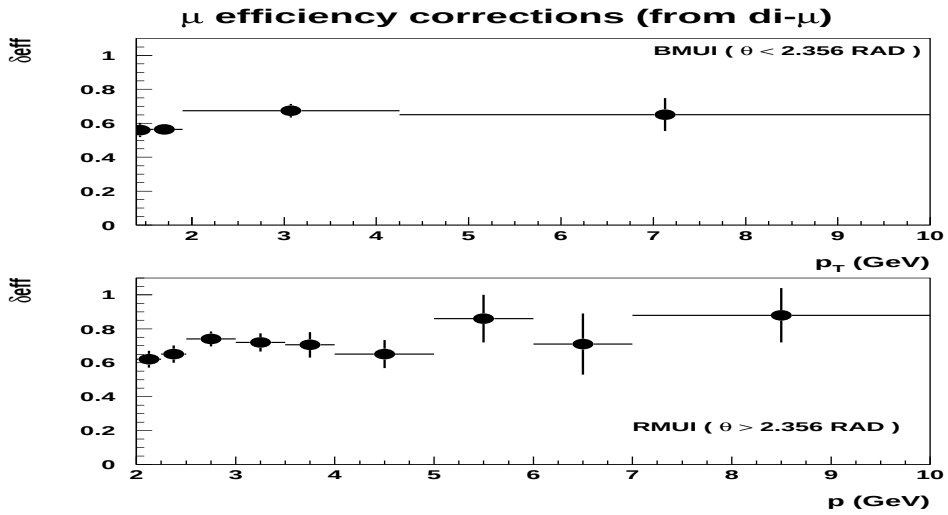

Figure 5.24: **Top** *plot: Muon efficiency corrections for tracks in the barrel region ($\theta < 2.356$ rad) as a function of their transverse momentum.* **Bottom** *plot: efficiency corrections for tracks in the rear region ($\theta < 2.356$ rad). The correction factors have been obtained from a dimuon sample as described in [166].*

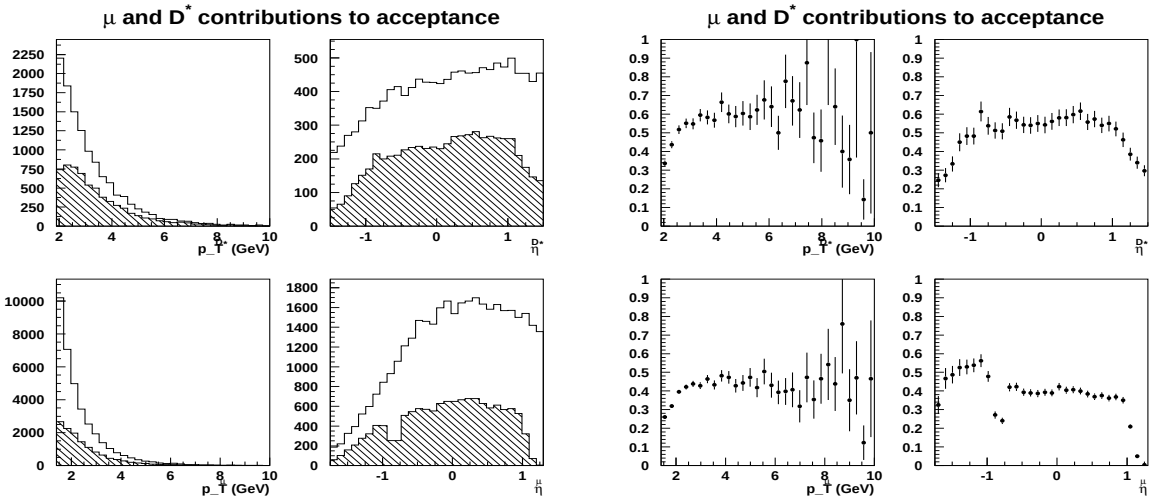

Figure 5.25: *Dependence of the acceptance on the muon and D^* variables.* **Left** *plots: Distributions of the muon and D^* p_T and η. Plain histograms refer to events in the kinematic region ($p_T^\mu > 1.4$, $-1/75 < \eta^\mu < 1.3$ for muons, $p_T^{D^*} > 1.9$, $|\eta^{D^*}| < 1.5$ for D^*), hatched histograms to the reconstructed events with the standard cuts.* **Right***: The ratio between the histograms of the Left part.*

background. The beauty component is determined as $f_b = (36.3 \pm 8.5\ (\text{stat.}))$ % from the fit to the ΔR distribution. The acceptance calculated with PYTHIA is 6.8 %. This result is referred to unlike sign combinations only, as in the definition. If we extend the acceptance definition to all muon-D^* pairs the result for this "detector" acceptance is 9.5 % (the unlike sign combinations which are ~ 73 % of the sample). These data converge to a cross section of:

$$\sigma(ep \to eb\bar{b}X \to eD^*\mu X) = 214 \pm 52\ (\text{stat.})\ \text{pb}$$

The reported statistical errors comes from the error on the number of fitted beauty events. The (relatively small) contribution due to the statistical uncertainty on the acceptance has also been included. After adjusting the values for differences in the selected kinematic range, this result is in good agreement with a similar measurement [167] by the H1 collaboration.

Monte Carlo	$N_b^{rec\ u.s.}$	N_b^{rec} $w.c.$	N_{kin}	$\mathcal{A}$ (%)
PHP+DIS				
PYTHIA $K\pi$	77.9	4.9	1077	6.8 ± 0.7
PYTHIA $K3\pi$	45.2	9.5	524	6.8 ± 1.1
HERWIG $K\pi$	114.0	2.1	1555	7.2 ± 0.6
HERWIG $K3\pi$	60.8	7.5	897	5.9 ± 0.7
PHP				
PYTHIA $K\pi$	73.0	3.9	920	7.5 ± 0.8
PYTHIA $K3\pi$	38.7	7.6	434	7.2 ± 1.2
HERWIG $K\pi$	88.4	2.2	1054	8.1 ± 0.7
HERWIG $K3\pi$	43.7	4.9	556	7.0 ± 1.0
DIS				
RAPGAP $K\pi$	25.5	3.9	412	5.2 ± 1.0
HERWIG $K\pi$	21.0	1.8	304	6.3 ± 1.2

Table 5.2: *Acceptances for different samples, Monte Carlo in the $K\pi$ and $K3\pi$ channels.*

After applying the photoproduction selection by introducing an upper cut at 34 GeV in the $E - p_z$, the number of unlike sign pairs reduces to 113 of which 15 come from combinatorial D^* background. The fitted fraction is $f_b = (36.2 \pm 9.6\ (\text{stat.}))\ \%$ from the ΔR distribution. The acceptance for $Q^2 < 1$ GeV^2 and $0.05 < y < 0.85$ in addition to the previous muon and D^* cuts is 7.5 % on unlike sign pairs only. The resulting photoproduction cross section is:

$$\sigma_{PHP}(ep \to eb\bar{b}X \to eD^*\mu X) = 159 \pm 41\ (\text{stat.})\ \text{pb}$$

The DIS subsample selection yields 26 unlike sign μD^* pairs with a combinatorial background of 5 events. The signal component, evaluated from a 2 bin ΔR distribution is (10.6 ± 5.2) events ($f_b = 51$ %). The detector acceptance is 8 %. The resulting visible cross section for $p_T^\mu > 1.4$ GeV, $-1.75 < \eta^\mu < 1.3$, $p_T^{D^*} > 1.5$ GeV, $|\eta^{D^*}| < 1.5$, $0.05 < y < 0.7$ and $Q^2 > 2$ GeV^2 is:

$$\sigma_{DIS}(ep \to eb\bar{b}X \to eD^*\mu X) = 71 \pm 34\ (\text{stat.})\ \text{pb}$$

5.10.2 Visible cross sections in the $K3\pi$ mode

In the $K3\pi$ mode the final inclusive sample consists of 103 unlike sign combinations with a combinatorial D^* contribution of 30 combinations. The fitted b fraction is: $f_b = 0.368 \pm 0.08(\text{stat.})$ % from a fit to the ΔR distribution. The PYTHIA Monte Carlo acceptance for unlike sign pairs only is 6.8 % and 9.7 % when also including like sign sample (detector acceptance). The resulting visible cross section is measured to be:

$$\sigma(ep \to eb\bar{b}X \to eD^*\mu X) = (68 \pm 16)\ \text{pb}$$

The photoproduction sample is composed by 79 unlike sign combinations with a combinatorial background of 24. The ΔR fit yields a signal component: $f_b = 0.286 \pm 0.09(\text{stat.})$ %. PYTHIA predicts an acceptance of 7.2 % (10.4 % for both like and unlike sign pairs) thus giving for the cross section the following value:

$$\sigma(ep \to eb\bar{b}X \to eD^*\mu X) = (37 \pm 11)\ \text{pb}$$

In order to check the internal consistency of the analysis, the measured visible cross sections in the $K3\pi$ channel have been extrapolated to the same visible region in which the $K\pi$ cross sections were calculated. The effect of loosening the $p_T^{D^*}$ cut from 3.8 to 1.9 GeV introduces in the PYTHIA Monte Carlo a factor of $4.03 \pm 0.3\ (\text{stat.})$ and $4.2 \pm 0.3\ (\text{stat.})$ in the inclusive and photoproduction samples respectively. We used HERWIG as a systematic check of this factor. The result is $3.4 \pm 0.2\ (\text{stat.})$ and $3.7 \pm 0.2\ (\text{stat.})$ for the inclusive and photoproduction samples. The results for the cross sections in the $K3\pi$ channel in the same kinematic region used for the $K\pi$ channel are:

$$\sigma^{PHP}_{K\pi \to K3\pi}(ep \to eb\bar{b}X \to eD^*\mu X) = (155 \pm 46)\ \text{pb}$$

$$\sigma^{PHP+DIS}_{K\pi \to K3\pi}(ep \to eb\bar{b}X \to eD^*\mu X) = (274 \pm 65)\ \text{pb}$$

while using HERWIG for extrapolation and acceptance corrections the results are: (143 ± 42) pb and (265 ± 61) pb. These values should be compared with a visible cross section of 159 ± 41 pb in photoproduction and 214 ± 52 pb for the inclusive sample. The results are in good agreement. The visible cross sections in the $K\pi$ and $K3\pi$ modes after the extrapolation of the latter to the $K\pi$ kinematic region are shown in Figure 5.26.

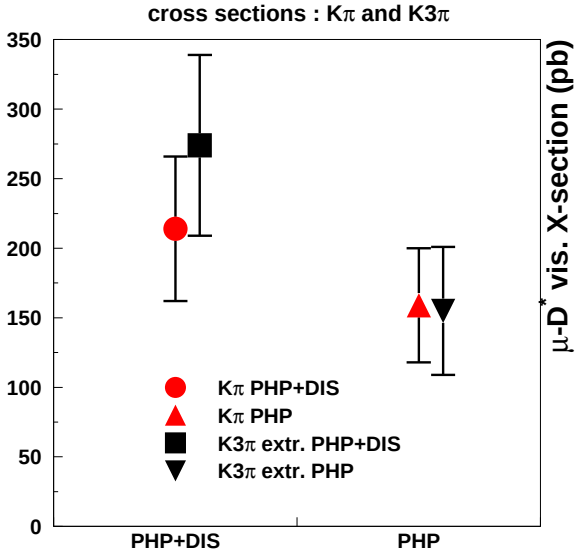

Figure 5.26: *Comparison between the measured visible cross section in the $K\pi$ mode and those in the $K3\pi$ in the $K\pi$ kinematic region. Left points refer to the inclusive sample, Right points to photoproduction.*

5.11 Systematic uncertainties

In this Section we will describe the contributions to the total systematic uncertainty. The checks we have performed are of different nature.

A first group concerns the systematic effects introduced by the selection cuts. In these checks the analysis is repeated changing one of the selection cuts in both data and Monte Carlo. The acceptance is thus affected as well as the final number of events in the data. Cuts have been varied within the expected resolution of the considered variable. With this procedure the uncertainty due to possible mismatches between the data and Monte Carlo in the vicinity of the value of our cuts is taken into account.

A second group of systematic errors considers the possibility that the Monte Carlo might be not reproducing some variables (e.g. $p_T^{\mu D^*}$) or underestimating some background components (fake muons, gluon splitting to heavy quarks in light flavour events) or not correctly implementing some relevant features e.g. the lepton spectrum from B mesons decay.

The model dependence (fragmentation model, $b\bar{b}$ correlations) of the acceptance calculation has also been taken into account by adopting HERWIG instead of PYTHIA and RAPGAP in PHP and DIS respectively.

The contributions which we have considered will be described in order of importance in terms of deviations from the central result.

- **Simulation of $p_T^{\mu D^*}$.** The largest error arises from the observation that, in the inclusive $K\pi$ sample, the muon and D^* p_T spectra in the b signal region of the data ($\Delta R_{\mu D^*} < 2, 3 < m_{\mu D^*} < 5$ GeV) appear to be somewhat softer than the ones predicted by the Monte Carlo(s) (see control plots in Appendix B). Qualitatively the same differences are seen in the DIS sample, but statistics is too low to make a meaningful study. We therefore applied the results from the inclusive study to the DIS sample. Since these momentum spectra are well reproduced in the charm region (with larger statistics) this can not be attributed to problems with the muon or D^* reconstruction. There are several ways to interpret these differences.

a) They can be statistical fluctuations. This assumption leads to the central result reported.

b) The signal distribution could really be softer. This would change the efficiency calculation for the extrapolation to the visible cross section. To evaluate this possibility, we have reweighted the muon and D^* (true level) distributions such as to reproduce the measured spectra of the inclusive sample. This yields the reported error of +44%.

c) There could be an additional unknown background contribution at low p_T, which occurs only in the b–enriched region. We see no indication that is the case (the like sign in the same kinematic range agree). To account for this possibility anyway, we significantly tightened the $p_T^{\mu D^*}/E_T$ cut from 0.1 to 0.15. This removes a significant fraction of the discrepancy, and the remaining part of the spectrum will yield a smaller number of signal events. Since only very few MC signal events are removed, this yields a lower cross section, and hence the quoted error of -25%.

In the $K3\pi$ case the situation is somewhat different since the $p_T^{\mu D^*}$ is, within statistics, reproduced by the Monte Carlo while a less good description of the $p_T^{\mu D^*}/E_T$ ratio seems to be due to an E_T distribution which appears to be harder in the data. In this situation we did not apply the reweighting procedure but rather estimated this effect by setting the $p_T^{\mu D^*}/E_T$ cut at 0.18 and 0.12. The cross section central values moves by -21%, +18 %.

- **Model dependence** HERWIG uses a different fragmentation model. It also yields a better description of the DIS part of the data. Finally, it yields different $b\bar{b}$ correlations from direct/resolved contributions and parton showering. The net effect is that the acceptance correction is in general higher with a corresponding reduction in the cross section.

- **Signal extraction procedure**. In addition to statistical fluctuations, different ways to fit the data can yield systematic differences due to binning effects and different systematics for different variables. To evaluate the error from this effect, we have evaluated the cross section using three different procedures: Fits to $\Delta R^{\mu D^*}$ and $\Delta\phi^{\mu D^*}$ ($m^{\mu D^*}$) and simple event counting.

- **Uncertainty on the estimation of the muon chambers efficiency**: The ratios between the measured and simulated muon reconstruction efficiencies have been discussed in Section 5.10. The correction factors have an uncertainty which is mostly due to the limited statistics of the used data sample. As a systematic check, the correction factors have been varied within one standard deviation and the acceptance was recalculated accordingly.

- **Fake muon background**. This contribution has been widely studied in Appendix A. The results on the pion fake muon probabilities, based on independent samples, tell that this contribution is underestimated by at most 50 % by the Monte Carlo. In the case of kaons the probabilities from data are overestimated by the Monte Carlo by about the same factor. Since the yield of fake from pions is about twice the contribution from kaons we should enhance this background by a factor 1.2 at most. To be cautious we varied it up by a factor 1.5. The effect is in any case small (~ -6 % at most).

- **Luminosity measurement**. The uncertainty associated with the luminosity measurement for the 1996-00 data taking periods used for this analysis was estimated to be $\pm$ 2 % [157]. This introduces an overall normalisation uncertainty on each measured cross section, which is correlated between all data points.

- The Δm **and** $m(D^0)$ mass windows have been extended and tightened on both sides by 0.5 and 20 MeV respectively.

- The cut on the p_T **of the** D^* **decay tracks** has been varied by 10 MeV for the π_s and 50 MeV for the pion and kaon.

- The **cut on** p_T^μ has been varied by $\pm$ 40 MeV.

- The cut on the **matching probability** of muons $\mathcal{P}_{4\ d.o.f.}$ has been varied by ± 0.005 units.

The relative variations of the cross section corresponding to the systematic checks we described are summarised in Table 5.3. Figure 5.27 shows the same information but in terms of the absolute values of the cross sections. The main contribution arise generally from the uncertainty on the $p_T(\mu D^*)$ and on the $p_T(\mu D^*)/E_T$ distributions. As we already noticed the discrepancy between the observed and simulated distributions could be due to a real effect or partially generated by a statistical fluctuation of our sample. For this reason we decided to quote this contribution to the systematic uncertainty separately from the rest. More future data will shed light on this issue. Other relevant sources

Source	*DIS+PHP* % var.		*PHP* % var.		*DIS* % var.		*DIS+PHP* % var.		*PHP* % var.		*Description*
fit sys.	+15	-4	+19	-17	0	0	0	-22	0	-28	ΔR, $\Delta\phi$ fit, event counting
HERWIG	0	-6	0	-8	0	-25	+13	0	+3	0	visible acceptance
combined	+15	-7	+19	-19	0	-25	+13	-22	+3	-28	
reweight	+41	0	+37	0	+43	0	/	/	/	/	to describe $p_T^{D^*}$ and p_T^{μ} distrib.
$p_T(\mu D^*)/E_T$	+2	-25	+2	-22	/	/	+18	-21	+18	-23	$\pm$ 0.05($K\pi$), $\pm$ 0.03($K3\pi$)
combined	+41	-25	+37	-22	+43	0	+18	-21	+18	-23	
Δm cut	0	-8	0	-8	0	-8	0	-9	0	-7	$\pm$ 0.5 MeV
$m(D^0)$ cut	+4	0	+4	0	+5	0	+1	0	+7	0	$\pm$ 20 MeV
$p_T(K,\pi)$	+4	-2	+4	-2	+1	-5	+3	-20	+3	-18	$\pm$ 50 MeV
$p_T(\pi_s)$	+2	0	+2	0	+5	-6	0	0	0	0	$\pm$ 10 MeV
muon acc.corr.	+5	-5	+5	-5	+5	-5	+5	-5	+5	-5	within corr. errors
$p_T(\mu)$	+3	0	+3	0	0	-6	+8	-5	+9	-6	$\pm$ 40 MeV
μ prob.	+1	0	+1	0	+6	-4	-2	-10	+1	-3	$\pm$ 0.005
luminosity	+2	-2	+2	-2	+2	-2	+2	-2	+2	-2	uncertainty
fake μ	0	-4	0	-4	0	-4	0	-6	0	-6	+ factor 1.5
combined	+9	-11	+9	-11	+11	-14	+10	-26	+13	-22	
TOTAL	+45	-28	+43	-31	+45	-29	+24	-40	+22	-42	

Table 5.3: *The relative variations of the measured visible cross sections (in different columns) for the considered systematic checks (rows) are given in the Table. The contributions coming from the description of $p_T^{\mu D^*}$ and $p_T^{\mu D^*}/E_T$ distributions are grouped separately as well as the part due to cut variations. The partial systematic errors, obtained by quadratic sum, are given in the rows denoted as "combined".*

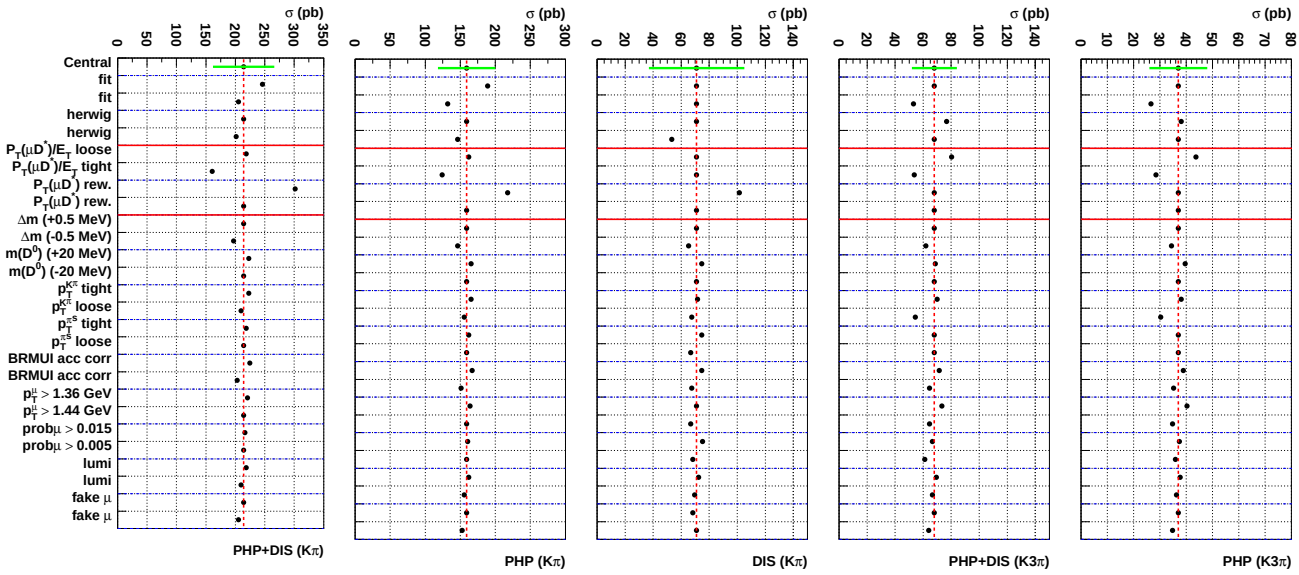

Figure 5.27: *Summary of the systematic checks. The variation of the central value of the visible cross sections is plotted for each systematic check. From Left to Right: inclusive, photoproduction and DIS in the $K\pi$ channel, inclusive and photoproduction in the $K3\pi$ channel. The horizontal upper segment indicates the statistical error.*

of variations in the cross section are the signal extraction procedure and the model dependence of the acceptance calculation. The variations of the analysis cuts generally contribute less.

Further more general checks concerning the reliability of the used Monte Carlo have been performed which will be here described.

5.11.1 Gluon splitting from light quark events

In our simulation the beauty and charm Monte Carlo samples were generated considering the cases in which both (flavour creation) or one (flavour excitation) of the heavy quarks are produced in the hard process. Additional heavy quarks from *gluon splitting* $g \to Q\bar{Q}$ in the parton shower phase are also simulated. Heavy flavours produced in events in which the hard scattering involves only light partons are instead not explicitly included. We estimated the contribution of gluon splitting in light quark events from a Monte Carlo in which both light and heavy flavours processes were generated [166]. The reconstructed Δm and $m(K\pi)$ distributions for D^* with $p_T > 1.9$ GeV and $|\eta^{D^*}| < 1.5$ are shown in Figure 5.28. The contributions from $g \to c\bar{c}$ and $g \to b\bar{b}$ in light quark events are shown cumulatively by the dashed histograms (see the legend). The dotted histogram represents instead events with primary heavy quark production and eventually gluon splitting to heavy flavours. At this stage the heavy quarks produced by gluon splitting in light quark events amount to $\sim 2\%$ of the total number of events with production of heavy quarks.

It is important to see the weight of this source at the level of the final selection. This concern derives from the possibility that a muon and a D^* from the $c\bar{c}$ pair could produce by gluon splitting an unlike sign μD^* pair in the same hemisphere thus faking the beauty signal. Only two events ($c\bar{c}$ g–splitting) survive the final selection which corresponds to about 1 % of the total heavy quark sample. Their distribution in ΔR, m and $\Delta\phi$ are shown in the shaded histogram in the Right hand plots of Figure 5.28. This contribution was considered as negligible.

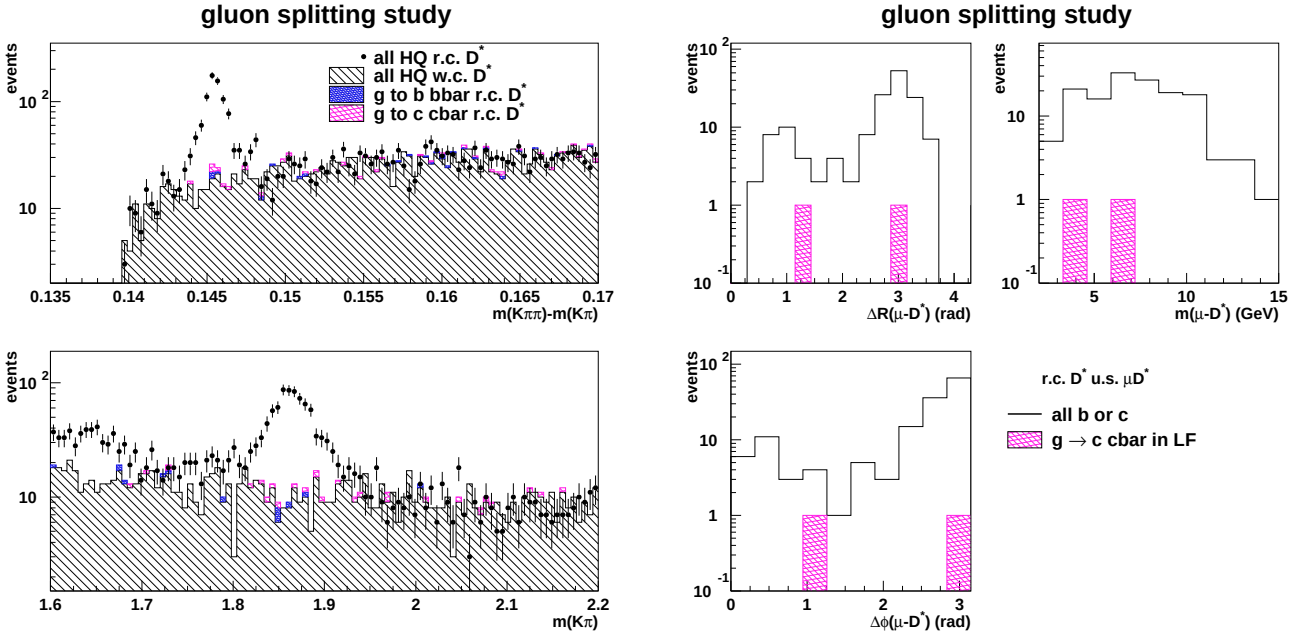

Figure 5.28: *The* **Right** *hand plots show the Δm (top) and $m_{K\pi}$ distributions for a Monte Carlo sample containing light and heavy flavour partonic processes. The events with charm and beauty in the hard process are shown by the bullets while the contribution from gluon splitting to $c\bar{c}$ and $b\bar{b}$ (in both light and heavy flavour processes) is shown in the differently hatched histograms (see the legend). The* **Left** *hand plots show the ΔR, m and $\Delta\phi$ distributions in the final selection for gluon splitting from light flavour events (shaded histogram) and all heavy flavour events (solid histogram).*

5.11.2 Monte Carlo implementations of the muon spectrum.

A proper description of the spectrum of muons from B-decay is an essential ingredient in order to calculate the acceptance factors correctly. The shape of the distribution of the true–level muon momentum in the B^0 rest frame for $B^0 \to D^*\mu\nu_\mu$ decays in our PYTHIA Monte Carlo is compared to the measurements recently performed by the BABAR and BELLE experiments using the electron semileptonic channel. The Monte Carlo parametrisation looks fine. It can also be noticed how the high tail in the data overshoots the Monte Carlo. This is due to the fact that data also include the small contribution from leptons coming from charmless B meson decays. Since the description is good, no additional contribution to the systematic error was then associated to this potential uncertainty.

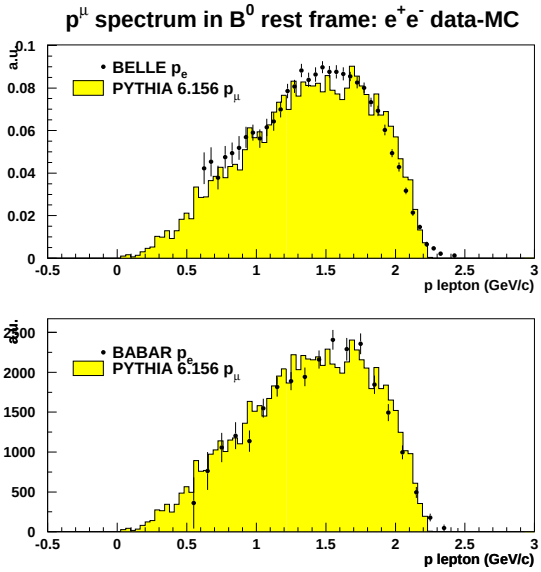

Figure 5.29: *Comparison of the spectrum of the muon with recent e^+e^- data for electrons. Note that in the experimental data the contributions from V_{ub} is also present as it is clear from the tail at high values of the momentum.*

5.12 Visible cross sections summary

The final results for the visible cross sections for $ep \to b\bar{b}X \to D^*\mu X'$ in the defined kinematic regions with the corresponding statistical and systematic errors are here summarised:

$$\begin{aligned}
\sigma^{K\pi}_{vis\ (PHP+DIS)}(ep \to b\bar{b}X \to D^*\mu X') &= 214 \pm 52\ (\text{stat.})^{+37}_{-27}(\text{sys.})^{+88}_{-45}(\text{main sys.})\ \text{pb} \\
\sigma^{K\pi}_{vis\ (PHP)}(ep \to b\bar{b}X \to D^*\mu X') &= 159 \pm 41(\text{stat.})^{+33}_{-34}(\text{sys.}))^{+59}_{-35}(\text{main sys.})\ \text{pb} \\
\sigma^{K\pi}_{vis\ (DIS)}(ep \to b\bar{b}eX \to D^*\mu eX') &= 71 \pm 34\ (\text{stat.})^{+8}_{-20}(\text{sys.})^{+31}_{0}(\text{main sys.})\ \text{pb} \\
\sigma^{K3\pi}_{vis\ (PHP+DIS)}(ep \to b\bar{b}X \to D^*\mu X') &= 68 \pm 16\ (\text{stat.})^{+11}_{-23}(\text{sys.})^{+12}_{-14}(\text{main sys.})\ \text{pb} \\
\sigma^{K3\pi}_{vis\ (PHP)}(ep \to b\bar{b}X \to D^*\mu X') &= 37 \pm 11(\text{stat.})^{+5}_{-13}(\text{sys.})^{+7}_{-9}(\text{main sys.})\ \text{pb}
\end{aligned}$$

The global systematic error has been obtained by summing quadratically the various contributions we estimated in the previous Section. The systematic error arising from the uncertainty on the $p_T(\mu D^*)$ has been quoted separately ("main sys.").

5.13 Comparison with the theoretical predictions

The measured visible cross sections will be compared first to the prediction of the Monte Carlo and, later in the Section, to the more reliable next–to–leading order calculations.

5.13.1 Monte Carlo predictions

As a first stage we will compare the measured cross section in the visible kinematical range to the expectation of the Monte Carlo. This is an estimation of the leading order contributions to the cross section with the corrections provided by the parton shower treatment. A description of the models implemented in the Monte Carlo programs in use has already been given in Chapter 3. The Monte Carlo visible cross sections (σ^{vis}_{MC}) were derived according to the following equation:

$$\sigma^{vis}_{MC} = \frac{N_{kin}}{N_{gen} \cdot \mathcal{B}} \cdot \sigma^{tot}_{MC} = \frac{N_{kin}}{\mathcal{L}_{eq} \cdot \mathcal{B}} \tag{5.13}$$

We denoted as N_{kin} the number of Monte Carlo events falling in the considered kinematic region, N_{gen} the number of generated events (eventually corrected for rejection factors due to generation level cuts), σ_{MC}^{tot} the total cross sections predicted by the Monte Carlo and $\mathcal{B}$ the branching ratio of the considered D^* decay channel. $\mathcal{L}_{eq}$, the equivalent luminosity of the Monte Carlo sample, is defined as the ratio of $N_{gen}/\sigma_{MC}^{tot}$.

The event is considered to belong to the kinematic region according to the true level variables. In the case of muon and D^* requirements the event was accepted if it contained at least a D^* and at least a muon satisfying the imposed p_T and η cuts. The D^* candidates were also required to decay into the reconstructed decay mode. The extrapolation to all D^* regardless of their decay is done by dividing this number by the corresponding branching ratios ($\mathcal{B}$). The Monte Carlo cross section, which refers to the whole phase space, is scaled to the particular region in which due to experimental constraints, the measurement could be performed.

The above–mentioned quantities for the different kinematic regions and different generators have been summarised in the following Table:

$D^* \rightarrow (K\pi)\pi_s$

Regime	*Monte Carlo*	N^{kin}	$\mathcal{L}_{eq}$	σ_{MC}^{vis} (pb)	σ_{meas}^{vis} (pb)
DIS+PHP	PYTHIA	1077	515	81 ± 2	$214 \pm 52\ (\text{stat.})^{+37}_{-27}(\text{sys.})^{+88}_{-45}(\text{main sys.})$
	HERWIG	1555	1250	48 ± 1	
PHP	PYTHIA	920	515	70 ± 2	$159 \pm 41(\text{stat.})^{+33}_{-34}(\text{sys.}))^{+59}_{-35}(\text{main sys.})$
	HERWIG	1054	1250	33 ± 1	
DIS	RAPGAP	412	619	26 ± 1	$71 \pm 34\ (\text{stat.})^{+8}_{-20}(\text{sys.})^{+31}_{0}(\text{main sys.})$
	HERWIG	304	1250	9.5 ± 0.5	

$D^* \rightarrow (K\pi\pi\pi)\pi_s$

Regime	*Monte Carlo*	N^{kin}	$\mathcal{L}_{eq}$	σ_{MC}^{vis} (pb)	σ_{meas}^{vis} (pb)
DIS+PHP	PYTHIA	524	515	20 ± 1	$68 \pm 16\ (\text{stat.})^{+11}_{-23}(\text{sys.})^{+12}_{-14}(\text{main sys.})$
	HERWIG	897	1250	14 ± 1	
PHP	PYTHIA	434	515	17 ± 1	$37 \pm 11(\text{stat.})^{+5}_{-13}(\text{sys.})^{+7}_{-9}(\text{main sys.})$
	HERWIG	556	1250	9 ± 1	

The error quoted in the Monte Carlo cross section just takes into account the uncertainty due to the statistical limit of the available samples. The cross sections predicted by the various Monte Carlo are in general considerably lower than the measured values. This is not surprising and was observed in the past in several beauty analyses at HERA. PYTHIA (used for the central signal extraction) is generally closer to the measured value which is undershot by factors ranging from two to three. HERWIG (used for systematic checks) and RAPGAP predict even lower values for the $\sigma(ep \rightarrow eb\bar{b}X \rightarrow eD^*\mu X)$.

We considered the possibility that the gap between the absolute normalization of the various Monte Carlo expectations might be related to considerable differences in the shape of the distributions on which we define our visible kinematic region. In Figure 5.30 the true level distributions in p_T of muons and D^* mesons, y and Q^2 have been compared for PYTHIA (plain line histogram) and HERWIG (bullets) before (Left side plots) and after (Right side plots) the requirements on the kinematic region. D^* were required to decay in the $K\pi$ channel. The same comparison has been performed in the DIS kinematic region for HERWIG and RAPGAP (Figure 5.31). PYTHIA and HERWIG remarkably agree in the PHP region while in the inclusive sample PYTHIA has a too soft Q^2 distribution. This is known and was the reason why Pythia was not considered in our analysis for the DIS regime subsample. In the case of RAPGAP and HERWIG the agreement is also good except for the inclusive y variable which exhibits significant deviations.

5.13.2 b–quark level cross section and comparison with the NLO prediction

If we want to compare our results with the NLO calculations we need to convert the visible cross section to a cross section given in terms of the b quarks properties since the NLO theoretical predictions are expressed at parton level. The gap between these two levels is covered by the Monte Carlo which implements the necessary hadronisation models. This conversion will be done separately for the DIS and PHP visible cross sections since a calculation covering both regimes is not available. We will compare to the NLO calculation from Harris and Smith (HVQDIS) [178, 179] which refers to deep inelastic scattering and the one performed by Frixione et al. (FMNR) [177] for the photoproduction part.

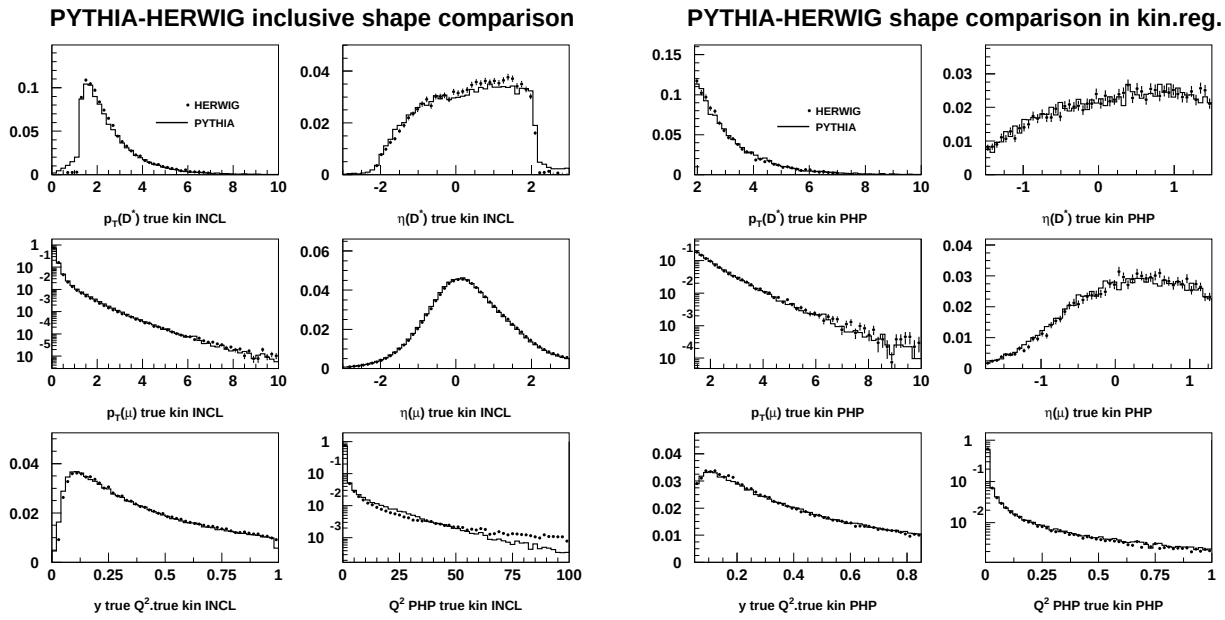

Figure 5.30: *Shape comparison of the distributions for the true p_T, and η of D^* and muons, y and Q^2 in the* PYTHIA *and* HERWIG *Monte Carlo. The comparison is done for all events (***Left** *plots) and only for those in the photoproduction kinematic region (***Right** *plots).*

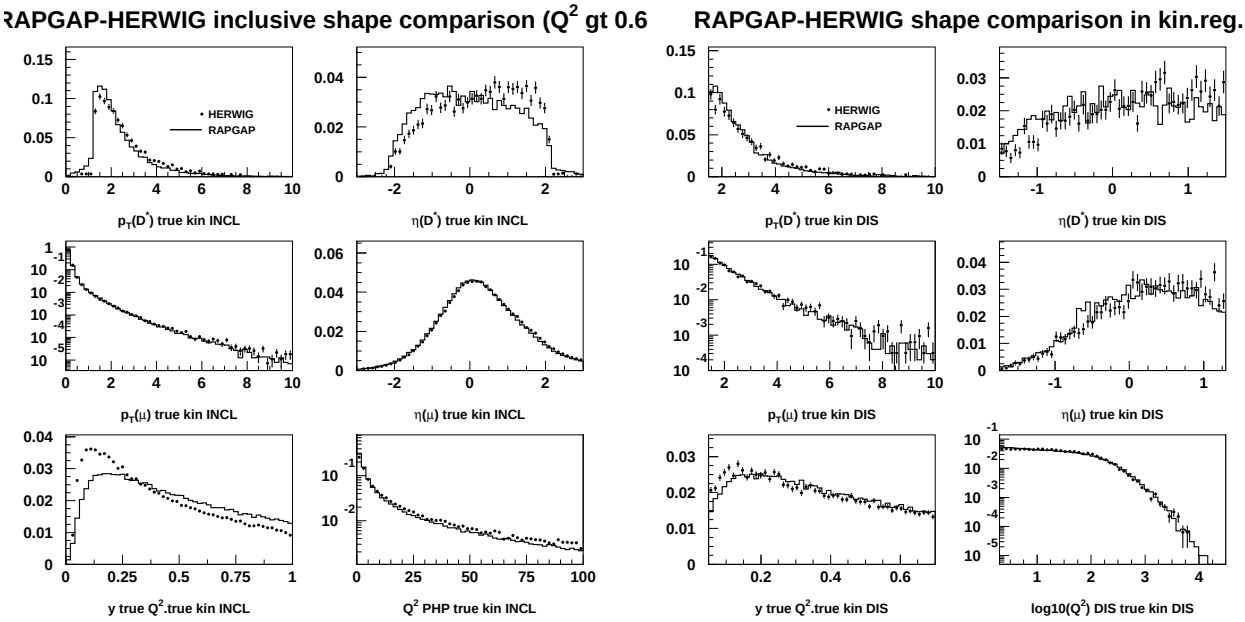

Figure 5.31: *Shape comparison of the distributions for the true p_T, and η of D^* and muons, y and Q^2 in the* RAPGAP *and* HERWIG *Monte Carlo. The comparison is done for all events (***Left** *plots) and only for those in the DIS kinematic region (***Right** *plots).*

As the D^* and muon in the beauty-enriched region are generally produced from the same b quark, we converted our visible level cross sections to a b-level cross section quoted for individual b or $\bar{b}$ production rather than for correlated $b\bar{b}$ pair production. This means that we counted individual b or $\bar{b}$ quarks rather than events.

A significant fraction of the parent b quarks of the selected events is expected to have very low p_T^b values. This can be

seen in Figure 5.32 where the distributions in p_T and y_{rap} for signal events satisfying all the analysis cuts are shown. Therefore, a cross section with no cut on p_T^b has been measured.

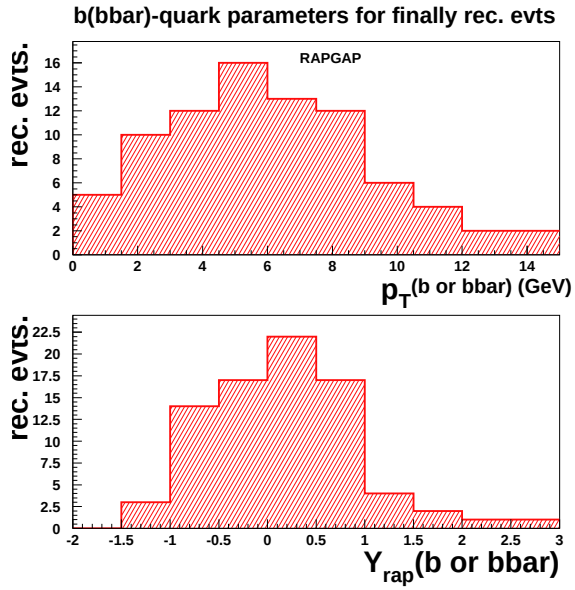

Figure 5.32: *Transverse momentum and rapidity of b and $\bar{b}$ quarks for signal events satisfying all the analysis cuts in the* RAPGAP *Monte Carlo.*

Furthermore, a strong correlation exists between the pseudorapidity of the μD^* system and the longitudinal rapidity of the parent b quark. This will be shown explicitly in the next Chapter. The main consequence of this correlation is that, due to the limited angular acceptance of the detector for both the D^* and the muon, we are mostly sensitive to quarks produced in the middle rapidity region. In order to reflect this experimental constraint in the quark level cross-section definition, we restricted to the b-quark rapidity range $y_{rap}^b < 1$.

The choice of this particular value is substantiated for photoproduction and DIS by the second and third plots in Figure 5.33 respectively. The full line histograms show the inclusive rapidity distributions for all b or $\bar{b}$ quarks in events with $0.05 < y < 0.85$ and $Q^2 < 1$ GeV^2 ($0.05 < y < 0.7$ and $Q^2 > 2$ GeV^2 in the case of DIS). If we require, in addition, the event to belong to the kinematical region in which the visible cross sections were calculated, i.e. if we require $-1.75 < \eta^\mu < 1.3$, $p_T^\mu > 1.4$ GeV, $|\eta^{D^*}| < 1.5$ and $p_T^{D^*} > 1.9$ in PHP, $p_T^{D^*} > 1.5$ in DIS, the dotted histograms are obtained. As anticipated these additional cuts introduce a rather sharp falling edge at $y_{rap}^b \sim 1$. Moreover it must be noticed that, as we saw in Chapter 1, the theoretical uncertainties in the middle rapidity regions are smaller than in the inclusive case.

The conversion of the visible level cross sections to the quark level cross section for b or $\bar{b}$ quarks with $y_{rap} < 1$ has been performed by applying a factor derived from inclusive beauty Monte Carlo samples. PYTHIA was used to extrapolate the visible photoproduction cross section, RAPGAP for the DIS one. This factor accounts for the effect of kinematics and branching fractions:

$$\sigma(ep \to b(\bar{b})X) = \sigma_{vis} \times \frac{N_b}{N_{kin}}$$

N_b denotes the number of b or $\bar{b}$ quarks with $y_{rap} < 1$ in events with $Q^2 < 1$ GeV^2 and $0.05 < y < 0.85$ ($Q^2 > 2$ GeV^2 and $0.05 < y < 0.7$ in the DIS case) while N_{kin} is the number of events in the kinematical region which has already been defined for the calculation of the acceptance. The obtained values for N_b, N_{kin} and the conversion factors are given in the following Table:

	N_b	N_{kin}	N_b/N_{kin}	*factor* ($\mathcal{B}\times$ phase space)
PHP	27816	293	95 ± 5.6	6.9×13.8
DIS	690509	12999	53.1 ± 0.5	6.9×7.7

The extrapolation factor for photoproduction is larger due to the higher cut in $p_T^{D^*}$. In the third column the ratio N_b/N_{kin} has been splitted into two numbers representing the contribution given to the extrapolation by the requirements on the presence of muons and D^* in the final state (branching fractions) and the contribution due to the kinematic cuts on p_T and η. The factor 6.9 is the inverse of the fraction of beauty events with at least a prompt muon and a D^* in the final state. In order to more easily cross check this value we calculated in the Monte Carlo the number of events with at least one muon, and the number of events with at least one D^*. We required in turn the muons to come from B mesons or D mesons. The values obtained for both PYTHIA and RAPGAP have been found to be consistent with the values extracted from the PDG [161]. This indicates that the correct decay tables have been implemented correctly in the Monte Carlo we are using.

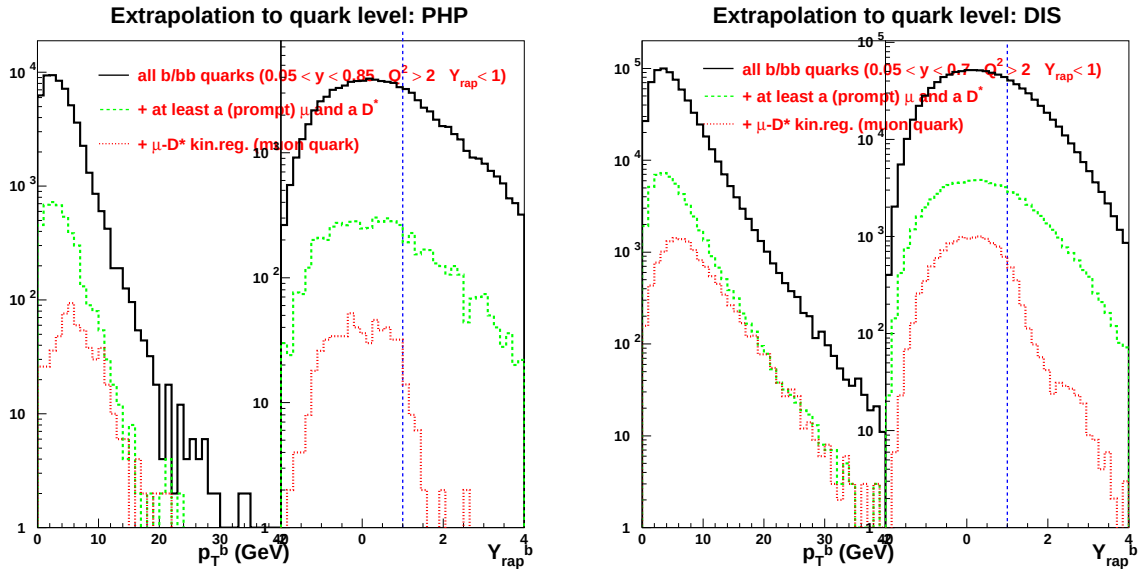

Figure 5.33: *The* **Left** *hand side refers to photoproduction while the* **Right** *hand side to DIS. In each case the Left plot shows the p_T^b distribution and the Right plot the y_{rap}^b distribution. The full line histogram contains all b or $\bar{b}$ quarks with $y_{rap}^b < 1$ in events with $0.05 < y < 0.85$ and $Q^2 < 1$ GeV^2 ($0.05 < y < 0.7$ and $Q^2 > 2$ GeV^2 for the DIS plot). In the p_T^b distributions $y_{rap}^b < 1$ is required in addition. The dashed line histogram contains events with in addition at least a D^* and a muon. In the dotted line histogram only events enter for which D^* and μ also belong to the kinematic regions.*

It is crucial for a meaningful extrapolation to use a Monte Carlo which reproduces the p_T^b shapes as calculated at the NLO. We checked that in the defined kinematic range, the p_T^b and y_{rap}^b distributions of PYTHIA (after parton showering) agree with the central NLO b-quark spectra from the FMNR program. Therefore, PYTHIA was used to extrapolate the visible cross section for the photoproduction region. Similarly, the corresponding RAPGAP spectra for the DIS case agree with the central NLO predictions of HVQDIS.

The p_T^b shapes in the PYTHIA Monte Carlo and in the NLO FMNR calculations have been compared explicitly in the Left hand plot of Figure 5.34. The same comparison for RAPGAP and HVQDIS is instead shown in the Right hand plot of the same Figure. The Left plot is for $0.05 < y < 0.85$, $Q^2 < 1$ GeV^2 and quarks with $y_b^{rap} < 1$, the Right one for $0.05 < y < 0.7$, $Q^2 > 2$ GeV^2 and $y_b^{rap} < 1$. The agreement is sufficiently good to safely use these Monte Carlo to calculate the extrapolation factor.

The extrapolation to b-level implies additional systematic uncertainties from the b-quark fragmentation and decay and the details of the shape of the p_T^b spectrum. These effect were estimated by adopting an inclusive HERWIG Monte Carlo. The effect is a rise in the extrapolation factor by 12 %.

The result for the extrapolated cross section for $y_{rap}^b < 1$, $Q^2 < 1$ GeV^2, $0.05 < y < 0.85$ and $m_b = 4.75$ GeV is:

$$\sigma(\gamma^* p \to b(\bar{b})X)^{K\pi}_{PHP} = 15.1 \pm 3.9(\text{stat.}) \,^{+3.2}_{-3.3}(\text{sys.}) \,^{+5.6}_{-3.3}(\text{main sys.}) \text{ nb}$$
$$\sigma(\gamma^* p \to b(\bar{b})X)^{K3\pi}_{PHP} = 14.8 \pm 4.4(\text{stat.}) \,^{+2.0}_{-5.3}(\text{sys.}) \,^{+2.7}_{-3.4}(\text{main sys.}) \text{ nb}$$

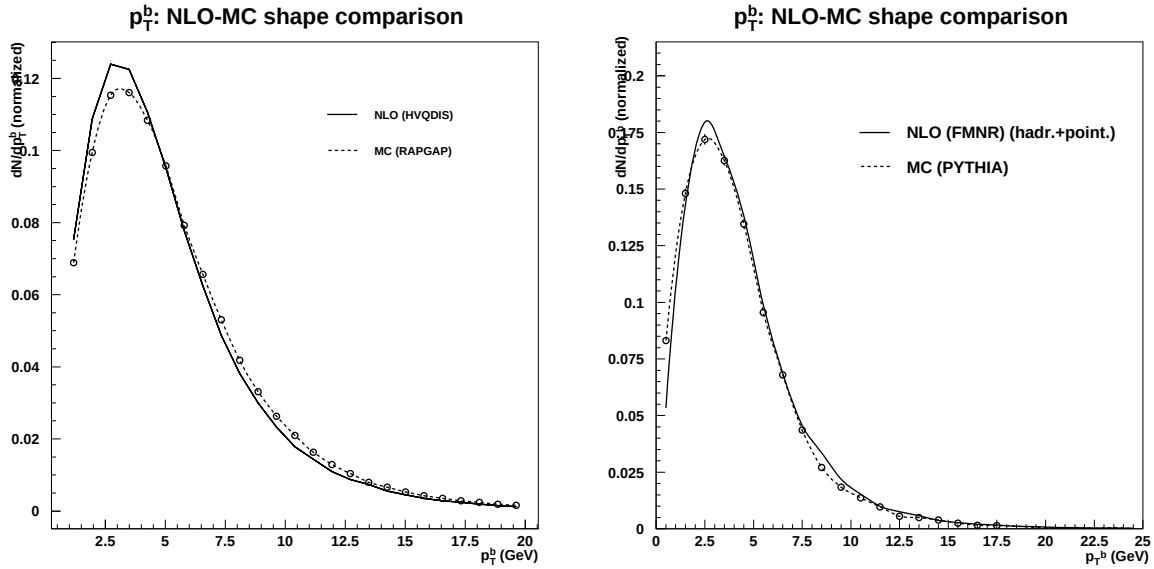

Figure 5.34: *Shape comparison of the p_T^b spectra in the NLO calculations and Monte Carlo. The* **Left** *plot compares* FMNR *and* PYTHIA. *The comparison is restricted to quarks with $y_b^{rap} < 1$ in events with $0.05 < y < 0.85$, $Q^2 < 1$ GeV^2. The* **Right** *hand plot shows a comparison between* HVQDIS *and* RAPGAP. *In this case quarks with $y_b^{rap} < 1$ in events with $0.05 < y < 0.7$, $Q^2 > 2$ GeV^2 were considered.*

for the $K\pi$ and $K3\pi$ channel respectively. The corresponding result for the extrapolated cross section for $y^b_{rap} < 1,\ Q^2 > 2\ \mathrm{GeV}^2,\ 0.05 < y < 0.7$ and $m_b = 4.75$ GeV is:

$$\sigma(\gamma^* p \to b(\bar{b})X)_{DIS} = 3.8 \pm 1.8(\mathrm{stat.})\ ^{+0.4}_{-1.1}(\mathrm{sys.})\ ^{+1.6}_{0}(\mathrm{main\ sys.})\ \mathrm{nb}$$

In addition to the errors propagated from the visible cross section, the systematic uncertainty includes the errors on b-quark fragmentation obtained from a comparison of the PYTHIA/RAPGAP and HERWIG acceptances, and assumes the validity of the NLO p_T^b shape used for the extrapolation. This is to be compared to the NLO prediction for the same kinematic range using the FMNR calculation [177] of

$$\sigma_{NLO}(\gamma^* p \to b(\bar{b})X)_{PHP} = 5.0^{+1.7}_{-1.1}\ \mathrm{nb}$$

for $\mu_R = \mu_F = \mu_0 = \sqrt{m_b^2 + p_T^{b2}}$ and $m_b = 4.75$ GeV, where μ_R and μ_F are the renormalisation and factorisation scales, respectively. The errors were calculated by simultaneously varying the above parameters in the range $\mu_0/2 < \mu < 2\mu_0$ and $4.5 < m_b < 5$ GeV. The parton density functions used in the calculation were the CTEQ5M and GRV-G HO for the proton and photon respectively.

The corresponding NLO HVQDIS [178, 179] prediction is

$$\sigma_{NLO}(\gamma^* p \to b(\bar{b})X)_{DIS} = 0.87^{+0.28}_{-0.16}\ \mathrm{nb}$$

for $\mu_R = \mu_F = \mu_0 = \sqrt{m_b^2 + Q^2}$ and $m_b = 4.75$ GeV, with the same variation of scales and m_b. The CTEQ5F4 proton structure function was used. These cross sections are visualised in the upper plot of Figure 5.35.

In order to compare our measurements to other beauty results performed at ZEUS in the photoproduction regime, we converted the visible cross sections to a different parton level region. The range of the transverse momentum and pseudorapidity of the b–quark was restricted to $p_T^b > 3$ GeV, $|\eta_b| < 2$. The kinematic region was also defined by $Q^2 < 1$ GeV^2 and $0.2 < y < 0.8$. The extrapolation factor including the branching ratio contribution amounts to ~ 42. It was evaluated using the PYTHIA Monte Carlo. The extrapolated cross sections are:

$$\sigma^{K\pi}_{extr} = 3.35 \pm 0.86(\mathrm{stat.})^{+0.7}_{-0.7}(\mathrm{sys.})^{+1.2}_{-0.7}(\mathrm{main\ sys.})\ \mathrm{nb}$$
$$\sigma^{K3\pi}_{extr} = 3.27 \pm 0.93(\mathrm{stat.})^{+0.4}_{-1.2}(\mathrm{sys.})^{+0.6}_{-0.7}(\mathrm{main\ sys.})\ \mathrm{nb}$$

These values are compared to the ZEUS beauty analysis using the jet+muon and jet+electron signatures. The comparison is shown in the lower plot of Figure 5.35. The FMNR expectation amounts to:

$$\sigma_{NLO}(p_T^b > 3 \text{ GeV}, |\eta_b| < 2, 0.2 < y < 0.8, Q^2 < 1 \text{ GeV}^2) = 1.3^{+0.2}_{-0.3} \text{ nb} \tag{5.14}$$

Our points significantly extend the reach in p_T^b keeping the extrapolation factor to an acceptable level . There seem to be an indication that the excess over theory might be more relevant at low p_T^b values.

In the next Chapter we will pursue this line of thought by studying the dependence of the cross section in terms of the quark transverse momentum and rapidity.

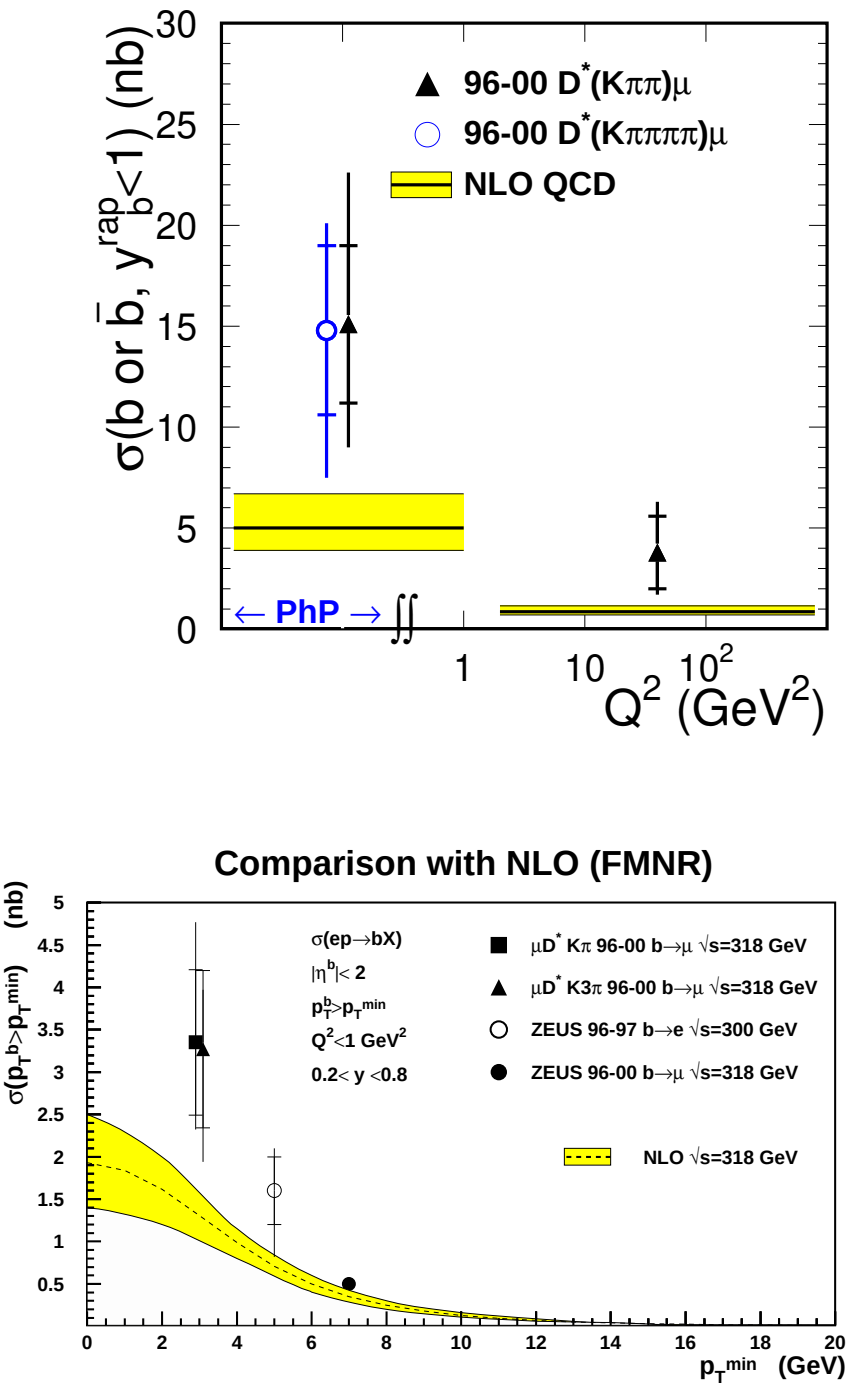

Figure 5.35: **Top**: *Cross section for single b or $\bar{b}$-quark production in the rapidity range $y^b_{rap} < 1$ for photoproduction (PHP, Left) and DIS (right), compared to NLO QCD predictions from FMNR (Left) and HVQDIS (right). The PHP cross section is for $0.05 < y < 0.85$, and the DIS cross section for $0.05 < y < 0.7$. The cross sections are integrated over the indicated Q^2 ranges, and over the full p^b_T range. More details on the QCD calculations are given in the text.* **Bottom** *The extrapolated beauty cross section at a fixed p_T^{min} value compared with theoretical predictions plotted as a function of p_T^{min}. The curves show the predictions from NLO QCD for varying the b–quark mass and the factorisation and renormalisation scales. The inner error bars indicate the statistical error while the full ones indicate the total error obtained by adding in quadrature the statistical and total systematic error.*

Chapter 6

Differential cross sections

In this chapter we will fully exploit the sample of our candidate beauty events by measuring differential cross sections in the transverse momentum and rapidity of the produced b quarks.

6.1 Kinematic correlations between the b–quarks and the μD^* system

In order to measure more directly the properties b–production at quark level we chose to restrict ourselves to the already defined signal region i.e. that containing events in which the muon and D^* pair have opposite charge, lie in the same hemisphere ($\Delta R_{\mu D^*} < 2$) and have an invariant mass compatible to a B meson semileptonic decay ($3 < m_{\mu D^*} < 5$ GeV). Beside providing information on the b–quark kinematics, as we already saw in the previous Chapter, this configuration is the most favourable since the charm background is small.

We have studied the level of accuracy with which it is possible to reconstruct the quark transverse momentum (p_T^b) and its rapidity (y_b^{rap}) by measuring the corresponding quantities for the μD^* system. A scatter plot of $\phi_{\mu D^*}$ vs ϕ_b, $y_{\mu D^*}^{rap}$ vs y_b^{rap} and $p_T^{\mu D^*}$ vs p_T^b as predicted by a mixture of the PYTHIA and HERWIG Monte Carlo is shown in the upper plots of Figure 6.1 for the $K\pi$ (Left plots) and $K3\pi$ (Right plots) case. The lower plots show the distributions of the difference between the quantity at reconstructed and true level.

Mostly due to the presence of the undetected neutrino the transverse momentum of the μD^* system underestimates that of the original b–quark. In order to correct for this effect a multiplicative factor of 1.26 was applied to the $p_T^{\mu D^*}$ variable. In the following we will refer with the same name to this corrected quantity. The variable shown in the scatter plots is the corrected one. Since the azimuthal angle and rapidity of the μD^* approximate with a good degree of accuracy the analogous quantities of the originating quark no correction was applied in these cases. The situation is similar if the $K\pi$ or $K3\pi$ mode is considered except that, due to the tighter cuts on $p_T^{D^*}$, this mode is more sensitive to quarks produced at higher transverse momenta ($p_T^b \gtrsim 5$ GeV). The $K\pi$ mode allows instead to gain sensitivity at quark transverse momenta up to $p_T^b \gtrsim 2-3$ GeV. Furthermore it can be noticed from the Right hand bottom plots in Figure 6.1 that at higher transverse momenta the resolution in ϕ is improved with a spread on the difference at the level of 5–10°.

The distributions of the (corrected) $p_T^{\mu D^*}$ and $y_{\mu D^*}^{rap}$ in the data after all the selection cuts (described in the previous Chapter) are shown in Figure 6.2. The $K\pi$ mode plots are on the Left side, the $K3\pi$ on the Right. The number of data amounts to 44 and 33 events respectively with a combinatorial background of about 10 in both cases. The binning was chosen in order to have a reasonable and equilibrated number of events in each interval. In the $K3\pi$ mode the same binning was adopted as for $K\pi$ for comparison's sake even if the lowest bin is not populated. The wrong charge D^* contribution was taken, as previously done, by averaging the like unlike and like sign muon contributions.

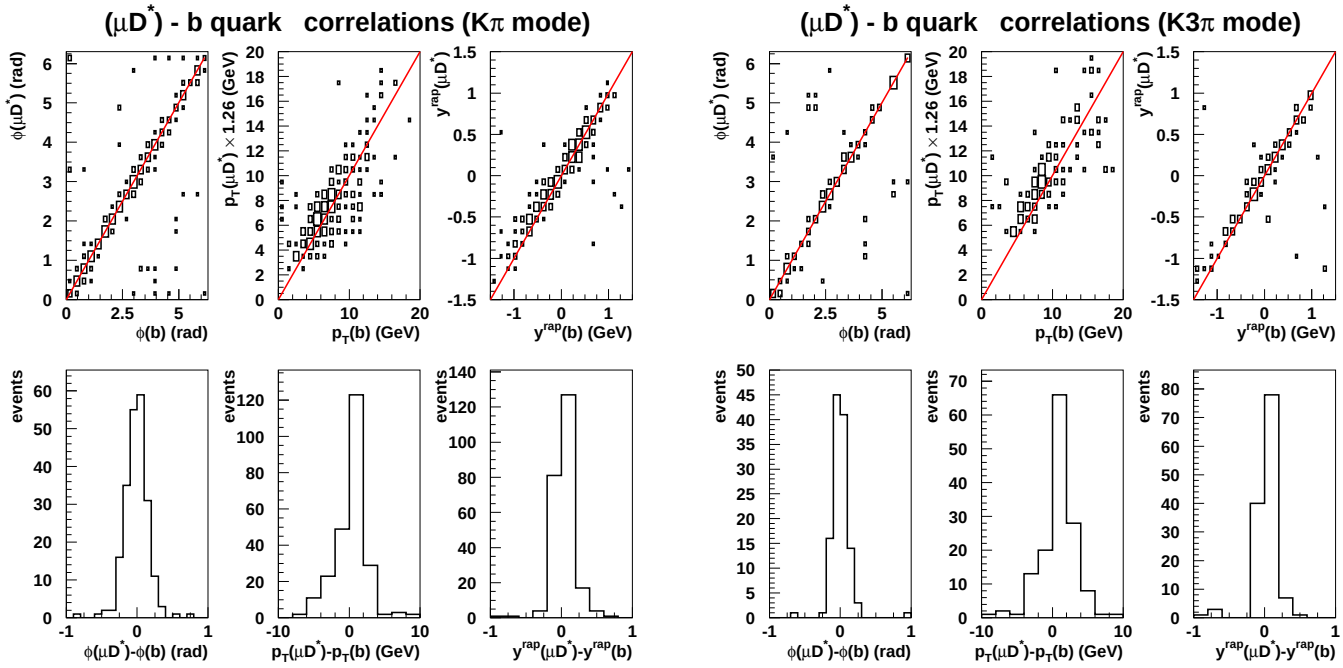

Figure 6.1: *The Left hand plots refer to $D^* \rightarrow (K\pi)\pi$ events while those on the Right to $D^* \rightarrow (K3\pi)\pi$ events. From Left to Right the upper plots show the correlation in the* PYTHIA *Monte Carlo between the azimuthal angle, transverse momentum and rapidity of the μD^* system and of the originating b or $\bar{b}$ quark. The lower plots show the distribution of the difference between these quantities at μD^* and b level.*

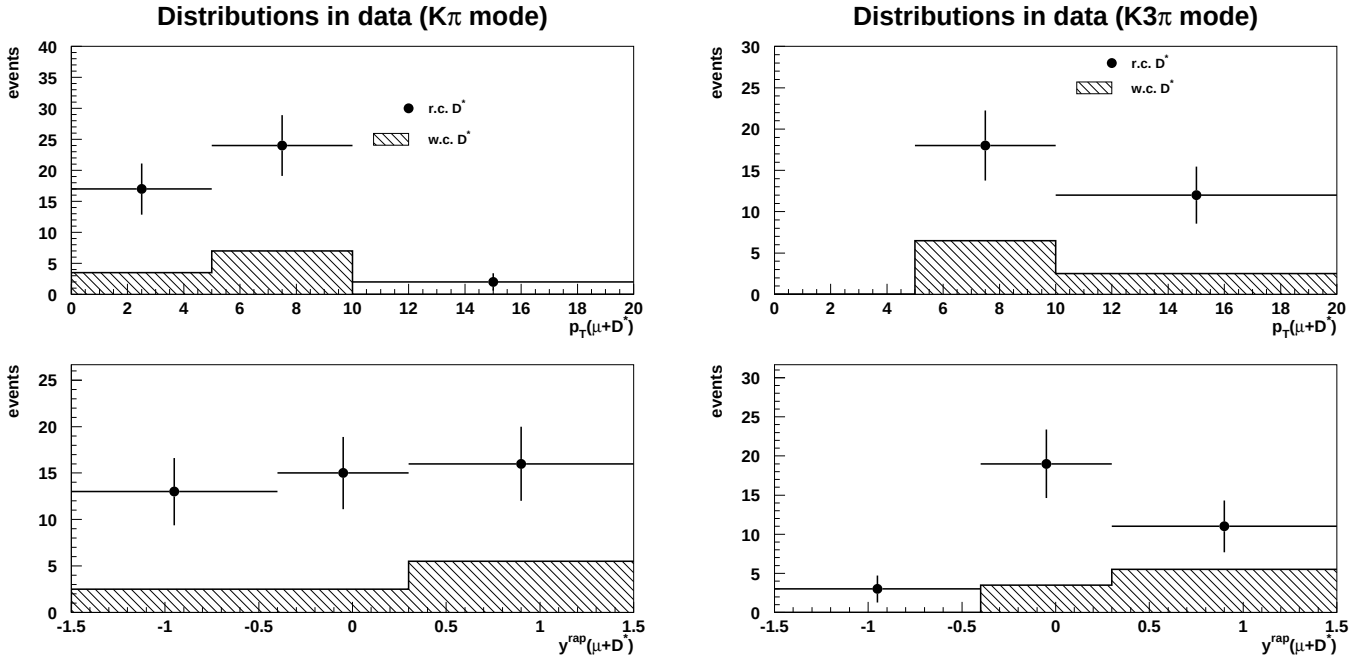

Figure 6.2: $p_T^{\mu D^*}$ *and* $y_{\mu D^*}^{rap}$ *distributions in the data. The wrong charge D^* contribution (average of like and unlike sign) is shown y the dashed histogram.*

6.2 Differential cross sections

We will now introduce the quantities which will be used in the differential cross section definition. We selected events in the kinematic region which is very similar to the one we already used to calculate the total visible cross sections. The kinematic region consists of events which at hadron level contain at least a muon with $p_T^{\mu} > 1.4$ GeV and $-1.75 < \eta^{\mu} < 1.3$ and at least a D^* decaying into $D^0(\rightarrow K\pi)\pi_s$ or $D^0(\rightarrow K\pi\pi\pi)\pi_s$ with $|\eta^{D^*}| < 1.5$. and $p_T^{D^*} > 1.9$ GeV for both the $K\pi$ and $K3\pi$ channels. In addition, with respect to the visible cross sections kinematic regions, we required both the μ and D^* to come from the same b (or $\bar{b}$) quark. In this way we are closer to the configuration which we are experimentally measuring. The occurrence of muon and D^* pairs coming from different b quarks in our selection ($\Delta R_{\mu D^*} < 2$, $3 < m_{\mu D^*} < 5$ GeV) has been estimated in our Monte Carlo to be of the order of 5 %. In such cases the b quark was arbitrarily chosen to be the one giving the muon. In these events the μD^* variables are not good estimators of the quark properties. This class of events accounts for the off–diagonal contributions in the correlation plots of Figure 6.1.

A bin–by–bin unfolding procedure was employed. The distributions of the variables at hadron level has been denoted as T_i ("true"), i being the bin index. R_i ("reconstructed") stands for the number of events in each bin satisfying all the cuts of the analysis at reconstructed level. The ratio R_i/T_i is the acceptance ($\mathcal{A}_i$) in the bin. It estimates the fraction of the events produced in the defined kinematic region which are actually detected after the experimental cuts.

If we indicate with N_i the distribution of (wrong charge D^* subtracted) beauty events in the data with respect to the chosen variable $\xi = p_T^b$, y_b^{rap}, and with $\Delta\xi_i$ the width of the i–th bin, the differential cross section is then expressed by:

$$\mathcal{A}_i = \frac{R_i}{T_i} \quad , \quad \left(\frac{d\sigma}{d\xi}\right)_i = \frac{N_i}{\mathcal{A}_i \cdot \mathcal{L} \cdot \mathcal{B} \cdot \Delta\xi_i} \tag{6.1}$$

$\mathcal{B}$ and $\mathcal{L}$ indicate the branching ration and the integrated luminosity. If we then define the vector containing in each bin the number of events which were generated and reconstructed inside that bin as $T_i \cap R_i$, then the so–called *efficiency* ($\mathcal{E}_i$) and *purity* ($\mathcal{P}_i$) are given by:

$$\mathcal{E}_i = \frac{T_i \cap R_i}{T_i} \qquad \mathcal{P}_i = \frac{T_i \cap R_i}{R_i} \qquad \mathcal{A}_i = \frac{\mathcal{E}_i}{\mathcal{P}_i} \tag{6.2}$$

The efficiency is the fraction of events which fall in a certain bin and are also reconstructed in the same bin while the purity is the fraction of the events which have been reconstructed in a certain bin and belong to that bin also at true level. With these quantities the effect of reduction in the final events in a certain bin due to the selection cuts and the effect of the uncertainty in the reconstruction of a certain variable are decoupled. If the hadronic quantities were perfectly reconstructed by an ideal detector there would be no migrations of the data between adjacent bins and the purity would be unitary in each bin. In this situation the efficiency would coincide with the acceptance and it would only be sufficient to correct the observed events for the inefficiency and the experimental level cuts.

The distributions of the rapidity and transverse momentum at μD^* (solid histogram) and quark level (dashed histogram) have been compared in Figure 6.3. The ratio between these distributions is shown in the Right hand plots of the same Figure. In both the $K\pi$ and $K3\pi$ case the shape of the distributions at true and reconstructed level is similar. This already indicates that the applied corrections and the binning choice reduced the importance of migrations. The results for purity, efficiency and acceptance are shown in Figure 6.4. The errors, $\delta\mathcal{E}_i$ and $\delta\mathcal{P}_i$ have been calculated using the following binomial expressions which take into account the correlations between T_i and R_i:

$$\delta\mathcal{E}_i = \sqrt{\frac{(1-\mathcal{E}_i)\cdot\mathcal{E}_i}{T_i}} \qquad \delta\mathcal{P}_i = \sqrt{\frac{(1-\mathcal{P}_i)\cdot\mathcal{P}_i}{R_i}} \qquad \delta\left(\frac{1}{\mathcal{A}_i}\right) = \sqrt{\frac{T_i}{R_i^3}\left[\, T_i + R_i - 2\, T_i \cap R_i \,\right]} \tag{6.3}$$

The observed acceptance (for unlike sign pairs) in the $K\pi$ channel rise with the transverse momentum of the b quark from about 5% to 12%. The purity is about flat at 70–80 %. As a function of rapidity the acceptance is higher in the middle rapidity region while the purity is more or less flat at about 80 %. The values for T_i, R_i, $T_i \cap R_i$, $\mathcal{E}_i$, $\mathcal{P}_i$, $\mathcal{A}_i$ and of the cross sections $(d\sigma/d\xi)_i$ for p_T^b and y_b^{rap} in the $K\pi$ and $K3\pi$ channels have been summarized in Table 6.1. The differential cross sections $\frac{d\sigma}{dp_T^b}$ $\frac{d\sigma}{dy_b^{rap}}$ are shown in the plots of Figures 6.5 and 6.6. The quoted errors are statistical only. They are larger than in the case of the total cross section due to the binning and become dominant if we compare

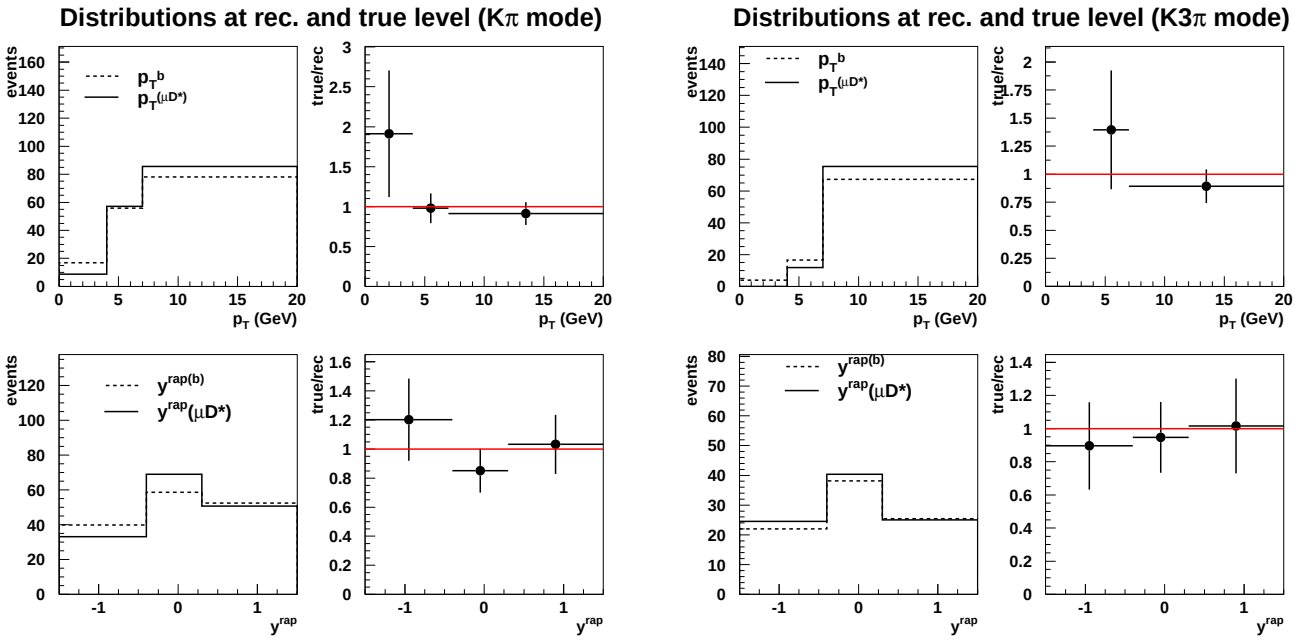

Figure 6.3: *The Left hand plots refer to $D^* \to (K\pi)\pi$ events while those on the Right to $D^* \to (K3\pi)\pi$ events. The plots show a comparison between the distributions of $p_T^{\mu D^*}$ and p_T^b and between $y_{\mu D^*}^{rap}$ and y_b^{rap}. The solid line histograms refer to the μD^* level variables while the dashed histograms represent the distributions at quark level. The histograms with bullets represent the ratio between the distributions at quark level and μD^* level.*

them with the systematic errors for the total visible cross sections (omitting the contribution due to the description of the $p_T^{\mu D^*}$ distribution).

The integrated values of the cross sections are compatible with those obtained in the previous Chapter within the uncertainty due to the acceptance corrections statistical fluctuations and taking into account that the kinematic region is smaller due to the requirement of the muon and D^* to come from the same beauty quark.

The comparison with the FMNR NLO calculation was performed by scaling the prediction expressed for $y_b^{rap} < 1$ $Q^2 < 1$ GeV^2 and $0.05 < y < 0.85$ to the kinematic region in which the visible differential cross sections were calculated namely:

$$\begin{aligned} p_T^{D^*} &> 1.9\,\text{GeV} \qquad |\eta^{D^*}| < 1.5 \\ p_T^{\mu} &> 1.4\,\text{GeV} \quad -1.75 < \eta^{\mu} < 1.3 \end{aligned}$$

with muon and D^* coming from the same b–quark. This rescaling was performed, as in the previous Chapter using the inclusive PYTHIA Monte Carlo, by counting the relative yield of events in the kinematic region from quarks in the parton level region. The theoretical error is represented by the filled band. The upper prediction has been calculated as for the total cross section, by assuming $m_b = 4.5$ GeV and $\mu = \mu_0/2$, while the lower one is obtained with $m_b = 5$ GeV and $\mu = 2\mu_0$.

The measured cross section in principle also include events with y and Q^2 outside of the regions in which the NLO prediction has been calculated. This choice was driven by the need to include as much statistics as possible. The small additional contribution to the NLO prediction has been in this context neglected.

By looking at the $K\pi$ $d\sigma/dp_T^b$ there is an indication for the excess over the NLO prediction to be more pronounced at low values of the quark transverse momentum. On the other hand the NLO undershoots the data uniformly over the whole rapidity range. The $K3\pi$ data, which, on average, refer to higher transverse momenta, agree with the $K\pi$ values and appear to be closer to the next–to–leading order. This is better seen in the plots of Figure 6.7 in which the data in the two channels and the theoretical prediction are shown together for p_T^b (top) and y_{rap}^b (bottom).

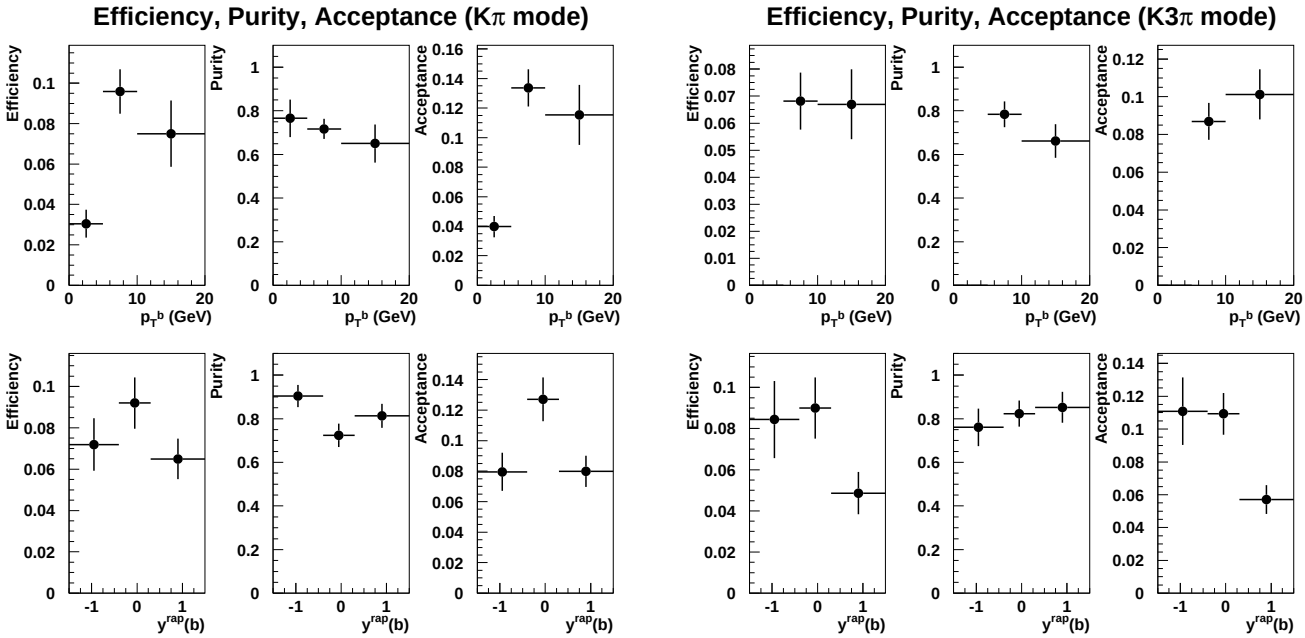

Figure 6.4: **Left***: The upper plots show the efficiency, purity and acceptance as a function of p_T^b in the $K\pi$ channel. The corresponding quantities as a function of y_b^{rap} are shown in the lower plots.* **Right***: As for the Left part for the $K3\pi$ channel.*

$d\sigma/dp_T^b$ $\quad D^* \to (K\pi)\pi_s$

bin	T_i	R_i	$T_i \cap R_i$	$\mathcal{E}_i$	$\mathcal{P}_i$	$\mathcal{A}_i$	σ_i
$[0,5]$	613	24.4	18.7	3.0 ± 0.7	76.6 ± 8.6	3.8 ± 0.7	24 ± 9
$[5,10]$	727	97.2	69.7	9.6 ± 1.1	71.7 ± 4.6	13.0 ± 1.3	9 ± 3
$[10,20]$	259	29.9	19.4	7.5 ± 1.6	65.0 ± 8.7	11.4 ± 2.0	0.6 ± 0.4

$d\sigma/dy_b^{rap}$ $\quad D^* \to (K\pi)\pi_s$

bin	T_i	R_i	$T_i \cap R_i$	$\mathcal{E}_i$	$\mathcal{P}_i$	$\mathcal{A}_i$	σ_i
$[-1.5,-0.4]$	416	33.1	29.9	7.2 ± 1.3	90.4 ± 5.1	7.7 ± 1.2	42 ± 17
$[-0.4,0.3]$	542	68.9	49.9	9.2 ± 1.2	72.4 ± 5.4	12.5 ± 1.4	49 ± 17
$[0.3,1.5]$	636	50.8	41.3	6.5 ± 1.0	81.3 ± 5.5	7.7 ± 1.0	39 ± 17

$d\sigma/dp_T^b$ $\quad D^* \to (K\pi\pi\pi)\pi_s$

bin	T_i	R_i	$T_i \cap R_i$	$\mathcal{E}_i$	$\mathcal{P}_i$	$\mathcal{A}_i$	σ_i
$[0,5]$	64	0	0	0	0	0	0
$[5,10]$	566	49.2	38.6	6.8 ± 1.1	78.4 ± 5.9	7.8 ± 1.0	5.1 ± 2.1
$[10,20]$	376	38.1	25.2	6.7 ± 1.3	66.2 ± 7.7	9.2 ± 1.3	1.8 ± 0.7

$d\sigma/dy_b^{rap}$ $\quad D^* \to (K\pi\pi\pi)\pi_s$

bin	T_i	R_i	$T_i \cap R_i$	$\mathcal{E}_i$	$\mathcal{P}_i$	$\mathcal{A}_i$	σ_i
$[-1.5,-0.4]$	221	24.5	18.6	8.4 ± 1.9	76.1 ± 8.6	10.8 ± 2.1	4.4 ± 2.7
$[-0.4,0.3]$	369	40.3	33.2	9.0 ± 1.5	82.4 ± 6.0	9.5 ± 1.3	40 ± 13
$[0.3,1.5]$	439	25.0	21.3	4.9 ± 1.0	85.2 ± 7.1	5.1 ± 0.9	16 ± 11

Table 6.1: *Summary of the quantities used in the differential cross section calculation. From top to bottom: $d\sigma/dp_T^b$ in the $K\pi$ mode, $d\sigma/dy_b^{rap}$ in the $K\pi$ mode, $d\sigma/dp_T^b$ in the $K3\pi$ mode, $d\sigma/dy_b^{rap}$ in the $K3\pi$ mode.*

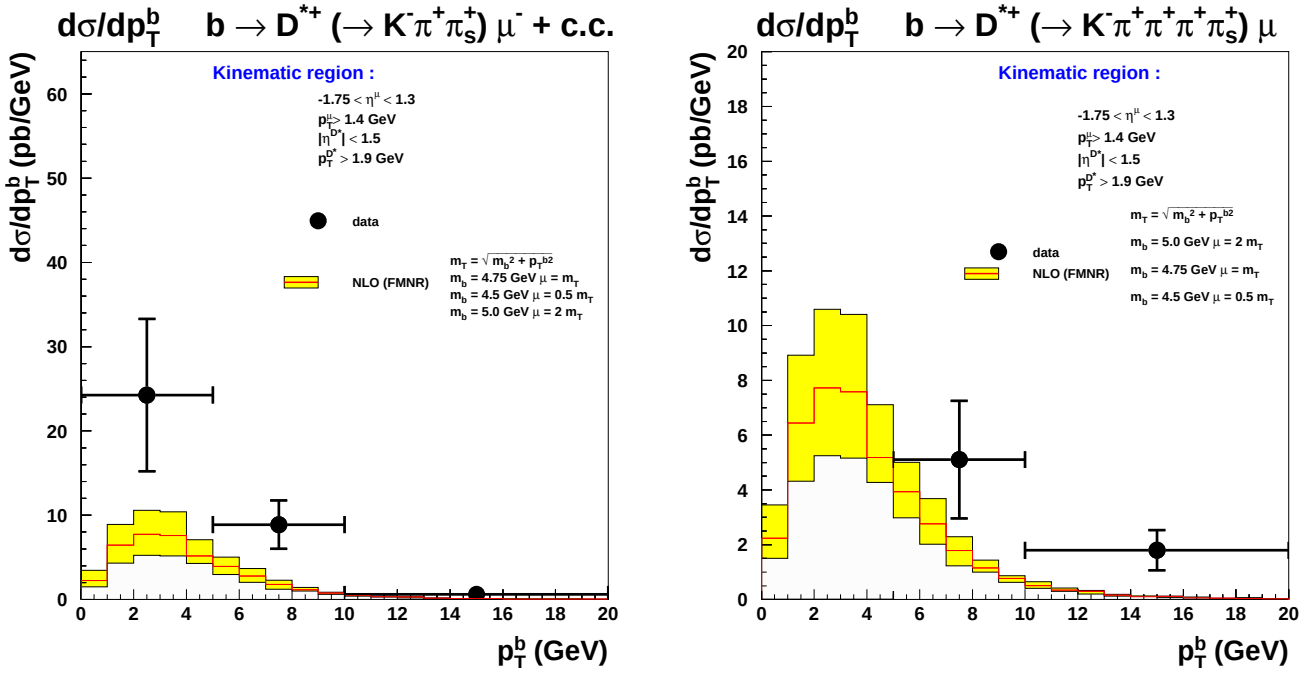

Figure 6.5: *Differential cross sections $d\sigma/dp_T^b$ for the $K\pi$ mode (***Left***) and $K3\pi$ (***Right***). The NLO FMNR prediction is indicated by the plain histogram.*

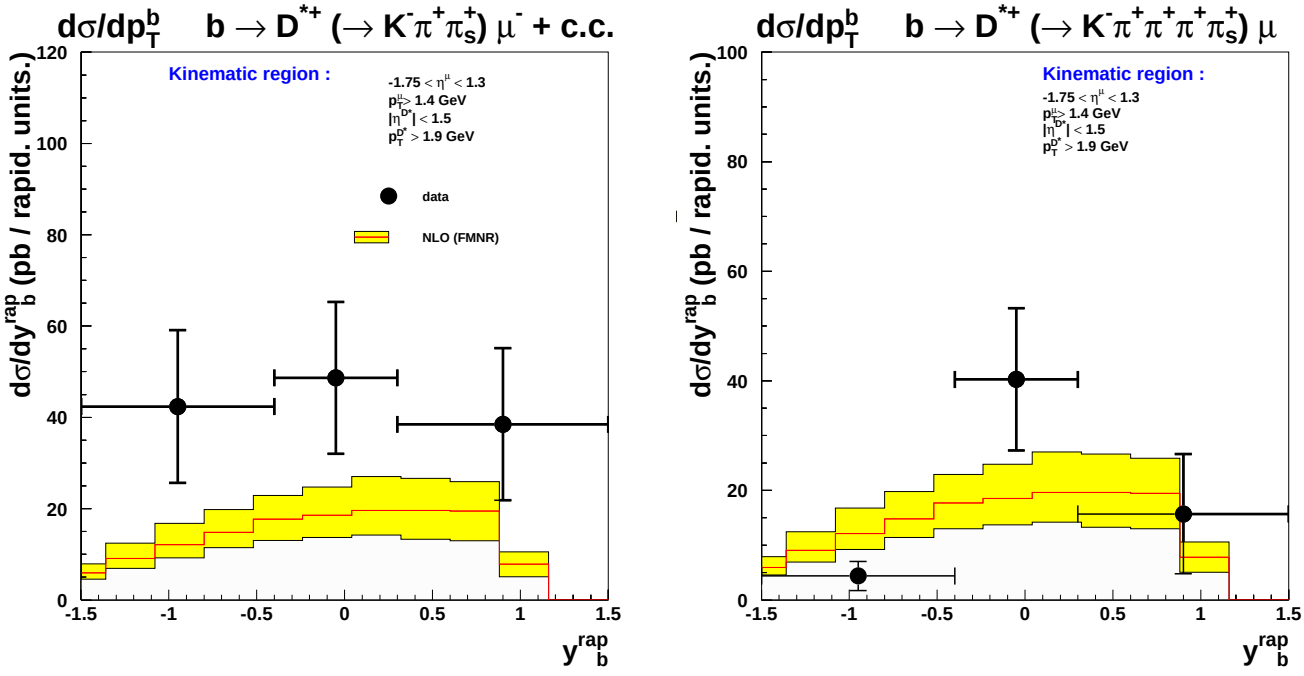

Figure 6.6: *Differential cross sections $d\sigma/y_b^{rap}$ for the $K\pi$ mode (***Left***) and $K3\pi$ (***Right***).*

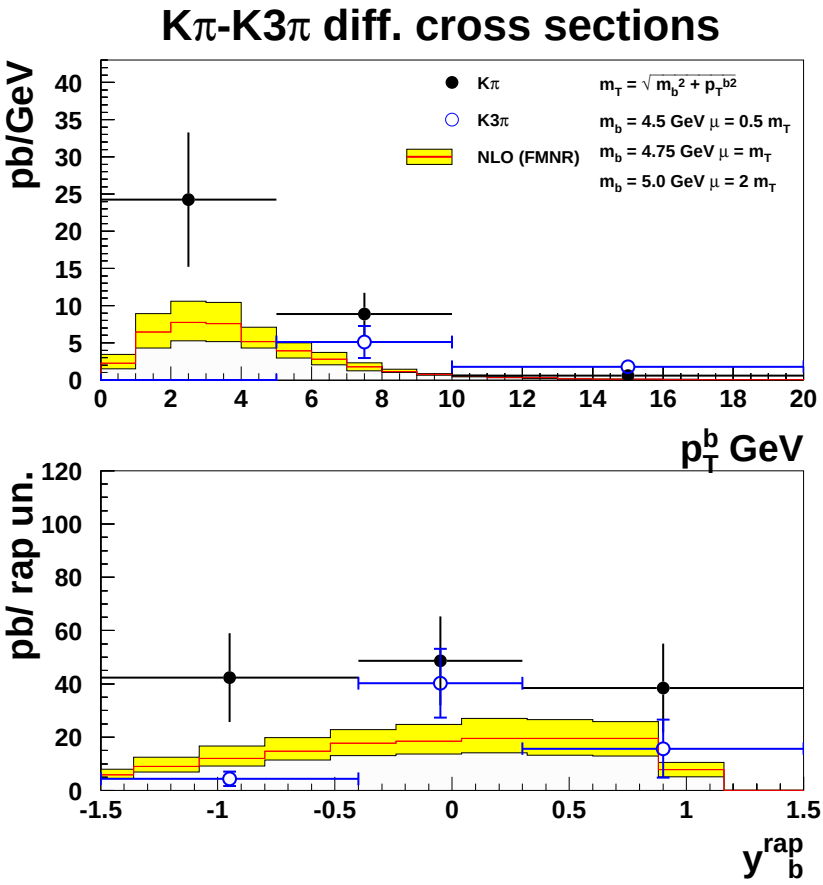

Figure 6.7: *Comparison of the differential cross sections in p_T^b (upper plot) and y_b^{rap} lower plot in the $K\pi$ (filled bullets) and $K3\pi$ channels (hollow bullets). The plain histogram represents the NLO FMNR prediction scaled to the visible region to which the cross sections refer (see text).*

Summary and outlook

In this thesis we presented a measurement of the beauty production cross section in ep collisions at HERA using an analysis technique based on the detection of a muon and D^* from a b and/or $\bar{b}$ decay. The data sample used for the analysis corresponds to an integrated luminosity of 114 pb^{-1} collected by the ZEUS experiment in the years between 1996 and 2000. Events were selected containing a charged D^* meson decaying in the $(K\pi)\pi$ or $(K\pi\pi\pi)\pi$ channel with a pseudorapidity within ± 1.5 and a transverse momentum ot at least 1.9 and 3.8 GeV respectively. Good muon candidates reaching the inner muon chambers and having a transverse momentum of at least 1.4 GeV were selected in the barrel and rear region ($1.3 < \eta^{\mu} < -1.75$). Muon and D^* mesons having opposite charge were combined and their separation in the $\eta - \phi$ plane and invariant mass were calculated. The signal was extracted by fitting the distribution of the distance between muon and D^* meson in the η–ϕ plane, after requiring the invariant mass of pairs lying in the same hemisphere to be compatible with a B–meson semileptonic decay. The applied selection proved very effective in reducing the importance of fake muon and fake D^* backgrounds. An extended study demonstrated the possibility to use the inner chambers muon sample and retain a reasonably good control of the fake muon contaminations.

Visible cross sections were calculated in the region of phase space defined by the experimental cuts, both for the inclusive sample and also separately for photoproduction ($Q^2 < 1$ GeV^2, $0.05 < y < 0.85$) and deep inelastic scattering ($Q^2 > 2$ GeV^2, $0.05 < y < 0.7$). The measured visible cross sections for the reaction $ep \to b\bar{b}X \to D^*\mu(e')X'$ are here given with the corresponding statistical and systematic errors:

$$\begin{aligned}
\sigma^{K\pi}_{vis\ (PHP+DIS)} &= 214 \pm 52\ (\text{stat.})^{+37}_{-27}(\text{sys.})^{+88}_{-45}(\text{main sys.})\ \text{pb} \\
\sigma^{K\pi}_{vis\ (PHP)} &= 159 \pm 41(\text{stat.})^{+33}_{-34}(\text{sys.}))^{+59}_{-35}(\text{main sys.})\ \text{pb} \\
\sigma^{K\pi}_{vis\ (DIS)} &= 71 \pm 34\ (\text{stat.})^{+8}_{-20}(\text{sys.})^{+31}_{0}(\text{main sys.})\ \text{pb} \\
\sigma^{K3\pi}_{vis\ (PHP+DIS)} &= 68 \pm 16\ (\text{stat.})^{+11}_{-23}(\text{sys.})^{+12}_{-14}(\text{main sys.})\ \text{pb} \\
\sigma^{K3\pi}_{vis\ (PHP)} &= 37 \pm 11(\text{stat.})^{+5}_{-13}(\text{sys.})^{+7}_{-9}(\text{main sys.})\ \text{pb}
\end{aligned}$$

The contribution to the systematic error denoted as "main sys." has been quoted separately since the assumptions on which it is based depend to a large extent on the limited statistics in the final sample. More data will probably reduce this source of uncertainty. The other systematic errors are included in the term denoted as "sys.".

After extrapolating for the different cut on the p_T of the D^* meson the measured cross sections in the $K\pi$ and $K3\pi$ are found to be in good agreement. The resulting visible cross sections significantly exceed leading-order plus parton–shower MC expectations. Since the analysis is sensitive to b-quark production near the kinematic threshold, the visible cross sections were extrapolated to b-quark production cross sections in photoproduction and deep inelastic scattering without an explicit cut on p_T^b and for rapidity of the produced quarks not exceeding one:

$$\begin{aligned}
\sigma(\gamma^* p \to b(\bar{b})X)^{K\pi}_{PHP} &= 15.1 \pm 3.9(\text{stat.})\ ^{+3.2}_{-3.3}(\text{syst.})\ ^{+5.6}_{-3.3}(\text{main sys.})\ \text{nb} \\
\sigma(\gamma^* p \to b(\bar{b})X)^{K3\pi}_{PHP} &= 14.8 \pm 4.4(\text{stat.})\ ^{+2.0}_{-5.3}(\text{sys.})\ ^{+2.7}_{-3.4}(\text{main sys.})\ \text{nb} \\
\sigma(\gamma^* p \to b(\bar{b})X)_{DIS} &= 3.8 \pm 1.8(\text{stat.})\ ^{+0.4}_{-1.1}(\text{syst.})\ ^{+1.6}_{0}(\text{main sys.})\ \text{nb}
\end{aligned}$$

These parton level cross sections were compared to QCD predictions to the NLO accuracy which were obtained using the calculation by Frixione, Mangano, Nason and Ridolfi for photoproduction and Harris and Smith for DIS which were implemented in the FMNR and HVQDIS programs.

$$\begin{aligned}
\sigma_{NLO}(\gamma^* p \to b(\bar{b})X)_{PHP} &= 5.0^{+1.7}_{-1.1}\ \text{nb} \\
\sigma_{NLO}(\gamma^* p \to b(\bar{b})X)_{DIS} &= 0.87^{+0.28}_{-0.16}\ \text{nb}
\end{aligned}$$

The central values were calculated with $m_b = 4.75$ GeV and $\mu = \sqrt{m_b^2 + {p_T^b}^2}$ ($\sqrt{m_b^2 + Q^2}$ for DIS) while the errors were estimated by simultaneously varying the scale in the range $[\mu/2, 2\mu]$ and m_b in $[4.5, 5]$ GeV.

In order to compare to other beauty results performed at HERA, the photoproduction visible cross sections were also extrapolated at quark level for $p_T^b > 3$ GeV and $|\eta_b| < 2$ in events with $0.2 < y < 0.8$ and $Q^2 < 1$ GeV^2. The obtained value are here given:

$$\sigma_{extr}^{K\pi} = 3.35 \pm 0.86(\text{stat.})^{+0.7}_{-0.7}(\text{sys.})^{+1.2}_{-0.7}(\text{main sys.}) \text{ nb}$$
$$\sigma_{extr}^{K3\pi} = 3.27 \pm 0.93(\text{stat.})^{+0.4}_{-1.2}(\text{sys.})^{+0.6}_{-0.7}(\text{main sys.}) \text{ nb}$$

The predictions tend to underestimate the measured cross sections for a factor of about three in both photoproduction and deep inelastic scattering. By comparing with previous measurements performed with analyses with lepton and jets there is indication for the discrepancy between NLO QCD and experimental data to be enhanced as lower values of the transverse momentum of the produced quarks are accessed.

In order to pursue this hypothesis more directly within our analysis differential cross sections have been calculated in the transverse momentum of the produced b–quark and its rapidity. This was possible by restricting to the signal enriched region by considering events with unlike sign μD^* pairs in the same hemisphere and with invariant mass between 3 and 5 GeV. The excess over the NLO prediction is found to be more relevant at low p_T^b. Events in the $K3\pi$ mode, which are mainly found at high p_T^b, are in agreement with the $K\pi$ results and closer to the NLO prediction. The excess seems to be uniformly distributed as a function of rapidity.

This analysis proved effective in studying b production at HERA in a peculiar and previously unexplored kinematic region. Its potentialities, in terms of providing strict constraint to the theory, will be fully exploited as larger data samples will become available with the operation of HERA with upgraded luminosity from present days up to the year 2006.

Appendix A

Fake–muon studies

A.1 Introduction

The understanding of how well our Monte Carlo simulation describes the various phenomena which can lead to muon misidentification is a topic which deserves investigation being relevant in various analyses on *beauty* production.

Furthermore keeping this background under control could be an important step toward interesting measurements such as charm production in the muon semi–leptonic channel. More generally speaking a better knowledge of this source of background is essential for all those analyses which could benefit from the use of the higher statistics sample of low–momentum "non–passing" muons which are detected in the inner muon chambers (BRMUI) but do not reach the outer muon chambers (BRMUO) (see Section 2.4.1).

For this same reason the study which will be presented in this Chapter has a direct interest as far as the analysis described in this work is concerned [1]. It should be noted that, if we exclude J/ψ analyses, this is actually the first analysis in ZEUS which makes use of muons matched in the inner muon chambers only.

The method described in this Chapter relies on the possibility to select large samples of hadrons with high purity by selecting particular decays for which enough statistics and low backgrounds are attainable. The absolute numbers and the distributions of the subsample of tracks which, according to the standard analysis matching criteria, are misidentified as muons will be compared to the Monte Carlo predictions. We will also consider how the fake–muon probability depends on the nature of the considered hadron and compare the results with the expectations.

A.2 Hadron samples

We chose to study the following two–body decay modes since they are relatively easy to reconstruct, they are statistically relevant and provide different final state particles:

- $K^0_S \to \pi^+\pi^-$
- $\Lambda \to p\pi^-$ + c.c.
- $\phi \to K^+K^-$
- $D^0 \to K^-\pi^+$ with $D^{*+} \to D^0\pi^+$ + c.c.

The K^0_S and Λ decays provide very high–statistics samples allowing the fake–muon probability for pions and (anti–) protons to be studied as a function of the tracks' momentum and orientation within the detector. In this case, thanks to the fact that the decay vertex is displaced from the main vertex, the combinatorial background is relatively low. Furthermore in this case, a sizable number of hadronic tracks is also matched to segments in the outer muon chambers (*BRMUO*) thus allowing further checks to be performed (outer muon chamber matching has been used widely by all the beauty analysis in the muon+dijet channel, see Section 1.4.1.1).

[1] In the specific case of the $\mu + D^*$ analysis additional constraints on the fake-μ background are provided thanks by considering the like-sign sample as described in Section 5.5.

Though more limited in statistics and more significantly affected by combinatorial background, ϕ and D^0 decays allow to measure separately the behaviour of kaons in addition to pions and (anti–)protons. In the case of D^0, in particular, the lower statistics is partially compensated by the fact that the momentum distribution is relatively hard if compared to the other larger hadron samples from K^0_S, Λ and ϕ. This fact results in a relatively higher fraction of tracks faking a muon. Furthermore this cross check is particularly important for our analysis since it is closely related to the kind of sample we are interested in.

For each decay mode, by using the Monte Carlo simulation, we will derive an estimate of possible contaminations to a "pure hadron sample" paying particular attention to possible "true–muon" sources which could bias the measurement. Anyhow the main focus will be to verify the level of description of the Monte Carlo rather than deriving absolute properties for each hadron. Indeed, as we will see, the details of the result depend, to a certain extent, from the details of the cuts and distributions of the original sample of tracks.

To normalize to a common set of data, we required the tracks from each decay mode [2] to satisfy both the following cuts :

$$\begin{aligned} p_T^{trk} &> 0.9 \text{ GeV} \\ -2 < \eta^{trk} &< 1.6 \end{aligned} \tag{A.1}$$

This choice is intended to ease comparison between the different results (in addition to the primary purpouse of comparing each set with the corresponding Monte Carlo expectation). The cuts in Equations A.1 represent the minimal requirement that a track has to satisfy in order to have a minimal chance to reach the BRMUON chambers. This is dictated by the geometry and conformation of the ZEUS detector. The values were chosen *a posteriori* by looking at the distributions of the matched tracks.

The Monte Carlo used for this study (for K^0_S, Λ and D^0) consists of an admixture of $c\bar{c}$ and $b\bar{b}$ events generated with a loose preselection involving the presence of charmed mesons and barions with mild cuts on their transverse momenta. This general D–meson Monte Carlo is the same which is used for the main $\mu + D^*$ analysis in this work and various other ZEUS analyses focusing on D^* production. It is based on the PYTHIA 6.156, HERWIG 6.301 and RAPGAP 2.08/18 generators and has been tuned to reproduce the measured branching ratios of charmed mesons. More details can be found in Section 3.6. In the case of ϕ a different set of Monte Carlo samples was used (see Section A.6).

This study focuses on testing the simulation of the interaction of the final state particles with the detector [3]. Nevertheless we decided to to use fully simulated physics events rather than single tracks for several reasons. First this choice allows us to be closer to the experimental situation which is found in real data. For example if the whole event is simulated the possibility of wrong matching by the algorithm is taken into account. More importantly the contaminations to the hadron sample due to true muons can be kept under control. As last benefit, if the physics of the processes is reasonably simulated, the correction factors needed to reweight these distributions to those found in the data are smaller.

Some typical events showing how a candidate track from a K^0_S decay can reach the inner muon chambers and be matched to an inner track are presented in Figure A.1.

A.3 Some definitions

In what follows tracks are labeled as "fake–muons" when they are matched by the BREMAT [163] matching package to a reconstructed segment in the inner muon chambers. This program performs an outward extrapolation of inner tracks taking into account the detailed distribution of materials and the magnetic field in ZEUS. The matching is based on the comparison between the position and orientation of the extrapolated track and those of the reconstructed segment (*4 d.o.f. matching*) in the inner muon chambers. When an outer segment is also reconstructed it is possible to include in the matching probability parameter the momentum as it is measured by the inner tracking devices and the muon chambers (*5 d.o.f. matching*). Both these two matching procedures have been considered in what follows. An exhaustive description of the functionalities of BREMAT can be found in Section 4.4 and in Reference [163].

[2] The only exceptions will be applied for a particular reason in the case of the decay $\phi \to K^+K^-$ as it will be described in Section A.6 and for kaons an pions from D^0 for which, in order to have a better signal, it is necessary to introduce harder cuts.

[3] The software simulating the ZEUS detector is based on GEANT 3.21. (MOZART : MOnte carlo for Zeus Analysis, Reconstruction and Trigger)[145]. See also Section 3.5

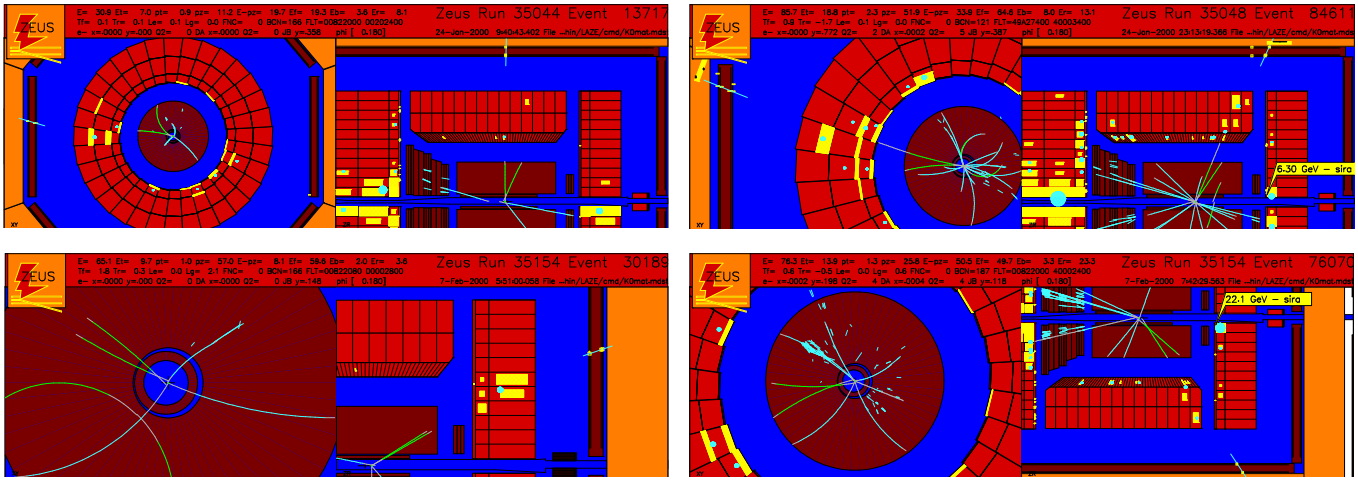

Figure A.1: *Display of four events with a candidate pion from K^0_S producing a fake–muon in BRMUI. Each plot shows a zoomed XY view (Left part) and a RZ view (Right part). The kaon tracks can be identified by the fact that their intersection is visibly displaced from the interaction point. They are shown in green.*

The central value for the cut on the matching probability used here is set to $\mathcal{P} > 1\%$ and $\mathcal{P} > 5\%$ for 4 $d.o.f.$ and 5 $d.o.f.$ matching respectively. This latter value has been used in the past for example in the beauty photoproduction and DIS analyses with jets by ZEUS ([44, 45, 52]).

The track preselection cuts applied on the tracks in order to be considered as candidates for extrapolation and matching are the following:

- $p > 1$ GeV
- $\theta > 20^o$
- at least 3 CTD super layers (see 2.2.2)
- χ^2_{trk}/n $d.o.f. < 5$
- $|D_H| < 10$ cm
- $|Z_H| < 75$ cm
- $\Delta < 150$ cm

Δ being the distance between the segment in the chambers and a linear extrapolation of the CTD track to the inner surface of the calorimeter (*VCATCAL* tracks [180]). What we will quote as "fake–muon probability" is defined as the ratio:

$$\mathcal{P}_{\rm fak}(p,\theta) = \frac{\#\text{ matched tracks}}{\#\text{ all tracks}}$$

this quantity will be calculated in several momentum, polar angle and azimuthal angle intervals. In the case of $K^0_S \to \pi\pi$, $\Lambda \to p\pi$ and $D^0 \to K\pi$ we also measured the momentum dependence of this ratio in bins of polar angle and vice versa (double–differentially). We used this quantity to compare the prediction of data and Monte Carlo. The quoted errors are based on binomial expressions and take into account correlations[4].

As explicitly expressed in the formula, the fake–muon probability is well defined for a given momentum (p) and polar angle (θ). For this reason a proper comparison between different samples and between data and Monte Carlo based on this quantity should be performed in sufficiently narrow bins of these two variables. The value integrated in p and θ is of course also comparable but one should make sure the distributions in these two variables to be similar in data and Monte Carlo. In principle the azimuthal angle of the track (ϕ) is also relevant since the geometry of the chambers is not exactly symmetric in ϕ nevertheless, since the initial samples of tracks are uniformly distributed in ϕ, integrating over this variable does not constitute a problem for an appropriate comparison.

In the fake–muon probability definition we have not distinguished the different processes which can produce fake–muons which we already introduced in Section 5.5.1. The reconstructed segment in the muon chambers can be due to:

[4]Instead of taking the ratio $r = a/b$ we take it as $r = \frac{a+1}{b+2}$ while the error is given by $\sigma_r = \sqrt{\frac{r(1-r)}{b+3}}$.

- secondary muons coming from in–flight decays (*DIF*) of kaons and pions ($\pi^{\pm} \to \mu^{\pm}\nu$ or $K^{\pm} \to \mu^{\pm}\nu$),
- hadrons transversing the *CAL* without interacting (*sail–through*s).
- secondary particles hitting the muon chambers from hadronic interactions in the *CAL* (*punch–through*s).

It is experimentally difficult to disentangle the relative importance of these components. We will estimate their relative importance in the final sample of matched tracks with the Monte Carlo and demonstrate how the shape of the matching χ^2 in the data (which is one of the variables which are partially sensitive the different sources of fake muons) is well described by the admixture of these processes as predicted by the Monte Carlo.

Bearing in mind that we might have a small contamination from prompt muons in the initial sample we should be aware that our definition of the fake–probability is a bit inadequate. It would be more desirable to quote the probability of fake as the ratio between matched ($N_{\rm fak}^{\rm match}$) and unmatched real–fake particles ($N_{\rm fak}$):

$$\mathcal{P}'_{\rm fak} = \frac{N_{\rm fak}^{match}}{N_{\rm fak}} \tag{A.2}$$

while we can decompose our $\mathcal{P}_{\rm fak}$ as :

$$\mathcal{P}_{\rm fak} = \frac{N_{\rm fak}^{match} + N_{\mu}^{match}}{N_{\rm fak} + N_{\mu}} \tag{A.3}$$

N_{μ} and N_{μ}^{match} being respectively the number of prompt muons in the initial sample and the number of matched tracks being prompt muons. If we define the *contamination* $C \equiv N_{\mu}/N_{\rm fak}$ then :

$$\mathcal{P}'_{\rm fak} = (1+C)\cdot\mathcal{P}_{\rm fak} - \frac{N_{\mu}^{\rm match}}{N_{\rm fak}} \tag{A.4}$$

This correction can be derived in the Monte Carlo but since we cannot do the same on real data we will assume that the Monte Carlo simulates correctly these contaminations (this is one of the reasons why we chose to use a full Monte Carlo simulation). We will anyway verify the contaminations C from prompt muons to be small. Once this is assumed, the only remaining context in which this could be a relevant concern, would be when doing a comparison of $\mathcal{P}_{\rm fak}$ for the same kind of particle for different samples. In this case the prompt muon contamination might be sensibly different in different samples thus biasing the comparison. Since we are not specifically interested in these details we will not correct for this effect and, on this topic, we will limit ourselves to semi-quantitative considerations.

A.4 Study of fake–muons from pions via the decay $K^0_S \to \pi^+\pi^-$

The event preselection was performed [5] by requiring the presence of at least one secondary vertex in the event (`Nsecvtx>0`). Further selection cuts we imposed are the following:

- two oppositely charged tracks fitted to the same secondary vertex (from *VCPARSEC* table [134, 180])
- $p_{trk_1,trk_2} > 0.9$ GeV, $\quad 2 < \eta_{trk_1,trk_2} < 1.6$
- $0.487 < m_{\pi\pi} < 0.507$ GeV
- $\cos(\alpha_{XY}) < 0.99$
- $m_{p\pi} > 1.121$ GeV or $m_{p\pi} < 1.111$ GeV (anti-Λ cut)

[5] The *ZES* database information was used [154, 155]

α_{XY} being the angle between the kaon transverse momentum and the vector determining the position of the secondary vertex in the transverse plane. This cut helps in reducing the combinatorial background. The last cut is intended to reject Λ barions decaying to $p\pi$ which happen to fall in the K^0 mass window if both tracks are assigned the pion mass. The contamination of protons is indeed not very critical in itself. Furthermore this (not so large) component is effectively rejected by the "anti–Λ" cut. This can be seen in the Right hand *Dalitz* plot of Figure A.12 which shows the invariant mass of secondary vertex track pairs assuming the $\pi\pi$ or $p\pi$ hypothesis.

This selection on the ZEUS data collected in the years 1996–2000 yields the invariant mass peak shown in Figure A.2. All the events having at least one of the two tracks in the kinematic region defined in Equations A.1 enter in the plot of Figure A.2 [6]. After restricting to the mass window $[0.487, 0.507]$ GeV (yellow band in Figure A.2) the number of pion candidates from K^0 in the kinematic region defined in A.1 amounts to about 2.2 million of tracks. The combinatorial background is of the order of 16 % of the entire sample.

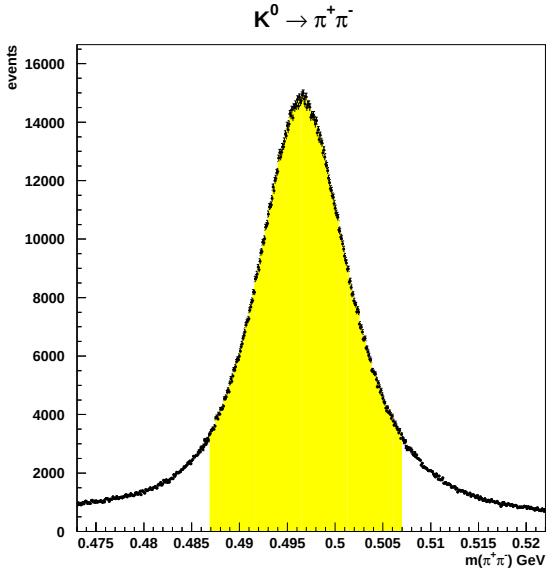

Figure A.2: *The plot shows the $K^0_S \to \pi^+\pi^-$ invariant mass peak using the statistics accumulated by ZEUS in the years 1996–2000. Events having at least one of the two tracks satisfying the requisites for being fake–muon candidates (see Equation A.1) are shown.*

About 5000 tracks in the pion sample are able to reach the BRMUON detector and be matched by BREMAT with a probability $4\ d.o.f.$ cut fixed at the commonly used value of 1 %. This corresponds to 0.23 % of the entire sample. The distributions in polar angle, momentum and azimuthal angle of these two samples of tracks are shown in the Left hand plots in Figure A.4. The upper bullets (in Red) represent all tracks, both matched and unmatched, while the sub–sample of matched tracks is shown by the shaded (yellow) histogram.

The first comparison with the Monte Carlo expectations has been carried out by evaluating in each bin the fake–muon probability considering the momentum, polar angle and azimuthal angle distributions globally. In this case, as already anticipated, differences between data and Monte Carlo within each bin might in principle arise. It could indeed happen that in a certain momentum bin the polar angle distribution in the initial sample in data and Monte Carlo to be sensibly different and the probability of fake depends on θ. In practice we have verified that in this particular case the relevance of this effect is not very important. The uncorrected distributions in θ and p for the global sample of tracks are only slightly different in data and Monte Carlo and the fake probability shows a relatively mild dependence on these variables which keeps the effect small. Anyway we decided to correct for this difference by reweighting the tracks' polar angle distribution in the Monte Carlo to the one in the data. The distributions in momentum and polar angle in the data and Monte Carlo samples are shown in the Left plots of Figure A.3 before and after the reweighting of the polar angle in the Monte Carlo. The result for the fake–probabilities in data and Monte Carlo after the polar angle reweighting is shown in the Right hand plots of Figure A.4.

[6] This is the convention which has been used for all the invariant mass plots in the rest of the Chapter.

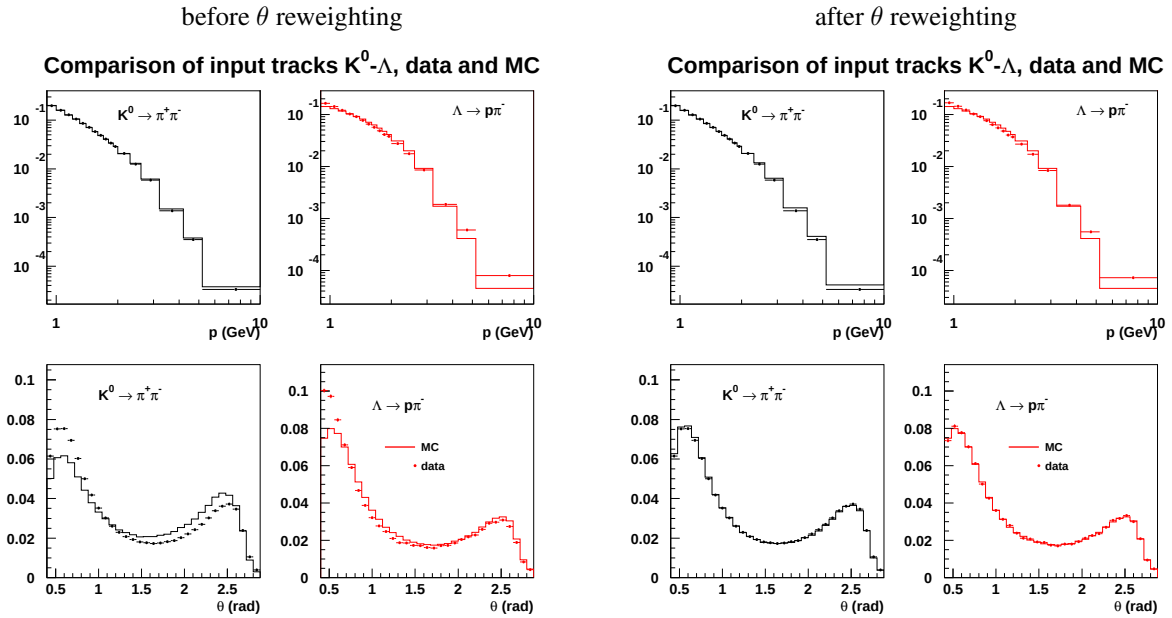

Figure A.3: *Data–Monte Carlo comparison of p and θ distributions for the initial samples of K^0_S (black) and Λs (red). Data are represented as bullets, Monte Carlo as the plain line histograms.* **Left***: before θ–reweighting in the Monte Carlo.* **Right***: after θ–reweighting.*

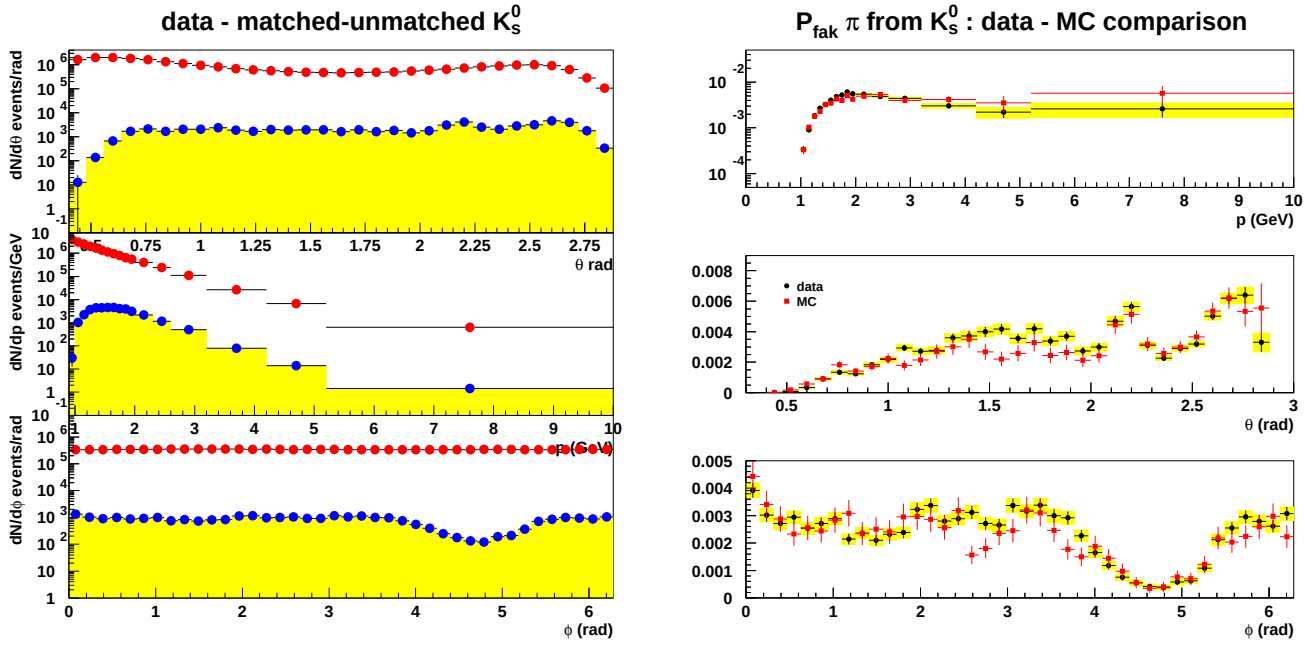

Figure A.4: **Left***: From Top to Bottom, distributions of polar angle, momentum and azimuthal angle of all K^0_S tracks (red bullets) and of those which are matched to BRMUI by* BREMAT *with $\mathcal{P}_{4\ d.o.f.} > 0.01$ (blue bullets, shaded yellow histogram). The ZEUS 1996-2000 statistics have been used.* **Right***: Data–Monte Carlo comparison of fake–muon probabilities for $4\ d.o.f.$ matching with* BREMAT *as a function of, from Top to Bottom, momentum, polar angle an azimuthal angle. Data are represented as black bullets with a yellow band for the statistical errors while Monte Carlo is represented by red squares.*

Taking benefit of the favourable statistics we decided to solve possible remaining ambiguities related to the fact that the fake probability is a function of both momentum and polar angle by evaluating the fake probabilities in bins of polar angle and momentum. In this way we get a kind of "double–differential" fake–muon probabilities and we are on a firmer ground in order to draw a comparison. The distributions in θ in bins of p and in p in bins of θ are shown respectively in the Right hand and Left hand plots in Figure A.5. The symbols have the same meaning as in Figure A.4. The differential fake–muon probabilities data–Monte Carlo comparison is shown in Figure A.6 as a function of

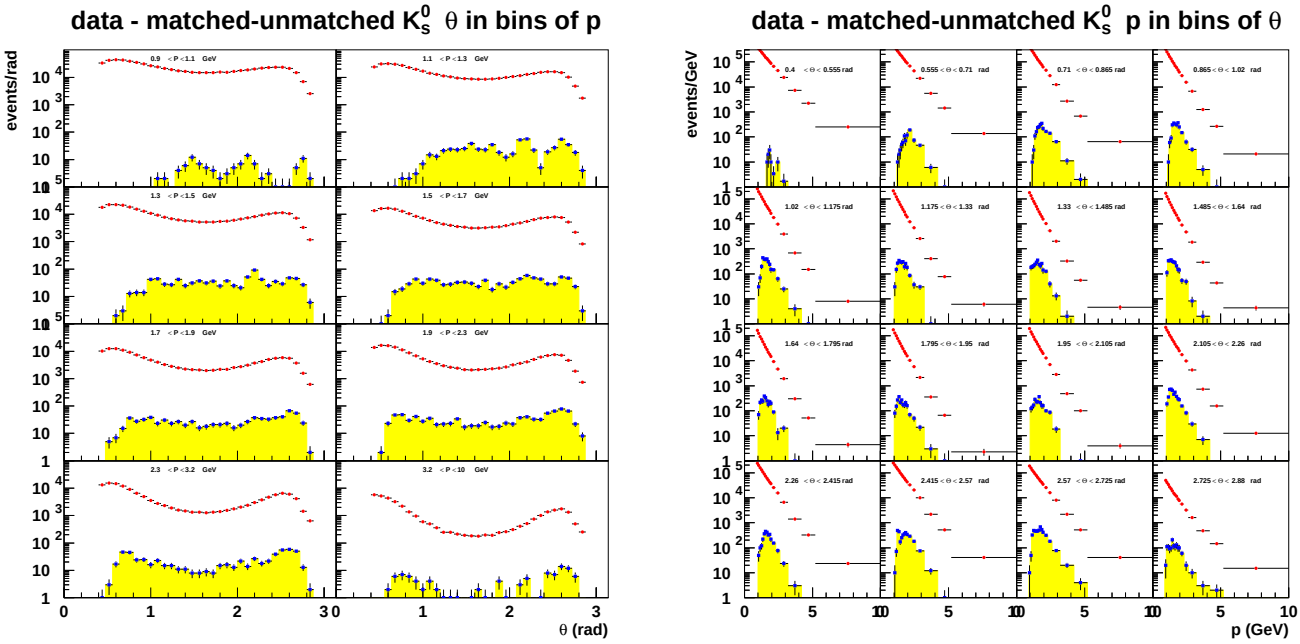

Figure A.5: **Left**: *θ distributions in bins of p ($[0.9, 1.1, 1.3, 1.5, 1.7, 1.9, 2.3, 3.2, 10]$ GeV) for pions from K^0_S. The meaning of the symbols is the same as in Figure A.4. The ZEUS 1996–2000 data have been used requiring a 4 d.o.f.* BREMAT *matching with $\mathcal{P} > 0.01$.* **Right** *: p distributions in bins of θ ($[0.4, 0.555, 0.71, 0.865, 1.02, 1.175, 1.33, 1.485, 1.64, 1.795, 1.95, 2.105, 2.26, 2.415, 2.57, 2.725, 2.88]$ rad). The chosen binning is also indicated in each plot.*

θ in bins of p and vice versa.

The level of accuracy of the Monte Carlo description looks remarkable. This is indeed to a certain extent fortuitous since one should keep in mind the fact that the detailed simulation of muon chambers' inefficiency is not fully implemented in the used Monte Carlo [7]. The inclusion of the additional inefficiency of the muon chambers in the Monte Carlo would put the number of fake–muons a bit down and this would mean the fake–muon component from pions is partially underestimated . The result is anyway satisfactory since the simulation reproduces the correct order of magnitude and the correct θ and p dependence for the fake–muon from pion contamination.

A.4.1 $5\ d.o.f.$ matching fakes

A sub–sample of tracks (about 1 % of those matched in the inner muon chambers) are also able to reach the outer muon chambers and be kept as good muon candidates using the 5 $d.o.f.$ matching. It includes, in addition to the 4 $d.o.f.$ matching, the information on the momentum as measured in the CTD and BRMUON. The cut on the 5 $d.o.f.$ probability was set to 5%. In the Left hand plots of Figure A.7 the distributions in the polar angle, momentum and azimuthal angle for all tracks and for those being matched in both the inner an outer chambers are presented. The fake probability with outer chambers has been compared to the Monte Carlo expectation in the Right hand plot of Figure A.7. This parameter is particularly sensitive to the difference in momentum between the initial samples in data

[7] This observation remains valid for the rest of this Chapter.

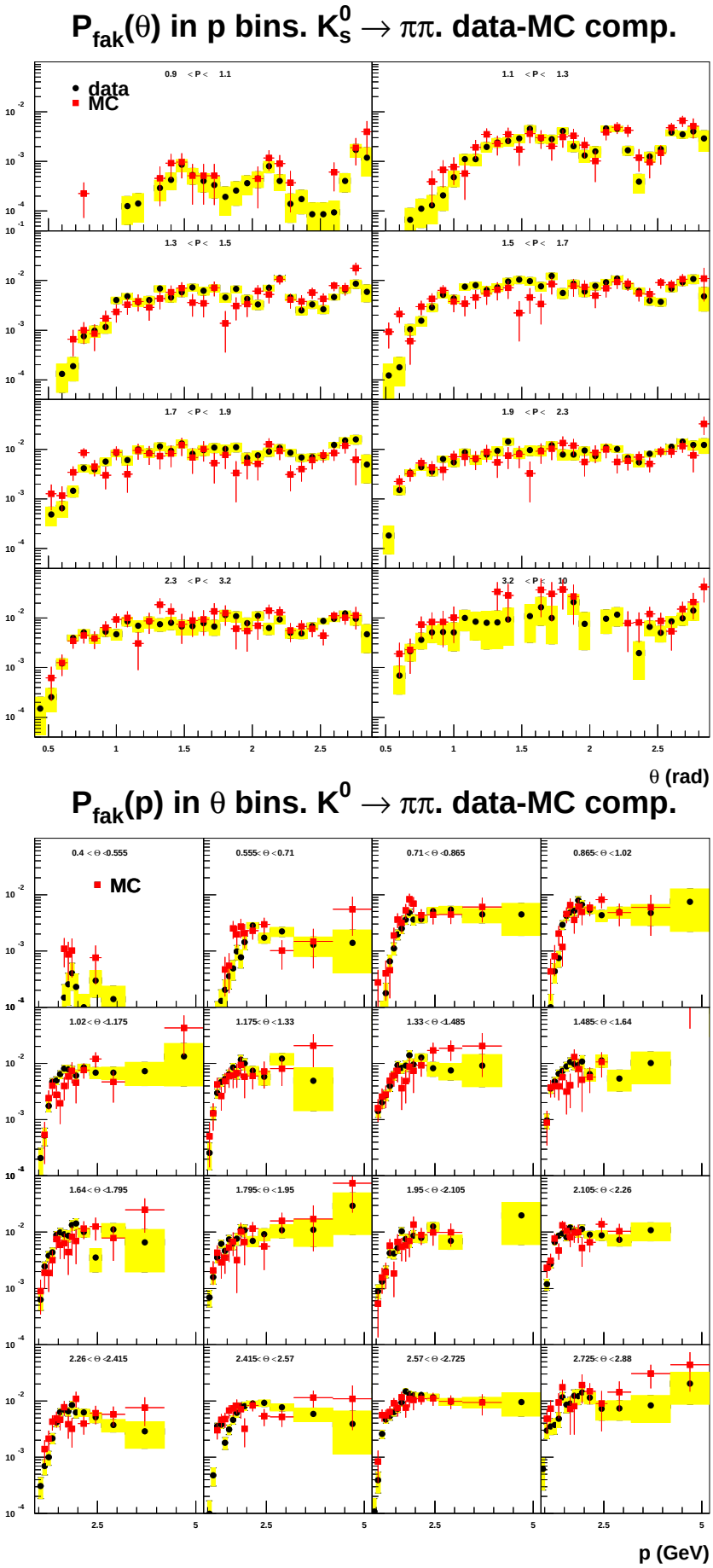

Figure A.6: *Data–Monte Carlo comparison of double differential fake–muon probabilities for pions from K^0_S adopting a $4\ d.o.f.$ matching with* BREMAT *($\mathcal{P} > 1\ \%$) as a function of polar angle in bins of momentum (***Top** *plots) and as a function of momentum in polar angle bins (***Bottom** *plots). Data are represented as black bullets with a yellow band for the statistical errors while Monte Carlo is represented by red squares.*

and Monte Carlo. In our case these distributions are reasonably close. The agreement between data and Monte Carlo is also in this case satisfactory with a slight tendency of the Monte Carlo to overestimate the number of fakes. It is interesting to notice how the minimum momentum threshold to produce a fake passed from ~ 1 GeV to ~ 2 GeV and that the most of fakes are concentrated in the rear region where the calorimeter is less thick.

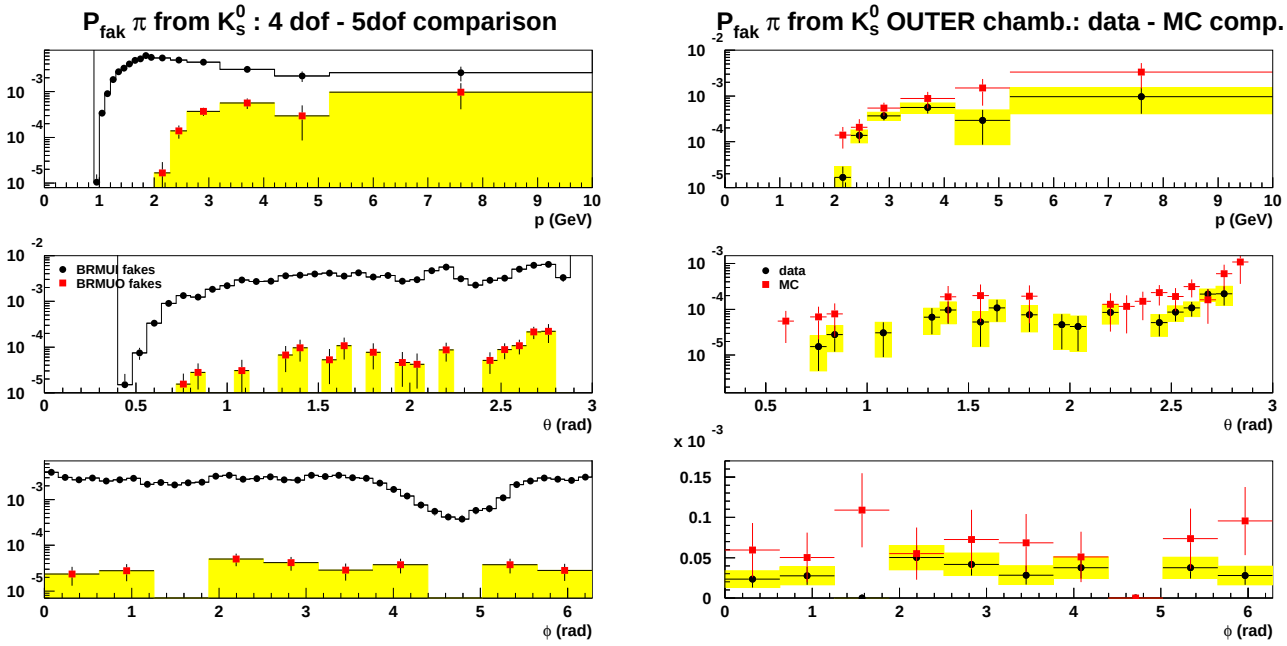

Figure A.7: **Left***: Comparison between the fake–muon probability using BRMUI matched tracks ($\mathcal{P}_{4\ d.o.f.} > 0.01$) or requiring a BRMUO match in addition ($\mathcal{P}_{5\ d.o.f.} > 0.05$).* **Right***: Data–Monte Carlo comparison for the fake–muon probability using the BRMUO match ($\mathcal{P}_{5\ d.o.f.} > 0.05$).*

We have used the Monte Carlo to estimate the possible contaminations to our pion sample. This check is performed to put a limit on the presence of true muons in the combinatorial background under the peak. Possible backgrounds (non–pion tracks) arise mostly from other decay modes of neutral kaons or Λs. The relevant decay modes with their branching fractions are here listed :

K^0_S	$\pi^+\pi^-$	(68.61 ± 0.28) %
	$\pi^\pm\mu^\mp\nu_\mu$	$(6.9 \pm 0.4) \cdot 10^{-4}$
	$\mu^+\mu^-$	$< 3.2 \cdot 10^{-7}$ CL = 90 %
K^0_L	$\pi^\pm\mu^\mp\nu_\mu$	(27.18 ± 0.25) %

The contributions of each of these modes to the total final sample are shown cumulatively in the K^0_S invariant mass plots in Figure A.8. The most dangerous source is given by $K^0_L \to \pi\mu\nu$ ($\mathcal{B} \simeq 27$ %) since it produces true muons which have of course a much higher probability to be detected than an hadron. Nevertheless, this class of events are heavily suppressed by both the invariant mass cut and the fact that very few K^0_L decay within the central drift chamber [8].

Overall the relative number of true muons in the initial sample is estimated from the Monte Carlo to be ~ 0.01 % of the total. We separated the misidentified tracks into the previously defined categories by considering the identity of the reconstructed tracks in the CTD and in BRMUI at true level in the GEANT simulation. We defined as "sail–through" those tracks which at true level are kaons (or pions) in both the inner drift chamber and the muon chambers, "decay–in–flights" those in which a kaon or pion in the CTD is matched to a true muon (of the correct sign) in the muon chambers, "true muons" those in which at both level tracks are muons with the same sign. For technical reasons

[8] The CTD has a radius of ~ 90 cm and $c\tau_{K^0_L} \simeq 15$ m

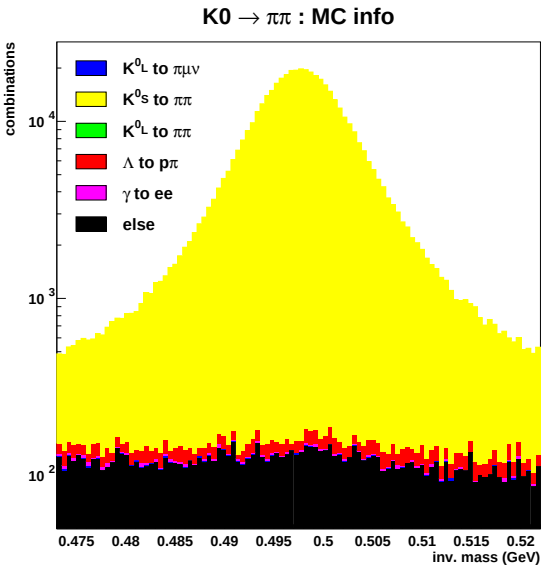

Figure A.8: *Distribution of the reconstructed $m_{\pi\pi}$ in the Monte Carlo. The plot shows cumulatively the various contributions in differently filled histograms. See the legend.*

this last class also includes early kaon and pion decays in flight in the CTD. In the case of K^0_S we have verified that this class of events is indeed the main contribution in the true muon category. The result is that about 25% (306/1221) of the tracks originate from sail–through, 38% (469/1221) are pions or kaons' decay–in–flights, 7% (91/1221) are real muons and 29% (355/1221) originate from other sources (punch–through or wrong matching). If the matching with the outer muon chambers is considered the only contributions playing a role arise from true muons, being either prompt (or early decay–in–flight), $\sim$ 30% (9/28), or from late decays–in–flight, $\sim$ 68% (19/28). As expected the number of fakes from real hadrons is greatly suppressed by the presence of a much more efficient shielding ($\sim$ 1 m of iron).

The distributions in momentum, polar angle and invariant mass for these samples separately are shown in Figure A.9. In the Left hand plot the distributions in momentum and polar angle are shown cumulatively, while the same distributions (with the addition of the invariant mass plot) are shown separately in the middle plot. The relative normalization of the samples is the one predicted by the Monte Carlo. It can be noticed how the distribution in θ is enhanced at high polar angles due to the fact that the rear calorimeter is less thick than the barrel one. A bump at $\theta \sim 2.2$ is related to the crack between the barrel and rear calorimeter. This feature is particularly evident, as expected, in the case of the sail–through sample. It also interesting to notice the invariant mass distribution broadening for the decay–in–flight events relatively to the other samples. Also in the case of 5 $d.o.f.$ matching the events (prompt and DIF muons) are concentrated in the rear (not shown).

One of the variables which are mostly sensible to the differences between these fake–muon categories is the χ^2 (or equivalently the probability $\mathcal{P}$ of the matching[9]). A shape comparison for the χ^2 of the misidentified muons is presented in Figure A.10. The Monte Carlo describes the data well both when the 4 $d.o.f.$ (Left hand plot in Figure A.10) and 5 $d.o.f.$ (Right hand plot in Figure A.10) matching are considered.

A.4.2 Dependence on the value of the minimal matching–probability

We decided to employ this large sample of fake–muons to study the effectiveness of the matching probability cut. The dependence of the relative fraction of matched tracks over the total number of hadron tracks is plotted against the matching probability cut in Figure A.11. The decrease in the number of misidentified tracks is very steep. It is

[9]The probability that a random variable having a χ^2 distribution with $N \geq 1$ degrees of freedom assumes a value which is larger than a given value $\chi^2 \geq 0$ ($\mathcal{P}(\chi^2, N)$) is given by the following relation: $\mathcal{P}(\chi^2, N) = \frac{1}{\sqrt{2^N}\Gamma(\frac{N}{2})} \int_{\chi^2}^{\infty} e^{-\frac{t}{2}} t^{\frac{N-1}{2}} dt$.

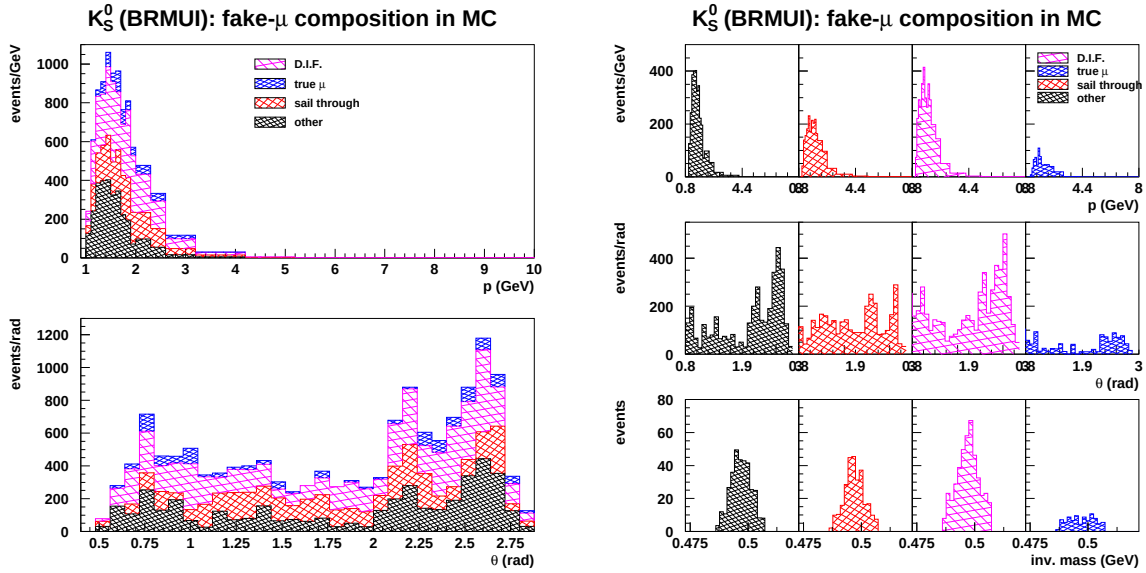

Figure A.9: **Left***: Distributions of momentum (Top plot) and polar angle (Bottom plot) for pions from K^0_S which are reconstructed as muons in the Monte Carlo. True muons, sail–through, decay–in–flight and contributions from other cases are shown cumulatively with different hatch coding (see the legend).* **Right***: The same distributions in the Left plot shown separately. The plots in the Bottom row show the invariant mass distributions.*

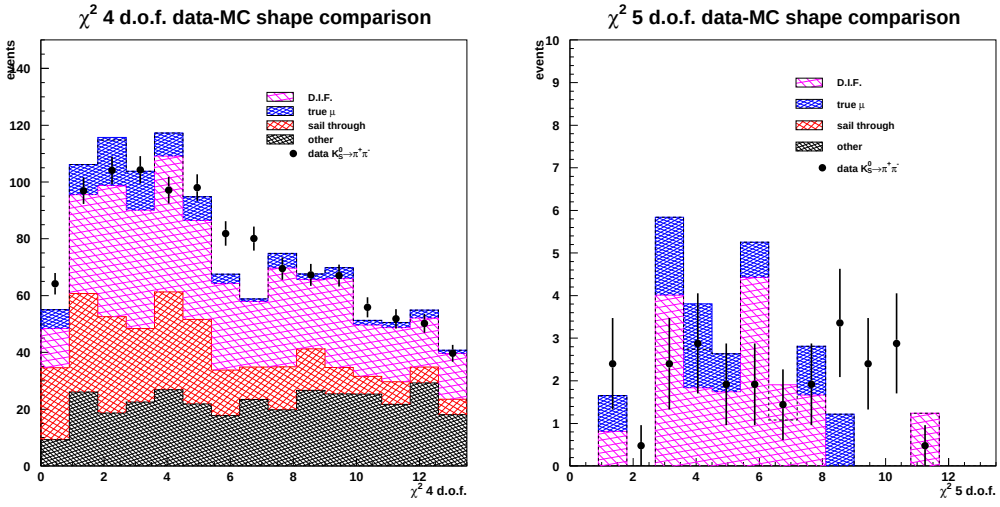

Figure A.10: *Distributions of the χ^2 at 4 d.o.f. (***Left** *plot) and 5 d.o.f. (***Right** *plot) for matched pion tracks from K^0_S decay. For the Monte Carlo true muons, sail–through, decay–in–flight and other cases are shown separately (see the legend). The corresponding distributions in data (bullets) are compared in shape to the Monte Carlo.*

seen how loosening the cut value at 0.1 % would not increase the fake–muon contamination significantly. Anyhow the default value of 1% safely rejects the bulk of the misidentified tracks.

The same check was repeated for the Monte Carlo. As it is seen in Figure A.11 the Monte Carlo (empty bullets) reproduces the trend observed in the data very well, at least if one keeps sufficiently away from very low values of probability. The Left hand plot in Figure A.11 shows how the distributions of the misidentified tracks in momentum, polar and azimuthal angle vary as the probability cut is tightened. No particular modification in the observed distributions is present.

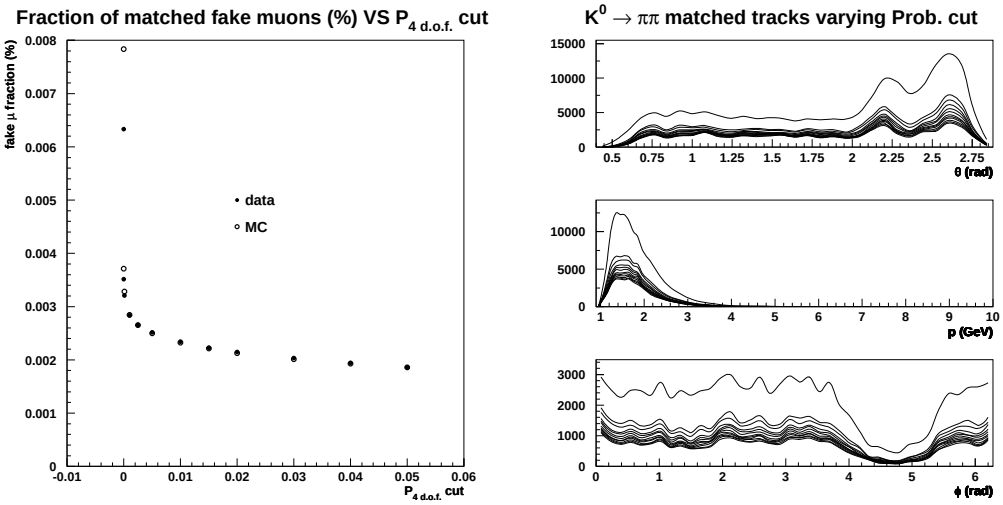

Figure A.11: **Left***: Fraction of matched tracks in the sample of pions from K_S^0 as a function of the cut in the 4 d.o.f. matching probability.* **Right***: From Top to Bottom, the various curves show the distribution in polar angle, momentum and azimuthal angle for the sample of matched tracks as the probability cut is varied (according to the Right hand plot values).*

A.5 Study of fake–muons from protons via the decay $\Lambda \rightarrow p\pi$

The selection of Λ barions is similar to that applied in the case on K_s^0 except for the following cuts which are different:

- $1.111 < m_{p\pi} < 1.121$ GeV
- $|m_{\pi\pi} - m_{K^0}| > 0.012$ GeV (anti-K^0 cut)
- $m_{\pi\pi} > 0.32$ GeV (anti–$\gamma \rightarrow e^+e^-$ cut)

This selection on the sample of data collected in the years 1996–2000 data yields the invariant mass peak shown in Figure A.12. After restricting to the previously defined mass window (yellow band in Figure A.12) the number of (anti–)proton-pion candidates from Λ in the predefined kinematic region amounts to about 750.000 tracks. The combinatorial background is of the order of 10 % of the entire sample.

Due to the kinematic of the decay the pion is quite slow. This is testified by the fact that, if the fastest particle is assigned the proton mass, a clear Λ peak is obtained while, with the other assignment, a much broader one is found. Due to this feature the pions from Λ are not a suitable sample for fake–muon studies. In our sample just one of these pions is able to reach the inner muon chambers.

Among the proton tracks about 500 are able to reach the BRMUON detector and be matched by BREMAT with a probability $4\ d.o.f.$ cut fixed at 1 %. This corresponds to 0.07 % of the entire sample. The distributions in momentum,

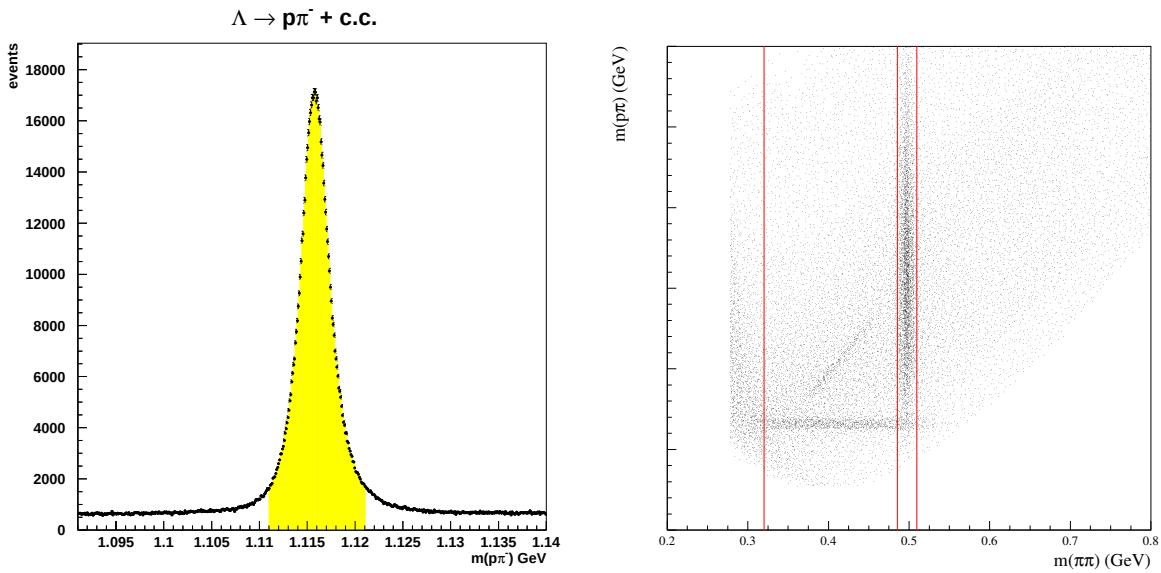

Figure A.12: *The upper plot shows the $\Lambda \to p\pi$ invariant mass peak. ZEUS 96–00 data were used. The scatter–plot shows the invariant masses obtained on a sample of secondary vertex tracks using the $\pi\pi$ mass hypothesis (x–axis) or the $p\pi$ one (y-axis). The vertical band corresponds to $K^0_S \to \pi\pi$ decays, the horizontal band corresponds to $\Lambda \to p\pi$ decays. The red lines show the anti–K^0 and anti–conversion cuts described in A.5.*

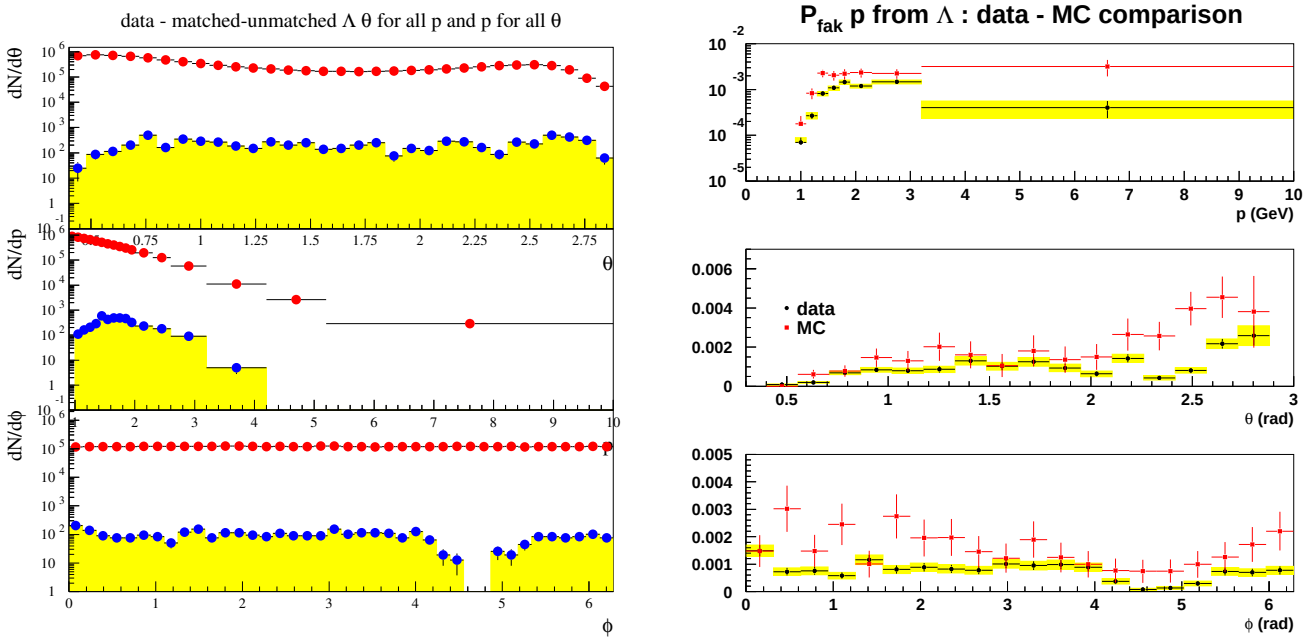

Figure A.13: **Left***: From top to bottom, distributions of momentum, polar angle and azimuthal angle of proton tracks from Λ decay (red bullets) and of those which are matched to BRMUI by* BREMAT *with $\mathcal{P}_{4\ d.o.f.} > 0.01$. ZEUS 96-00 data have been used.* **Right***: Data–Monte Carlo comparison of fake–muon probabilities for $4\ d.o.f.$ matching with* BREMAT *as a function of, top to bottom, momentum, polar angle an azimuthal angle.*

polar angle and azimuthal angle of these two samples of tracks are shown in Figure A.13. The (red) bullets represent all tracks, both matched and unmatched, while the sub–sample of matched tracks is shown by the shaded (yellow) histogram.

As it can be seen in the Right hand plots in Figure A.13 the efficiency uncorrected Monte Carlo tends to overestimate by about a factor two the fake–muons found in the data. Before performing the comparison we reweighted the polar angle in the Monte Carlo as in the K^0_S case. The entity of the reweighting and the result in the θ and p distribution is visualized in the Right hand plots in Figure A.3. The fake–muon probabilities in bins of θ and p are shown in Figure A.14. The binning is the same as for pions from K^0_S. The same trend seen in the integrated data– Monte Carlo comparison is observed more or less equally in all the considered bins.

In the following Table it can be seen how the mode we selected has a high branching ratio while the only source of true muons from Λ is the 3–body decay $\Lambda \to p\mu^-\bar{\nu_\mu}$ which has a very low branching ratio. Other spurious prompt muon tracks can come from the semileptonic decay of the K^0_L. Some of the most relevant decays yielding tracks which happens to be in the reconstructed Λ peak are shown in Figure A.15. The relative number of true muons in the initial sample is estimated from the Monte Carlo to be ~ 0.07 % (65/87107) of the total.

Λ	$p\pi^-$	(63.9 ± 0.5) %
	$p\mu^-\bar{\nu_\mu}$	$1.57 \pm 0.35 \cdot 10^{-4}$

According to the simulation about 7% (8/110) of the tracks originate from K/π sail–through, 14% (15/110) are pions or kaons' decay–in–flights, 22% (24/110) are real muons, 8% (9/110) originate from p sail–through and 49% (54/110) arise from other sources (punch–through or wrong matches). If a match with the outer muon chambers is considered the misidentified tracks are for the $\sim$ 50% (3/6) true muons and $\sim$ 50% (3/6) muons from decay–in–flight according to the previous definitions.

A.6 Study of fake–muons from kaons via the decay $\phi \to K^+K^-$

Only elastic diffractive ϕ events (i.e. consisting of two tracks only) were selected in this case to keep the combinatorial background low. We preselected events with *ZES* asking only for two tracks events with low energy deposition in the *FCAL* (< 1 GeV). Further cuts were:

- oppositely charged primary–vertex tracks
- $1.01 < m_{K^+K^-} < 1.03$ GeV
- $|Z_{vtx}| < 50$ cm
- $3.5^\circ < \Omega < 174^\circ$ anti–cosmic cut

Ω stands for the acollinearity angle[10]. The lower cut is justified by the presence (verified directly scanning suspicious events) of cosmic events resulting in two almost coincident high–momentum tracks occasionally having the ϕ invariant mass.

This selection on ZEUS 96–00 data yields the invariant mass peak shown in the Right hand plot in Figure A.16. After restricting to the mass window $[1.01, 1.03]$ GeV (yellow band in Figure A.16) the number of kaons candidates from ϕ in the predefined kinematic region amounts to about 63.000 tracks. The combinatorial background is of the order of 45 % of the entire sample.

About 100 tracks in the kaon sample are able to reach the BRMUON detector and be matched by BREMAT in the $4\ d.o.f$ mode. This corresponds to $\sim$ 0.2 % of the entire sample. The distributions in polar angle, momentum and azimuthal angle of these two samples of tracks are shown in the Left hand plots in Figure A.17. The (red) bullets represent all tracks, both matched and unmatched, while the sub–sample of matched tracks is shown by the shaded (yellow) histogram.

[10]The angle in space between the momenta of the two tracks.

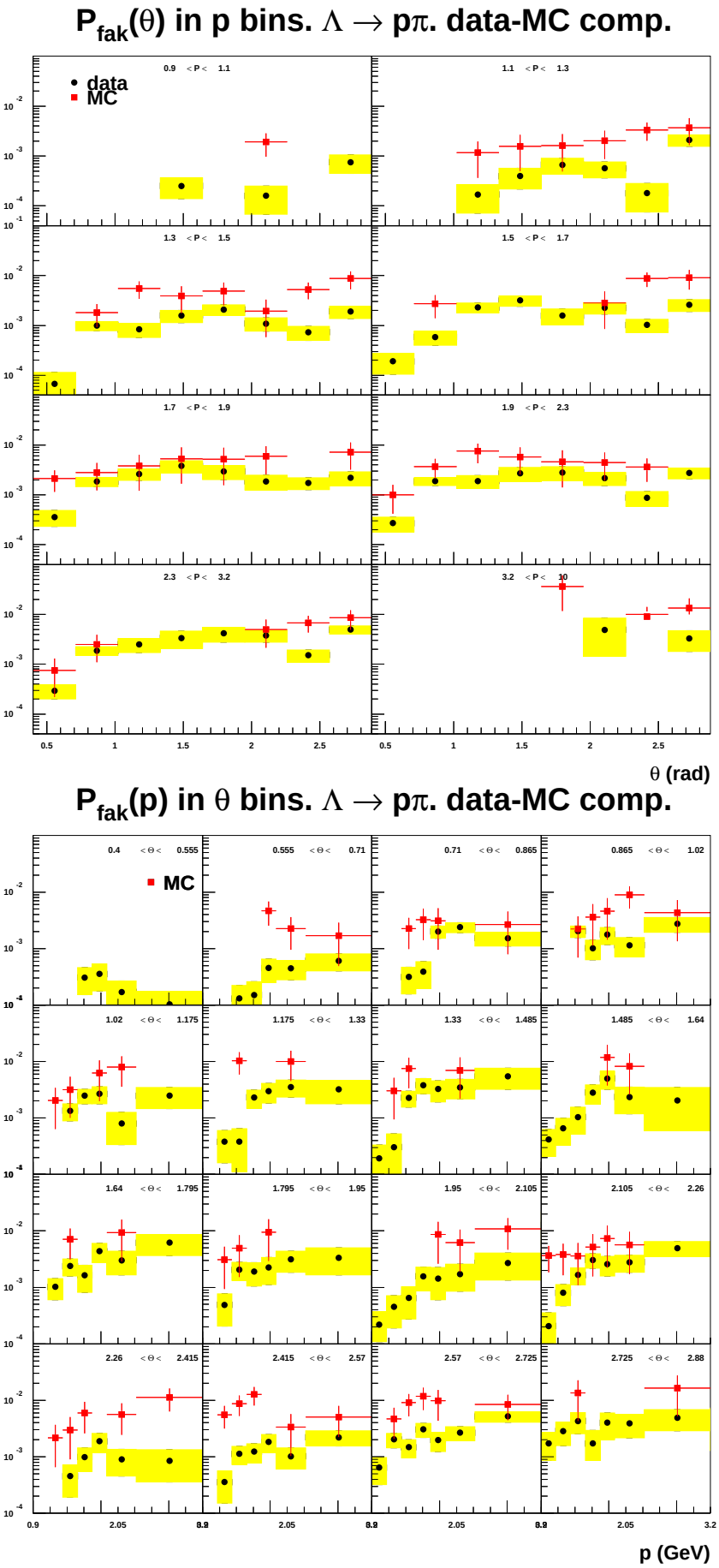

Figure A.14: *Data–Monte Carlo comparison of double differential fake–muon probabilities for protons(anti-protons) from $\Lambda(\bar{\Lambda})$ adopting a 4 d.o.f. matching with* BREMAT *($\mathcal{P} > 1$ %) as a function of polar angle in bins of momentum (***Top** *plots) and as a function of momentum in polar angle bins (***Bottom** *plots). Data are represented as black bullets with a yellow band for the statistical errors while Monte Carlo is represented by red squares.*

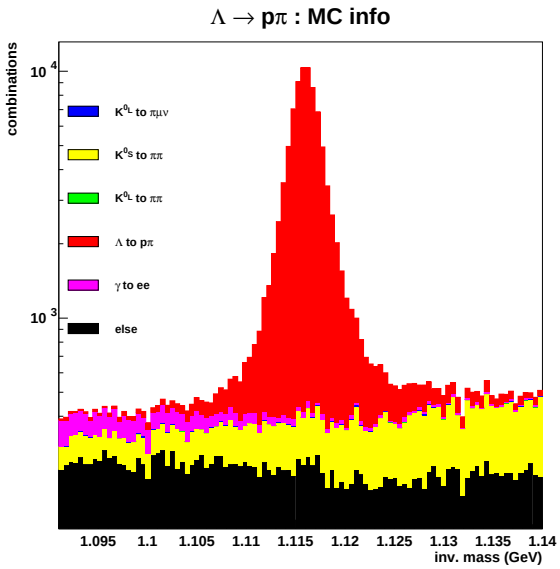

Figure A.15: *Distribution of the reconstructed $m_{p\pi}$ in the Monte Carlo. The plot shows cumulatively the various contributions in differently filled histograms. See the legend.*

Since the distributions in both θ and p in the Monte Carlo and the data were very different, in order to avoid a complicate bi-dimensional reweighting of the Monte Carlo in these two variables we decided to perform the comparison in a restricted kinematical range, asking the tracks to have $\eta > -0.88$ [11] instead of $\eta > 2$ as in Equations A.1. The m_{KK} invariant mass plot in the data after this further cut is shown in the Left hand plot of Figure A.16. The new sample consists of 21348 tracks of which about 30 reach the inner muon chambers. The θ distribution was reweighted to match that in the data. After such reweighting the Monte Carlo reproduces the shape of both the momentum and polar angle in the data. A shape comparison of the distributions of all the tracks (both matched and unmatched) in θ and p in data and Monte Carlo is shown in the Top plot of Figure A.23 for all the samples we have considered (see the legend).

The data–Monte Carlo comparison for the kaon sample from ϕ is shown in the Right hand plot in Figure A.17. The Monte Carlo description is satisfactory with a slight tendency of the Monte Carlo to overestimate the fake–muons with respect to the data.

A.7 Study of fake–muons from pions and kaons via the decay $D^* \to D^0(\to K\pi)\pi_s$

D^0 mesons coming from D^*s were chosen because in this case, using the Δm tag, a lower level of combinatorial background is attainable with respect to the inclusive D^0 case. In addition to this, the presence of the D^* allows to distinguish between kaons and pions from the D^0 since, if we disregard the Cabibbo–suppressed decay of the D^0 ($\to K^+\pi^-$), the pion is always the particle having the same charge of the slow pion from the D^*. The applied cuts are the following:

$$\begin{array}{ll} p_T^{\pi_s} > 0.125 \text{ GeV} & p_T^{D^*} > 1.9 \text{ GeV} \\ p_T^{K,\pi} > 0.5 \text{ GeV} & |\eta^{D^*}| < 1.5 \\ p^{K,\pi} > 0.9 \text{ GeV} & 1.6 < \eta^{K,\pi} < -2 \end{array}$$

These are essentially the same D^* cuts which we used in the main analysis for the photoproduction sample. The combinatorial background in this case is sizeable amounting to about 45 % of the entire sample. To correct for this background we adopted the usual "wrong-charge" [12] D^* sample. The "wrong–charge" sample distributions have been

[11] This corresponds to neglecting tracks in the region covered by the rear muon chambers

[12] This sample consists of those combinations in which the kaon and pion tracks have the same instead of opposite charge

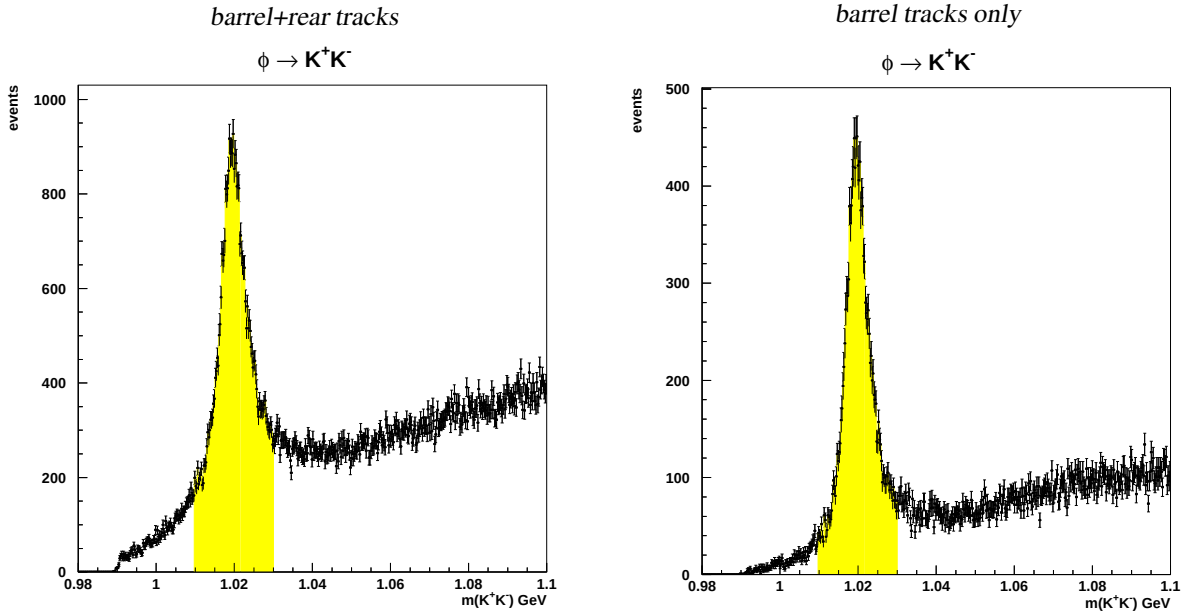

Figure A.16: *The two plots show the $\phi \to K^+K^-$ invariant mass peak. Events having at least one of the two tracks with $p_T > 0.9$ GeV and $-2 < \eta < 1.6$ are shown in the* **Left** *plot. The* **Right** *hand plot is instead for $p_T > 0.9$ GeV and $-0.88 < \eta < 1.6$. In order to compare with the Monte Carlo we restricted to this second region (see text for details).*

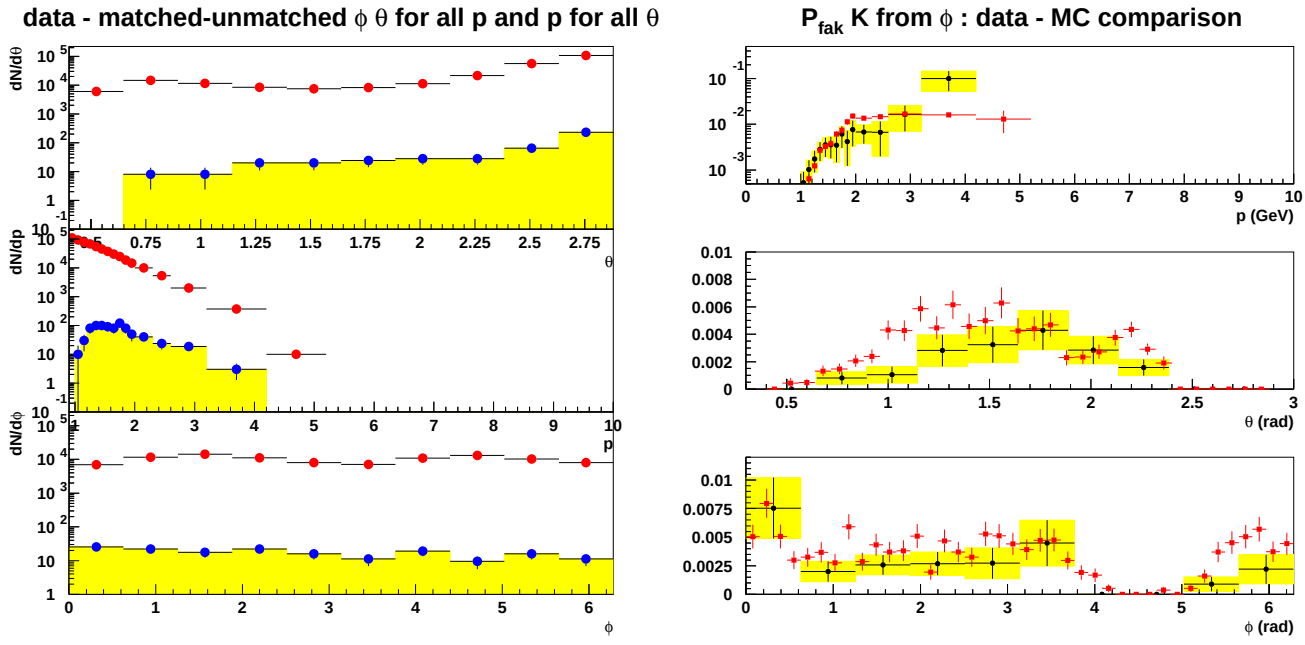

Figure A.17: **Left***: From top to bottom, distributions of momentum, polar angle and azimuthal angle of all ϕ tracks (red bullets) and of those which are matched to BRMUI by* BREMAT *with $\mathcal{P}_{4\ d.o.f.} > 0.01$ (shaded histogram). ZEUS 1996-2000 data have been used.* **Right***: Data–Monte Carlo comparison of fake–muon probabilities for 4 $d.o.f.$ matching with* BREMAT *as a function of, top to bottom, momentum, polar angle an azimuthal angle.*

subtracted to the "right–charge" ones for both matched and unmatched tracks. The fake–muon probability has been calculated on these subtracted distributions.

The imposed cuts on the ZEUS data collected in the years 1996–2000 yield the invariant mass peak shown in Figure A.18. After restricting to the mass windows $m_{K\pi} \in [1.81, 1.92]$ GeV and $m_{K\pi\pi_s} - m_{K\pi} \in [0.1435, 0.1475]$ GeV (yellow bands in the plots of Figure A.18) and subtracting the wrong–charge sample, the number of kaon (pion) candidates from D^0 amounts to 49380(48280) tracks.

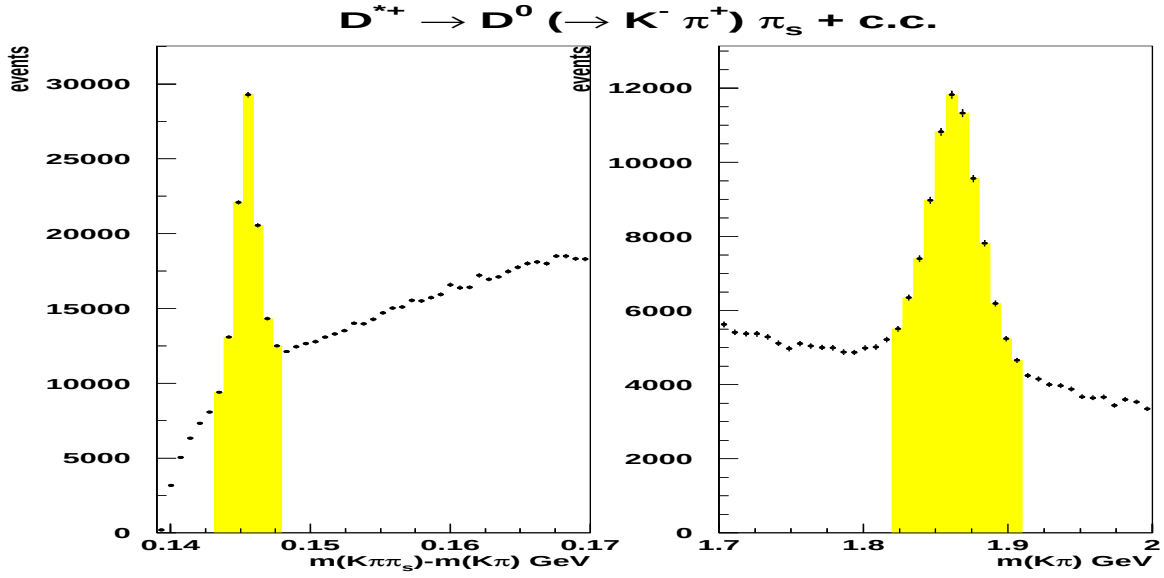

Figure A.18: *The reconstructed $m_{K\pi\pi_s} - m_{K\pi}$ (**Left**) and $m_{K\pi}$ (**Right**) distributions in the data after the cuts in A.5. Data collected in the years 1996-2000 were used.*

The number of pion (kaon) tracks being matched by the BREMAT algorithm is 291 (234) corresponding to 0.59% (0.48%) of the total number of tracks. The distributions in polar angle, momentum and azimuthal angle for pions and kaons are shown in the Left hand plots in Figure A.19. The meaning of the symbols is consistent with the one used so far. In the same Figure the comparison between data and Monte Carlo is presented (Right hand plots). The Monte Carlo describes the fake–muon probabilities reasonably well. The probability for pions is a bit underestimated by the Monte Carlo while for kaons the trend is reversed but the discrepancy is anyway limited. As we did for pions from K^0_S and protons from Λs the fake–muon probabilities have been evaluated against p in θ bins and vice versa as shown in Figure A.20.

The decay mode we are using and those which can produce prompt muons entering our selection are listed in the following Table:

$K^-\pi^+$	(3.83 ± 0.09) %
$K^-\mu^+\nu_\mu$	(3.22 ± 0.17) %
$\mu^+\mu^- <$	$4.1 \cdot 10^{-6}$ CL = 90 %

Possible prompt–muon contaminations arise essentially from the semi–leptonic decay mode of the $D^0 \to K\mu\nu$ ($\mathcal{B} \simeq 3.2\%$). The importance of this contribution has been estimated using the Monte Carlo. In Figure A.21 the one and two–dimensional distributions of D^0 and Δm at reconstructed level are shown separately for events containing a genuine $D^0 \to K\pi$ decay and for events with a $D^0 \to K\mu\nu$ decay. The presence of the neutrino shifts and broadens the $K\pi$ invariant mass towards lower values and smears the Δm distribution. As the above mentioned plot suggests this class of events are heavily suppressed by the double invariant mass cut. The relative number of true muons in the initial sample is estimated from the Monte Carlo to be ~ 0.07 % (732/100748) of the total.

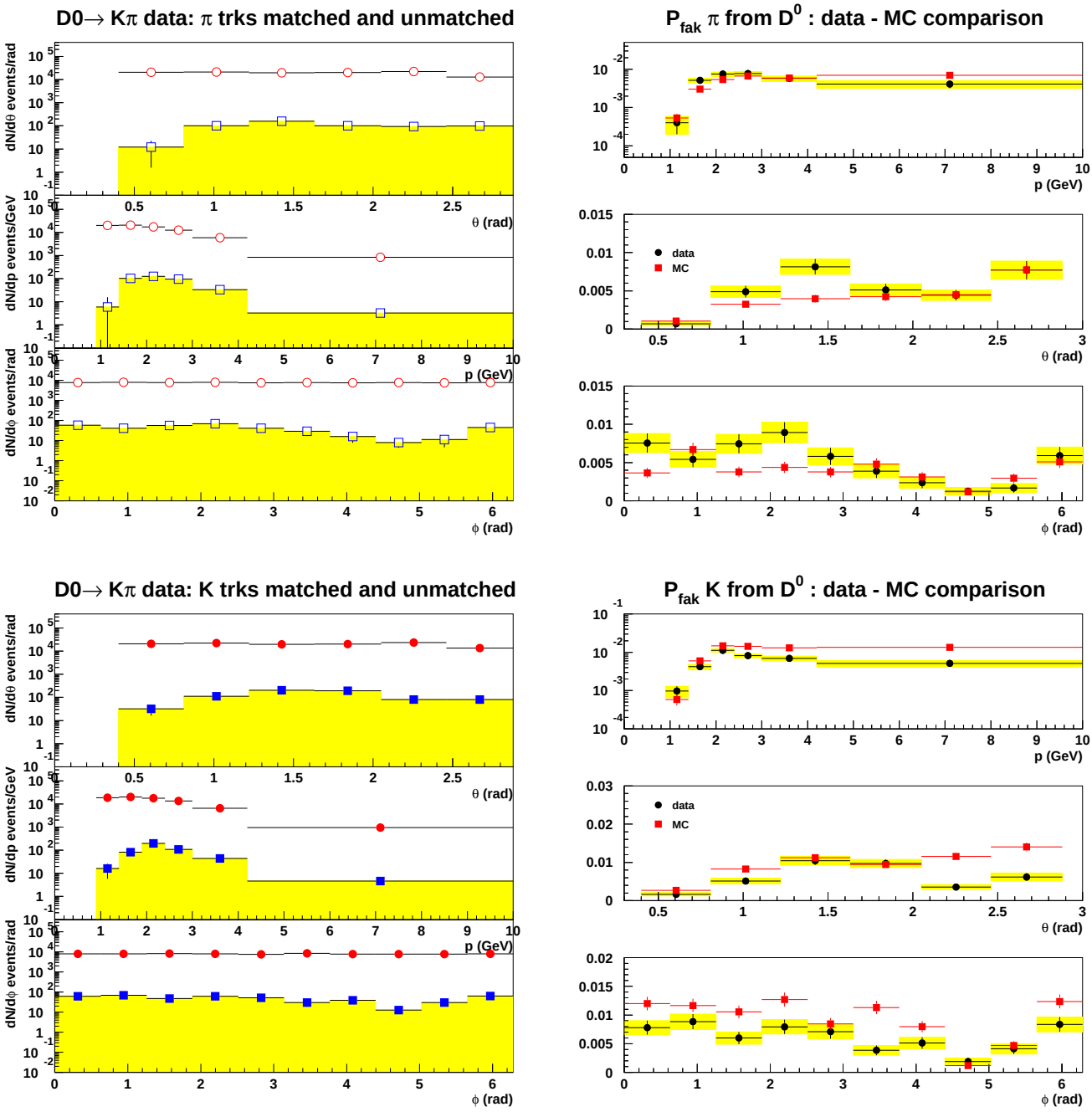

Figure A.19: **Top Left**: *From top to bottom, distributions of momentum, polar angle and azimuthal angle of pion tracks from D^0 (red hollow bullets) and of those which are matched to BRMUI by* BREMAT *with $\mathcal{P}_{4\ d.o.f.} > 0.01$ (shaded yellow histogram). ZEUS 96-00 data have been used.* **Top Right**: *Data–Monte Carlo comparison of fake–muon probabilities for $4\ d.o.f.$ matching with* BREMAT *as a function of, top to bottom, momentum, polar angle an azimuthal angle for pions from D^0. The equivalent plots for kaons from D^0 are shown in the lower half of the Figure.*

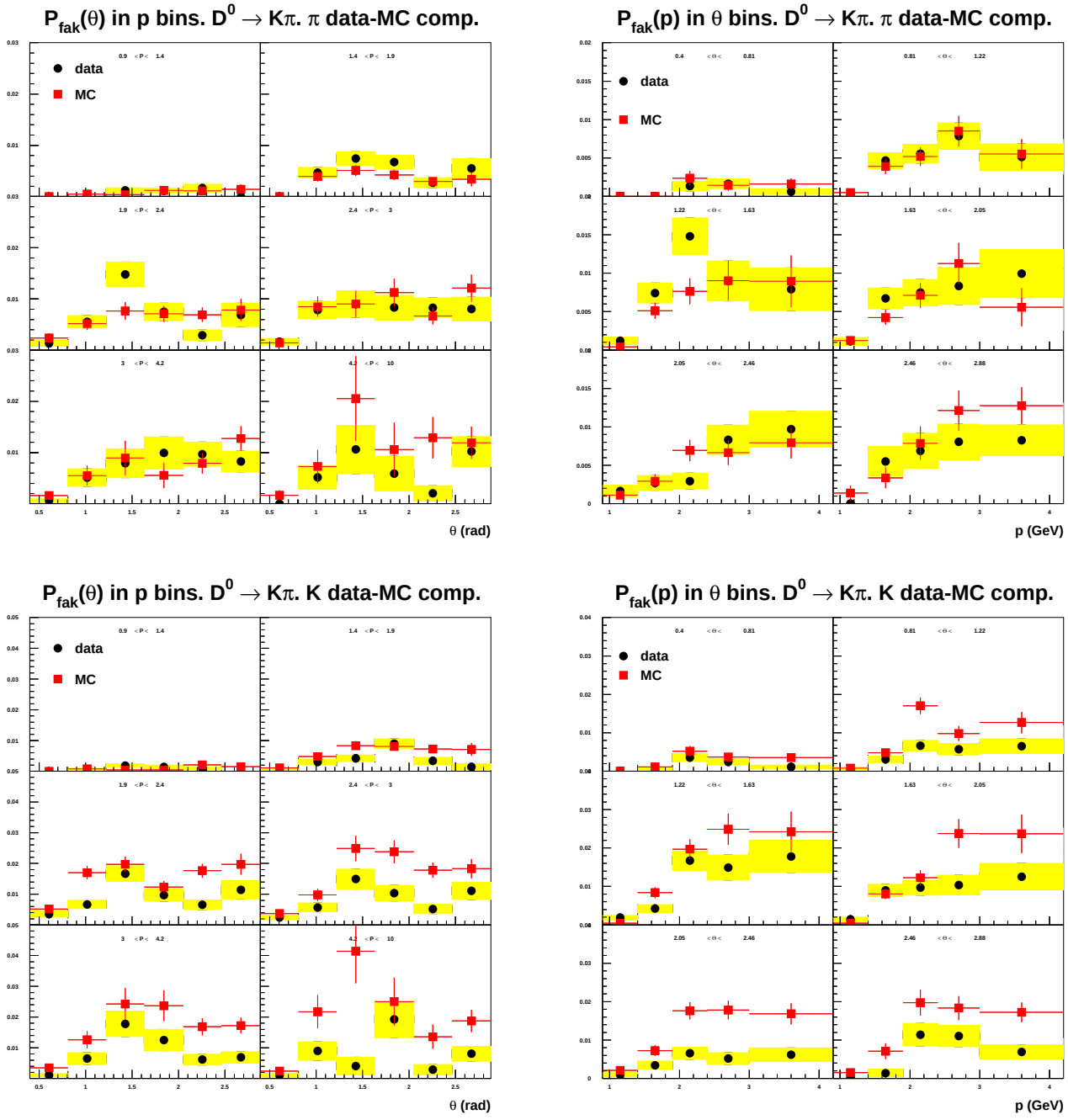

Figure A.20: *Data–Monte Carlo comparison of double differential fake–muon probabilities for pions (***Top** *plots) and kaons (***Bottom** *plots) from D^0 adopting a 4 d.o.f. matching with* BREMAT *($\mathcal{P} > 1\ \%$) as a function of polar angle in bins of momentum (***Left** *plots) and as a function of momentum in polar angle bins (***Right** *plots). Data are represented as black bullets with a yellow band for the statistical errors while Monte Carlo is represented by red squares.*

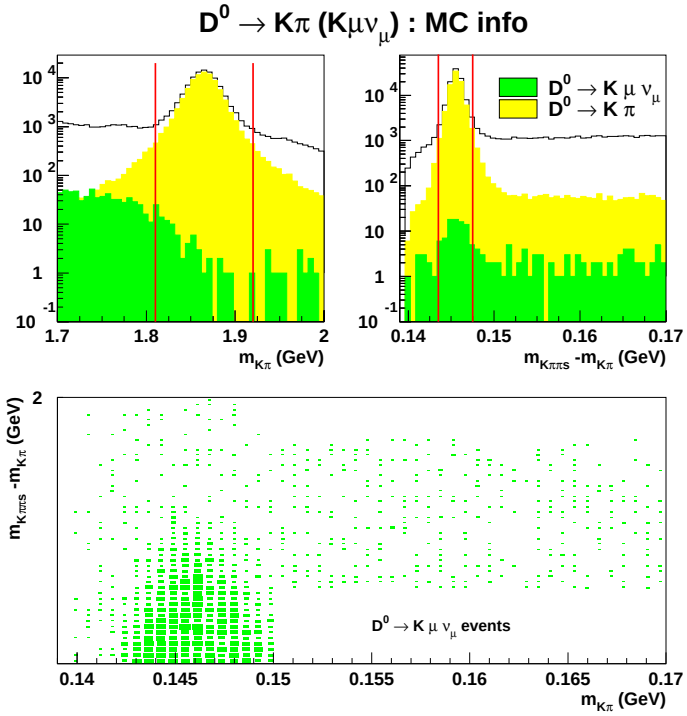

Figure A.21: **Top**: *Distributions of the reconstructed m_{D^0} (Left plot) and Δm (Right plot) in the Monte Carlo. The light (yellow) filled histogram shows the same distributions for events with a true decay $D^0 \to K\pi$, the darker (green) histogram corresponds to events containing a $D^0 \to K\mu\nu$ decay.* **Bottom**: *Reconstructed m_{D^0} VS Δm in the Monte Carlo for events with a $D^0 \to K\mu\nu$ decay.*

If we consider the sample of candidate pions from D^0 we find that about $\sim$ 34 % (109/319) of the tracks originate from sail–through, $\sim$ 40 % (127/319) are pions' decay–in–flights, $\sim$ 24 % (76/319) are real muons and $\sim$ 2 % (7/319) originate from other sources (punch–through or wrong matches).

If instead we consider the sample of candidate kaons from D^0 we find that about $\sim$ 63 % (495/780) of the tracks originate from sail–through, $\sim$ 30 % (236/780) are kaons' decay–in–flights, $\sim$ 2 % (17/780) are real muons and $\sim$ 4 % (32/780) originate from other sources (punch–through or wrong matches).

Some relevant distributions of the various contributions to the final D^0 fake–muon sample are visualised in Figure A.22 as it was similarly done in the case of pions from K^0_S in Figure A.9. The relative normalisation has been respected.

The fact that the contamination from true muons is higher in the case of pions arise from the semi–leptonic decay of the $D^0 \to K\mu\nu$. The higher rate of decay–in–flight muons from pions with respect to kaons also confirms the expectation. [13]

A.8 Fake–muon probabilities: comparison of the different samples

We have superimposed in the Top plot in Figure A.23 the distributions in momentum (upper plot) and polar angle (lower plot) for the various hadron samples compared so far. Data are represented with markers while the corresponding Monte Carlo distributions are shown as histograms (see the legend). The normalization has been set arbitrarily to a

[13] For a given particle with mass m, lifetime τ an momentum p the probability to decay in the length l is proportional to:

$$1 - e^{-\frac{l}{c\beta\gamma\tau}} = 1 - e^{-\frac{lm}{c\tau|\vec{p}|}}$$

So, for a fixed length and momentum, the relevant parameter is m/τ. The pion has a longer lifetime than the kaon so it should decay less but the fact that it is much lighter overcompensates this property ending with the fact that the pion is more likely to decay than a kaon. In detail: $m_\pi = 0.1396$ GeV, $m_K = 0.494$ GeV, $\tau_\pi = 2.6 \cdot 10^{-8}$ s ($c\tau_\pi = 7.8$ m), $\tau_K = 1.24 \cdot 10^{-8}$ s ($c\tau_\pi = 3.7$ m), $(m/\tau)_\pi \simeq 8 \times (m/\tau)_K$.

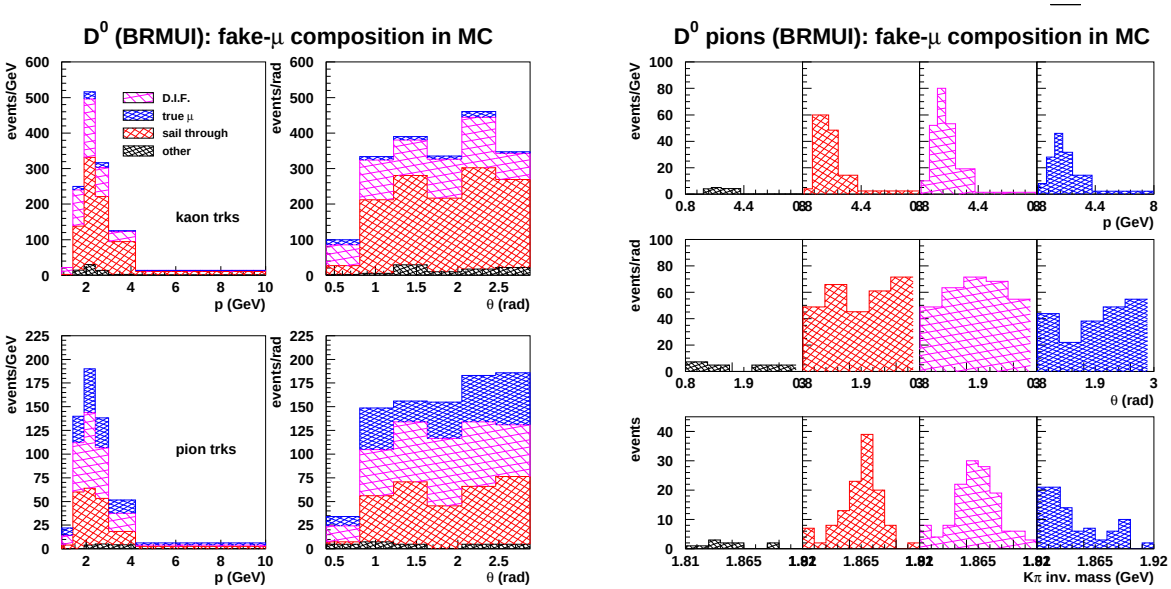

Figure A.22: **Left**: *Distributions of momentum and polar angle for kaon (Top plots) and pion (Bottom plots) from D^0 which are reconstructed as muons in the Monte Carlo. True muons, sail–through, decay–in–flight and contributions from other cases are shown cumulatively with different hatch coding (see the legend).* **Right**: *The same distributions in the Left plot shown separately. The plots in the Bottom row show the invariant mass distributions.*

common value in order to easily compare the different shapes. It can be noticed that data and Monte Carlo distributions have similar shapes. This is true by construction for θ since, as we already said, these distributions were reweighted in the K^0, Λ and ϕ Monte Carlo to compare to the data fake–muon probabilities. The momentum distributions are also well described.

The fake–muon probabilities for the different samples are shown in the Bottom plot in Figure A.23. The observed dependence in p, θ and ϕ is similar in the various cases. The probability rises from about 1 GeV and reaches a plateau at about 2 GeV. The effect of gaps in the geometrical coverage of the chambers are seen in the θ and ϕ probabilities.

The sample of pions from K^0_S is definitely the most statistically significant. It provides a detailed information also at high momenta even though most of events are concentrated at lower values.

The initial distributions in θ and p are similar to those for pions from K^0_S. Fakes from protons are less probable than from protons for about a factor three. The fake probability for kaons from ϕ is similar to that of pions from K^0. These samples have similar momentum distributions even though kaons from ϕ are more concentrated in the rear. The similarity between pion and kaons probabilities is the result of a compensation effect: the showers induced by kaons are longer than those induced by pions (the hadronic shower longitudinal profile scales with the interaction length) but on the other hand they produce less secondary muons from decays in flight. This same observation holds also in the case of kaons and pions from D^0. In this case the probabilities are higher by a factor of about two. This is consistent with the fact that pions and kaons from D^0 have on average higher momenta than those from ϕ and K^0_S (see the first plot in Figure A.23). In order to check that the behaviour of pions and kaons is universal and does not depend on the source, we performed a more direct comparison between the fake muon probability for pions from K^0_S and D^0 and kaons from ϕ and D^0. In order to correct for the very different momentum spectra in the K^0_S and D^0 samples, the higher statistics sample of pions from K^0_S was reweighted to the one of pions from D^0 and subsequently the fake muon probability as a function of θ was compared. The momenta distributions and $\mathcal{P}_{\rm fak}(\theta)$ plots are compared before and after the reweighting in Figure A.24.

As expected the fake muon probability for pions from K^0_S gets enhanced at higher momenta and after the reweighting it matches the one found for the same particles in D^0 decay. The shape an normalization is now in good agreement. The same comparison was repeated for kaons. In this case, since the statistics of kaons from ϕ at high momenta is not so as good as it was for pions from K^0_S we chose to reweight the momentum distributions of kaons from D^0 to that of

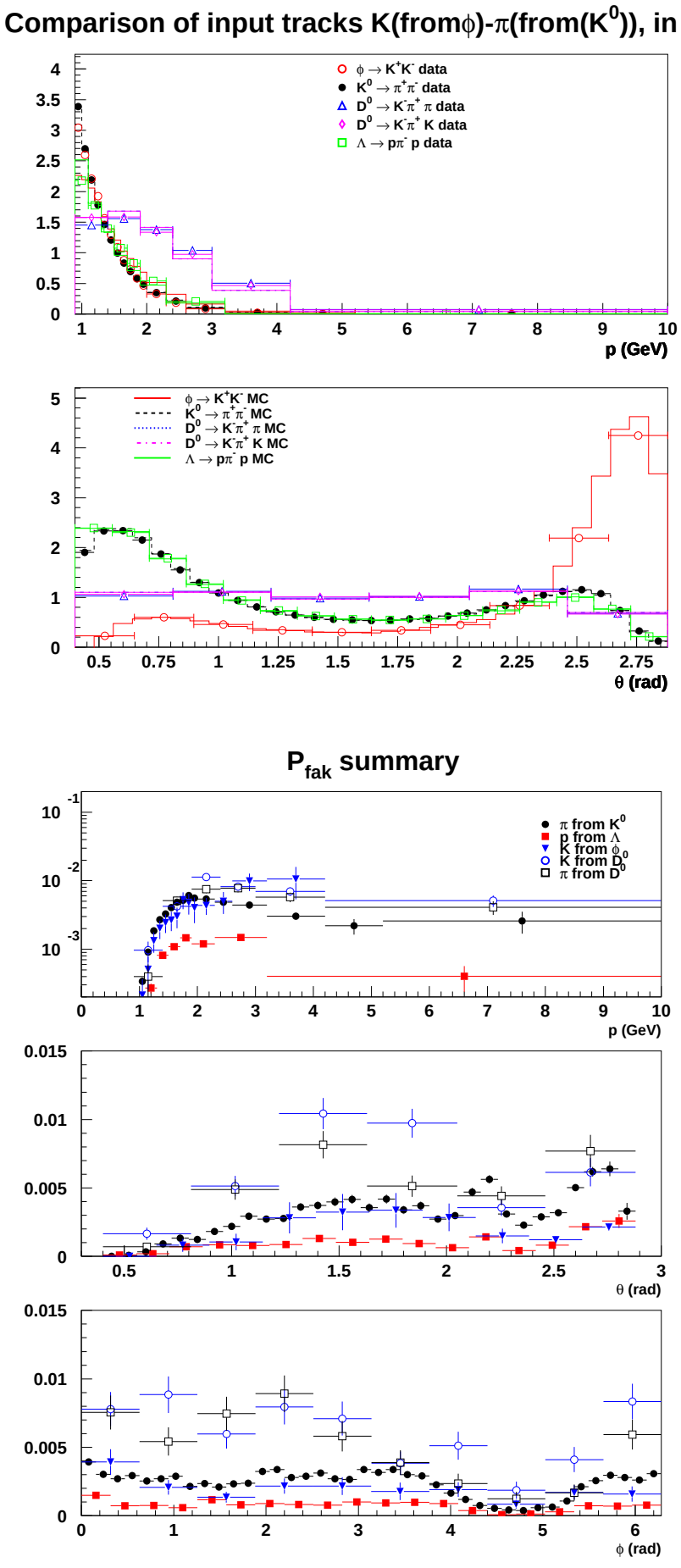

Figure A.23: **Top**: *Shape comparison between the distributions of input tracks in the* $K^0_S \to \pi^+\pi^-$, $\Lambda \to p\pi$, $\phi \to K^+K^-$, $D^0 \to K\pi$ *samples (see the legend). Momentum is shown in the upper plot, polar angle in the lower one.* **Bottom**: *Fake probabilities summary plot.*

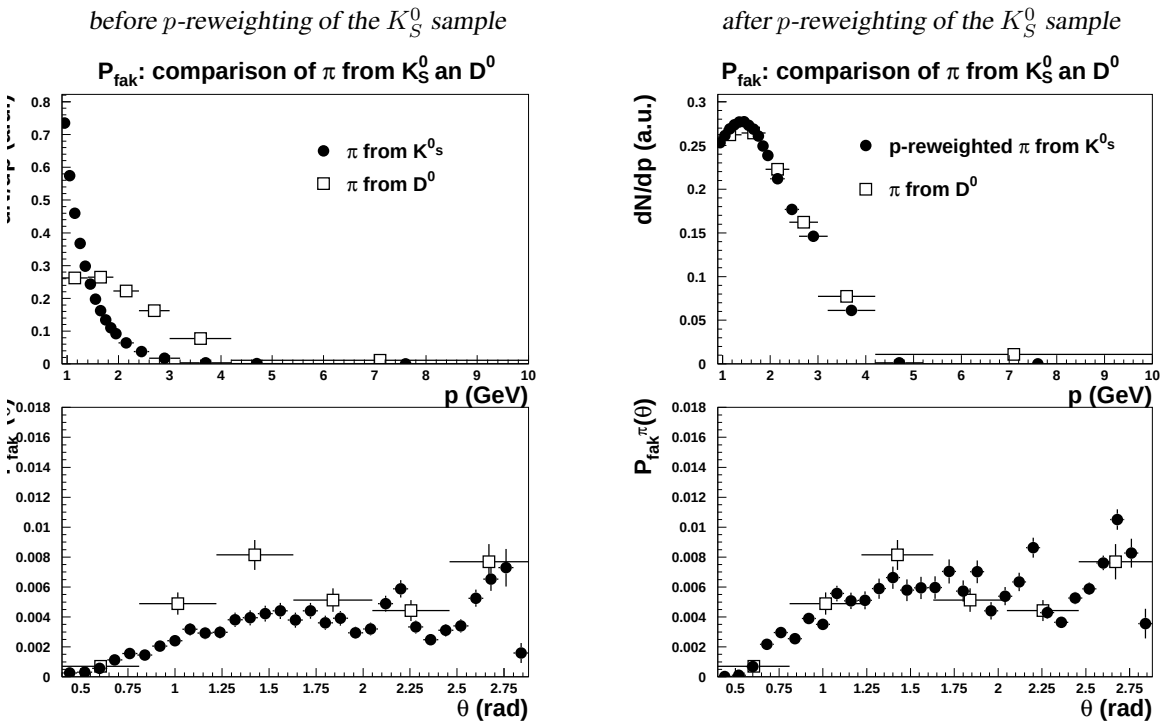

Figure A.24: *The* **Left** *hand top plot shows the comparison between the momentum distributions of pion tracks from K^0_S (black bullets) and D^0 (hollow squares) with an arbitrary normalization factor. The* **Left** *bottom plot shows the $\mathcal{P}_{\rm fak}(\theta)$ probability with analogous symbols. The same quantities are compared after the reweighting of the pions from K^0_S momentum to the one for pions from D^0 in the* **Right** *hand plots.*

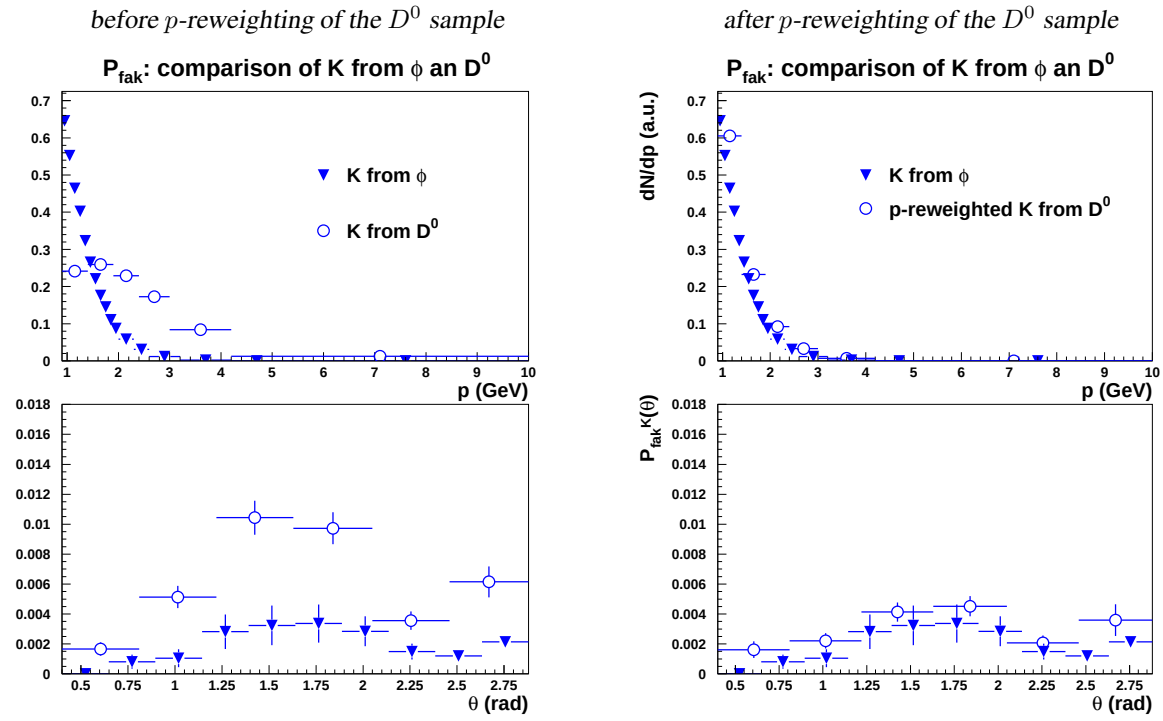

Figure A.25: *The* **Left** *hand top plot shows the comparison between the momentum distributions of kaon tracks from ϕ (blue triangles) and D^0 (hollow bullets) with an arbitrary normalization factor. The* **Left** *bottom plot shows the $\mathcal{P}_{\rm fak}(\theta)$ probability with analogous symbols. The same quantities are compared in the* **Right** *hand plots after the reweighting of the kaons from D^0 momentum to the one for kaons from ϕ.*

kaons from ϕ and not vice versa (to avoid the enhancement of statistical fluctuations). The result is shown in Figure A.25. After the reweighting the two distributions gets very close as expected.

The results presented in all the previous plots have been summarized in Table A.1. For each sample and both data and Monte Carlo the number of hadron tracks satisfying the specific cuts we imposed for each channel are listed together with the number of tracks misidentified as muons and the resulting fake–muon probability. The second column indicates whether a 4 $d.o.f.$ or 5 $d.o.f.$ matching is considered.

Sample		DATA			MONTE CARLO		
		# tracks	# matched	%	# tracks	# matched	%
$K^0_S \to \pi\pi$	I	2150110	5029	0.23	525434	1221	0.23
	O		51	0.0024		28	0.0053
$\Lambda \to p\pi$	I	748913	539	0.07	85632	110	0.128
	O		5	0.0007		6	0.007
$\phi \to KK$	I (b+r)	63409	107	0.17	440308	2065	0.47
	I (b)	21348	33	0.16	193169	523	0.27
$D^0 \to K\pi$	I (K)	49380	291	0.59	85250	780	0.91
	I (π)	48280	234	0.48	83020	319	0.38

Table A.1: *Summary on fake–muons probabilities for data and Monte Carlo in different samples with 4 d.o.f. and 5 d.o.f.* BREMAT. *See the text for more details.*

A.9 Conclusions

The level of accuracy with which the Monte Carlo describes the fake muon probability is overall satisfactory for both the inner chambers and outer chambers matching. Different trends are observed depending on the considered sample. Misidentified muons from kaons (from ϕ and D^0) in general appear to be a bit overestimated by the Monte Carlo. If we consider the fact that the Monte Carlo efficiency is higher than in data the situation is probably fine. The same conclusion holds in the case of fake–muons from proton tracks. On the contrary, in the case of pions (from K^0_S and D^0), the Monte Carlo slightly underestimates the result found in data.

The presence of several samples allowed us to perform some cross checks on the internal consistency of the various results. The behaviour observed as different hadron species and different kinematics are considered follows a coherent picture. In particular the fake muon probabilities calculated for kaons from ϕ and for kaons from D^0 and corrected for the different momentum spectrum of the samples have been found to be in good agreement. The same has been proved to hold for pions from K^0_S and D^0.

Appendix B

Data Monte Carlo comparison - additional plots

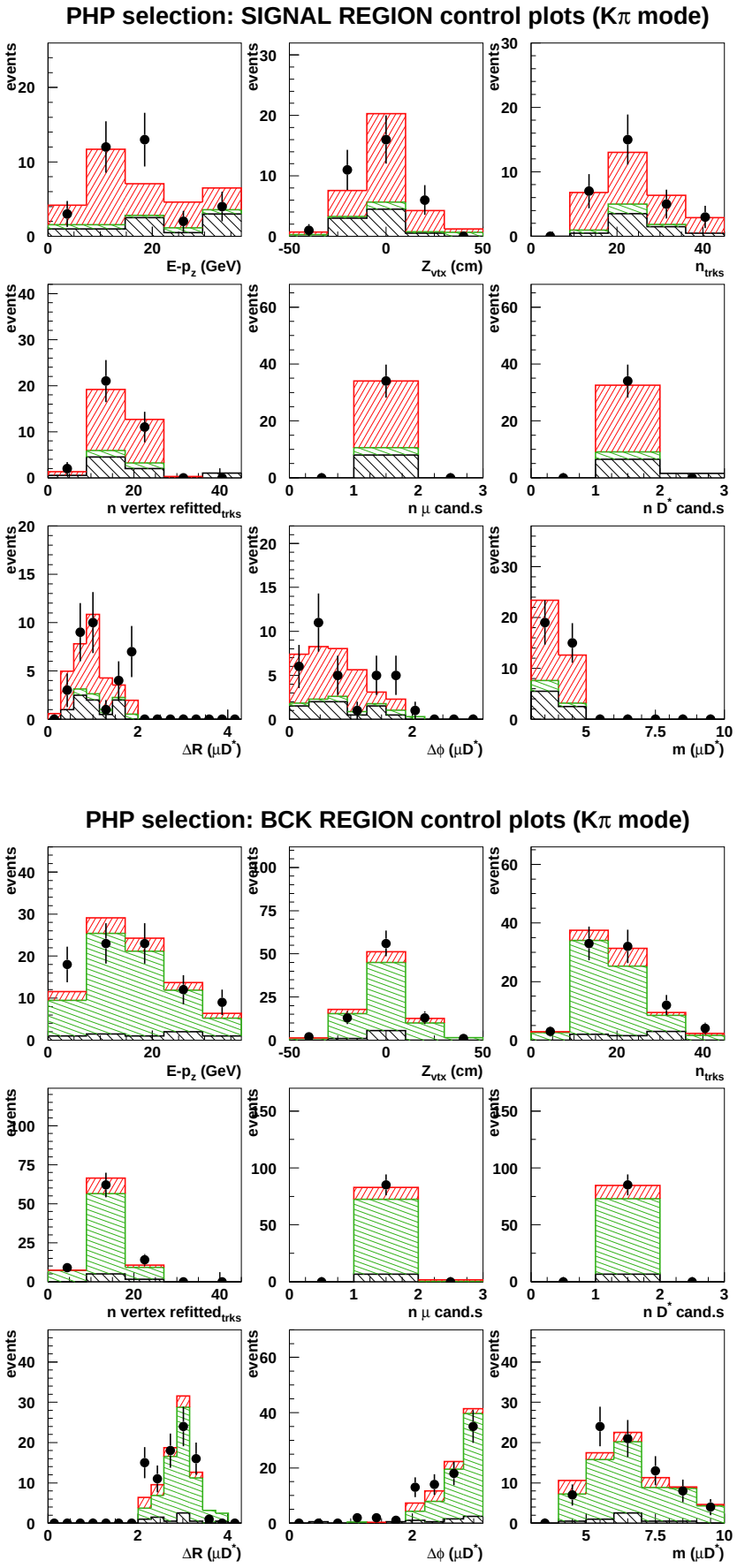

Figure B.1: *Control plots for the photoproduction selection for events with $D^* \to (K\pi)\pi_s$ in the signal (***Top***) and background (***Bottom***) region.*

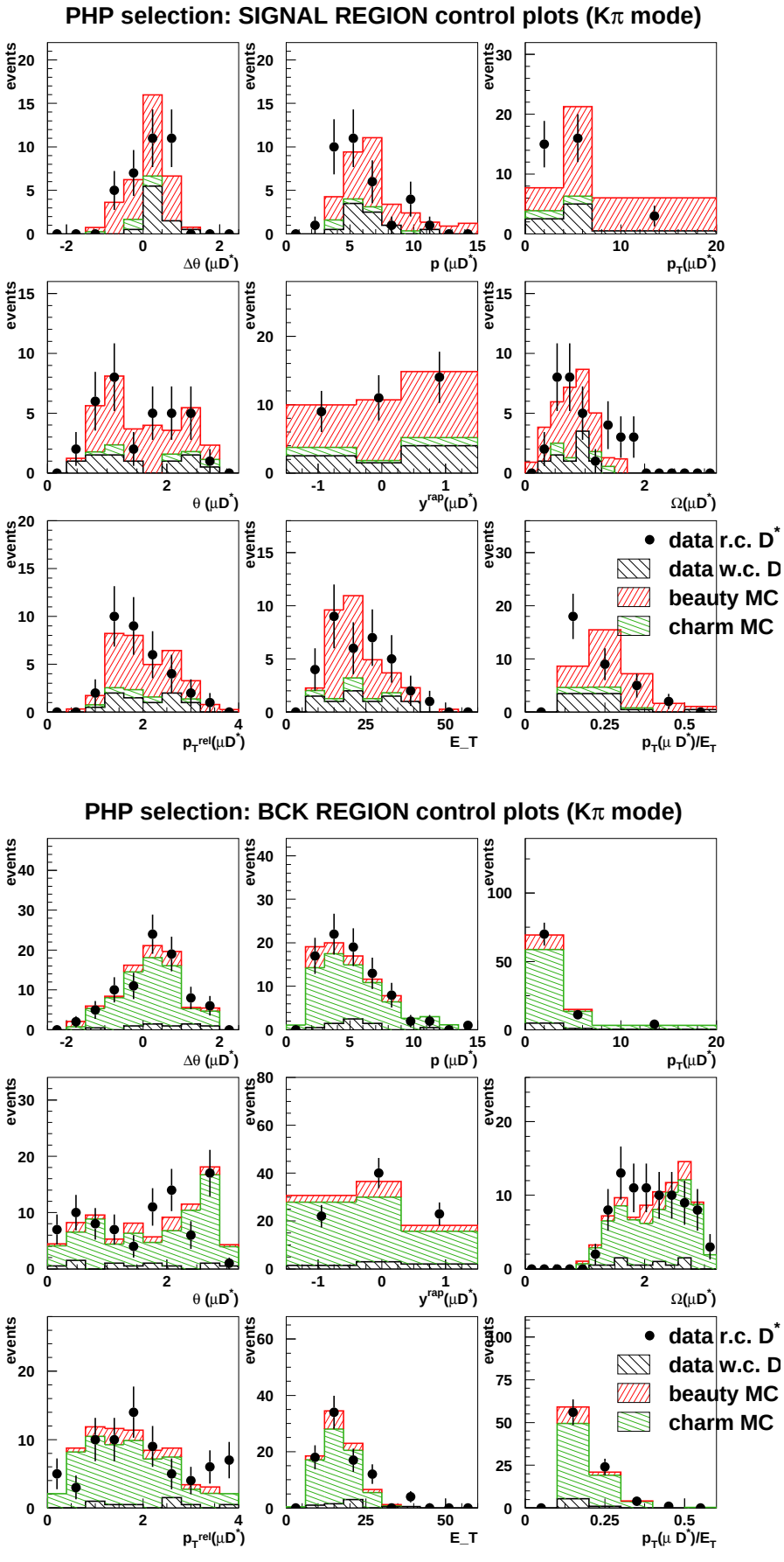

Figure B.2: *Control plots for the photoproduction selection for events with* $D^* \rightarrow (K\pi)\pi_s$ *in the signal (***Top***) and background (***Bottom***) region.*

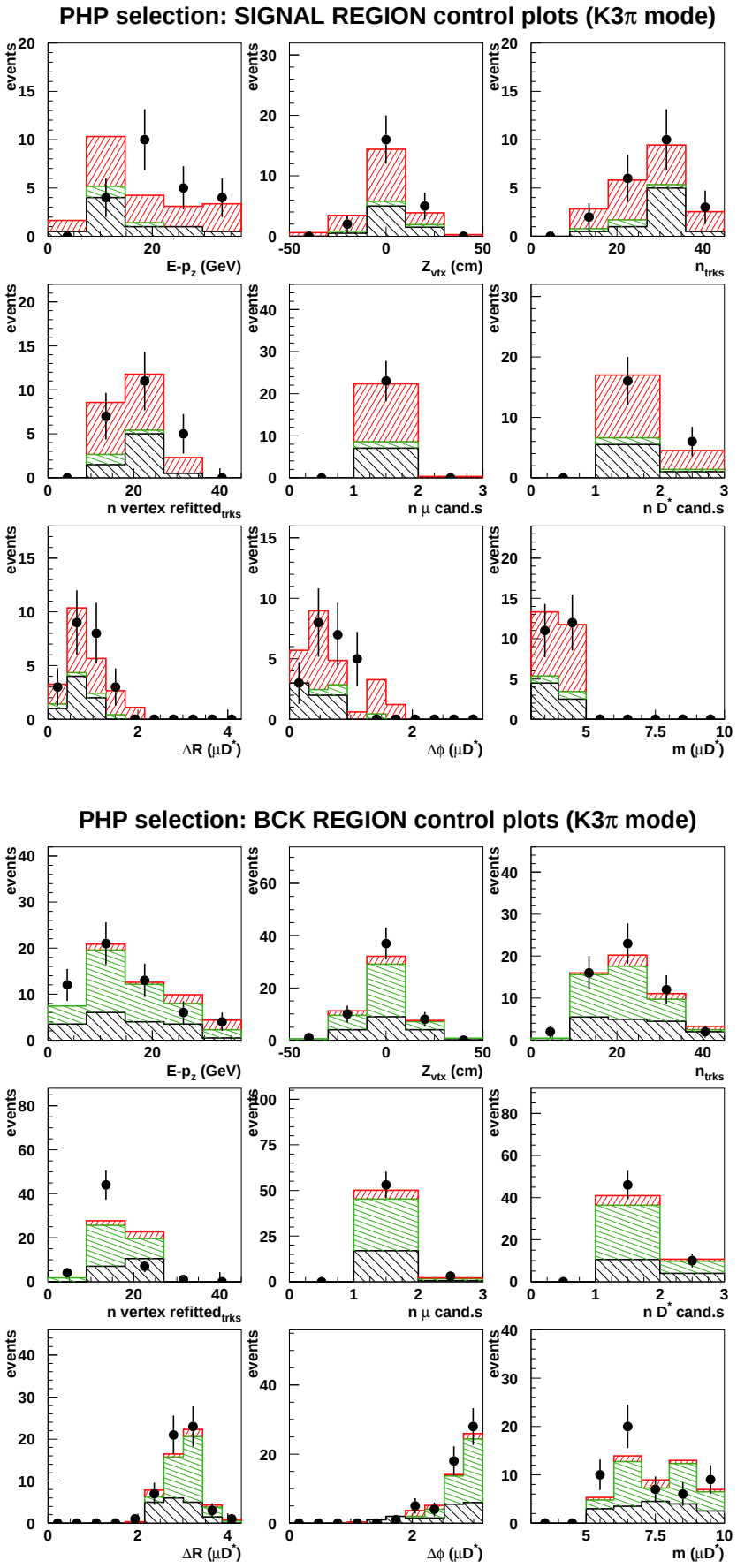

Figure B.3: *Control plots for the photoproduction selection for events with $D^* \to (K\pi\pi\pi)\pi_s$ in the signal (***Top***) and background (***Bottom***) region.*

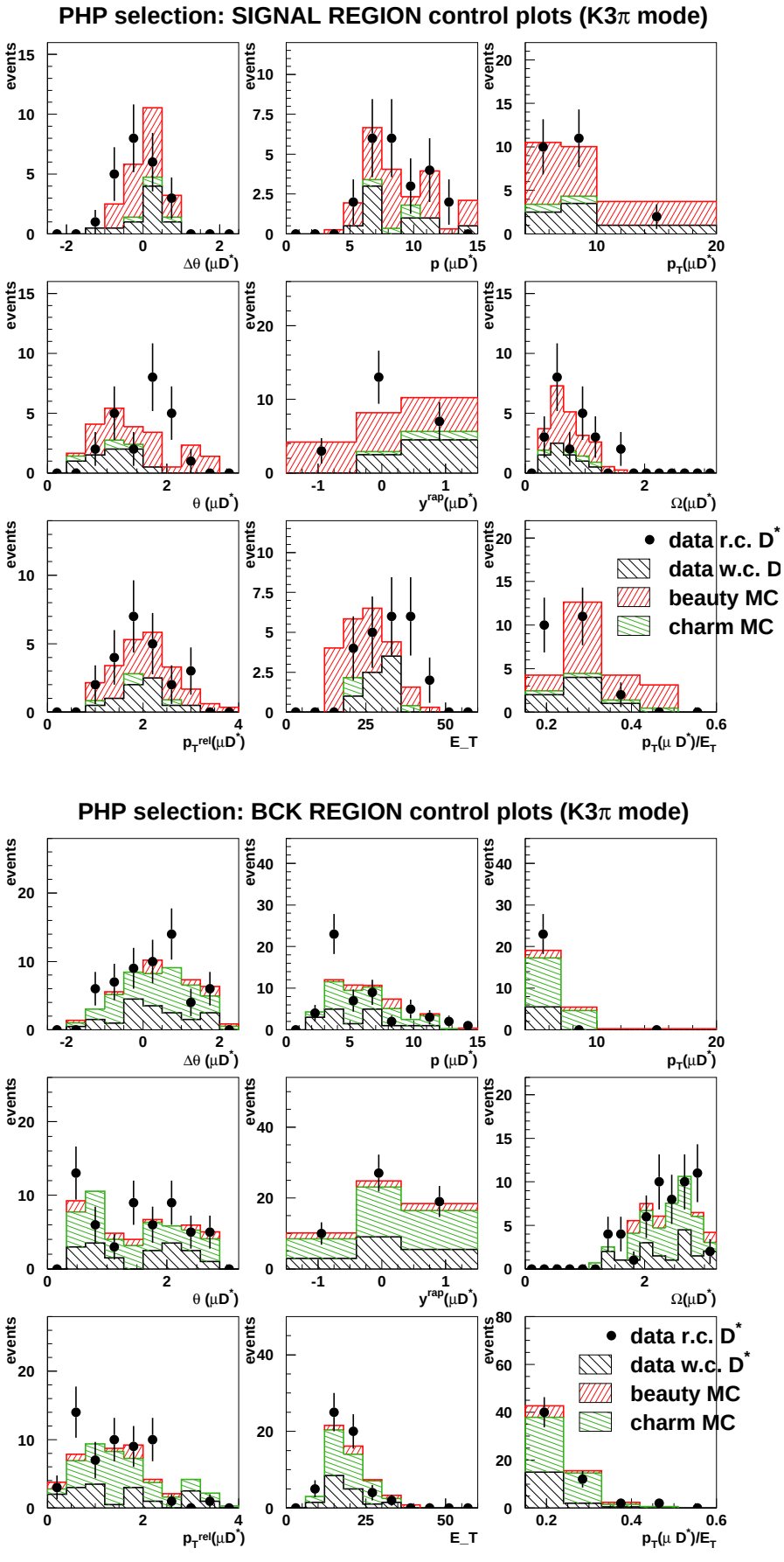

Figure B.4: *Control plots for the photoproduction selection for events with* $D^* \rightarrow (K\pi\pi\pi)\pi_s$ *in the signal (***Top***) and background (***Bottom***) region.*

Bibliography

[1] ZEUS Coll. *Measurement of open beauty production at HERA using a D^*+ muon tag* Abstract 784, ICHEP02, Amsterdam, The Nederlands, July 24-31 2002

[2] ZEUS Coll. *Measurement of open beauty production at HERA using a D^*+ muon tag*. Abstract 575, EPS03, Aachen, Germany, July 17-23 2002

[3] M. P. Alvarez et al., NA14/2 Collaboration, Z. Phys. **C 60** 53, (1993)
J. C. Anjos et al.,E691 Collaboration, Phys. Rev. Lett. **62** 513, (1989)
J. C. Anjos et al.,E691 Collaboration, Phys. Rev. Lett. **65** 2503, (1990)

[4] J.J. Sakurai, Ann. Phys. **11** (1960) 1

[5] S. Frixione et al., Nucl. Phys. **B412** (1994) 225 (`hep-ph/9306337`)

[6] T. Uematsu, I.F. Walsh, Nucl. Phys. **B 199**, 93 (1982)

[7] F. Borzumati, G.A. Schuler, Z. Phys. **C 58**, 139 (1993)

[8] M. Drees, R.M. Godbole, Phys. Rev. **D 50**, 3124 (1994)

[9] M. Glück, E. Reya, M. Stratmann, Phys. Rev. **D 54**, 5515 (1996) (`hep-ph/9605297`)

[10] M. Glück, E. Reya e A. Vogt, Z. Phys. **C 67** 443 (1995)

[11] M. Glück, E. Reya e M. Stratmann, Phys. Rev. **D 51** 3320 (1995)

[12] R.K. Ellis et al., Nucl. Phys. **B152** (1979) 285

[13] G. Altarelli, G. Parisi, Nucl. Phys. **B126** (1977) 298

[14] E. Witten, Nucl. Phys. **B 120** 189 (1977)
C.H. Llewellyn Smith, Phys. Lett. **B 79** 83 (1978)
W.A. Bardeen, A.J. Buras, Phys. Rev. **D 20** 166 (1979)
R.J. DeWitt et al., Pyhs. Rev. **D 19** 2046 (1979)

[15] C.F. Weiszäcker, Z. Phys. **88** (1934) 612; E.J. Williams, Phys. Rev. **45** (1934) 729

[16] R.K. Ellis, P. Nason, Nucl. Phys. **B312** (1989) 551

[17] J. Smith, W.L. Van Nerveen, Nucl. Phys. **B374** 36 (1992)

[18] L.M. Jones, H.W. Wyld, Phys. Rev. **D17** (1978) 759

[19] S. D. Holmes, W. Lee e J.E. Wiss, Ann. Rev. Nucl. Part. Sci. **35** (1985) 397

[20] J. Smith, W.L. van Neerven, Stony Book Report, ITP-SB-91-40 (1991)

[21] P. Nason, S. Dawson, R.K. Ellis, Nucl. Phys. **B303**, 607 (1988)
P. Nason, S. Dawson, R.K. Ellis, Nucl. Phys. **B327**, 49 (1989)

[22] W. Beenakker et al., Phys. Rev. **D 40**, 54 (1989)
W. Beenakker et al., Nucl. Phys. **B351**, 507 (1991)

[23] S. Frixione et al., Nucl. Phys. **B 412** 225 (1994) (hep-ph/9306337)

[24] M.L. Mangano, P.Nason, G. Ridolfi, Nucl. Phys. **B 373** 295 (1992)

[25] B.W. Harris, J. Smith, Nucl. Phys. **B 452**, 109 (1995)
Phys. Lett. **B 353**, 535 (1995); Phys. Rev. **D 57**, 2806 (1998)

[26] J. Collins, F. Wilczek, A. Zee, Phys. Rev. **D 18**, 242 (1978)
W.J. Marciano, Phys. Rev. **D 29**, 580 (1984)

[27] M. Cacciari, M. Greco, Z. Phys. **C 69**, 459 (1996) (hep-ph/9505419)

[28] S. Frixione et al., Phys.Lett. **B348** (1995) 633 (hep-ph/9412348)

[29] A.D Martin, R.G. Roberts, J.Stirling, RAL-94-055, DTP/94/34

[30] P. Harriman et al., Phys. Rev. **D 37** 798 (1990)

[31] J.C.Collins, R.K. Ellis, Nucl. Phys. **B 360**, 3 (1990)

[32] M.Derrick et al., ZEUS Collaboration, Phys. Lett. **B 345**, 576 (1995)

[33] H1 Collab., T. Ahmed et al., H1 Collaboration, Nucl. Phys. **B445** 195 (1995) (hep-ph/9504004)

[34] M. Glück, E. Reya e A. Vogt, Phys. Rev. **D 46** (1992) 1973

[35] H. Abramowicz, K. Charchula e A. Levy, Phys. Lett. **269 B** (1991) 458

[36] M. Derrick et al., ZEUS Coll., Phys. Lett. **B 349** (1995) 225

[37] S. Aid et al., H1 Coll., Nucl. Phys., **B472** (1996) 32

[38] S. Frixione, Proceedings del Workshop *Future Physics at HERA*, vol. 1, Hamburg 1996, 408

[39] C. Adloff et al., H1 Collaboration, Phys. Lett. **B 467**, 156 (1999)
Erratum-ibid. **B 518**,331 (2001)

[40] F. Pitzl et al.,*The H1 Vertex Detector*, hep-ex/0002044

[41] H1 Collaboration, *Measurement of Beauty Production Cross section at HERA Using Lifetime Information* abstract 979,982, submitted to the 30th International Conference on High Energy Physics ICHEP 2000, Osaka, Japan, July 2000

[42] H1 Collaboration, *Measurement of Beauty Production at HERA Using Semi–Muonic Decays* abstract 117, submitted to the International Europhysics Conference on High Energy Physics, EPS03, Aachen, Germany, July 17-23

[43] ZEUS Coll. *Measurement of the Beauty Photoproduction Cross Section at HERA for Events with a Lepton and Two Jets* EPS99, Tampere, Finland, 1999

[44] ZEUS Coll. *Beauty Photoproduction in Muon Semi–Leptonic Decay Mode at HERA* EPS01, Budapest, Hungary, 2001

[45] ZEUS Coll. *Measurement of Beauty Photoproduction at HERA* ICHEP02, Amsterdam, The Nederlands, 2002

[46] S. Catani et al.,Y.L. Dokshitzer, M.H. Seymour, B.R. Webber, Nucl. Phys. **B 406**, 186 (1993)

[47] F. Jacquet, A. Blondel, *Proceedings of the Study of an ep facility for Europe*, Ed. U. Amaldi, DESY 79/48, 391

[48] M. Cacciari and P. Nason, *Is there a significant excess in bottom hadroproduction at the TEVATRON ?* Preprint hep-ph/020425, 2002

[49] E. norbin and T. Sjöstrand. Eur. Phys.J. **C 17**, 137,(2000)

[50] OPAL Collaboration, G. Abbiendi et al.

[51] J. Breitweg et al., ZEUS Collaboration, Eur. Phys.J. **C 18**, 625 (2001)

[52] ZEUS Collaboration, *Measurement of Beauty Production in Deep Inelastic Scattering at HERA* abstract 783, submitted to the 31st International Conference on High Energy Physics ICHEP 2002, Amsterdam, The Nederlands, July 2002

[53] G. Marchesini et al.,Comp. Phys. Comm. **67**, 465 (1992)

[54] J. Breitweg et al., ZEUS Collaboration, Eur. Phys. J. **C6** 67 (1999)

[55] H.U. Bengtsson, T. Sjöstrand.,Comp. Phys. Comm. **46**, 43 (1987)

[56] D. E. Groom et al., Eur. Phys. J. **C 15**, 1 (2000)

[57] S. Frixione et al., Nucl. Phys. **B454** (1995) 3.

[58] A.D. Martin et al., Eur. Phys. J. **C 4**, 463 (1998) A.D. Martin et al., Eur. Phys. J. **C 14**, 133 (2000)

[59] H1 Collaboration, *Beauty Production in Deep Inelastic ep Scattering* abstract 807, submitted to the International Europhysics Conference on High Energy Physics EPS 2001, Budapest, Hungary, July 2001

[60] M. Glück, E. Reya e A. Vogt, Eur. Phys. J. **C 5**, 461 (1998) (`hep-ph/9806404`)

[61] H.Jung, Comp. Phys. Comm. **86**, 147 (1994)

[62] H.L. Lai et al., CTEQ Collaboration, Eur. Phys. J. **C 12**, 375 (2000)

[63] ZEUS Collaboration, *Measurement of D^* photoproduction at HERA* Abstract 786, submitted to the International Conference on High Energy Physics, ICHEP02, Amsterdam, The Nederlands, July 24-31 2002

[64] R.M. Barnett et al., Particle Data Group., Phys. Rev., **D 54** 1 (1996)

[65] CTEQ Coll., H.L. Lai et al., Eur. Phys. J. **C 12**, 375 (2000).

[66] M. Glück, E. Reya and A. Vogt, Phys. Rev. **D 46**, 1973 (1992).

[67] S. Frixione et al., Nucl. Phys. B 454, 3 (1995); S. Frixione et al., Phys. Lett. **B 348**, 633 (1995).

[68] M. Cacciari, S. Frixione and P. Nason, JHEP 0103, 006 (2001).

[69] C. Peterson et al., Phys. Rev. D 27, 105 (1983).

[70] P. Nason and C. Oleari, Phys. Lett. **B 447**, 327 (1999); P. Nason and C. Oleari, Preprint hepph/9903541, 1999.

[71] ARGUS Coll., H. Albrecht et al., Z. Phys. C 52, 353 (1991).

[72] OPAL Coll., R. Akers et al., Z. Phys. **C 67**, 27 (1995).

[73] S. Frixione and P. Nason, JHEP 0203, 053 (2002).

[74] ZEUS Collab., J. Breitweg et al., Eur. Phys. J. **C 12**, 35 (2000).

[75] H1 Collab., C. Adloff et al., Phys. Lett. **B 528**, 199 (2002).

[76] ZEUS Collab., DESY 03-115 (2003).

[77] V.N. Gribov and L.N. Lipatov, Sov. J. Nucl. Phys. 15, 438 (1972);

[78] B.W. Harris and J. Smith, Nucl. Phys. **B 452**, 109 (1995); B.W. Harris and J. Smith, Phys. Lett. B 353, 535 (1995). Erratum, Phys. Lett. B 359, (1995) 423.

[79] E. Laenen et al., Nucl. Phys. **B 392**, 162 (1993); E. Laenen et al., Nucl. Phys. B 392, 229 (1993).

[80] ZEUS Collab., S. Chekanov et al., Phys. Rev. **D 67**, 012007 (2003).

[81] Public access to ZEUS 2002 PDFs, available on `http://www-pnp.physics.ox.ac.uk/~cooper/zeus2002.html`.

[82] C. Peterson et al., Phys. Rev. **D 27**, 105 (1983).

[83] L. Gladilin, Preprint hep-ex/9912064 (1999).

[84] P. Nason and C. Oleari, Nucl. Phys. **B 565**, 245 (2000).

[85] I. Redondo, Ph.D. Thesis, Universidad Autonoma de Madrid, Report DESY-THESIS-2001-037, 2001.

[86] L. M. Lederman et al., Phys. Rev. Lett., **39-5**, 252, (1977)

[87] UA1 Collaboration, C. Albajar et al., Phys. Lett. **B 256**, 112 (1991)

[88] CDF Collaboration, F. Abe et al., Phys. Rev. Lett. **71**, 500 (1993)
CDF Collaboration, F. Abe et al., Phys. Rev. Lett. **71**, 2396 (1993)
CDF Collaboration, F. Abe et al., Phys. Rev. **D 53**, 1051 (1996)
CDF Collaboration, F. Abe et al., Phys. Rev. **D 55**, 2546 (1997)
D0 Collaboration, S. Abachi et al. Phys. Rev. Lett. **73**, 3548 (1995)
D0 Collaboration, S. Abachi et al. Phys. Lett. **B 370**, 239 (1996)
D0 Collaboration, B. Abbott et al. Phys. Lett. **B 487**, 264 (2000)

[89] L3 Collaboration, M. Acciarri et al., Phys. Lett. **B 503**, 10 (2001)
OPAL Collaboration, *Measurement of Open Beauty Production in Photon- Photon Collisions at* $\sqrt{s} = 189 - 202\ GeV$. Abstract 203, International Europhysics Conference on High Energy Physics, Budapest, Hungary, July 12-18, 2001

[90] S. Frixione et al., Adv. Ser. Direct. High Energy Phys. **15**, 609 (1998) (`hep-ph/9702287`)

[91] R. Bonciani et al., Nucl. Phys. **B 529** (1998), 424.

[92] A. D. Martin et al., Phys. Lett. **B 531** (2002), 216

[93] N. Kidonakis et al., Phys. Rev. **D 64** (2001), 114001.

[94] D. M. Jansen et al., Phys. Rev. Lett. **74** (1995), 3118.

[95] T. Alexopoulos et al., Phys. Rev. Lett. **82** (1999), 41.

[96] A. Csilling for the OPAL Collaboration, *Charm and bottom production in two-photon collisions with OPAL* hep-ex/0010060

[97] DELPHI Collaboration, *Measurement of the beauty and charm production cross section in* $\gamma\gamma$ *collisions using semi–leptonic decays and double tagging at* $\sqrt{s} = 189 - 209$ *GeV* Contributed papaer for EPS 2003 (Aachen) and LP 2003 (FNAL)

[98] L3 Collaboration, *Measurement of the cross section for open charm and beauty production in* $\gamma\gamma$ *collisions at* $\sqrt{s} = 189 - 202$ *GeV* hep-ex/0011070, Submitted to Phys. Lett. B.

[99] M. Drees et al., Phys. Lett. **B 306**, 371, (1993)

[100] C. Albajar, et al., *Beauty Production at the Cern* $p\bar{p}$ *Collider.* Phys. Lett. B 256 (1991) 121. C. Albajar, et al., *Measurement Of The Bottom Quark Production Crosssection In Proton AntiProton Collisions at* $\sqrt{s} = 0.63$ *TeV*. Phys. Lett. **B 213** (1988) 405. 163. C. Albajar, et al., *Beauty Production at the Cern Proton AntiProton Collider.* (Paper 1.). Phys. Lett. **B 186** (1987) 237.

[101] C. Albajar, et al., *Measurement of* $b\bar{b}$ *Correlations at the CERN* $p\bar{p}$ *Collider.* Z. Phys. **C 61** (1994) 41.

[102] F. Abe et al., CDF Collaboration, Phys. Rev. Lett. **71** 500 (1993)
F. Abe et al., CDF Collaboration, Phys. Rev. Lett. **79** 572 (1997)
F. Abe et al., CDF Collaboration, Phys. Rev. Lett. **75** 1451 (1995)
B. Abbot et al., D0 Collaboration, Phys. Rev. Lett. **487** 264 (2000)
B. Abbot et al., D0 Collaboration, Phys. Rev. Lett. **85** 5068 (2000)

[103] D. Acosta et al., CDF Collaboration, Phys. Rev. Lett. **D 65** 052005 (2002).

[104] F. Abe et al., CDF Collaboration, Phys. Rev. Lett. **75** 1451 (1995).

[105] M. Cacciari, P. Nason, `hep-ph/0204025`

[106] J. Chrin, Z. Phys. **C 36**, 163 (1987)

[107] C. Peterson et al., Phys. Rev. **D 27**, 105 (1983)

[108] M. Cacciari, M. Greco, Nucl. Phys. **B 421**, 530 (1994)

[109] M. Cacciari, M. Greco, P. Nason, JHEP **05**, 007 (1998)

[110] M. Cacciari, M. Greco, Phys. Rev. **D 55**, 7134 (1997); P.Nason, C. Oleari, Nucl. Phys. **B 565**, 245 (2000)

[111] A. Heister et al., Phys. Lett. **B 512**, 30 (2001)

[112] F. Abe et al., CDF Coll., Phys. Rev. **D 50**(1994)2966.

[113] P. Nason and C. Oleari, Phys. Lett. **B387** (1996) 623, hep-ph/9607347.

[114] A. Geiser, PhD thesis, RWTH Aachen, 1992, Aachen Report PITHA 92/31.

[115] C. Albajar et al., UA1 Coll., Z. Phys. **C 61** (1994) 41.

[116] C. Albajar et al., UA1 Coll., Phys. Lett. **B 369** (1996) 46.

[117] F. Abe et al., CDF Coll., Fermilab-Pub-94/131-E.

[118] F. Abe et al., CDF Coll., Phys. Rev. **D 53** (1996)1051, hep-ex/9508017.

[119] F. Abe et al., CDF Coll., Fermilab-Pub-96/216-E, to appear in Phys. Rev. **D**

[120] ZEUS Collaboration, U. Holm,*The ZEUS Detector*, Status Report (unpublished), 1993, `http://www-zeus.desy.de/bluebook/bluebook.html`

[121] *HERA: A Proposal for a Large Electron Proton Colliding Beam Facility at DESY*, DESY-HERA 81-10 (1981)

[122] N. Harnew et al., Nucl. Instr. & Meth. **A279** (1989) 290
C.B. Brooks et al., Nucl. Instr. & Meth. **A283** (1989) 477
B. Foster et al., Nucl. Instr. & Meth. **A338** (1994) 254

[123] R.Hall-Wilton, N.McCubbin, P.Nylander, M.Sutton, M.Wing, *The CTD Tracking Resolution*, Zeus-Note 99-024

[124] A. Bamberger et al.,*The Small-angle Rear Track Detector for ZEUS*, ZEUS-Note 95-095 (1995);

[125] M. Derrick et al., Nucl. Instr. & Meth. **A 309** (1991) 77;
A. Andresen et al., Nucl. Instr. & Meth. **A 309** (1991) 101;
A. Bernstein et al., Nucl. Instr. & Meth. **A 336** (1993) 23;
A. Caldwell et al., Nucl. Instr. & Meth. **A 321** (1992) 356.

[126] J. Krüger, *The Uranium Scintillator Calorimeter for the ZEUS detector at the Electron-Proton Collider HERA*, DESY-Report F35-92-02 (1992)

[127] L. Hervàs, *The pipelined readout for the ZEUS calorimeter* Doctoral thesis U. Autónoma de Madrid (1991) DESY F35D-91-01

[128] E. Iarocci et al., Nucl. Instr & Meth. **A 217** (1983) 30.

[129] G. Abbiendi et al., Nucl. Instr & Meth. **A 333** (1993) 342.

[130] H. Bethe and W. Heitler, Proc. Roy. Soc. **A 146** (1934) 83.

[131] M.Van der Horst *Theoretical calculations for electron–proton scattering*. Doctoral thesis, University of Amsterdam (1990) RX-1278 (Amsterdam, 1990)

[132] ZEUS Luminosity Monitor Group, J. Andruszkow et al., DESY-92-066 (1992)
ZEUS Luminosity Monitor Group, J. Andruszkow et al., DESY-01-041 (2001)

[133] D. Kisielewska et al., DESY-HERA 85-25 (1985);
J. Andruszkow et al., DESY-92-066 (1992).

[134] S.M. Fisher, M. Palazzi, *The ADAMO data system*, 1993

[135] V.M. Budnev et al., Phys. Rep., 15 C, 181 (1975).

[136] H.L. Lai et al., Phys. Rev. D 55, 1280 (1997).

[137] M. Glück, E. Reya and A. Vogt, Phys. Rev. D 46, 1973 (1992).

[138] J.C. Collins, D.E. Soper and G. Sterman, Nucl. Phys. B 308, 833 (1988).

[139] G.A. Schuler, Nucl. Phys. B 299, 21 (1988).

[140] D. Amati and G. Veneziano, Phys. Lett. B 83, 87 (1979); Yu.L. Dokshitzer and S.I. Troian, Leningrad Nuclear Physics Institute preprint N922 (1984);

[141] C.F. Weizsäcker, Z. Phys., 88, 612 (1934); E.J. Williams, Phys. Rev., 45, 729 (1934).

[142] B. Andersson et al.,G. Gustavson, G. Ingelman e T.Sjöstrand,
Phys. Rep. **97** (1983) 31;
T. Sjöstrand, Nucl. Phys. **B248** (1984) 469

[143] T. Sjöstrand, Proceedings del Workshop *Physics at HERA*, vol.3, Hamburg 1991, 1405

[144] T. Sjostrand, Nucl. Phys. 248, 469 (1984).

[145] `http://www-zeus.desy.de/components/funnel/MONTE_CARLO/mozart.html`

[146] *GEANT 3.13*, R. Brun, CERN DD/EE 84-1 (1984).
R. Brun et al., *GEANT 3*, CERN DD/EE/84–1 (1987).
GEANT, Detector description and simulation tool, CERN program library long writeup W5013.

[147] ZGANA, ZEUS trigger simulation library, Els de Wolf (ed.) et al.

[148] S.M. Fisher and A. Palazzi, *The ADAMO Data System Programmmer's Manual*.

[149] H. Jung, Comp. Phys. Comm. 86 (1995) 147.

[150] H. Jung, *The RAPGAP Monte Carlo for Deep Inelastic Scattering*, version 2.08/01, `http://www-h1.desy.de/jung/rapgap.html`.

[151] A. Kwiatkowski, H. Spiesberger, H.-J. Mohring, *HERACLES 4.1 – An event generator for ep interactions at HERA including radiative processes*, in Proc. of the Workshop on Physics at HERA, Vol. 3, edited by W. Buchmuller, G. Ingelman (1991), p. 1294.

[152] A. Kwiatkowski, H. Spiesberger, H.-J. Mohring, *HERACLES – An event generator for ep interactions at HERA including radiative processes*. version 4.6, 1996,
`http://www.desy.de/\~hspiesb/heracles.html`.

[153] H. Plothow-Besch,
Proceedings P. Dragovitsch, S.L. Linn and M. Burbank World Sci., Singapore, 1994 (265)

[154] *An OO Tag Database for Physics Analysis at HERA*
Proceedings of *Computing In High Energy And Nuclear Physics* Conference Feb. 2000, Padova (Italy).

[155] DESY-Note 01-045

[156] A. Bertolin, R. Brugnera, M.Turcato private communication. For a list, see:
`http://www-zeus.desy.de/mturcato/ZEUS ONLY/BMUON/mbtake.fpp`
`http://www-zeus.desy.de/mturcato/ZEUS ONLY/BMUON/mbtake9800.fpp`

[157] L. Adamczyk et al., *Luminosity measurement in the ZEUS experiment*, ZEUSNOTE 01-004.

[158] *Observation of J/ψ in the first 275 nb^{-1} of 1993 run* G. Abbiendi, A. Bertolin, R. Brugnera, R. Carlin, F. Dal Corso, M. De Giorgi, U. Dosselli, S. Limentani, M. Morandin, M. Posocco, L. Stanco, R. Stroili, C. Voci. ZEUS–NOTE 93-120

[159] H.Abramowicz, A.Caldwell, R.Sinkus, *Neural Network Based Electron Identification in the ZEUS Calorimeter*, DESY 95-054. R.Sinkus, Nucl. Instrum. Methods **A361** (1995) 290.

[160] S. Nussinov, Phys. Rev. Lett. **35** (1976) 1672; G. Feldmann et al., Phys. Rev. Lett. **38** (1977) 1313.

[161] K. Hagiwara et al, Phys. Rev. **D 66**, 010001 (2002)

[162] R.Graciani et al. *Study of D^* photoproduction in ep collisions at HERA* ZEUS-Note 96-124.

[163] G. Abbiendi, *Global Tracking of muons in the Barrel and Rear region*, Zeus-Note 99-063

[164] V.Innocente, M. Maire e E. Nagy, *GEANE: average tracking and error propagation package*, procs. of MC91: Detector and event simulation in high energy physics (Amsterdam 1991).

[165] R. Barlow C. Beeston. *Fitting using finite Monte Carlo Samples*. Comp. Phys. Comm. **77** (1993) 219-228

[166] M. Turcato, *Measurement of beauty at HERA* PhD Thesis

[167] J. Wagner, H1 Collaboration, H1prelim-02-071, talk presented at DIS2002, Cracow, Poland, April 30 - May 4, 2002.

[168] H1 Collaboration, C. Adloff et al., *Measurement of Open Beauty Production at HERA*, Phys. Lett. **B 467** 1999, 156, hep-ex/9909029,

[169] ZEUS Collaboration, J. Breitweg et al., *Measurement of Open Beauty Production in Photoproduction at HERA*, Eur. Phys. J.,2001, **C 18**, 625,hep-ex/0011081.

[170] H1 Collaboration, Abstract 807, International Europhysics Conference on High Energy Physics, Budapest, Hungary, July 12-18, 2001.

[171] ZEUS Collaboration, Abstract 785, International Conference on High Energy Physics, Amsterdam, The Netherlands, July 24-31, 2002.

[172] ZEUS Collaboration,Abstract 561, International Europhysics Conference on High Energy Physics, Aachen, Germany, July 17-23, 2003.

[173] ZEUS Collaboration, Abstract 784, International Conference on High Energy Physics, Amsterdam, The Netherlands, July 24-31, 2002.

[174] T. Sjöstrand, *High-Energy Physics Event Generation with PYTHIA 5.7 and JETSET 7.4* , Comp. Phys. Comm., 1994, **82**, 74

[175] H. Jung, *Hard Diffractive Scattering in High Energy ep Collisions and the Monte Carlo Generator RAPGAP*, Comp. Phys. Comm., 1995, **86**, 147

[176] G. Marchesini et al.,*HERWIG: A Monte Carlo Event Generator for Simulating Hadron Emission Reactions With Interfering Gluons*, Comp. Phys. Comm., 1992, **67**, 465

[177] S. Frixione, P. Nason and G. Ridolfi, Nucl. Phys., 1995, **B 454**, 3

[178] B.W. Harris and J. Smith, Nucl. Phys.,1995, **B 452**, 109

[179] B.W. Harris and J. Smith,Phys. Lett., 1995, **B 353**, 535

[180] G.F. Hartner et al., Y. Iga, J.B. Lane, N.A. McCubbin, M. Wing,
VCTRAK (3.07/04): Offline Output Information, ZEUS-Note 97-064

Acknowledgments

The analysis presented in this thesis was possible also thanks to the cooperation or just to the presence of many people which, directly or indirectly, gave their contribution.

With many colleagues in ZEUS I could really feel being part of a Collaboration, in the literal sense ...! Starting in causal–chronological order I would like to mention *Leonid Gladilin* who, I would say, threw the seed ... by provoking and encouraging in me the will to measure beauty production in such an intriguing way. He also patiently generated the so called "general D meson" or "Leonid" Monte Carlo which was used successfully in our study. Special merit I would like then to tribute to *Achim Geiser* who enthusiastically joined me in doing this analysis. Thanks to his competence and expertise he always gave me a lot of interesting inputs. His overwhelming passion was of great help especially during the days of indefatigable work which preceded the the ICHEP02 conference. I would also like to thank *Massimo Corradi* who, besides giving me interesting suggestions on the study of fake muons, first produced the PHP NLO calculation and introduced me to the FMNR code. A note of gratefulness also goes to the other heavy flavour physics coordinators, *Matthew Wing* and *Richard Hall Wilton* for their suggestions and efforts toward the publication of the results. I would also like to mention *Manuel Zambrana* who helped us with the HVQDIS code. This work is also indebted to the studies on muon efficiency correction performed by *Monica Turcato* on dimuons (the one and only guru in this field !).

I spent these three years of PhD among the colleagues and friends of the Padova group. Here being detailed would lead me much too far away [1] ... and the 31st of October is getting nearer ! In any case I want to first thank *Riccardo Brugnera*, my supervisor for patiently reading and correcting these pages and in general for the scientific and human qualities which he always demonstrated during our collaboration. The fact that this thesis has been successfully completed owes much to Riccardo's directives and his wise pragmatism, a key quality for experimental physicists! Even if he is -already- among the top ten quoted physicists in the last ten years *Luca Stanco* (will they count this Luca ...?) deserves for sure my gratefulness for the passion which he uses in solving our problems and for the continuous support he gave to our PhD activities. How not to thank Prof. *Roberto Carlin* ? If the fact that he recently became deputy spokesmen was not enough ... I would mention his contagious enthusiasm and the absolute light–heartedness with which he faces the most complicated problems. I must not forget the elegant presence of Prof. *Silvia Limentani* whose remarks on our work came often very pleased to us. Among the living beholders of the deepest BRMUON knowledge I want to mention *Enrico Borsato* and *Flavio Dal Corso* whose sympathy and competence I always admired. I could share with them heroic moments in the, not at all comfortable, environment of the ZEUS balconies or in front of the radiation monitor crates. *Alessandro Bertolin* has always been a solid presence during my work, the pole position ... man when you need some help ! I would like to thank him for his kindness and the, up to know undefeated, competence under each ZEUS–related question. If I had to consider the time I spent with

[1] Th so called acknowledgments divergence.

them an the sandwiches we ate together, my "ZEUS PhD colleagues" *Andrea Parenti*[2] and *Monica Turcato* [3] would have already been mentioned too late! I shared with them a lot of experiences and in a certain sense I always felt in communion with them for the fact of "being on the same boat" as we say and not only for this. The PhD period was really an interesting experience thanks to them and a lot of other people sharing the same crowded and with time more and more full–optional "office". The lively and gently ironic atmosphere which characterised our lunch breaks and beyond was really magic and made for sure our work much more easy and profitable. Under this category I want to mention *Marcello* ○, *Moreno*[4], *Enrico*[5], *Federico*[6], *Fulvio*[7], *Alvise*, *Gionni*, *Martino*, *Antonio*s, and the indomitable "laureandi" or summer students *Marta*, *Melisa*, *Roberto*, *Enrico* and lately *Laura*, *Paolo* and *Piero*, the future of HEP! I would also like to thank *Stefano Dusini* and *Alberto Garfagnini* for their collaboration and help. Hamburg was not less prodigal in terms of important and charitable people who helped me in distracting from the fatal temptation of working overdoses. One of the most successful was *Alessandro B. Montanari* from Borello with whom I shared industrial quantities of original Penny Markt frozen pizzas and delicious cakes [8] even while watching ER[9] on TV. I am also grateful to him for introducing me in the international and happy group of the "Nouar aficionados". I remember them all and in particular the brilliant *Vincenzo* and never unsuccessful *Devis*. I would like then to particularly thank *Amita* for the nice time we spent in Hamburg and the profitable German and non German lessons [10]. I just started revising in my mind all the interesting people I had the opportunity to meet in DESY. Many. I address collective thank to all of them. Many other people would probably have the luck not to read this thesis, especially many of my friends which had anyway a very important role in these months. I include them all with those which I would have liked to thank but I forgot.

I would also like to mention *Sara*[11] here (even if she will become a brilliant doctor in medicine and not a physicist!) since this thesis and her exams were like the historical leit-motiv over which our lives in the last months happened to be so tightly and beautifully inter-weaved. All the rest she knows.

Finally but very importantly a special thank to my good parents. Grazie.

Andrea

[2] I thank him for using words as *stamane* or *sciocco*.

[3] Born in Schio, Italy (?)

[4] S. Apollinare, Ohio, USA.

[5] Now at Dresden University.

[6] Now seduced by the world of business.

[7] "Quello di Babar . . . "

[8] It must be noticed that the cooking talents which most of these people demonstrated in the Padova apartment at DESY gave a non negligible contribution to the general quality of life during the periods spent in Hamburg.

[9] Or "Lo zio d'America"

[10] i.e. on the use of CTRL-J in pine and on the ZEUS instrumented "iron joke".

[11] See also page 3.

List of Figures

1.1 *Electron–proton scattering in Neutral Current (NC) (***Left***) and Charged Current (CC) (***Right***) processes.* 16

1.2 **Left***: (x,Q^2) plane covered by HERA in comparison to fixed target experiments. The coverage of x and Q^2 is extended by about two orders of magnitude.* **Right***: Neutral Current and Charged Current cross sections as a function of Q^2* 17

1.3 *Leading order direct photon processes:* **Left***: QCD Compton.* **Right***: Boson–gluon fusion.* 22

1.4 *Examples of leading order resolved photon processes.* 22

1.5 *A photon–proton interaction. If the virtuality k_T of the propagator shown in the figure is lower than the factorisation scale μ_γ the process is included in the resolved calculation at leading order, otherwise it is thought of as a direct process at next–to–leading order.* 22

1.6 *The ratio of the resolved to the direct contribution to beauty production cross section in LO QCD as a function of the $\gamma^* p$ center of mass energy for various fixed values of the photon virtuality Q^2 (referred as P^2 in the plot) (in GeV^2 units).* 23

1.7 **Left***: The $O(\alpha_{em}\alpha_S)$ γg, $O(\alpha_{em}\alpha_S^2)$ γg and $O(\alpha_{em}\alpha_S^2)$ γq contributions to the total charm photoproduction cross section as a function of the variable $\tau = \frac{w}{W}$. The proton renormalisation and factorisation scales have been taken equal to the charm mass, while the proton parton densities used are MRSA.* **Right** *As for the Left plot, but with HMRS B proton parton densities (from Reference [28]).* 29

1.8 **Left***: total cross section for $c\bar{c}$ photoproduction as a function of the p centre–of–mass energy. Theoretical predictions and experimental data from Reference [36] and [37] are shown.* **Right***: total cross section for $c\bar{c}$ production in γN collisions, compared to NLO QCD predictions.* 30

1.9 *Uncertainty on the B–hadron transverse momentum for beauty electroproduction in the Weizsäcker-Williams approximation with Peterson fragmentation and a cut on pseudorapidity of the hadron.* . . . 31

1.10 *Distribution of impact parameter δ (Left) and p_T^{rel} (Right) of the muon track. The data (points) are compared with the Monte Carlo simulation (solid line). The decomposition of the Monte Carlo distribution into the b (dashed line), the c (dotted line) and the light quark (dashdotted line) components is determined from a fit to the two-dimensional distribution of δ and p_T^{rel}.* 33

1.11 *From top to bottom: differential dijet muon beauty production cross sections $d\sigma/d\eta^\mu$, $d\sigma/dp_T^\mu$, $d\sigma/dx_{obs}^\gamma$ in the range $Q^2 < 1$ GeV^2, $0.2 < y < 0.8$, $p_T^\mu > 2.5$ GeV, $-0.55 < \eta^\mu < 1.1$, $p_T^{j1(2)} > 7(6)$ GeV and $|\eta_j| < 2.5$. The inner error bars show the statistical error, the outer error bars represent the statistical and systematic uncertainty added in quadrature. In the Left column plots the measurements are compared to the predictions from the Monte Carlo generator program* PYTHIA *(solid line), the resolved contribution to the* PYTHIA *cross section (dashed-dotted line) and* CASCADE *(dashed line). In the right column plots the measurements are compared to the prediction from a pQCD NLO calculation at parton level (dashed line) and hadron level (solid line). The band shows the uncertainty obtained from a simultaneous variation of the b–quark mass, μ_R and μ_F (see text).* 35

1.12 *The p_T^{rel} distribution for events with muons in the Forward, Barrel and Rear regions. The data (points) are compared to the mixture of beauty and charm+LF background obtained from the p_T^{rel} fit (full line). The shaded band shows the uncertainty from the Monte Carlo statistics. The hatched histogram represents the beauty component while the dashed–line histogram is the background.* . . . 37

1.13 *Beauty cross sections for events with two jets and a muon, in the Forward, Barrel and Rear regions (Left plot), and differential cross–section as a function of x^{γ}_{obs} (Right plot). The data (dots) are compared to the predictions of NLO QCD (dashed line: parton–level jets, solid line: jets corrected to the hadron–level). The full error bars are the quadratic sum of the statistical (inner part) and systematic uncertainties. The band around the NLO represents the variation on the theoretical predictions obtained by varying the b–quark mass and μ_R and μ_F as explained in the text. The data are also compared to the predictions of* PYTHIA *(solid line histogram) and* CASCADE *(dot–dashed line histogram) Monte Carlo models.* 37

1.14 *Beauty differential cross sections as a function of the pseudorapidity, η^{jb} and transverse momentum p_T^{jb} of the jet containing the B hadron for events with two jets. The data (dots) are compared to the predictions of NLO QCD (dashed line: parton–level jets, solid line: corrected to hadron–level jets). The full error bars are the quadratic sum of the statistical (inner part) and systematic uncertainties. The band around the NLO represents the variation on the theoretical predictions obtained by varying the b–quark mass and μ_R and μ_F as explained in the text. The data are also compared to the predictions of* PYTHIA *(solid line histogram) and* CASCADE *(dot–dashed line histogram) Monte Carlo models.* 39

1.15 *The b-quark cross section for b-quark transverse momentum larger than p_T^{min} , for b–quark pseudorapidity $|\eta_b| < 2$, compared to the predictions of NLO QCD. The full error bars are the quadratic sum of the statistical (inner part) and systematic uncertainties. The band around the NLO represents the variation on the theoretical predictions obtained by varying the b–quark mass and μ_R and μ_F as explained in the text. The result is compared to the previous ZEUS measurement in the electron channel [51].* 40

1.16 **Left***: differential cross section $d\sigma/dp_T^{rel}$ for heavy flavour production. The shaded band represents the effect of the uncertainty on the calorimeter energy scale. The experimental data are compared to the* HERWIG *Monte Carlo prediction (solid line) for all quark flavours, fitted to the data and scaled up by a factor 3.8. The contributions from beauty (forward–diagonally hatched histogram) and from charm processes (backward–diagonally hatched histogram) predicted by the Monte Carlo model are shown separately.* **Right***: differential cross section $d\sigma/dx_{\gamma}^{OBS}$ for heavy quark decays. The direct (forward–diagonally hatched histogram) and resolved photon components (backward–diagonally hatched histogram) are shown separately. From Reference [51].* 41

1.17 *Differential beauty cross section as a function of Q^2 (Left) and x (Right) for events with at least one jet reconstructed in the Breit frame and a muon, compared to the NLO QCD calculations. The error bars on the data points correspond to the statistical uncertainty (inner error bars) and to the statistical and systematic uncertainty added in quadrature (outer error bars). The shaded bands show the uncertainty of the theoretical prediction coming from the variation of the renormalisation and factorisation scale, μ, and the b-quark mass.* 42

1.18 *The distribution of the mass difference, $\Delta m = m(K\pi\pi_S) - m(K\pi)$, for $D^{*\pm}$ candidates (solid dots). The histogram shows the Δm distribution for wrong charge combinations.* 43

1.19 **Left** *part: Differential cross sections for inclusive $D^{*\pm}$ production in the in the kinematic region defined in the text. a) $d\sigma/dp_T$, b) $d\sigma/d\eta$, c) $d\sigma/dW$ and d) $d\sigma/dz$. The inner error bars represent statistical uncertainties and the outer bars show statistical and systematic uncertainties added in quadrature. The predictions of NLO calculations with the central choice of parameters are given by the solid histograms. The upper (lower) dashed histograms correspond to the upper (lower) bounds of the predictions. The FONLL predictions, whenever available, are shown as dotted curves and their uncertainties are given by the shaded bands. The parameters used for the NLO and FONLL calculations are described in the text.* **Right** *part: $d\sigma/dp_T(D^*)$ in bins of $\eta(D^*)$* 44

1.20 **Left** *part: $d\sigma/d\eta(D^*)$ in bins of $p_T(D^*)$* **Right** *part: $d\sigma/dp_T(D^*)$ in bins of $z(D^*)$* 45

1.21 **Left** *part: $d\sigma/d\eta(D^*)$ in bins of $z(D^*)$* **Right** *part: $d\sigma/dz(D^*)$ in bins of $p_T(D^*)$* 45

1.22 *The distribution of the mass difference, $\Delta m = (m_{K\pi\pi_s} - m_{K\pi})$, for D^* candidates (solid dots). The Δm distribution from wrong-charge combinations, normalised in the region $0.15 < \Delta M < 0.165$ GeV, is shown as the histogram. The $m_{K\pi}$ distribution for the D^0 candidates in the range $0.143 < \Delta M < 0.148$ GeV is shown as an inset. The fit is the sum of a modified Gaussian to describe the signal and a second-order polynomial to describe the background.* 46

1.23 **Left**: *Differential D^* cross sections, for e^-p and e^+p data combined, as a function of Q^2, x, $p_T(D^*)$ and $\eta(D^*)$ compared to the NLO QCD calculation of* HVQDIS. *The inner error bars show the statistical uncertainties and the outer bars show the statistical and systematic uncertainties added in quadrature. Predictions from the ZEUS NLO QCD fit are shown for $m_c = 1.35$ GeV (solid line) with its associated uncertainty (shaded band) as discussed in the text. Predictions using the CTEQ5F3 PDF (dashed-dotted line) and an alternative hadronisation scheme (dotted line) are displayed. The ratios of the cross sections to the central* HVQDIS *prediction are also shown beneath each plot.* **Right** *As for the Left plots but for $Q^2 > 40$ GeV^2.* 47

1.24 **Left** *The measured $F_2^{c\bar{c}}$ at Q^2 values between 2 and 500 GeV^2 as a function of x.* **Middle** *The measured $F_2^{c\bar{c}}$ at x values between 0.00003 and 0.03 as a function of Q^2.* **Right** *The measured ratio $F_2^{c\bar{c}}/F_2$ at Q^2 values between 2 and 500 GeV^2 as a function of x. The current data (solid points) are compared with the previous ZEUS measurement (open points). The data are shown with statistical uncertainties (inner bars) and statistical and systematic uncertainties added in quadrature (outer bars). The lower and upper curves show the fit uncertainty propagated from the experimental uncertainties of the fitted data.* 49

1.25 **Left**: *Υ discovery in 1977 at Fermilab [86]* **Right**: *The comparison of the HERA–B $\sigma_{b\bar{b}}$ value with other experiments and with the theoretical predictions of R. Bonciani et al. [91] updated with the NNLL parton distribution function in [92] (solid line: central value, dashed lines: upper and lower bounds) and N. Kidonakis et al. [93] (dot–dashed line: central value, dotted lines: upper and lower bounds).* 49

1.26 **Left**: *HF production diagrams in $\gamma\gamma$ collisions.* **Right**: *Energy cut used in the $\gamma\gamma$ sample selection.* . 50

1.27 **Left** *: DELPHI fit to the p_T^{rel} distribution.* **Right**: *LEP heavy quark cross sections compared to theory expectations.* 51

1.28 *Bottom production measurements at the SppS ($\sqrt{s} = 630$ GeV)* **Left**: *UA1 measurements [100] of b quark integrated crosssection.* **Right**: *UA1 $\Delta\phi$ measurement [101] using μ–μ* 52

1.29 **Left**: *Differential cross section $d\sigma/dp_T^{B^+}$ compared to NLO QCD prediction. The solid curve represents the theoretical prediction for $m_b = 4.75$ GeV, $\mu_R = \mu_F = \mu = \sqrt{m_b^2 + p_T^2}$, while the dashed curves are obtained by setting $m_b = 4.5$ GeV, $\mu_R = \mu_F = \mu/2$, and $m_b = 5.0$ GeV, $\mu_R = \mu_F = 2\mu$ (from Reference [103]).* **Right**: *Moments of the measured B meson fragmentation function compared with the perturbative NLL calculation supplemented with different non–perturbative fragmentation forms $D(z)$. The solid line is obtained using a one–parameter form fitted to the second moment. section is influenced by this effect since the transverse momentum spectrum of the b–quark is steeply falling. In Reference [105]* 53

1.30 **Left**: *Prediction for the B cross section obtained using the calculation in [109], supplemented with the $N = 2$ fit of the non–perturbative fragmentation function, compared to the CDF data in Reference [103].* **Right**: *Theoretical prediction of the differential cross sections $d\sigma/dp_T^B$, calculated with different schemes and forms of the fragmentation function.* 54

1.31 *CDF results on the $b\bar{b}$ correlations using μ + b–tagged jet final states [118], compared to NLO QCD. Solid points correspond to the default theoretical prediction, with scales $\mu = \mu_0$, empty circles correspond to the difference between the choice $\mu = \mu_0/2$ and $\mu = 2\mu_0$. Top figure: tagged–jet E_T distribution. Central: muon p_T spectrum. Bottom: azimuthal correlations.* 55

1.32 *Results on $b\bar{b}$ correlations using dimuon final states, compared to NLO QCD. Left: azimuthal–correlation results from D0. Right: p_T distribution of the slowest muon from CDF.* 55

2.1 *Schematic view of the HERA storage ring and of its injection system.* 57

2.2 *The trend of integrated luminosity as a function of time in days is shown for years 1993 to 2000. On the* **Left** *the HERA delivered luminosity is presented while the faction used by ZEUS is on the* **Right**. . 59

2.3 *Beam currents intensity development during a run taken in 1997.* 59

2.4 *Cross section of the ZEUS detector in the vertical plane: side view (top), top view (middle). Cross section in transverse plane containing the nominal interaction point (bottom left)). The ZEUS reference frame (bottom Right)* . . . 61

2.5 **Left***: Cross section of the inner tracking detectors along the beam plane.* **Right***: Layout of a CTD octant in the transverse plane. The wires of the four superlayers with even numbers are slightly tilted with respect to the beam (stereo superlayers). The value of this angle is displayed below the corresponding superlayer in the figure.* . . . 63

2.6 **Left***: Momentum resolution as a function of the track's momentum.* **Right***: Momentum resolution as a function of the track's η and ϕ.* . . . 63

2.7 **Left***: Layout of the ZEUS high resolution Uranium-scintillator calorimeter. The picture shows the three sections of the UCAL and the polar-angle acceptance of each section.* **Right***: Internal structure of an FCAL module. The RCAL modules are very similar but they contain only two EMC cells instead of the four in FCAL and BCAL. One module in BCAL follows the same distribution as in FCAL but its geometry is adapted to the barrel requirements.* . . . 66

2.8 *Location of the barrel and rear muon chambers within the ZEUS detector.* . . . 68

2.9 *Three dimensional exploded view of the barrel and rear muon chambers.* . . . 68

2.10 **Left***: Cross section of a barrel-rear muon chamber in the transverse plane.* **Right***: Cross section of an LST tube used in the BRMUON chambers.* . . . 69

2.11 *Correlation between the momentum of the muon as measured in the CTD and in the BRMUON chambers. Distribution of the difference between the momentum measured in the CTD and the muon chambers. The systematic shift is due to energy loss in the dead material).* . . . 70

2.12 *Layout of the FMUON detector.* . . . 71

2.13 *Positions of the electron and photon taggers along the beam–line.* . . . 73

3.1 *Schematic representation of the processes involved in a typical hard QCD interaction.* . . . 77

3.2 *A schematic diagram of ZEUS data and Monte Carlo reconstruction chain.* . . . 81

4.1 *Trigger chain distribution for the photoproduction selection in data (bullets), charm Monte Carlo (middle histogram) and beauty Monte Carlo (bottom histogram).* . . . 87

4.2 *Check on the stability of the trigger selection with time. For each interval in integrated luminosity ($\sim$ 1 pb^{-1}) the ratio between the number of selected data events and the luminosity of the interval is plotted (bullets).* . . . 88

4.3 *The filled histogram shows the fraction of selected events over the number of analysed events for a beauty DIS Monte Carlo with an arbitrary normalisation factor.* . . . 88

4.4 **Left***: Correlation plots between the p_T and θ of the D^* reconstructed in the $K\pi\pi$ mode and the daughter π_s, K, π tracks (from top to bottom).* **Right***: the same for D^* decaying in the $K3\pi$ channel. A beauty DIS Monte Carlo has been used.* . . . 92

4.5 *Signal to background ratio dependence on the $p_T^{\pi_s}$ and $p_T^{D^*}/E_T$ cuts for $D^* \to K\pi$ in real data.* . . . 93

4.6 *Signal to background ratio dependence on the $p_T^{\pi_s}$ and $p_T^{D^*}/E_T$ cuts for $D* \to K3\pi$ in real data.* . . . 94

4.7 **Left***: D^* invariant mass peaks for the 1996-2000 data with a loose preselection on muon candidates and no trigger requirements. The upper histograms refer to the $K\pi$ mode, the lower ones to the $K3\pi$ mode. The right charge sample is represented with bullets while the wrong charge one is represented by the hatched histogram. The shaded area show the selected D^* signal region.* **Right***: The meaning is the same as for the Left plots but these histograms after applying the cuts described in Section 4.3.4.* 95

4.8 *The* **Left** *hand plots refer to* $D^* \to (K\pi)\pi$ *while those on the* **Right** *to* $D^* \to (K\pi\pi\pi)\pi_s$*. Each panel shows the reconstructed* Δm *and* $m(K\pi)$ $(m(K\pi\pi\pi))$ *distributions in the Monte Carlo under different assumptions. From top to bottom the following requirements were imposed at true level: 1) at least one* D^**, 2) at least one* $D^* \to (K\pi)\pi_s$*, 3) at least one* $D^* \to (K\pi\pi\pi)\pi_s$*, at least a* $D^* \to (K\pi\pi^0)\pi_s$*.* 95

4.9 **Left***: Data–Monte Carlo shape comparison of the* BREMAT *pulls.* **Right***: Shape comparison of the normalised distributions in the* BREMAT *4 d.o.f.* χ^2*, for an elastic dimuon sample and a beauty Monte Carlo true–muons sample. Data are shown as bullets while the (beauty) Monte Carlo is shown as the plain filled histogram.* 97

4.10 *Shape comparison of the normalised distributions in the* BREMAT *4 d.o.f.* χ^2 *for* BREMAT *matching candidates. The true muon, sail–through, decay in flight and other cases are shown separately. Charm Monte Carlo has been used.* 98

4.11 **Left***: from Top Left in counterclockwise order the* p_T*,* η*,* $\mathcal{P}_{4\ d.o.f.}$ *and* p_T *vs* η *for loose muon preselection.* **Right***: As for the Left plots but after applying the muon cuts outlines in Section 4.4.2.* 99

4.12 **Left** *: Distributions of* Δm *and* $m(D^0)$ *for events with at least a good* D^* *and a good muon candidate according to the cuts defined in Section 4.3.4 and 4.4.2. The upper plots refer to the* $K\pi$ *channel, the lower ones to the* $K3\pi$ *channel. The right charge sample is represented with bullets while the wrong charge one is represented by the hatched histogram. The shaded area show the selected* D^* *signal region.* **Right***: The distributions in* p_T*,* η*,* $\mathcal{P}_{4\ d.o.f.}$ *and* p_T *vs* η *for muons for the same sample used for the Left plots in this Figure.* 100

4.13 **Left***:* y_{JB} *resolutions in photoproduction. The upper plots show, from Left to Right,* y_{JB} *vs* y_{true}*,* $y_{JB} - y_{true}$ *vs* y_{true}*, the distribution of* $y_{JB} - y_{true}$*. The same plots are shown in the lower plots after a constant correction has been applied.* **Right***:* y_e *and* Q^2_{el} *resolutions in DIS. Upper plots:* y_{el} *vs* y_{true}*,* $y_{el} - y_{true}$ *vs* y_{true}*, distribution of* $y_{el} - y_{true}$*. Lower plots:* Q^2_{el} *vs* Q^2_{true}*,* $Q^2_{el} - Q^2_{true}$ *vs* Q^2_{true}*, distribution of* $Q^2_{el} - Q^2_{true}$ 101

4.14 *Distance in the* $\eta - \phi$ *plane between the* D^* *(upper plot) and* μ *(lower plot) at true and reconstructed level.* 101

4.15 **Left***: correlation between true and reconstructed values for the* p_T *and* η *of the muon and the* D^**.* **Right***: difference between the true and reconstructed values over the true value for the* p_T *and* η *of the muon and the* D^* 102

4.16 *Correlation between the true and reconstructed values for, from Left to Right, the* μD^* *angle in the azimuthal plane* $(\Delta\phi(\mu D^*))$*, the distance in the* η*–*ϕ *plane* $(\Delta R(\mu D^*))$ *and the invariant mass* $(m(\mu D^*))$*.* 102

5.1 *The plots shows the distribution of the transverse momentum of the produced beauty quark* (p^b_T)*. The arrows indicate roughly the sensibility achieved by the* μD^* *analysis and lepton+jets analyses.* 104

5.2 *Quark level cartoon for* $D^{*+} \to D^0$ *and* $D^0 \to K^-\pi^+$ *decay.* 105

5.3 *Diagrams showing the physics configurations yielding events with a* μ *and a* D^{*+}*. The upper Left diagram refers to* $c\bar{c}$ *production, the upper Right and lower ones to* $b\bar{b}$ *production. For simplicity's sake the charge conjugate modes have been omitted.* $c\bar{c}$ *events produce unlike sign* μD^* *pairs in different hemispheres while* $b\bar{b}$ *events produce unlike sign* μD^* *pairs in both the same or different hemispheres and like sign* μD^* *pairs in different hemispheres. Full explanation can be found in the text.* 107

5.4 *Dependence of the* p^μ_T *distributions on the parent hadron. The* **Left** *plot shows the* p^μ_T *distributions at hadron level for an inclusive DIS beauty Monte Carlo. The* **Right** *plot instead refers to reconstructed muons (i.e. matched to a track by the* BREMAT *algorithm with a* $\mathcal{P}_{4\ d.o.f.} > 0.01$*). A beauty* D^* *Monte Carlo was used in this case.* 108

5.5 **Left***: Correlation between the rapidity and transverse momentum of* b $(\bar{b})$ *quarks produced via the dominant boson gluon fusion mechanism in DIS at HERA.* **Right***: Kinematical correlations between the* p_T*,* y^{rap}*,* ϕ*, and* θ *in the laboratory frame, of* b *and* $\bar{b}$ *quarks for the same process.* 108

5.6 **Left**: *ΔR distributions at reconstructed level after the analysis cuts for the unlike sign and like sign samples in the beauty Monte Carlo (Left and Right upper plots), and in the charm Monte Carlo (Left and Right lower plots).* **Right**: *The same for $m_{\mu D^*}$.* 110

5.7 **Left**: *The bi-dimensional distributions of $m_{\mu D^*}$, $\Delta R_{\mu D^*}$, is presented for charm and beauty Monte Carlo. The cut in m between 3 and 5 GeV if $\Delta R < 2$ allows to reject a good fraction of fakes from charm without reducing the signal significantly.* **Right**: *The reconstructed ΔR distributions for beauty (top) and charm (bottom) after the cut outlined in the scatter plot on the Right.* 111

5.8 *Each plot shows the Δm reconstructed distribution for D^* in the $K3\pi$ mode for the unlike (Left side) and like sign (Right side) samples. The shaded histograms represent the wrong charge combinatorial D^* estimator under different assumptions (top and bottom) as explained in the text.* 113

5.9 *Each plot shows the sideband region (filled area) in the $\Delta m - m(K\pi)$ plane for the right charge (upper histogram) and wrong charge combinations (lower histogram). The rectangle indicates the signal mass region while the other area is the region where preselected D^* data are available. The $K\pi$ channel is shown on the Left side while the $K3\pi$ channel on the Right one. The sideband is defined in the following intervals in ($m(D^0)$,Δm) for the $K\pi$ and $K3\pi$ channels respectively: ([1.78,1.95],[0.15,0.17]) GeV and ([1.68,2.05],[0.15,0.165]) GeV.* 113

5.10 *The ΔR (***Left** *plots) and m (***Right** *plots) distributions in the right charge (bullets) and wrong charge (hatched histogram) sample in the sidebands have been compared for the $K\pi$ D^* mode. The wrong charge sample is taken averaging in the muon sign as described in the text. The unlike sign sample is shown in the upper plots, the like sign sample in the lower ones. The signal enriched region $\Delta R < 2$, $3 < m < 5$ GeV is shown in the Left column, the charm enriched region ($\Delta R > 2$) on the Right. All the analysis cuts have been applied. Both DIS and photoproduction have been included.* 114

5.11 *The ΔR (***Left** *plots) and m (***Right** *plots) distributions in the right charge (bullets) and wrong charge (hatched histogram) sample in the sidebands have been compared for the $K3\pi$ D^* mode. The wrong charge sample is taken averaging in the muon sign as described in the text. The unlike sign sample is shown in the upper plots, the like sign sample in the lower ones. The signal enriched region $\Delta R < 2$, $3 < m < 5$ GeV is shown in the Left column, the charm enriched region ($\Delta R > 2$) on the Right. All the analysis cuts have been applied. Both DIS and photoproduction have been included.* 114

5.12 **Left**: *Distribution of $p_T^{\mu D^*}/E_T$ in the unlike sign sample for data in the $K\pi$ channel after all cuts except the cut on $p_T^{\mu D^*}/E_T$. The right (bullets) and wrong charge (dashed histogram) D^* samples are shown separately.* **Right**: *Distributions of $p_T^{\mu D^*}/E_T$ for charm (plain line) and beauty (dotted line) in the unlike (top) and like (bottom) sign sample. The vertical line indicates the value of the cut.* 116

5.13 *Display of a candidate $ep \to b\bar{b}e'X \to \mu D^* X'$ event.* **Left**: *view in the transverse plane.* **Right**: *radial view in a plane parallel to the beam axis.* 117

5.14 *Distribution of $\Delta m(D^* - D^0)$ (***Left** *side) and $m(D^0)$ (* **Right** *side) for data (bullets), and combinatorial background (hatched histogram). The inclusive $K\pi$ data sample (PHP+DIS) has been used. The unlike sign (a)) and like sign (b)) μD^* combinations are shown separately in the upper and lower plots respectively. The D^* signal region is indicated by the shaded area.* 118

5.15 *Distribution of $\Delta m(D^* - D^0)$ (***Left** *side) and $m(D^0)$ (* **Right** *side) for data (bullets), and combinatorial background (hatched histogram) for the $K\pi$ DIS sample. The unlike sign (a)) and like sign (b)) muon-D^* combinations are shown separately in the top bottom plots respectively. The D^* signal region is indicated by the shaded area.* 119

5.16 *Distribution of $\Delta m(D^* - D^0)$ for $K3\pi$ data (bullets), and combinatorial background (hatched histogram) for a) inclusive unlike sign b) inclusive like sign. In the like sign plot the wrong charge component obtained by averaging on the muon sign overestimates the like sign combinatorial background by a factor 1.7. The hatched histogram shown in the like sign plot has then been weighted accordingly in order to reproduce the like sign combinatorial background. The D^* signal region is indicated by the shaded area.* 120

5.17 *Distribution of $\Delta m(D^* - D^0)$ (**Left**) $\Delta R(D^* - \mu)$ (**Center**) and $m(D^* - \mu)$ (**Right**) for data (bullets), heavy flavour signal (red hatched: beauty, green hatched: charm) and background (blue: fake μ, gray: D^*). Cuts described in the text are indicated by red arrows.* 121

5.18 *a) ΔR and b) $\Delta\phi$ distributions of the μD^* system for inclusive unlike sign events, after subtraction of the fake D^* background. Data points (bullets) are shown together with the fitted contributions from beauty and charm, as indicated in the legend. The fake muon contribution from charm is shown separately, but fitted together with the charm contribution. The beauty contribution includes a very small fraction of fake muons from beauty.* 123

5.19 *$\Delta m(D^* - D^0)$ distributions for four different regions of inclusive phase space. The data are shown as full circles. The beauty and charm contributions, and the fake muon and combinatorial D^* backgrounds are indicated as shown in the legend. The number (rounded to the nearest integer) of beauty, charm and fake muon candidates is indicated in each figure.* 124

5.20 *a) ΔR and b) $\Delta\phi$ distributions of the μD^* system for inclusive unlike sign events, after subtraction of the fake D^* background. Data points (bullets) are shown together with the fitted contributions from beauty and charm, as indicated in the legend. The fake muon contribution from charm is shown separately, but fitted together with the charm contribution. The beauty contribution includes a very small fraction of fake muons from beauty.* 125

5.21 *Control plots for the photoproduction selection for events with a $D^* \to (K\pi)\pi_s$ in the beauty (**Left** plots) and charm (**Right** plots) enriched region. The beauty, charm and fake D^* components are indicated with different hatch styles (see legend).* 126

5.22 *Control plots for the DIS subsample in the $K\pi$ mode. The meaning of hatch styles is the same of Figure 5.21.* 126

5.23 *Control plots for the photoproduction selection for events with $D^* \to (K\pi\pi\pi)\pi_s$ in the signal (**Left**) and background (**Right**) region. The beauty, charm and fake D^* components are indicated with different hatch styles (see legend).* 127

5.24 **Top** *plot: Muon efficiency corrections for tracks in the barrel region ($\theta < 2.356$ rad) as a function of their transverse momentum.* **Bottom** *plot: efficiency corrections for tracks in the rear region ($\theta < 2.356$ rad). The correction factors have been obtained from a dimuon sample as described in [166].* . 129

5.25 *Dependence of the acceptance on the muon and D^* variables.* **Left** *plots: Distributions of the muon and D^* p_T and η. Plain histograms refer to events in the kinematic region ($p_T^\mu > 1.4$, $-1/75 < \eta^\mu < 1.3$ for muons, $p_T^{D^*} > 1.9$, $|\eta^{D^*}| < 1.5$ for D^*), hatched histograms to the reconstructed events with the standard cuts.* **Right***: The ratio between the histograms of the Left part.* 129

5.26 *Comparison between the measured visible cross section in the $K\pi$ mode and those in the $K3\pi$ in the $K\pi$ kinematic region. Left points refer to the inclusive sample, Right points to photoproduction.* . . . 131

5.27 *Summary of the systematic checks. The variation of the central value of the visible cross sections is plotted for each systematic check. From Left to Right: inclusive, photoproduction and DIS in the $K\pi$ channel, inclusive and photoproduction in the $K3\pi$ channel. The horizontal upper segment indicates the statistical error.* 133

5.28 *The* **Right** *hand plots show the Δm (top) and $m_{K\pi}$ distributions for a Monte Carlo sample containing light and heavy flavour partonic processes. The events with charm and beauty in the hard process are shown by the bullets while the contribution from gluon splitting to $c\bar{c}$ and $b\bar{b}$ (in both light and heavy flavour processes) is shown in the differently hatched histograms (see the legend). The* **Left** *hand plots show the ΔR, m and $\Delta\phi$ distributions in the final selection for gluon splitting from light flavour events (shaded histogram) and all heavy flavour events (solid histogram).* 134

5.29 *Comparison of the spectrum of the muon with recent e^+e^- data for electrons. Note that in the experimental data the contributions from V_{ub} is also present as it is clear from the tail at high values of the momentum.* 135

5.30 *Shape comparison of the distributions for the true p_T, and η of D^* and muons, y and Q^2 in the* PYTHIA *and* HERWIG *Monte Carlo. The comparison is done for all events (***Left** *plots) and only for those in the photoproduction kinematic region (***Right** *plots).* 137

5.31 *Shape comparison of the distributions for the true p_T, and η of D^* and muons, y and Q^2 in the* RAPGAP *and* HERWIG *Monte Carlo. The comparison is done for all events (***Left** *plots) and only for those in the DIS kinematic region (***Right** *plots).* 137

5.32 *Transverse momentum and rapidity of b and $\bar{b}$ quarks for signal events satisfying all the analysis cuts in the* RAPGAP *Monte Carlo.* 138

5.33 *The* **Left** *hand side refers to photoproduction while the* **Right** *hand side to DIS. In each case the Left plot shows the p_T^b distribution and the Right plot the y_{rap}^b distribution. The full line histogram contains all b or $\bar{b}$ quarks with $y_{rap}^b < 1$ in events with $0.05 < y < 0.85$ and $Q^2 < 1$ GeV^2 ($0.05 < y < 0.7$ and $Q^2 > 2$ GeV^2 for the DIS plot). In the p_T^b distributions $y_{rap}^b < 1$ is required in addition. The dashed line histogram contains events with in addition at least a D^* and a muon. In the dotted line histogram only events enter for which D^* and μ also belong to the kinematic regions.* 139

5.34 *Shape comparison of the p_T^b spectra in the NLO calculations and Monte Carlo. The* **Left** *plot compares* FMNR *and* PYTHIA. *The comparison is restricted to quarks with $y_b^{rap} < 1$ in events with $0.05 < y < 0.85$, $Q^2 < 1$ GeV^2. The* **Right** *hand plot shows a comparison between* HVQDIS *and* RAPGAP. *In this case quarks with $y_b^{rap} < 1$ in events with $0.05 < y < 0.7$, $Q^2 > 2$ GeV^2 were considered.* 140

5.35 **Top***: Cross section for single b or $\bar{b}$-quark production in the rapidity range $y_{rap}^b < 1$ for photoproduction (PHP, Left) and DIS (right), compared to NLO QCD predictions from FMNR (Left) and HVQDIS (right). The PHP cross section is for $0.05 < y < 0.85$, and the DIS cross section for $0.05 < y < 0.7$. The cross sections are integrated over the indicated Q^2 ranges, and over the full p_T^b range. More details on the QCD calculations are given in the text.* **Bottom** *The extrapolated beauty cross section at a fixed p_T^{min} value compared with theoretical predictions plotted as a function of p_T^{min}. The curves show the predictions from NLO QCD for varying the b–quark mass and the factorisation and renormalisation scales. The inner error bars indicate the statistical error while the full ones indicate the total error obtained by adding in quadrature the statistical and total systematic error.* 142

6.1 *The Left hand plots refer to $D^* \to (K\pi)\pi$ events while those on the Right to $D^* \to (K3\pi)\pi$ events. From Left to Right the upper plots show the correlation in the* PYTHIA *Monte Carlo between the azimuthal angle, transverse momentum and rapidity of the μD^* system and of the originating b or $\bar{b}$ quark. The lower plots show the distribution of the difference between these quantities at μD^* and b level.* 144

6.2 *$p_T^{\mu D^*}$ and $y_{\mu D^*}^{rap}$ distributions in the data. The wrong charge D^* contribution (average of like and unlike sign) is shown y the dashed histogram.* 144

6.3 *The Left hand plots refer to $D^* \to (K\pi)\pi$ events while those on the Right to $D^* \to (K3\pi)\pi$ events. The plots show a comparison between the distributions of $p_T^{\mu D^*}$ and p_T^b and between $y_{\mu D^*}^{rap}$ and y_b^{rap}. The solid line histograms refer to the μD^* level variables while the dashed histograms represent the distributions at quark level. The histograms with bullets represent the ratio between the distributions at quark level and μD^* level.* 146

6.4 **Left***: The upper plots show the efficiency, purity and acceptance as a function of p_T^b in the $K\pi$ channel. The corresponding quantities as a function of y_b^{rap} are shown in the lower plots.* **Right***: As for the Left part for the $K3\pi$ channel.* 147

6.5 *Differential cross sections $d\sigma/dp_T^b$ for the $K\pi$ mode (***Left***) and $K3\pi$ (***Right***). The NLO FMNR prediction is indicated by the plain histogram.* 148

6.6 *Differential cross sections $d\sigma/y_b^{rap}$ for the $K\pi$ mode (***Left***) and $K3\pi$ (***Right***).* 148

6.7 *Comparison of the differential cross sections in p_T^b (upper plot) and y_b^{rap} lower plot in the $K\pi$ (filled bullets) and $K3\pi$ channels (hollow bullets). The plain histogram represents the NLO FMNR prediction scaled to the visible region to which the cross sections refer (see text).* 149

A.1 *Display of four events with a candidate pion from K^0_S producing a fake–muon in BRMUI. Each plot shows a zoomed XY view (Left part) and a RZ view (Right part). The kaon tracks can be identified by the fact that their intersection is visibly displaced from the interaction point. They are shown in green.* 155

A.2 *The plot shows the $K^0_S \to \pi^+\pi^-$ invariant mass peak using the statistics accumulated by ZEUS in the years 1996–2000. Events having at least one of the two tracks satisfying the requisites for being fake–muon candidates (see Equation A.1) are shown.* 157

A.3 *Data–Monte Carlo comparison of p and θ distributions for the initial samples of K^0_S (black) and Λs (red). Data are represented as bullets, Monte Carlo as the plain line histograms.* **Left***: before θ–reweighting in the Monte Carlo.* **Right***: after θ–reweighting.* 158

A.4 **Left***: From Top to Bottom, distributions of polar angle, momentum and azimuthal angle of all K^0_S tracks (red bullets) and of those which are matched to BRMUI by* BREMAT *with $\mathcal{P}_{4\ d.o.f.} > 0.01$ (blue bullets, shaded yellow histogram). The ZEUS 1996-2000 statistics have been used.* **Right***: Data–Monte Carlo comparison of fake–muon probabilities for $4\ d.o.f.$ matching with* BREMAT *as a function of, from Top to Bottom, momentum, polar angle an azimuthal angle. Data are represented as black bullets with a yellow band for the statistical errors while Monte Carlo is represented by red squares.* 158

A.5 **Left***: θ distributions in bins of p ($[0.9, 1.1, 1.3, 1.5, 1.7, 1.9, 2.3, 3.2, 10]$ GeV) for pions from K^0_S. The meaning of the symbols is the same as in Figure A.4. The ZEUS 1996–2000 data have been used requiring a 4 d.o.f.* BREMAT *matching with $\mathcal{P} > 0.01$.* **Right** *: p distributions in bins of θ ($[0.4, 0.555, 0.71, 0.865, 1.02, 1.175, 1.33, 1.485, 1.64, 1.795, 1.95, 2.105, 2.26, 2.415, 2.57, 2.725, 2.88]$ rad). The chosen binning is also indicated in each plot.* 159

A.6 *Data–Monte Carlo comparison of double differential fake–muon probabilities for pions from K^0_S adopting a $4\ d.o.f.$ matching with* BREMAT *($\mathcal{P} > 1\ \%$) as a function of polar angle in bins of momentum (***Top** *plots) and as a function of momentum in polar angle bins (***Bottom** *plots). Data are represented as black bullets with a yellow band for the statistical errors while Monte Carlo is represented by red squares.* 160

A.7 **Left***: Comparison between the fake–muon probability using BRMUI matched tracks ($\mathcal{P}_{4\ d.o.f.} > 0.01$) or requiring a BRMUO match in addition ($\mathcal{P}_{5\ d.o.f.} > 0.05$).* **Right***: Data–Monte Carlo comparison for the fake–muon probability using the BRMUO match ($\mathcal{P}_{5\ d.o.f.} > 0.05$).* 161

A.8 *Distribution of the reconstructed $m_{\pi\pi}$ in the Monte Carlo. The plot shows cumulatively the various contributions in differently filled histograms. See the legend.* 162

A.9 **Left***: Distributions of momentum (Top plot) and polar angle (Bottom plot) for pions from K^0_S which are reconstructed as muons in the Monte Carlo. True muons, sail–through, decay–in–flight and contributions from other cases are shown cumulatively with different hatch coding (see the legend).* **Right***: The same distributions in the Left plot shown separately. The plots in the Bottom row show the invariant mass distributions.* 163

A.10 *Distributions of the χ^2 at 4 d.o.f. (***Left** *plot) and 5 d.o.f. (***Right** *plot) for matched pion tracks from K^0_S decay. For the Monte Carlo true muons, sail–through, decay–in–flight and other cases are shown separately (see the legend). The corresponding distributions in data (bullets) are compared in shape to the Monte Carlo.* 163

A.11 **Left***: Fraction of matched tracks in the sample of pions from K^0_S as a function of the cut in the 4 d.o.f. matching probability.* **Right***: From Top to Bottom, the various curves show the distribution in polar angle, momentum and azimuthal angle for the sample of matched tracks as the probability cut is varied (according to the Right hand plot values).* 164

A.12 *The upper plot shows the $\Lambda \to p\pi$ invariant mass peak. ZEUS 96–00 data were used. The scatter–plot shows the invariant masses obtained on a sample of secondary vertex tracks using the $\pi\pi$ mass hypothesis (x–axis) or the $p\pi$ one (y-axis). The vertical band corresponds to $K^0_S \to \pi\pi$ decays, the horizontal band corresponds to $\Lambda \to p\pi$ decays. The red lines show the anti–K^0 and anti–conversion cuts described in A.5.* 165

A.13 **Left**: *From top to bottom, distributions of momentum, polar angle and azimuthal angle of proton tracks from Λ decay (red bullets) and of those which are matched to BRMUI by* BREMAT *with $\mathcal{P}_{4\ d.o.f.} > 0.01$. ZEUS 96-00 data have been used.* **Right**: *Data–Monte Carlo comparison of fake–muon probabilities for $4\ d.o.f.$ matching with* BREMAT *as a function of, top to bottom, momentum, polar angle an azimuthal angle.* 165

A.14 *Data–Monte Carlo comparison of double differential fake–muon probabilities for protons(anti-protons) from $\Lambda(\bar{\Lambda})$ adopting a $4\ d.o.f.$ matching with* BREMAT *($\mathcal{P} > 1\ \%$) as a function of polar angle in bins of momentum (***Top** *plots) and as a function of momentum in polar angle bins (***Bottom** *plots). Data are represented as black bullets with a yellow band for the statistical errors while Monte Carlo is represented by red squares.* 167

A.15 *Distribution of the reconstructed $m_{p\pi}$ in the Monte Carlo. The plot shows cumulatively the various contributions in differently filled histograms. See the legend.* 168

A.16 *The two plots show the $\phi \to K^+K^-$ invariant mass peak. Events having at least one of the two tracks with $p_T > 0.9$ GeV and $-2 < \eta < 1.6$ are shown in the* **Left** *plot. The* **Right** *hand plot is instead for $p_T > 0.9$ GeV and $-0.88 < \eta < 1.6$. In order to compare with the Monte Carlo we restricted to this second region (see text for details).* 169

A.17 **Left**: *From top to bottom, distributions of momentum, polar angle and azimuthal angle of all ϕ tracks (red bullets) and of those which are matched to BRMUI by* BREMAT *with $\mathcal{P}_{4\ d.o.f.} > 0.01$ (shaded histogram). ZEUS 1996-2000 data have been used.* **Right**: *Data–Monte Carlo comparison of fake–muon probabilities for $4\ d.o.f.$ matching with* BREMAT *as a function of, top to bottom, momentum, polar angle an azimuthal angle.* 169

A.18 *The reconstructed $m_{K\pi\pi_s} - m_{K\pi}$ (***Left***) and $m_{K\pi}$ (***Right***) distributions in the data after the cuts in A.5. Data collected in the years 1996-2000 were used.* 170

A.19 **Top Left**: *From top to bottom, distributions of momentum, polar angle and azimuthal angle of pion tracks from D^0 (red hollow bullets) and of those which are matched to BRMUI by* BREMAT *with $\mathcal{P}_{4\ d.o.f.} > 0.01$ (shaded yellow histogram). ZEUS 96-00 data have been used.* **Top Right**: *Data–Monte Carlo comparison of fake–muon probabilities for $4\ d.o.f.$ matching with* BREMAT *as a function of, top to bottom, momentum, polar angle an azimuthal angle for pions from D^0. The equivalent plots for kaons from D^0 are shown in the lower half of the Figure.* 171

A.20 *Data–Monte Carlo comparison of double differential fake–muon probabilities for pions (***Top** *plots) and kaons (***Bottom** *plots) from D^0 adopting a $4\ d.o.f.$ matching with* BREMAT *($\mathcal{P} > 1\ \%$) as a function of polar angle in bins of momentum (***Left** *plots) and as a function of momentum in polar angle bins (***Right** *plots). Data are represented as black bullets with a yellow band for the statistical errors while Monte Carlo is represented by red squares.* 172

A.21 **Top**: *Distributions of the reconstructed m_{D^0} (Left plot) and Δm (Right plot) in the Monte Carlo. The light (yellow) filled histogram shows the same distributions for events with a true decay $D^0 \to K\pi$, the darker (green) histogram corresponds to events containing a $D^0 \to K\mu\nu$ decay.* **Bottom**: *Reconstructed m_{D^0} VS Δm in the Monte Carlo for events with a $D^0 \to K\mu\nu$ decay.* 173

A.22 **Left**: *Distributions of momentum and polar angle for kaon (Top plots) and pion (Bottom plots) from D^0 which are reconstructed as muons in the Monte Carlo. True muons, sail–through, decay–in–flight and contributions from other cases are shown cumulatively with different hatch coding (see the legend).* **Right**: *The same distributions in the Left plot shown separately. The plots in the Bottom row show the invariant mass distributions.* 174

A.23 **Top**: *Shape comparison between the distributions of input tracks in the $K^0_S \to \pi^+\pi^-$, $\Lambda \to p\pi$, $\phi \to K^+K^-$, $D^0 \to K\pi$ samples (see the legend). Momentum is shown in the upper plot, polar angle in the lower one.* **Bottom**: *Fake probabilities summary plot.* 175

A.24 *The* **Left** *hand top plot shows the comparison between the momentum distributions of pion tracks from K^0_S (black bullets) and D^0 (hollow squares) with an arbitrary normalization factor. The* **Left** *bottom plot shows the $\mathcal{P}_{\rm fak}(\theta)$ probability with analogous symbols. The same quantities are compared after the reweighting of the pions from K^0_S momentum to the one for pions from D^0 in the* **Right** *hand plots.* 176

A.25 *The* **Left** *hand top plot shows the comparison between the momentum distributions of kaon tracks from ϕ (blue triangles) and D^0 (hollow bullets) with an arbitrary normalization factor. The* **Left** *bottom plot shows the $\mathcal{P}_{\rm fak}(\theta)$ probability with analogous symbols. The same quantities are compared in the* **Right** *hand plots after the reweighting of the kaons from D^0 momentum to the one for kaons from ϕ.* . 176

B.1 *Control plots for the photoproduction selection for events with $D^* \to (K\pi)\pi_s$ in the signal (***Top***) and background (***Bottom***) region.* 180

B.2 *Control plots for the photoproduction selection for events with $D^* \to (K\pi)\pi_s$ in the signal (***Top***) and background (***Bottom***) region.* 181

B.3 *Control plots for the photoproduction selection for events with $D^* \to (K\pi\pi\pi)\pi_s$ in the signal (***Top***) and background (***Bottom***) region.* 182

B.4 *Control plots for the photoproduction selection for events with $D^* \to (K\pi\pi\pi)\pi_s$ in the signal (***Top***) and background (***Bottom***) region.* 183

List of Tables

1.1 *Partial and total cross sections (nb) for the process $\sigma(ep \to b\bar{b}X)$ at HERA ($\sqrt{s}$ =314 GeV) in the DIS and $\overline{MS}$ renormalisation schemes. $m_b = 4.75$ GeV is assumed. (Reference [20])* 26

1.2 *Pointlike component of the total beauty cross section (nb), in p collisions, for different choices of the input parameters.* 31

1.3 *Hadronic component of the total beauty cross section (nb), in p collisions, for different choices of the input parameters.* 31

2.1 *Nominal parameters of the HERA storage ring.* 58

2.2 *Luminosity collected by ZEUS in 1993-2000. The difference between "on-tape" and "physics" comes from the rejection of data considered not useful for analysis by the offline data quality monitoring.* . . 74

3.1 *Equivalent luminosities of the beauty and charm Monte Carlo samples for the year 1996-2000 used in the analysis.* 82

5.1 *All possible prompt muon + D^* configurations in $b\bar{b}$ events assuming that the D^* will not produce muons (i.e. $D^* \to K\pi\pi_s$ and $D^* \to K\pi\pi\pi\pi_s$). The following branching ratios have been adopted ([161]): $\mathcal{B}(\bar{b} \to D^{*-}\,\mathrm{X}) = (17.3 \pm 2)\,\%$, $\mathcal{B}(\bar{b} \to \mu^+\,\mathrm{X}) = (10.7 \pm 0.7)\,\%$, $\mathcal{B}(\bar{b} \to D^{*-}\,\mu^+\,\mathrm{X}) = (2.75 \pm 0.19)\,\%$. We have denoted with $\mathcal{B}$ in the last column the branching ratio (not taken in %) for the D^* decays to $K\pi\pi_s$ and $K\pi\pi\pi\pi_s$. They are given in Equations 5.1 and 5.2.* 106

5.2 *Acceptances for different samples, Monte Carlo in the $K\pi$ and $K3\pi$ channels.* 130

5.3 *The relative variations of the measured visible cross sections (in different columns) for the considered systematic checks (rows) are given in the Table. The contributions coming from the description of $p_T^{\mu D^*}$ and $p_T^{\mu D^*}/E_T$ distributions are grouped separately as well as the part due to cut variations. The partial systematic errors, obtained by quadratic sum, are given in the rows denoted as "combined".* . 133

6.1 *Summary of the quantities used in the differential cross section calculation. From top to bottom: $d\sigma/dp_T^b$ in the $K\pi$ mode, $d\sigma/dy_b^{rap}$ in the $K\pi$ mode, $d\sigma/dp_T^b$ in the $K3\pi$ mode, $d\sigma/dy_b^{rap}$ in the $K3\pi$ mode.* 147

A.1 *Summary on fake–muons probabilities for data and Monte Carlo in different samples with 4 d.o.f. and 5 d.o.f.* BREMAT. *See the text for more details.* 177